Simulated spin qubits in silicon quantum dots and enhancement of InGaAs photodetectors

by

Zach D. Merino

A thesis
presented to the University of Waterloo
in fulfillment of the
thesis requirement for the degree of
Doctor of Philosophy
in
Physics (Quantum Information)

Waterloo, Ontario, Canada, 2025

© Zach D. Merino 2025

Examining Committee Membership

The following served on the Examining Committee for this thesis. The decision of the Examining Committee is by majority vote.

External Examiner:	Jason Kestner Associate Professor, Dept. of Physics, University of Maryland
Supervisor(s):	Jonathan Baugh Professor, Dept. of Chemistry, University of Waterloo
Internal Member:	Raffi Budakian Professor, Dept. of Physics and Astronomy, University of Waterloo
Internal-External Member:	Na Young Kim Associate Professor, Dept. of Electrical and Computer Engineering, University of Waterloo
Other Member(s):	Matteo Mariantoni Associate Professor, Dept. of Physics and Astronomy, University of Waterloo

Author's Declaration

This thesis consists of material all of which I authored or co-authored: see Statement of Contributions included in the thesis. This is a true copy of the thesis, including any required final revisions, as accepted by my examiners.

I understand that my thesis may be made electronically available to the public.

Statement of Contributions

Chapter 2 Contributions: Bohdan Khromets and I developed various modules of the Quantum Dots in Python (QuDiPy) simulation package, both significantly contributing to the design decisions. Bohdan Khromets took a leading role in suggesting the module structure for optimal data flow, while I took a greater lead in data structure design and code/memory efficiency. We have both contributed to the design of the physical models implemented in QuDiPy; Bohdan Khromets developed many key aspects of the theoretical framework, and I have made minor revisions. Specifically, I developed a module to process simulated 3D electrostatic potentials, construct a QD Hubbard model, and determine the regions of charge stability in QD devices under various externally applied voltage conditions. Additionally, I have implemented numerical methods isolating QD potentials, constructing multidimensional interpolation functions, and solving Schrödinger's equation on non-uniformly spaced coordinate grids. Bohdan Khromets developed the theory for an optimal control strategy to design voltage pulses for semiconductor spin qubit arrays and rewrote the code of our control pulse module for improved voltage pulse design. I initially developed the code to perform spin qubit optimal control based on Bohdan Khromets' theoretical MSc thesis work [1], which was later rewritten by Bohdan Khromets to increase state fidelity that resulted from simulated voltage pulse gate operations. Part of Andrija Paurevic's MSc thesis developed a version of GRAPE optimal control [2] which has started to be integrated with the simulator. Dr. Brandon Buonacorsi was the primary developer of the simulator at its initial inception in 2019, with Stephen R. Harrigan as a supporting developer, prior to Bohdan Khromets and me performing a full rewrite of the codebase.

This chapter is based on a manuscript currently being prepared for submission to a journal and adaptations from:

Z. D. Merino, B. Khromets, and J. Baugh, *Simulated Charge Stability in a MOSFET Linear Quantum Dot Array.* Springer International Publishing, Cham, Switzerland, 2025.

B. Khromets, **Z. D. Merino**, and J. Baugh, *Hamiltonian engineering with time-ordered evolution for unitary control of electron spins in semiconductor quantum dots.* Springer International Publishing, Cham, Switzerland, 2025.

Chapter 3 Contributions: Rubaya Absar proposed the creation of a spin qubit compact model and wrote the compact model simulator using Verilog-A in the [3] and [4] circuit simulation software packages. The master equation solutions for a global Electron Spin Resonance (ESR) spin Hamiltonian and the analytic Hamiltonian effective functions were derived by me. Programmatic design decisions in Verilog-A were made jointly by Rubaya Absar and me.

This chapter is based on a manuscript currently being prepared for submission to a journal.

Chapter 4 Contributions: I performed the experimental work characterizing photodetectors and Nanocrystal (NC) solutions for drop casting, data analysis and plotting, and led the writing of the manuscript. Gyorgy Jaics synthesized and characterized NC samples and contributed to writing the manuscript. Andrew Jordan fabricated the photodetectors. Arjun Shetty conducted initial photodetector fabrication and characterization. Penghui Yin conducted initial nanocrystal synthesis and characterization. Man Chun Tam grew the InGaAs wafer. Xinning Wang performed optical measurement work.

This chapter is adapted from the publication:

Z. D. Merino, Gy. Jaics, A. W. M. Jordan, A. Shetty, P. Yin, M. C. Tam, X. Wang, Z. R. Wasilewski1, P. V. Radovanovic, J. Baugh, Enhancement of Photoresponse for InGaAs Infrared Photodetectors Using Plasmonic WO_{3-x}/Cs_yWO_{3-x} Nanocrystals. *Nanotechnology*, vol. 36, p. 015201, Oct. 2024.

Abstract

Semiconductor quantum dot spin qubits are a leading candidate for scalable, fault-tolerant quantum computing. Their advantages include nanoscopic device size, compatibility with foundry fabrication processes, and long coherence times relative to gate durations. The fabrication and control of a quantum processing unit composed of tens of thousands to millions of physical qubits pose many engineering challenges. These challenges fall broadly into two categories: device design, such as optimizing the geometry for high-quality qubit formation, and qubit control, which involves the precise manipulation of spin or charge states in qubits that are capacitively coupled to numerous neighboring electrodes. In this thesis, we develop a simulation tool that accelerates device design iteration prior to fabrication by providing a priori knowledge of the quantum dot electrostatic potential landscape as a function of external electrode voltages. This enables effective spin and Hubbard Hamiltonian parameters to be computed before experimental characterization, facilitating early-stage control method development and device performance prediction. The tool, implemented as the Python-based QuDiPy package, integrates three-dimensional finite-element Poisson solutions with modules for electrostatic reconstruction, Hamiltonian parameter extraction, and control pulse optimization. Unlike previous disjointed toolchains, QuDiPy offers a unified workflow for full-stack qubit control simulations, including automated voltage-to-Hamiltonian mapping for exploring high-dimensional gate voltage spaces and mitigating crosstalk in dense qubit arrays. The simulator is designed to be memory- and CPU-efficient to enable computationally efficient simulation of linear quantum dot arrays consisting of several qubits. Simulation of small quantum dot arrays serves as a design tool for control protocols within multi-node quantum processors. Simulation of spin qubit dynamics in many-qubit nodes connected in a network enables the study of required voltage ranges for maintaining stable charge configurations in the device. It also supports the design of experimental input pulses to generate maximally entangled Greenberger–Horne–Zeilinger (GHZ) states between nodes, a key step for implementing surface code error correction protocols.

Spin qubit control requires a precise understanding of the impact of experimental controls, such as electrode voltages or radio-frequency magnetic field amplitude and phase, on effective parameters such as electronic g-factor, exchange energy, chemical potential, etc. A mapping between experimental and effective parameters is created by performing effective parameter calculations on two-dimensional cross-sections of the electrostatic potential landscape obtained from a 3-dimensional Poisson solver `nextnano++`, a commercially available, 3D Poisson solver chosen for its robustness, flexibility in defining quantum device geometries, and proven accuracy in modeling semiconductor heterostructures at cryogenic

temperatures. First, a 2D cross-section of the electrostatic potential landscape is taken along the growth direction of the quantum dot device, near the heterojunction where qubit formation occurs. This region is selected because it captures the horizontal confinement profile most relevant to charge localization and wavefunction shape. The cross-section is extracted for all simulated voltage configurations applied to the gate electrodes. Second, the single-particle ground state or first excited state wavefunctions are determined using a non-uniform grid Schrödinger solver for all voltage configurations and for each isolated quantum dot or nearest-neighbor quantum dot pair. The non-uniform grid provides higher spatial resolution near confinement potential minima, enabling more accurate modeling of localized wavefunctions where precision is most critical. The mapping between input voltage and single-particle wavefunctions is leveraged, along with numerical integration routines, to calculate the desired effective parameters as a function of voltage. The chemical potential, tunnel coupling, and onsite and interdot Coulomb parameters are computed for each voltage configuration. This enables exact diagonalization of the Hubbard Hamiltonian at every point in voltage space and identifies the regions of charge stability for a multiqubit quantum dot device. This step is essential for establishing control over the quantum processor.

The second part of this thesis investigates optoelectronic device enhancement using localized surface plasmons in nanocrystals. Fast and accurate detection of light in the near-infrared (NIR) spectral range plays a crucial role in alleviating speed and capacity bottlenecks in optical communications and in enhancing the control and safety of autonomous vehicles through NIR imaging systems. Several technological platforms are currently under investigation to improve NIR photodetection, aiming to surpass the performance of established III–V semiconductor p-i-n (PIN) junction technology. These platforms include in situ-grown inorganic nanocrystals (NCs) and nanowire arrays, as well as hybrid organic–inorganic materials such as graphene-perovskite heterostructures. However, challenges remain in NC and nanowire growth, large-area fabrication of high-quality 2D materials, and the fabrication of devices for practical applications. Here, we explore the potential for tailored semiconductor NCs to enhance the responsivity of planar metal–semiconductor–metal (MSM) photodetectors. MSM technology offers ease of fabrication and fast response times compared to PIN detectors. We observe enhancement of the optical-to-electric conversion efficiency by up to a factor of $\sim$2.5 through the application of plasmonically-active semiconductor nanorods and NCs. We present a protocol for synthesizing and rapidly testing the performance of non-stoichiometric tungsten oxide (WO) nanorods and cesium-doped tungsten oxide (Cs_yWO) hexagonal nanoprisms prepared in colloidal suspensions and drop-cast onto photodetector surfaces. The results demonstrate the potential for a cost-effective and scalable method exploiting tailored NCs to improve

the performance of NIR optoelectronic devices.

Acknowledgements

I would like to thank my supervisor, Jonathan Baugh, for the opportunity to attend the Institute for Quantum Computing (IQC), without which the work in this thesis would not be possible. I am fortunate to have studied under such a professional researcher and curious scientist. I would also like to thank my advisory committee members, Raffi Budakian, Na Young Kim, and Matteo Mariantoni, for all of their constructive advice on this body of work. I would like to thank Jason Kestner for being part of my examination committee and for providing valuable feedback. A large thanks to all of the IQC and QNFCF cleanroom staff members I have had the joy of interacting with over the years.

My thanks extend to all of the present and past Coherent Spintronics Group (CSG) members that I have had the fortune to work beside and get to know. In particular, I would like to thank Dr. François Sfigakis for his selfless sharing of his semiconductor, cryogenic, and nanofabrication knowledge, but more importantly, his time spent having discussions and his help in the lab. I would like to thank Bohdan Khromets for all of the stimulating and productive conversations we have had. You are one of the most curious minds I know. I have enjoyed the several trips we have embarked on together while spending my time in Waterloo, and I am glad to be able to call you a friend. I would also like to thank György Jaics for the many instructive conversations and his willingness to selflessly share his time. You are one of the hardest-working and most dedicated people I know. I have appreciated our many brunches, late-night pool hall sessions, and your patience with my lacking table tennis skills (which I'm told is on the rise). I feel lucky to call you a friend. I would also like to thank Stephen R. Harrigan for the many hours we have spent bouncing ideas off one another, your willingness to help people in the lab, and your innate sense of community building. I'm happy to call you a friend (as well as Daisy, despite my allergies). I must thank Rubaya Absar for the many hours we have spent working together; I have been impressed with your dedication. I would also like to thank Dr. Arjun Shetty, Dr. Annelise Bergeron, Dr. Kaveh Gharavi, Camille Lacroix, Andrija Paurevic, and Tanmay Joshi, for whom I am grateful to have known and who have taught me something during my time at IQC. I would like to thank all others whom I have been fortunate to know while pursuing my studies; you all have profoundly impacted me.

I would also like to thank Christine Dietrich, who has always supported the student body that comes and goes in the RAC facility, as well as for her service to the IQC community more broadly.

Finally, I would like to thank my parents and family. Without their support, this thesis would not be possible. They have shared much advice and wisdom during my time at IQC,

which has immensely helped me grow as a person and tackle the research challenges I have faced. I love you all.

Dedication

This is dedicated to my parents and my grandmother, Jean Seaver. I'm so grateful for the influence you all have had on my life and for your unwavering support in my pursuit of higher education.

Table of Contents

Examining Committee ii

Author's Declaration iii

Statement of Contributions iv

Abstract vi

Acknowledgements ix

Dedication xi

List of Figures xvi

List of Tables xxvii

List of Abbreviations xxix

1 Introduction 1

1.1 Thesis Overview 2

1.2 Background 4

1.2.1 Semiconductor Quantum Dots 4

1.2.2 Spin Qubits 12

1.2.3 Plasmonically Enhanced Photocurrent 18

2 Quantum Dot Spin Qubit Simulator in Python **22**
2.1 Introduction . . . 22
2.2 Quantum Dot Spin Qubit Simulator . . . 26
2.2.1 Modeling Electrostatic Potentials . . . 29
2.2.2 Solving Time-Independent Schrödinger Equation . . . 30
2.2.3 Single-Particle Ground State Wavefunctions . . . 36
2.2.4 Spin interactions in a semiconductor quantum processor . . . 37
2.2.5 Predicting Spin Qubit Dynamics . . . 42
2.3 Double Quantum Dot Exchange Interaction . . . 45
2.3.1 Heitler-London Exchange Energy . . . 47
2.3.2 Hund-Mulliken Exchange Energy . . . 51
2.3.3 Results . . . 55
2.4 Quantum Dot Hubbard Model . . . 57
2.4.1 Hamiltonian . . . 58
2.4.2 Example: Double QD System with 2 electrons . . . 60
2.4.3 Generalization: Many QD System . . . 63
2.4.4 Regions of Charge Stability . . . 64
2.4.5 Automated Extraction of Capacitance Matrix . . . 65
2.5 Node Network . . . 68
2.5.1 2 Node Bell State Preparation . . . 71
2.5.2 3 Node GHZ State Preparation . . . 73
2.5.3 4 Node GHZ State Preparation . . . 75
2.6 Conclusions . . . 78

3 Spin Qubit Compact Model for Control Electronic Design **79**
3.1 Introduction . . . 79
3.2 Single Spin Qubit Compact Model . . . 83
3.2.1 System Master Equation . . . 83

3.2.2 Mapping Voltage to δg . . . 87
3.3 Two Spin Qubit Compact Model . . . 89
3.3.1 Mapping Voltage to delta g and Exchange . . . 95
3.4 Conclusions . . . 98

4 Metal-Semiconductor-Metal InGaAs Photodetector Enhancement 99
4.1 Introduction . . . 99
4.2 Materials and Methods . . . 102
4.2.1 Molecular Beam Epitaxy of InGaAs Heterostructures . . . 102
4.2.2 Nanocrystal Synthesis . . . 103
4.2.3 Photodetector Fabrication . . . 104
4.2.4 Characterization of Nanocrystals . . . 104
4.2.5 Photocurrent Measurement Setup . . . 104
4.2.6 Nanocrystal Drop-Casts . . . 106
4.3 Results . . . 107
4.3.1 Nanocrystal Characterization . . . 107
4.3.2 Photodetector Characterization . . . 110
4.3.3 Enhancement of Photodetector Spectral Responsivity . . . 112
4.4 Discussion . . . 115
4.5 Conclusion . . . 117

5 Conclusions 118

References 120

APPENDICES 144

A Compact Model Master Equations 145
A.1 2 Spin Qubit Hamiltonian to Circuit Representation . . . 145

B Photodetector Supplementary Information **157**

B.1 Nanocrystal (NC) Characterization 157

B.2 Light Source Characterization 162

B.3 Spectral Responsivity Normalization and Incident Power 163

B.4 InAlAs/InGaAs Wafer Morphology 165

B.5 Schottky Contact Model 166

B.6 Spectral Specific Detectivity D(lambda) 167

B.7 Photodetector Drop-Casts 168

List of Figures

1.1 An example cross-section of a single QD device fabricated in Si, in addition to the band edge diagrams along the growth axis and conductance channel through the QD. Voltages V_S and V_D can be applied to ohmic leads, fabricated from the implantation of n-type dopants near the QD location. The ohmic leads act as electron reservoirs, supplying or accepting electrons, while the metallic electrodes V_{g1}, B_1, and B_2 are used as gates to form the QD, control the electron occupancy, as well as control the tunneling rates. 5

1.2 Schematics showing electron transport conditions through a single QD (a) Current as a function of plunger gate and source/drain bias voltage displaying regions of Coulomb blockade. The electron occupancy, N, is shown as the plunger gate shifts the QD chemical potentials relative to the source/drain bias window. (b-d) Energy diagrams under various source/drain bias and plunger gate voltage 7

1.3 Setup to indirectly measure a QD charge state using a single Electron Transistor (SET) charge sensor. (a) Schematic for a charge sensor capacitively coupled to a QD with charge q. The charge sensor is tuned so that the tunnel rates through the sensor, Γ, produces a measurable current signal and sharp Coulomb peaks are resolved (b) The bottom-right graph shows the Coulomb blockade cross-section along V_{g1} from Figure 1.2(a) for the charge sensor. The charge sensor is first tuned to operate on a Coulomb peak which makes the current through the sensor, I_{CS}, sensitive to changes in capacitance of the QD. The top-right graph shows a red/blue/green line representing the measured changes in I_{CS} over time as the occupancy of the QD is varied; red/green/blue points in the bottom-right graph show I_{CS} along a Coulomb peak as a function QD occupancy. 8

1.4 (a-b) Two chemical potential configurations where electron transport is blocked, yielding no current through the system. (c) Chemical potentials of the QDs fall within the bias window and allow for electron transport between each QD, yielding current through the system. 9

1.5 Capacitive couplings between QDs, metal gates, and source/drain leads for a double QD system. Compared to a single QD, the double QD has additional inter-QD capacitive coupling, C_m, as well as cross capacitances C_{g1d2} and C_{g2d1}. An additional barrier gate W is added for tuning the tunnel barrier between QD 1 and QD 2. 10

1.6 Double QD electron occupancy as a function of plunger gate voltage when (a) the QDs have no mutual capacitive coupling and (b) a finite mutual capacitive coupling. While the single QD Coulomb diamond Figure 1.2(a) shows charge stable regions, these double QD diagrams (or N-QD diagrams) are commonly referred to as charge stability diagrams. Note that these plots are cross-sections of stability regions for a larger voltage configuration space. Black lines indicate electron transfer between QDs or a QD and lead. The blue/red points in (b) indicate the electron-hole triple point pairs where three different charge configurations are in equilibrium. The change in slope of transition lines from (a) to (b) is observed when crosstalk from nearest neighbor electrodes is included, influencing the chemical potential μ of the respective QD. 11

1.7 Schematic for energy selective Elzerman readout [5] of a QD spin qubit connected to an electron reservoir at mK temperature such that $E_z \gg k_B T$. (a-c) Show the current reading of a nearby charge sensor I_{CS} as electrons tunnel onto or off of the QD. (a) QD chemical potential is tuned to be higher than the chemical potential of the reservoir, preventing a single spin-up or down electron from tunneling onto the QD. (b) The QD energy levels are lowered such that the spin-up single electron energy level is lower than the chemical potential of the reservoir. This enables deterministic loading of the spin-up state. (c) After exciting the spin qubit from a quantum gate operation, the electron is able to tunnel out of the QD and is replaced by another electron in the ground spin state. 13

1.8 Schematic for Pauli spin blockade readout in a double QD system. The two QDs are initialized with a single electron in each QD, i.e., the (1,1) charge state. A singlet state S(1,1) has total spin angular momentum $s = 0$ while the triplet states T(1,1) have total angular momentum $s = 1$. A charge sensor is located near the left QD and is tuned to produce a measurable current signal I_{CS}. A bias is applied to the double QD system, lowering the S(0,2) charge state energy compared to S(1,1), and I_{CS} is monitored. (a) An initialized S(1,1) state enables an electron to tunnel between QDs from the S(1,1) to the S(0,2) state. (b) An initialized T(1,1) state suppresses electron tunneling between QDs due to the Pauli exclusion principle as long as the T(0,2) state is energetically unavailable. 17

1.9 Common metal-semiconductor-metal (MSM) photodetector design (a) Metal contacts are deposited on a semiconductor (such as AlGaAs) producing a double Schottky barrier junction (b) MSM device along growth direction cross-section showing electron-hole pair generation in an InGaAs absorption layer (c) Bandedge diagram along electrode contact axis (d) Bandedge diagram along growth axis. 19

1.10 The responsivity of a general semiconductor photodetector with bandgap energy cutoff E_B is given by $R(\lambda) = \frac{\eta q \lambda}{hc}$, where η is the quantum efficiency, q is the electron charge, h is Planck's constant, and c is the speed of light. In general, the penetration depth of photons decreases with decreasing wavelength, i.e., the absorption coefficient increases, leading to greater surface recombination of electron-hole pairs and a reduction in photon-to-current conversion efficiency. Wavelengths beyond the bandgap cutoff do not possess enough energy to generate electron-hole pairs, resulting in zero response from the photodetector. 20

1.11 Sub-wavelength nano-particle structures exhibit enhanced electric fields locally from resonant charge fluctuations driven by external electro-magnetic field excitations. 21

2.1 Mosaic of simulated electrostatic potential landscapes for a silicon, MOSFET style, double QD device as a function of the applied plunger gate voltages. Moving along the diagonal, top-left to bottom-right, shows the potential well depth increases without any detuning between the QDs. Conversely, the anti-diagonal, bottom-left to top-right, shows how to deepest potential well depth changes from the left to the right QD as the detuning voltage $V_{\text{detuning}} = V_1 - V_2$ is symmetrically varied from -200mV to 200mV. 27

2.2 High level representation of data processing in the QuDiPy simulator for a double QD, i.e. 2 spin qubit, example (a) User designs a layered metal/semiconductor device and uses finite-element Poisson solutions to determine 3D electrostatic potential landscape for electrode voltage configurations in the range of expected experimental operation (b) The simulator extracts 2D electrostatic potential at the position of the 2DEG and calculates single particle ground state wave functions, i.e. $\psi_1(r)$ and $\psi_2(r)$, for isolated QD potentials at each simulated voltage configuration (see Section 2.2.3 for further discussion) (c) Python modules construct spin and Hubbard Hamiltonians allowing the user to initialize a given input density matrix, set of experimental gate operations, and construct a desired quantum circuit (d) The evolution module contains tools to visualize quantum gate operations. . . . 29

2.3 Cross-sections from figure 2.2 along lines (black dashed lines) (a) Cross-section perpendicular to QD array. (b) Cross-section along QD array. (c) Reduced 3D model geometry used for finite-element Poisson calculations of the electrostatic potential landscape in the plane of the induced 2DEGs. . 30

2.4 Example of a triple QD (a) Electrostatic potential in the plane of the 2DEG with regions showing $\approx 65\%$, $\approx 95\%$, and $\approx 99\%$ containment of the SPGSW (b) An example of potential masking for the left QD to determine the SPGSWs in that region (c) An example potential masking for the right QD pair used to determine the exchange energies. Both masking procedures in (b)-(c) show an example of Gaussian masking, which performs a fit of an inverted Gaussian function to local minima for QDs or QD pairs; however, other masking routines can be specified by the user. 37

2.5 Effective parameters of the spin Hamiltonian calculated from Equation 2.29 and formulas discussed in Section 2.3 for a triple QD system. (a-c) g-factor deviation, i.e. $\delta \mathrm{g}(\vec{V})$, for electrons in all three QDs as a function of plunger or tunnel barrier gate voltage. (d-e) exchange energy calculation using a Hund-Mulliken exchange approximation (cf. Section 2.3) for each pair of QDs as a function of plunger or tunnel barrier gate voltage. 40

2.6 Examples of wave function (blue) behavior under varying potential (green) and out-of-plane electric field (magenta) landscapes in a triple QD system when the voltage is swept for individual gates. The plots are zoomed in on the left and middle QD region. 41

2.7 Simulated single QD Rabi-chevron map showing qubit spin-up probability as a function of ESR detuning frequency, $f_L - f_{RF}$, and ESR pulse time. A Zeeman field of $\approx 1T$ is applied, causing a Larmor frequency ≈ 28 GHz. . . 43

2.8 Examples of (a) Chevron patterns for a double QD device when g-factor detuning is induced by varying the plunger gate voltage, V_1, on QD 1. (b) Exchange oscillations between two electrons in a double QD pair when varying tunnel gate voltage, W_1. 44

2.9 A schematic MOSFET double QD device in Si: (b) Top-view cross-section showing the double well confining potential formed by the plunger (V_1, V_2) and tunnel (W_1) electrodes. The electrostatic potential energy at the SiO_2/Si interface is calculated by a finite element Poisson solver based on a 3D device model. (a) Contour plot of the potential energy landscape in (b). Zoomed in electrostatic potential energy, Φ, regions for: (c) left single QD and masked right QD (d) right single QD and masked left QD. Regions are encircled where there is a $\approx 99\%$, $\approx 95\%$, and $\approx 65\%$ probability of finding an electron. 50

2.10 Exchange energy as a function of barrier voltage, W_1. All exchange calculations exhibit an exponential relationship of exchange energy vs W_1. 56

2.11 (a) Calculated effective parameters of the Hubbard Hamiltonian for a double QD system. Hubbard parameters are a function of $\vec{\mathcal{V}} = [V_1, W_1, V_2]$, however, W_1 has been chosen to be in the low tunnel barrier regime of -0.4V for the sweep of the plunger gates. (b) CSD resulting from exact diagonalization of the Hubbard Hamiltonian constructed with the Hubbard effective parameters in subfigure (a) with a constant tunnel coupling set to 3 meV. . 65

2.12 Honeycomb region for an example double QD showing a single charge state with along with the electron-hole triple point pairs. The voltage spacings between electron-hole, electron-electron, and hole-hole triple point pairs allows capacitance matrix estimates to be made using the constant interaction model. 66

2.13 Figure showing the automated extraction of triple point pairs used to determine capacitance and lever arm matrices. 68

2.14 Quantum circuits for generating maximally entangled GHZ states. The examples assume entanglement creation in separate QD nodes if two-qubit gate operations can be applied between node pairs. 69

2.15 Series of single- and two-qubit gate operations to achieve a two-qubit CNOT gate. The top wire represents the control qubit channel, while the bottom is the target channel. 70

2.16 Quantum circuit diagram illustrating distributed entanglement between QD nodes A and B by preparing a two-qubit maximally entangled Bell state. Singlet states S_1 and S_2 are shared between QDs 1 and 2 in both node A and B. CNOT gates are applied to each node separately and a single $Z(\pi)$ rotation gate is applied to the qubit in A_1 which forms a Bell state between qubits in A_1 and B_1. 71

2.17 Quantum circuit diagram illustrating distributed entanglement between QD nodes A, B, and C by preparing a three-qubit maximally entangled GHZ state. Singlet states S_1 and S_2 are shared between QDs in nodes A, B, and C. A $X(-\pi)$ gate is applied to ancilla 1 in node A, in parallel with a CNOT gate between ancilla qubits in node B. A conditional $X(\pi)$ gate is applied to ancilla one in node C after a Z-basis measurement of the second ancilla qubit in node B, forming a GHZ state between the first ancilla qubits across all three nodes. 73

2.18 4-qubit maximally entangled GHZ preparation from a series of Hadamard and CZ gate operations. CZ gate is realized as a CPHASE(π) gate operation in QuDiPy. The required effective parameter evolution (g-factor and exchange J) is determined, and the resultant experimental control pulses (plunger gate V, tunnel gate W, and ESR field B_{RF}) are plotted. 76

2.19 (a) Triple QD and four-node GHZ preparation and X/Z surface code stabilizer operation. Singlet states $|S\rangle$ are distributed between ancilla 1 in nodes A-B, ancilla 1 in nodes C-D, and ancilla 2 in nodes A-D. Single- and two-qubit gates are performed, X-basis measurement on ancilla qubits 2 in nodes A and C, and conditional $X(\pi)$ gates on ancilla qubits 1 in nodes A and B to form a GHZ state across all ancilla 1 qubits. (b) Additional gates are conditionally applied to achieve an X or Z stabilizer operation. (c-f) Show the resultant density matrix elements for the qubit state across ancillas A_1, B_1, C_1, and D_1. Density matrix elements ar show at intermediate steps when preparing the 4-qubit GHZ state: (c) initial state after singlet distribution, (d) state after single- and two-qubit rotation gates, (f) state after an X-basis measurement is applied to ancilla qubits A_2 and C_2 (measuring odd parity), and (e) the final GHZ state after corrective $X(\pi)$ gates are applied for an odd parity measurement between A_2 and C_2. 77

3.1 An abstract circuit representation of a qubit compact model. The voltage across each capacitor, C_{qubit}, represents the quantum state density matrix elements as the system evolves under experimental control inputs. Voltage-controlled current sources vary the voltage across the capacitors as the density matrix elements and system Hamiltonian evolve under experimental input controls. 82

3.2 Numerical solutions for the Lindblad master equation with an initial state vector defined by $\phi = 0$ and $\theta = \frac{\pi}{2}$. Off-diagonal elements rapidly decay to 0 from dephasing, while the $\text{Re}\{\rho_{00}\}$ converges to 1 from spin relaxation to the external Zeeman field. 86

3.3 Simulated Rabi oscillations as a function of qubit g-factor detuning generated by a single qubit compact model. 87

3.4 Quadratic fit for δg-factor as a function of plunger gate voltage with an $R^2 = 0.9996$. 88

3.5 Simulated state evolution of a qubit under ESR field and voltage pulses to realize a $\text{X}\left(\frac{\pi}{2}\right)$. ESR and voltage pulses were determined by QuDiPy's optimal control module. 89

3.6 (a) Experimental control pulses to realize a CZ gate from a sequence of single and two-qubit gate operations generated by QuDiPy. (b) Zoomed-in figures showing experimental input pulses for a $\sqrt{SWAP}$ gate. 91

3.7 simulated Density matrix element evolution under ESR field and voltage pulses generated by QuDiPy and consistent with the two-qubit compact model results. 92

3.8 Bloch sphere projections of a two-qubit CZ gate operation consistent with the two-qubit compact model. 94

3.9 QuDiPy interpolated function for δg_n plotted as a function of the two plunger gates with $W_1 = -0.1V$. 95

3.10 Percent relative error for the δg_1 and the fitted analytic function for various W_1 cross-sections (a) $W_1 = -0.1V$ (b) $W_1 = -0.019V$ (c) $W_1 = 0.016V$. The missing data points in (c) are from NaNs in the δg interpolation, caused intentionally after a dot merging event occurs. 96

4.1 Structure of the IR metal-semiconductor-metal (MSM) photodetectors. (a) Semiconductor heterostructure layers grown by molecular beam epitaxy. The $In_{0.53}Ga_{0.47}As$ active region is grown between $In_{0.52}Al_{0.48}As$ barriers on an InP substrate. (b) Top view schematic of the interdigitated metal electrode geometry, where design parameters are electrode width (W $\sim$ 10 μm), spacing (S $\sim$ few μm), length (L $\sim$ 500 μm), and active area (A $\sim$ 500 μm $\times$ 540 μm) indicated by dashed red box. 102

4.2 Measurement setup for characterizing photodetector responsivity. (1) The broadband light source generates a beam that is collimated and then focused on the monochromator entrance slit; (2) wavelengths are selected by mechanical positioning of diffraction gratings; (3) the monochromator output is filtered and focused onto the wire-bonded MSM device; (4) a bias voltage is applied to the device and the photocurrent is measured using a current-voltage (I-V) amplifier. The output of the I-V amplifier is read out with a digital multimeter (DMM). Responsivity is determined from the DMM output and incident beam power measurements. 105

4.3 Characterization of crystalline structure and morphology of the synthesized NCs. (a-b) X-ray diffraction (XRD) spectra of WO_{3-x} and Cs_yWO_{3-x} NCs with background signal subtracted. Reference spectra of the bulk materials are reproduced from ICSD no. 24731 and no. 56223. (c) TEM images of drop-cast WO_{3-x} nanorods; (right inset) lateral cross-section of a single nanorod; (magnified inset) lattice spacing along $\langle 010 \rangle$ direction. (d) TEM images of drop-cast Cs_yWO_{3-x} NCs; (top right inset) end cross-section of a single NC; (bottom right inset) lateral cross-section image of a single NC. . 107

4.4 (a-b) Optical extinction spectra measured for colloidal solutions and drop-cast WO_{3-x}/Cs_yWO_{3-x} NCs showing plasmonic resonance in the NIR-IR wavelength range. Colloidal solutions were prepared using tetrachloroethylene (TCE). Spectra are normalized by the peak extinction and vertically shifted for comparison. 109

4.5 Optical microscope images of a MSM photodetector with a similar geometry to the photodetectors measured in this study: a) Upper half of the MSM device with no NCs, b) lower half of the MSM device after drop-casting Cs_yWO_{3-x} NCs from a 150 g/L solution. The lower image indicates a relatively uniform distribution of NCs. 110

4.6 Characterization of photodetector performance versus bias voltage and illumination. Dark current and photocurrent for the as-fabricated InGaAs photodetectors A (a) and B (b) used in this study. Photocurrent was acquired at a wavelength of 1550 nm with an incident beam power of 176 $\frac{\mu W}{mm^2}$ over the photodetector active area. 112

4.7 Responsivity measured at a bias voltage -1 V with and without (a) WO_{3-x} NCs (device A) and (b) Cs_yWO_{3-x} NCs (device B). Significant increases in responsivity are observed for both types of NC. Responsivity is determined by subtracting the dark current and normalizing the photocurrent with respect to the measured power spectrum of the light source. Note that the fluctuations in responsivity versus wavelength are reproducible and not due to measurement noise (uncertainty due to noise is smaller than the plot line width). These fluctuations may arise from sharp features in the broadband light source spectrum that are not fully removed by our normalization protocol (see Supplementary Information) or by wave interference due to the electrode geometry. 112

4.8 Relative percent change in responsivity (RPD) as a function of wavelength due to the addition of (a) WO_{3-x} and (b) Cs_yWO_{3-x} NCs. The optical extinction measurement for drop-cast NCs (red line), plotted on the right vertical axis in each plot, shows overall agreement with the RPD. Note that the relative scaling of the two vertical axes is arbitrary. 114

4.9 External quantum efficiency (EQE) of each photodetector with and without the addition of (a) WO_{3-x} and (b) Cs_yWO_{3-x} NCs. EQEs based on the data shown in Figure 4.7 demonstrate improved photodetector optical-to-electrical conversion efficiency for both NC types. 115

B.1 Length and width distributions of WO_{3-x} NCs determined from post-processed TEM images using ImageJ software. 157

B.2 Length and width of distributions Cs_yWO_{3-x} NCs determined from post-processed TEM images using ImageJ software. 158

B.3 Energy dispersive X-ray spectroscopy (EDS) measurement on Cs_yWO_{3-x} NCs that determined the atomic fraction of Cs and W to be 4.78% and 17.67%, respectively. From this, the ratio of Cs/W in Cs_yWO_{3-x} NCs was determined to be $y = 0.27$. 158

B.4 Characterization of two additional substoichiometric monoclinic WO_{3-x} NC samples demonstrating the synthetic reproducibility of the NCs via XRD patterns (a), UV-Vis-NIR spectra (b), and (c-e) TEM micrographs. (Blue traces in (a) and (b) correspond to the WO_{3-x} in the main text. The red trace in (a) is a simulated pattern of bulk monoclinic WO_3 (ICSD no. 24731). 160

B.5 Characterization of two additional Cs_yWO_{3-x} bronze NCs demonstrating the synthetic reproducibility of the samples. (a) XRD patterns, (b) UV-Vis-NIR spectra, and (c-e) TEM micrographs of the Cs_yWO_{3-x} NCs. (Blue traces in (a) and (b) are the data shown in the main text. The red trace in (a) is the simulated pattern of bulk $Cs_{0.29}WO_3$ (ICSD no. 56223)). 161

B.6 Xenon-Halogen light source (a) beam profile upon exiting the monochromator and (b) power spectrum over a wavelength range 750-1800 nm, where a 750 nm or 1400 nm filter was used to block higher-order modes of diffracted light from the monochromator gratings. 162

B.7 Example showing how the power spectrum and photocurrent data are processed to account for changes in power transmission through different diffraction gratings used in the monochromator. Two gratings are used over the range of wavelength values selected; the grating change occurs at 1500 nm. 163

B.8 Characterization of surface defects using a Nomarski microscopy scan of MBE-grown $In_{0.52}Al_{0.48}As/In_{0.53}Ga_{0.47}As$ on InP, taken at the center of the wafer. (left inset) Magnified view of pitting surface defects suspected to result from defects in the InP growth substrate. 166

B.9 Dark current versus bias voltage for the as-fabricated InGaAs photodetectors A (a) and B (b) used in this study (black lines). Plotted in red are simulated I-V curves from the double Schottky barrier model described above. Schottky barriers (Φ), ideality factors (n), and Normalized Root Mean Square Errors (NRMSE) determine by the fitting are listed. 167

B.10 Specific Detectivity (in Jones, i.e. $\frac{cm\sqrt{Hz}}{W}$) is plotted as a function of incident wavelength for devices A and B, with and without the addition of NCs. Maxmum detectivity prior to adding NCs is $\sim 10^9$ Jones for device A and $\sim 10^{10}$ Jones for device B. 168

B.11 Optical image of a photodetector taken at 5X magnification (a) before and (b) after drop-casting of WO_{3-x} NCs. The NC concentration and quality of the drop-cast yielded an increased photoresponse compared to the bare photodetector. 168

B.12 Optical image of a photodetector taken at 5X magnification (a) before and (b) after drop-casting Cs_yWO_{3-x} NCs. The NC concentration and poor quality of the drop-cast yielded a decreased photoresponse compared to the bare photodetector. 169

B.13 Scanning electron microscope (SEM) images of drop-cast NC films on the active areas of MSM photodetectors. Images show the distribution of (a) Cs_yWO_{3-x} NCs and (b) WO_{3-x} NCs. The solution concentrations were similar to those used in the main study. Both samples were loaded into the SEM at the same time and imaged under identical conditions (beam current, acceleration voltage, focus, and contrast settings). 170

B.14 The effect of successive drop-casts of Cs_yWO_{3-x} NCs using a concentration of 135g/L. (a) Responsivity as a function of wavelength for successive drop-casts. (b) Relative percent difference in responsivity for successive drop-casts, measured at several bias voltages. The median (data points) and standard deviation (bars) of the relative percent difference are calculated over the full wavelength range shown in (a). 171

B.15 The effect of drop-cast concentration on the change in responsivity (RPD) for Cs_yWO_{3-x} NCs. Samples were diluted in hexane. The RPD is measured over the full spectrum (900-1800 nm), and the median value is plotted (bars indicate the standard deviation). 172

List of Tables

3.1 Two-qubit Pauli operator matrices. 90

3.2 Summary of gate operations, input/output test states, analytic fit models with simulated g_1, g_2, and J_{12} behavior, optimized parameters determined by Nelder-Mead optimization using L^2 regularization with a scale factor of $10^{-3} - 10^{-6}$, and infidelity values. Note that the initial cost function uses mean square error (MSE) to compare theoretical gate pulses as a function of voltage to the proposed analytic models, then the L^2 norm of the fit coefficients is added to help reduce infidelities. 97

4.1 Resistance values for as-fabricated photodetectors measured on a probe station with (R_{light}) and without (R_{dark}) illumination under a white light source to characterize photodetector performance. The applied bias ranged from -10 mV to +10 mV. The optical power was approximately 18 $\frac{\mu W}{mm^2}$ with the probe station lamp on and 32 $\frac{nW}{mm^2}$ with the lamp turned off (ambient light). Devices A and B were chosen for the plasmonic enhancement study because they exhibited significant decreases in resistance under illumination and had the same electrode geometry. ΔR refers to the percentage change in resistance under illumination. The mean resistance (μ) and standard deviation (σ) across the array of 16 detectors are also indicated. 111

B.1 Summary of crystallographic and optical characterization of WO_{3-x} NC samples from independent syntheses. The maximum plasmonic resonant wavelengths from extinction measurements (UV-NIR) and peak XRD angles for a given crystal orientation with Full-Width Half-Maximum ((crystal orientation)-FWHM) are tabulated. This demonstrates a high degree of reproducibility in the synthesis of WO_{3-x} NCs. 159

B.2 Summary of crystallographic and optical characterization of Cs_yWO_{3-x} NC samples from independent syntheses. The aspect ratios (AR), maximum plasmonic resonant wavelengths from extinction measurements (UV-NIR), and peak XRD angles for a given crystal orientation with Full-Width Half-Maximum ((crystal orientation)-FWHM) are tabulated. This demonstrates a high degree of reproducibility in the synthesis of Cs_yWO_{3-x} NCs. 159

List of Abbreviations

2DEG 2-Dimensional Electron Gas 23, 49

2DHG 2-Dimensional Hole Gas 23

CMOS complementary metal-oxide-semiconductor 22

CNOT Control-X 15

CROT Control-ROT($\theta, \hat{n}$) 15

CSD Charge Stability Diagram 57

CZ Control-Z 15

DAC Digital to analog converter 79

EDSR Electron Dipole Spin Resonance 24

ESR Electron Spin Resonance iv, 14

FCI Full Configuration Interaction 24

GHZ Greenberger–Horne–Zeilinger vi

GRAPE Gradient Ascent Pulse Engineering 25

HL Heitler-London 40, 47

HM Hund-Mulliken 40, 51

IR Infrared 4, 99

LSPR Localized Surface Plasmon Resonance 4, 18, 100

MSM Metal Semiconductor Metal 4, 19, 99

NC Nanocrystal v, 101

NIR Near-Infrared 4, 99

QC Quantum Computer 1, 5, 12, 22

QD Quantum Dot 2, 4, 12, 22, 45, 47, 58, 79, 81

QPU Quantum Processing Unit 23

QuDiPy Quantum Dots in Python iv, 3, 26, 47, 79

RF Radio Frequency 24

SET single Electron Transistor xvi, 8

SPGSW Single Particle Ground State Wavefunction 28, 47

TISE Time Independent Schrödinger Equation 30

Chapter 1

Introduction

Over the past century, advancements in quantum mechanics have played a pivotal role in understanding mesoscopic and nanoscopic physical phenomena, leading to the development of many groundbreaking technologies. Perhaps most notable is the advent of the transistor in 1948 [6], which revolutionized modern electronics. This was shortly followed by numerous technological advancements such as the development of lasers [7] in 1960, the development of MRI imaging [8] in 1973, as well as efficiency improvements of solar cells [9] in 1990, just to name a few. At the turn of the 21st century, many quantum technologies started to emerge that made improvements to metrology [10], sensing [11, 12], biomedical [13], and communication [14, 15] technologies. In recent decades, research has increasingly focused on harnessing quantum mechanics for computational purposes, with the potential to surpass classical computing for specific tasks. This idea was first proposed by Paul Benioff in 1980 [16] and Richard Feynman [17] in 1982. Since then, significant progress has been made in identifying problems where quantum computing could offer a computational advantage over classical methods, such as database search, prime factorization, and molecular simulation [18, 19]. The potential to solve these problems has driven efforts to build large-scale Quantum Computers (QCs) capable of leveraging quantum superposition and entanglement for computation. This challenge has attracted significant interest from both researchers and private companies. Over the past two decades, progress has been made in developing high-quality quantum-bit (qubit) devices that can perform high-fidelity quantum logic gate operations—an essential requirement for scalable quantum computation.

Many physical architectures are being pursued as alternative paths toward demonstrating the quantum advantage of a QC over classical computation. These included ion traps [20], superconducting circuits [21, 22], photonics-based approaches [23, 24], topolog-

ical qubits [25], nitrogen-vacancy centers [26], and semiconductor-based electron or hole confinement [27], among others. Each of these architectures must satisfy the DiVincenzo criteria [28], which outline the essential requirements for physical implementations of quantum computing:

1. a scalable system of well-defined qubits,
2. the ability to initialize qubits to a known state,
3. long coherence times relative to gate operation time scales for maintaining quantum information,
4. a universal set of high-fidelity quantum gates for general-purpose computation,
5. and reliable qubit-specific measurement capabilities.

The feasibility of different architectures is often compared based on how well they meet these criteria, as well as their scalability to large numbers (e.g., millions or billions) of physical qubits, the speed and fidelity of gate operations, and the complexity of qubit initialization, control, and readout as the system grows. As a system's number of physical qubits scales, quantum error correction (e.g., a surface code [29]) and fault-tolerant gate protocols [30] become a requirement for practical large-scale QC. In addition to the DiVincenzo criteria, different architectures are compared by how well the physical qubit error rates fall below the fault tolerance threshold for the given system. In this thesis, electron spin qubits confined in electrostatically defined Quantum Dots (QDs), as proposed by Loss and DiVicenzo in 1998 [31], are investigated as a potential candidate for large-scale quantum computation. In particular, small-scale QD device properties are simulated to aid in rapid prototyping of device design and qubit control. Such simulations are increasingly desired as the complexity of the device grows with the number of qubits.

1.1 Thesis Overview

The background section of this chapter will provide an introduction that focuses primarily on electron transport in semiconductor QDs, as well as semiconductor QD electron spin qubit initialization, control, and readout. Additional work discussed in this thesis involves a separate research topic on plasmonic enhancement of photodetectors; therefore, we conclude this chapter with a brief overview of relevant material. Further reading on QDs can

be found in [27, 32–37], while further reading on photon detection in semiconductors and plasmonics can be found in [38–42].

Chapter 2 presents the development of QuDiPy, a Python-based simulation framework designed for modeling and optimizing QD spin qubit systems. The simulator enables calculations of electrostatic potentials, single-particle wavefunctions, and effective Hamiltonian parameters for multi-qubit devices. Using finite-element Poisson solutions, QuDiPy determines potential landscapes and computes relevant parameters, including exchange interaction and Hubbard model coefficients, which are essential for mapping out stable charge configurations as a function of gate voltages and spin dynamics.

A key application of the simulator is its ability to impose constraints on optimal control voltage pulse-finding methods by constructing charge stability diagrams and extracting capacitance matrices. This allows for feedback optimization between simulation and experimental data, facilitating increased predictive power of the simulator and its ability to emulate real QD systems. The simulation framework also extends to modeling qubit operations, including controlled interactions for generating entangled states. Examples of two- and three-qubit operations are provided, demonstrating the preparation of Bell and GHZ states across an interconnected network of QD devices (referred to as nodes). Finally, experimentally relevant parameters are simulated to generate figures of merit for characterizing real QD devices. These figures of merit can then be used as validation checks for the simulator's accuracy, highlighting its utility for both theoretical studies and experimental design.

Chapter 3 introduces a compact modeling approach for simulating spin qubit dynamics within classical circuit simulation environments. This model provides a bridge between quantum device physics and control electronics, enabling efficient simulation of multi-qubit evolution under realistic experimental conditions. The compact model is built upon the QuDiPy framework and maps the system's Hamiltonian to an equivalent electrical circuit representation.

The chapter begins by formulating the system's master equation in terms of circuit components, allowing the simulation of voltage-dependent variations in qubit parameters. An analytical mapping between control voltages and effective qubit parameters, such as the g-factor and exchange interaction, is derived and incorporated into the model. A key feature of the approach is the use of Verilog-A for embedding quantum dynamics into classical circuit simulators such as SPICE, enabling integrated simulations of control pulse sequences. The compact model is validated against full numerical simulations, demonstrating its ability to reproduce experimentally relevant evolution of the qubit system, including decoherence, with significantly reduced computational overhead. The chapter concludes

with an analysis of potential extensions for this work.

Chapter 4 shifts focus to a separate topic of research, investigating the enhancement of InGaAs Metal Semiconductor Metal (MSM) photodetectors using Localized Surface Plasmon Resonance (LSPR) effects. The study explores the integration of plasmonic nanocrystals to increase light absorption and photocurrent generation, with a focus on Near-Infrared (NIR) and infrared Infrared (IR) detection applications.

The chapter begins with an overview of MSM photodetector fabrication and the synthesis of tungsten oxide-based nanocrystals, which are drop-cast onto the device surface to introduce plasmonic effects. Structural and optical characterizations confirm the formation of plasmonic resonances in the NIR range, while electrical measurements demonstrate an increase in photocurrent response. The impact of nanocrystal concentration, particle size, and incident wavelength on photodetector performance is systematically analyzed.

Experimental results show that the addition of nanocrystals enhances spectral responsivity by up to a factor of 2.5, with improvements in external quantum efficiency and specific detectivity. These enhancements are attributed to the strong electromagnetic field confinement induced by the plasmonic nanostructures. The chapter concludes by discussing the potential of this approach for cost-effective and scalable enhancements in semiconductor photodetector technology.

Chapter 5 synthesizes the results and insights gained from the core areas of this thesis: simulation and modeling of QD spin qubits, compact modeling for control electronics, and plasmonic enhancement of photodetectors. It reflects on the broader implications of the work, emphasizing how the developed tools and experimental strategies advance the understanding and optimization of quantum device behavior and photodetection technologies. The chapter also outlines key directions for future research, including enhanced modeling accuracy through experimental feedback, machine learning-driven device control, and improved photodetector fabrication techniques, setting the stage for continued progress in both quantum information and optoelectronic applications.

1.2 Background

1.2.1 Semiconductor Quantum Dots

We begin with an introduction to QDs formed in semiconductor devices made through nanofabrication processes. Portions of this section are based on the theses of Buonacorsi [43] and Holloway [44]. To begin, we consider a single QD formed at a SiO2/Si

heterojunction which is capacitively coupled to source and drain ohmic contacts, as seen in Figure 1.1. The ohmic source and drain leads form reservoirs of electrons that can tunnel onto or off the QD. These reservoirs enable initialization and readout of electron spin states on the QD for QC applications, which is discussed in Section 1.2.2. The QD is formed by applying voltage to a metal plunger gate V_{g1} and two additional barrier gates B_n, which are capacitively coupled to the QD with the strengths C_{g1}, C_{B1}, and C_{B2}. The plunger gate voltage V_{g1} enables tuning of the energy levels within the QD while the voltages applied to each barrier gate allow tuning of the energy of the conduction band edge between the dot and the reservoirs, forming tunnel barriers. Electrons fill the quasi-continuum of states of the source and drain up to the respective chemical potentials of the leads μ_S and μ_D, as shown in Figure 1.1. The chemical potentials of the leads are controlled by applying an external bias voltage $V_{\text{bias}} = V_S - V_D$, i.e., $eV_{\text{bias}} = \mu_S - \mu_D$. The chemical potential of the QD $\mu_d(N) = E(N) - E(N-1)$ is the energy required to add an additional N^{th} electron to the QD, where $E(N)$ is the energy of the QD containing N electrons.

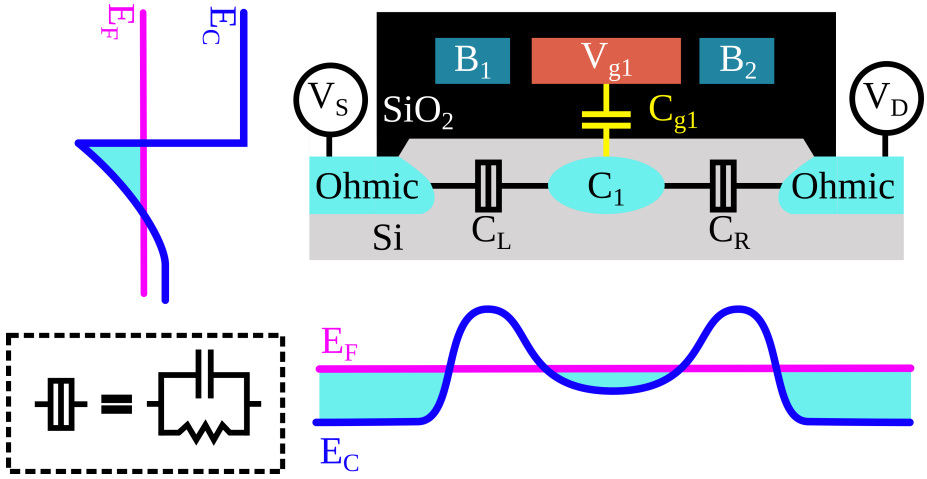


Figure 1.1: An example cross-section of a single QD device fabricated in Si, in addition to the band edge diagrams along the growth axis and conductance channel through the QD. Voltages V_S and V_D can be applied to ohmic leads, fabricated from the implantation of n-type dopants near the QD location. The ohmic leads act as electron reservoirs, supplying or accepting electrons, while the metallic electrodes V_{g1}, B_1, and B_2 are used as gates to form the QD, control the electron occupancy, as well as control the tunneling rates.

To accurately determine the chemical potential of the QD from physical first principles is a complex challenge. However, the semi-classical constant interaction model proves to

be an adequate model for describing the electron transport behavior of QDs [33–35, 45], leading to,

$$\mu_d(N) = \epsilon_N + \frac{N - N_0 - 1/2}{C_1} + |e|\alpha_{g1}V_{g1}, \tag{1.1}$$

where ϵ_N is the orbital energy of the N^{th} electron, N_0 is the number of electrons on the QD when $V_{g1} = 0V$, $\alpha_{g1} = C_{g1}/C_1$ is the lever arm between gate V_{g1} and the QD, and C_1 is the self-capacitance of the QD. Now we consider the discrete orbital energy spectrum due to quantum confinement along all three spatial dimensions of the QD. The spacing of the discrete orbital energy levels can be approximated using the commonly taught "particle in a box" toy model, which gives orbital energies:

$$\epsilon_{orb} = \frac{\hbar^2\pi^2}{2m^*}\left(\frac{n_x^2}{L_x^2} + \frac{n_y^2}{L_y^2} + \frac{n_z^2}{L_z^2}\right), \tag{1.2}$$

where m^* is the electron effective mass and n_i are the quantum numbers for each spatial dimensions for a box of side lengths L_i. The energy for adding an additional electron to the QD is then simply calculated from the difference between the chemical potential for a QD with N versus $N + 1$ as,

$$\mu_d(N+1) - \mu_d(N) = \epsilon_{N+1} - \epsilon_N + \frac{e^2}{C_1}, \tag{1.3}$$

which gives the difference in orbital energy and charging energy required to overcome the Coulomb repulsion of adding another electron onto the QD. In the regime where $e^2/C_1 \gg \epsilon_{N+1} - \epsilon_N$, the separation between chemical potentials for $N+1$ vs N electrons will be the charging energy required to add or remove an electron from the QD.

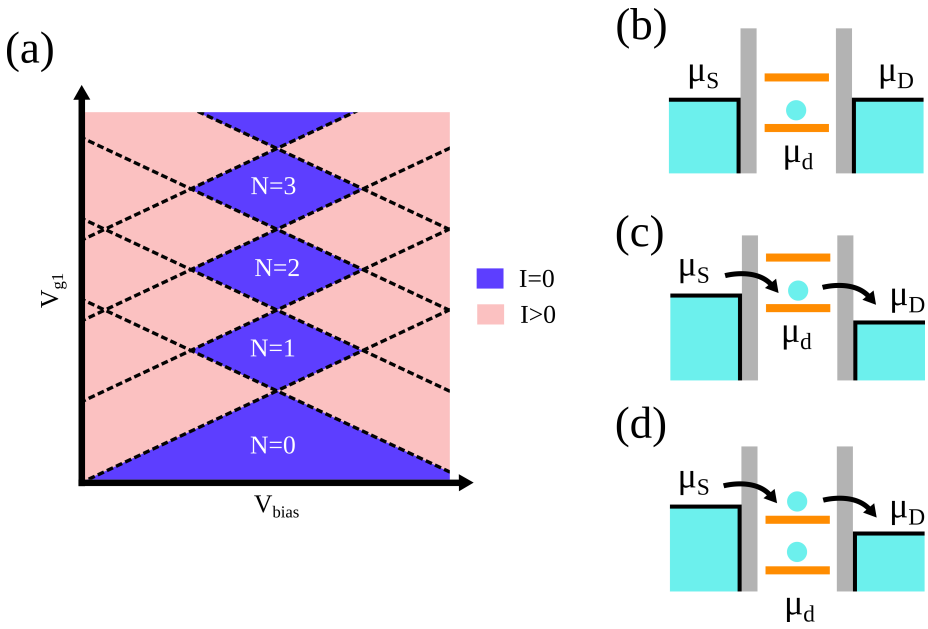


Figure 1.2: Schematics showing electron transport conditions through a single QD (a) Current as a function of plunger gate and source/drain bias voltage displaying regions of Coulomb blockade. The electron occupancy, N, is shown as the plunger gate shifts the QD chemical potentials relative to the source/drain bias window. (b-d) Energy diagrams under various source/drain bias and plunger gate voltage

In the regime $e^2/C_1 \gg \epsilon_{N+1} - \epsilon_N$, the occupancy of the QD is directly controlled by applying an external plunger gate voltage, which enables the tuning of μ_d in the QD. Applying a bias V_{bias} to the leads creates an energy separation between μ_S and μ_D, causing a bias window to open. When the QD chemical potential lies within the source/drain bias window, $\mu_S > \mu_d(N) > \mu_D$, current flows from source to drain, as seen in Figure 1.2(a). When the QD chemical potential does not lie within the source/drain bias window, $\mu_d(N+1) > \mu_S > \mu_D > \mu_d(N)$, addition or removal of an electron onto the QD is blocked, creating Coulomb blockaded regions where no current transport occurs. In the absence of bias V_{bias}, no current transport occurs between leads, however a QD occupied by N electrons can have an electron tunnel from the leads into the QD if $\mu_S, \mu_D > \mu_d(N+1)$, or out of the QD if $\mu_d(N) > \mu_S, \mu_D > \mu_d(N-1)$.

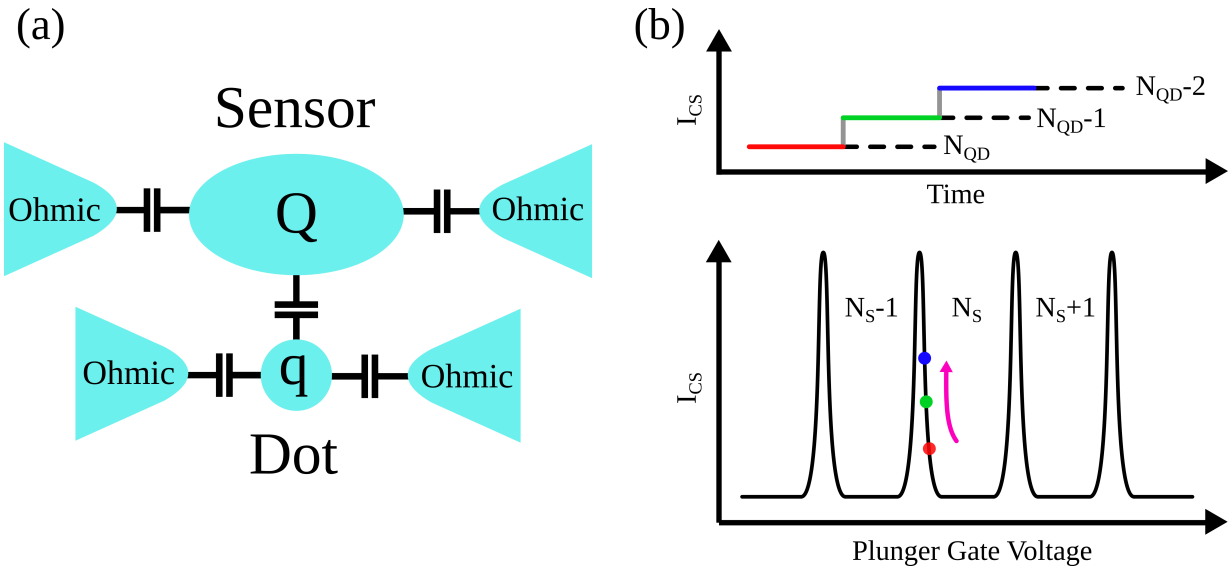


Figure 1.3: Setup to indirectly measure a QD charge state using a SET charge sensor. (a) Schematic for a charge sensor capacitively coupled to a QD with charge q. The charge sensor is tuned so that the tunnel rates through the sensor, Γ, produces a measurable current signal and sharp Coulomb peaks are resolved (b) The bottom-right graph shows the Coulomb blockade cross-section along V_{g1} from Figure 1.2(a) for the charge sensor. The charge sensor is first tuned to operate on a Coulomb peak which makes the current through the sensor, I_{CS}, sensitive to changes in capacitance of the QD. The top-right graph shows a red/blue/green line representing the measured changes in I_{CS} over time as the occupancy of the QD is varied; red/green/blue points in the bottom-right graph show I_{CS} along a Coulomb peak as a function QD occupancy.

Up to this point, we have implicitly assumed that system parameters, such as the QD capacitance and tunneling barriers, are constant quantities. However, both of these parameters depend on the electrode voltages defining the QD. Lowering the voltage V_{g1} decreases electron occupancy on the QD to the few- or single-electron regime, which effectively increases the tunnel barriers between the leads and the QD. When the tunnel barriers become sufficiently large, the tunneling rates of electrons between leads and the QD do not have high enough frequencies to produce an appreciable current that can be measured with commonly used experimental equipment. For this reason, the charge state of a QD in the few-electron regime is typically measured indirectly using a charge sensor. A charge sensor is formed using a second QD and is capacitively coupled to the desired nearby QD as seen in Figure 1.3(a). The charge sensor is tuned to operate on a Coulomb blockade

peak, which enables the current through the charge sensor to be sensitive to capacitance changes in the QD. As the electron occupancy on the QD changes, discrete current shifts are measured by the charge sensor as shown in Figure 1.3(b). The magnitude of the current shift measured by the charge sensor is proportional to the capacitive coupling to the QD. This enables the charge sensor to measure the electron occupancy on a desired nearby QD. If implemented in a multi-QD system, in practice, a single charge sensor can be used to readout ≈ 3 nearby dots in a linear array [46].

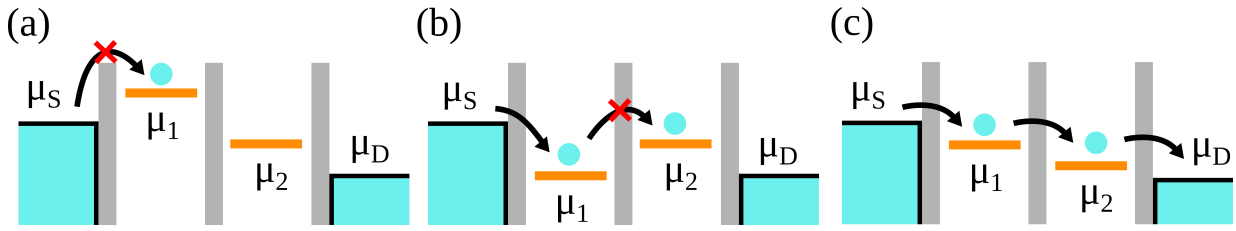


Figure 1.4: (a-b) Two chemical potential configurations where electron transport is blocked, yielding no current through the system. (c) Chemical potentials of the QDs fall within the bias window and allow for electron transport between each QD, yielding current through the system.

Our discussion above has focused on the charging and transport characteristics for a single QD system, but QC requires many QDs to construct large qubit systems, as will be discussed in more detail in Section 1.2.2. For this reason, we now turn our discussion to a double QD device, which serves as a building block for understanding larger QD systems.

A double QD system can be pictured as two single QDs in parallel or series between two ohmic contact electron reservoirs; however, we consider QDs in series since parallel QD systems serve little utility. When bias voltage V_{bias} is applied to the ohmic leads, electron transport can occur when the chemical potentials $\mu_{1(2)}$ in QDs 1(2) fall inside of the bias window and are positioned such that electrons can flow from high-to-low energy levels or resonant tunneling when the QD chemical potentials are equal $\mu_1 = \mu_2$. The energy level diagrams depicting various μ_S, μ_1, μ_2, μ_D configurations are shown in Figure 1.4. Figures 1.4(a-b) shows configurations which block electron transport, and Figure 1.4(c) shows cascading energy levels $\mu_S \geq \mu_1 \geq \mu_2 \geq \mu_D$ enabling electron transport through both QDs.

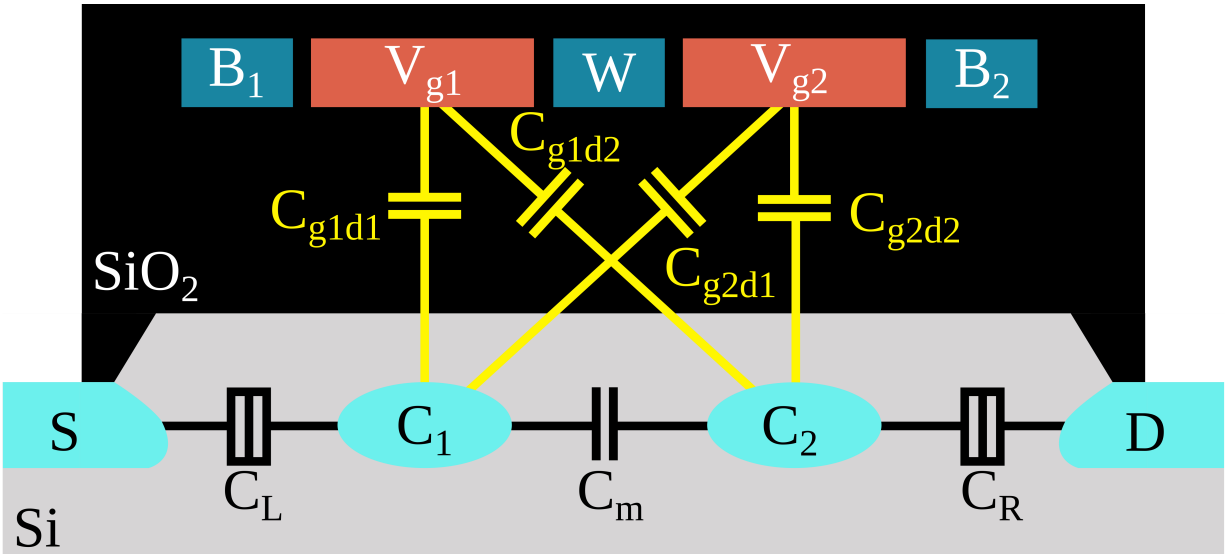


Figure 1.5: Capacitive couplings between QDs, metal gates, and source/drain leads for a double QD system. Compared to a single QD, the double QD has additional inter-QD capacitive coupling, C_m, as well as cross capacitances C_{g1d2} and C_{g2d1}. An additional barrier gate W is added for tuning the tunnel barrier between QD 1 and QD 2.

Similar to the single QD device from Figure 1.1, a double QD system is composed of a set of electron reservoirs and gate electrodes, as seen in Figure 1.5. In addition to a second plunger gate V_{g2}, which primarily controls μ_2, a tunnel gate W is added to help control the tunnel barrier between QDs 1 and 2. Current through the double QD system can be studied similarly using the constant interaction model as in the case of a single QD. Thus, the following discussion focuses on the electrostatic conditions that form stable charge configurations of the two QDs. To start, it is assumed that there are no couplings between the two QDs, such that $\mu_{1(2)}$ are independently controlled by their respective plunger gates. This implies that there is zero mutual capacitive coupling C_m between QDs and zero cross-capacitive couplings to neighboring plunger gates (i.e., crosstalk). Under very small V_{bias} electron loading can occur only when $\mu_{1(2)}$ aligns with $\mu_{S(D)}$ and enables measurement of a 2D charge stability diagram by varying the voltages on each plunger gate, as seen in Figure 1.6(a). The solid lines in Figure 1.6(a) indicate charge transitions between the two QDs or from lead to a single QD, determining the regions where the charge configuration in the two QDs is stable. Looking at the stable charge configurations for the lowest energy charge configuration for a given set of gate voltages, charge transition lines are observed, which are analogous to the single QD case from Figure 1.2(a).

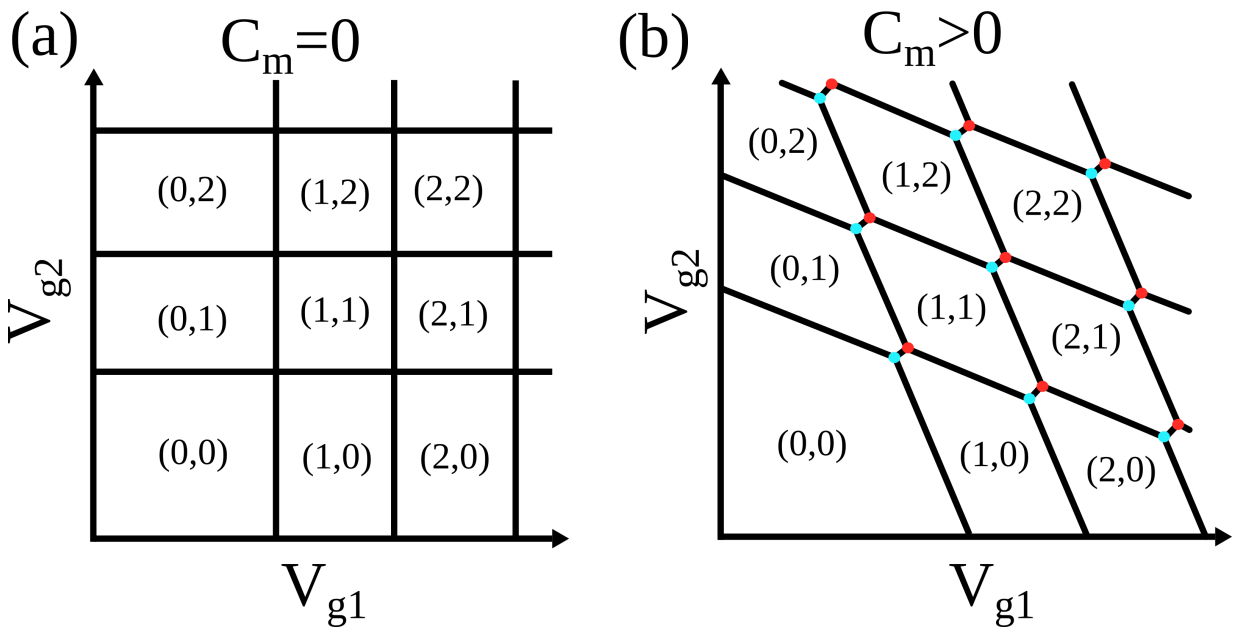


Figure 1.6: Double QD electron occupancy as a function of plunger gate voltage when (a) the QDs have no mutual capacitive coupling and (b) a finite mutual capacitive coupling. While the single QD Coulomb diamond Figure 1.2(a) shows charge stable regions, these double QD diagrams (or N-QD diagrams) are commonly referred to as charge stability diagrams. Note that these plots are cross-sections of stability regions for a larger voltage configuration space. Black lines indicate electron transfer between QDs or a QD and lead. The blue/red points in (b) indicate the electron-hole triple point pairs where three different charge configurations are in equilibrium. The change in slope of transition lines from (a) to (b) is observed when crosstalk from nearest neighbor electrodes is included, influencing the chemical potential μ of the respective QD.

It was instructive to examine the charge occupancy for the two QDs assuming independent electrostatic control. However, capacitive couplings to neighboring plunger gates, crosstalk, and capacitive coupling between QDs influence the charge stability diagram. An example of a double QD system with cross-couplings is shown in Figure 1.6(b). In this case, the charge transition lines become sloped, due to neighboring plunger gate voltage crosstalk, and charge transition intersections split into two points due to inter-QD capacitance C_m. Hexagonal regions of charge stability form, which are commonly referred to as honeycombs. The labeled points in Figure 1.6(b) are known as triple points, where three charge states are degenerate and current can flow through the double QD, enabling sequential tunneling of electrons or holes. The colored blue(red) triple point shows the location

of sequential s(hole) charge transfer. At the electron triple point, the QDs cycle through the sequence, $(N_1, N_2) \rightarrow (N_1 + 1, N_2) \rightarrow (N_1, N_2 + 1) \rightarrow (N_1, N_2)$, sequentially tunneling an electron through the double QD system. At the other triple point location, the charge transfer process is $(N_1 + 1, N_2 + 1) \rightarrow (N_1, N_2 + 1) \rightarrow (N_1 + 1, N_2) \rightarrow (N_1 + 1, N_2 + 1)$, sequentially tunneling a "conduction band hole" through the double QD system.

1.2.2 Spin Qubits

Various methods have been developed to encode the spin of charges in QDs as logical qubits, including single-spin [5, 31, 47], singlet-triplet [48–50], exchange-only [51–53], and donor-spin approaches [54–56]. Loss and DiVincenzo [31] first proposed using single-spin qubits in QDs, which is the focus of this thesis. The first step in realizing such a QC is to form a two-level system capable of encoding a qubit within a QD. From Stern-Gerlach experiments and the Dirac equation, we know that an electron confined in a QD exhibits quantized spin-$\frac{1}{2}$ angular momentum. In the absence of an external magnetic field, the spin states $|\uparrow\rangle$ and $|\downarrow\rangle$ are degenerate. Applying a strong static magnetic field, B_0, lifts this degeneracy via the Zeeman effect, creating two distinct energy levels, $E_{|\downarrow\rangle} > E_{|\uparrow\rangle}$. This allows for driven transitions, via magnetic resonance, and readout through energy-selective tunneling. Naturally, the spin states $|\uparrow\rangle$ and $|\downarrow\rangle$ can be mapped to the logical qubit states $|0\rangle$ and $|1\rangle$ for QC. Constructing a QC with QDs requires assembling a quantum processor from a large network of interconnected QDs capable of storing individual electrons, performing nearest-neighbor exchange, and enabling single-qubit rotations to realize a universal gate set.

To initialize a spin qubit in a QD, an electron is loaded by connecting the QD to an electron reservoir and tuning the chemical potential, μ_d, of the QD to allow electron loading, as discussed in Section 1.2.1. When the chemical potential of the reservoir $\mu_{\text{reservoir}}$ is lower than $E_{|\uparrow\rangle}$, electrons do not have enough energy to tunnel onto the dot, seen in Figure 1.7. Adjusting μ_d to lie between the ground and excited states of the electrons in the reservoir enables a single electron with spin state $|\uparrow\rangle$ to tunnel onto the QD, as shown in Figure 1.7(b). Occupation of electron energy states in the reservoir follows the Fermi-Dirac distribution. At $T = 0$, electrons in the reservoir occupy all energy levels up to $\mu_{\text{reservoir}}$ and cannot access any energy levels greater than $\mu_{\text{reservoir}}$. At temperature close to absolute zero, the electrons in the reservoir mainly occupy energy levels up to $\mu_{\text{reservoir}}$, however, there is a high energy tail that follows a Fermi function $p(\varepsilon) = \left(e^{-(\varepsilon-\mu)/k_B T} + 1\right)^{-1}$, where $p(\varepsilon)$ is the probability of an electron to have energy ε at a given temperature T. The blue schematic in Figure 1.7 represents thermal smearing of the electron energy distribution in the reservoir when $T > 0$. Therefore, the probability of initializing a spin state $|\uparrow\rangle$ depends

on the effective electron temperature of the reservoir and strength of the Zeeman energy splitting $E_z = E_{|\downarrow\rangle} - E_{|\uparrow\rangle}$. The magnitude of E_z is given by $E_z = g\mu_B B_0$, where $g \approx 2$ is the electron g-factor in bulk silicon, but can substantially vary from spin orbit coupling in QDs, and μ_B is the Bohr magneton. Experimental magnitudes for B_0 typically are on the order of ~ 1 T, which gives a Zeeman splitting of ≈ 116 μeV. If the thermal energy of the reservoir, $k_B T$, is comparable to the Zeeman splitting, then some $|\downarrow\rangle$ spin state electrons in the reservoir have enough energy to tunnel onto the QD with nonzero probability. To ensure nearly deterministic initialization of the qubit in the $|\uparrow\rangle$ spin state, the effective temperature of the reservoir must satisfy $k_B T \ll E_Z$. Due to the small energy scale of the Zeeman splitting, experiments are typically conducted in dilution refrigerators operating at millikelvin temperatures. However, recent experiments have demonstrated the operation of spin qubits above 1K by decoupling the QDs from the electron reservoir, which could enable experiments to be conducted in more relaxed experimental conditions and with much higher cooling powers, which could enable the co-integration of conventional CMOS circuits for control and readout [57–63].

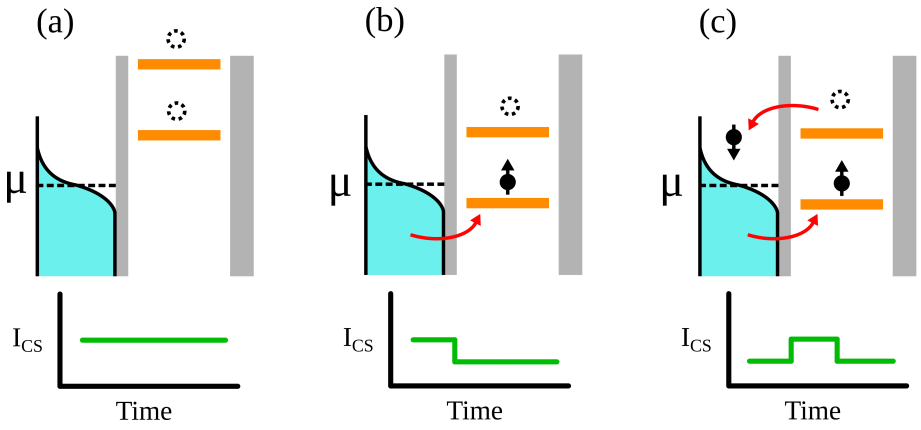


Figure 1.7: Schematic for energy selective Elzerman readout [5] of a QD spin qubit connected to an electron reservoir at mK temperature such that $E_z \gg k_B T$. (a-c) Show the current reading of a nearby charge sensor I_{CS} as electrons tunnel onto or off of the QD. (a) QD chemical potential is tuned to be higher than the chemical potential of the reservoir, preventing a single spin-up or down electron from tunneling onto the QD. (b) The QD energy levels are lowered such that the spin-up single electron energy level is lower than the chemical potential of the reservoir. This enables deterministic loading of the spin-up state. (c) After exciting the spin qubit from a quantum gate operation, the electron is able to tunnel out of the QD and is replaced by another electron in the ground spin state.

A strong advantage of QDs is the ability to readily generate entangled two-qubit states using a single QD. Loading two electrons into the same orbital state (e.g., the orbital ground state) of a QD forms an entangled singlet state $|S\rangle = (|\uparrow\downarrow\rangle - |\downarrow\uparrow\rangle)/\sqrt{2}$ due to the Pauli exclusion principle. The electron charges can be subsequently separated and shuttled such that the spin singlet becomes non-local. This principle can be used to share entanglement between different processor nodes in a network, for example. Entanglement distribution is necessary for performing non-local two-qubit quantum gate operations required for QC constructed from a network of QDs [64] and is further discussed in Section 2.5.

Qubit Control Executing quantum algorithms on a large processor requires large arrays of qubits [46, 65], but controlling many spin qubits in QDs with high fidelity remains a fundamental challenge [66]. Variations in qubit properties [67], coupled with decoherence and crosstalk [68–70], introduce significant obstacles to scaling up quantum processors. The fundamental operations in QC are comprised of single- and two-qubit gates, and any practical QC implementation requires methods for achieving these gates with high fidelity. Single-qubit gates are comprised of rotations of individual spin states, achieved through magnetic resonance, while two-qubit gates, such as the $\sqrt{\text{SWAP}}$ gate, are enabled by nearest-neighbor exchange, generating entanglement between qubits. Implementing high-fidelity versions of these gates is essential for constructing reliable quantum circuits and achieving fault-tolerant quantum computing architectures. The following discussion reviews the fundamental gate operations required to manipulate spin qubits in QDs.

A standard approach for implementing single-qubit rotations in QD spin qubits is ESR [71–73], where a microwave magnetic field B_1 is applied perpendicular to a static Zeeman field B_0. When the microwave frequency matches the electron's Larmor precession frequency, which is the same as the Zeeman energy splitting, the spin state undergoes coherent oscillations between $|\uparrow\rangle$ and $|\downarrow\rangle$, i.e., performing rotations about the Bloch sphere. Spin state transitions can be realized between $|+\rangle$ and $|-\rangle$, or $|i\rangle$ and $|-i\rangle$, states by selectively choosing the phase of the ESR field, ϕ, to be zero of $\frac{\pi}{2}$ respectively. ESR is typically performed by delivering microwave power through either a resonant cavity or a microstrip line positioned near the QD. While resonant cavities can generate large B_1 fields across an area spanning many qubits, they also induce strong electric fields, leading to photon-assisted tunneling, which results in loss of the qubit. Microstrip lines, placed within a few hundred nanometers of the dot, require less power, mitigating photon-assisted tunneling, but occupy significant space and provide only local control over a subset of qubits. While microstrip lines have demonstrated high-fidelity single-qubit gates, achieving fidelities of > 0.999 at $T = 20$ mK [73] and > 0.998 for $T > 1$ K [63], a global ESR field generated by a microwave resonator [74] will be assumed throughout the rest of this thesis.

Applying a microwave ESR pulse perpendicular to the Zeeman field implements x-axis and/or y-axis qubit rotations on the Bloch sphere; however, a rotation about the z-axis can be done by combining rotations about the x-axis and y-axis. It can also be done by a phase shift of subsequent pulses (i.e., change of frame). Therefore, implementing a single-qubit gate in a single QD system is straightforward in an experiment. However, control complexity increases rapidly when addressing single qubits in multi-QD systems due to local disorder causing variations in the electron g-factor between QDs [46, 75]. To mitigate this challenge, single qubits can be selectively tuned on or off resonance with the global ESR field by electrostatically creating a Stark shift of the electron g-factor caused by the small but finite spin–orbit coupling for electrons in silicon [76]. The ability to address individual qubits by applying external gate voltages results from the small but nonzero spin-orbit coupling in silicon.

Implementing two-qubit gates is quite natural in QD systems through control over the exchange interaction strength, J, which has been demonstrated in [47, 62, 63, 72, 77–80] and manifests as rotations between $|\uparrow\downarrow\rangle \leftrightarrow |\downarrow\uparrow\rangle$. The exchange interaction is a quantum mechanical phenomenon arising from the combination of Coulomb repulsion between electrons and the requirement that their total wavefunction (spin + spatial) be antisymmetric under particle exchange. This antisymmetry leads to an energy difference between spin triplet and singlet states, where the triplet state is higher in energy for $J > 0$. The magnitude of J arises from the tunnel coupling, t, and detuning energy, ε, magnitudes between nearest-neighbor pairs of QDs, effectively controlling the relative overlap of single-particle orbital states [81],

$$J = \frac{4t^2U}{U^2 - \varepsilon^2},$$

where U is the intra-Coulomb charging energy required to add an additional electron onto the QDs. Both tunnel coupling and detuning energy can be controlled electrostatically, enabling two-qubit entanglement gates to be controlled solely through externally applied electrode voltages. Controlling the strength of J over the duration of an applied electrode voltage pulse enables two-qubit rotations on nanosecond time scales [82], allowing SWAP and $\sqrt{\text{SWAP}}$ two-qubit exchange gate operations. Constructing general two-qubit gate operations, such as Control-Z (CZ) or Control-ROT$(\theta, \hat{n})$ (CROT), requires additional single-qubit gates. Implementing a CZ gate can be achieved using three single-qubit gates and two $\sqrt{SWAP}$ gates, as proposed in [31], while a Control-X (CNOT) gate can be realized with an additional two single-qubit gates. Instead of independently performing exchange and ESR gates, some two-qubit gates, such as CZ, can be implemented as a single gate operation by simultaneously pulsing J and the ESR field [72].

Qubit Measurement Direct measurement of the electron's magnetic moment, though desirable, is not realistically feasible due to the small magnetic moment of the electron, $\mu_e = -9.284 \times 10^{-24}\text{JT}^{-1}$. Instead, spin-correlated proxy measurements are conducted to monitor the spin state of a single qubit. One of the earliest and most common approaches to measuring the spin state of a qubit is often referred to as Elzerman readout [5] and depicted in Figure 1.7. A charge sensor is coupled to a nearby QD and tuned to operate on a Coulomb blockade peak, as in Figure 1.3(b). The QD chemical potential, μ_d, is modified to load a spin-up electron from a coupled electron reservoir, while blocking the loading of spin-down electrons. No change in current is observed from the charge sensor, I_{CS}, since the spin-up electron cannot tunnel off the QD. However, if the spin state is excited to $|\downarrow\rangle$ by a resonant ESR pulse, then the excited state has enough energy to tunnel off the QD, allowing another spin state $|\uparrow\rangle$ to tunnel onto the QD. This sequential tunneling process manifests as a blip in I_{CS}, which is shown in Figure 1.3(c). Elzerman readout establishes a foundation for measuring electron spin in QDs through spin-to-charge conversion, although it suffers from two primary limitations:

1. It is a destructive measurement, i.e, the electron spin state is lost after the electron tunnels off of the QD.

2. Reduced readout fidelity from the coupling of the QD to a reservoir at a finite effective temperature, limiting the resolution to discriminate between the two spin states.

An alternative type of spin-to-charge conversion is based on Pauli spin blockade in a double QD [83, 84], which preserves the total number of electrons in the system, as shown in Figure 1.8. Two electrons are loaded into the (1,1) charge state of a double QD and form a singlet or one of the three triplet states, $s_z \in \{-1, 0, 1\}$. When the chemical potentials of the two QDs are equal, a single electron occupies each QD, creating a (1,1) charge configuration. Applying a bias between the two QDs produces an energy level difference $\mu_1 > \mu_1$, leading to the (0,2) charge state being energetically favorable.

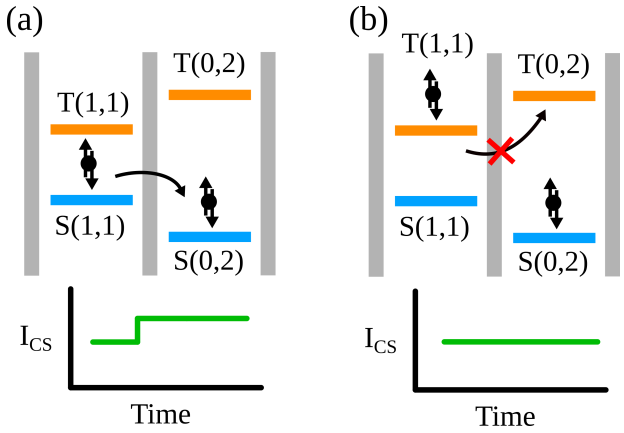


Figure 1.8: Schematic for Pauli spin blockade readout in a double QD system. The two QDs are initialized with a single electron in each QD, i.e., the (1,1) charge state. A singlet state S(1,1) has total spin angular momentum $s = 0$ while the triplet states T(1,1) have total angular momentum $s = 1$. A charge sensor is located near the left QD and is tuned to produce a measurable current signal I_{CS}. A bias is applied to the double QD system, lowering the S(0,2) charge state energy compared to S(1,1), and I_{CS} is monitored. (a) An initialized S(1,1) state enables an electron to tunnel between QDs from the S(1,1) to the S(0,2) state. (b) An initialized T(1,1) state suppresses electron tunneling between QDs due to the Pauli exclusion principle as long as the T(0,2) state is energetically unavailable.

Tunneling preserves spin, so T(1,1) cannot become S(0,2). The only possibility is T(0,2), but that is higher in energy by roughly the orbital excited state energy, so T(1,1) is blocked from tunneling into (0,2). Under small bias conditions, the electron on the left QD is allowed to tunnel onto the right QD, forming S(0,2), if the initial two-particle state was S(1,1), however, tunneling is suppressed if the initial state was T(1,1) since the energy level for T(0,2) is inaccessible. The resultant current I_{CS} monitoring the double QD spin state of a nearby charge sensor is shown in Figure 1.8.

Although high-fidelity measurements are performed using Pauli spin blockade readout [85, 86], the requirement to fabricate additional nearby charge sensor QDs to readout the qubit states increases the device complexity and overall processor footprint, which is undesirable for scalable QC. To mitigate this limitation, an alternative charge sensing gate-base dispersive readout technique can be performed using radio frequency reflectometry [87–89]. Dispersive readout uses a surface-mounted LC tank circuit connected directly to the plunger gate of a QD to measure changes in the quantum capacitance of the double QD system (i.e., in the Pauli spin blockade regime) [90], significantly reducing the total number of fabricated electrodes.

Outlook for Spin Qubits Spin qubits in semiconductor quantum dots have emerged as one of the leading candidates for scalable quantum computing due to their long coherence times, compatibility with CMOS processes, and compact device footprint. Recent years have seen significant progress in materials engineering, device fabrication, and coherent control, culminating in high-fidelity single- and two-qubit gates exceeding 99.9% and 99.5% [78, 79, 91, 92], as well as spin readout fidelities above 99% [76, 79, 93, 94]. Control mechanisms such as electric-dipole spin resonance (EDSR) using micromagnets [46, 67, 70] and globally applied ESR fields [64, 74] are actively being optimized for scalable, addressable architectures. The field is also transitioning toward automation, reproducibility, and ML-assisted calibration to reduce device tuning overheads [95, 96], while large-scale arrays—demonstrated up to 16 qubits [65]—are pushing toward error-corrected operation using surface codes. However, challenges remain in qubit variability, noise mitigation, and high-fidelity gate operation when scaling the quantum processor size. This work aims to address these bottlenecks by developing simulation-based tools that bridge experimental device design with predictive modeling, enabling more rapid design iteration and control optimization in QD-based quantum processors.

1.2.3 Plasmonically Enhanced Photocurrent

Beyond spin-based quantum systems, another area of focus in this work involves the development and enhancement of photodetectors by the application of plasmonic nanocrystals.

Metal-semiconductor-metal (MSM) photodetectors are a widely studied class of photodetectors that leverage the fast carrier transport properties of semiconductors and the built-in electric field between interdigitated metal contacts to achieve high-speed photodetection. These devices rely on the absorption of incident photons to generate electron-hole pairs, which are then collected by the metal electrodes under an applied bias. While MSM photodetectors offer advantages such as simple fabrication, high-speed operation, and broad spectral response, their performance is often limited by low quantum efficiency due to weak light absorption in the semiconductor. LSPR provides a promising route to enhance the efficiency of MSM photodetectors by leveraging the strong optical near-fields generated by metal nanostructures. Plasmonic nanostructures integrated with the detector can concentrate incident light into subwavelength regions, increasing the effective absorption cross-section and enhancing carrier generation. Additionally, plasmonic effects can modify the local density of optical states, enabling improved photocarrier extraction and reduced recombination losses. These enhancements make LSPR-engineered MSM photodetectors attractive for applications requiring high-speed, high-sensitivity photodetection across a range of wavelengths.

Metal-Semiconductor-Metal Photodetectors MSM photodetectors are fast and highly responsive optical sensors that operate based on the modulation of carrier transport within a semiconductor material. They consist of two interdigitated metal electrodes (typically made of gold, platinum, or titanium) deposited on a semiconductor substrate, forming Schottky contacts shown in Figure 1.9(a). When illuminated by incident photons with energy greater than the semiconductor bandgap, electron-hole pairs are generated in the depletion region near the metal contacts shown in Figure 1.9(c)-(d). The applied bias voltage then drives the photogenerated carriers toward the respective electrodes, resulting in a measurable photocurrent, as shown in Figure 1.9(b). The performance of MSM photodetectors is characterized by their high-speed response, large bandwidth, and low dark current, making them suitable for applications in high-speed optical communication, biomedical imaging, and ultraviolet detection. Their response time is primarily limited by carrier transit time and recombination effects, which can be optimized by engineering the electrode spacing, semiconductor material layer thickness, and surface passivation techniques to enhance efficiency and speed.

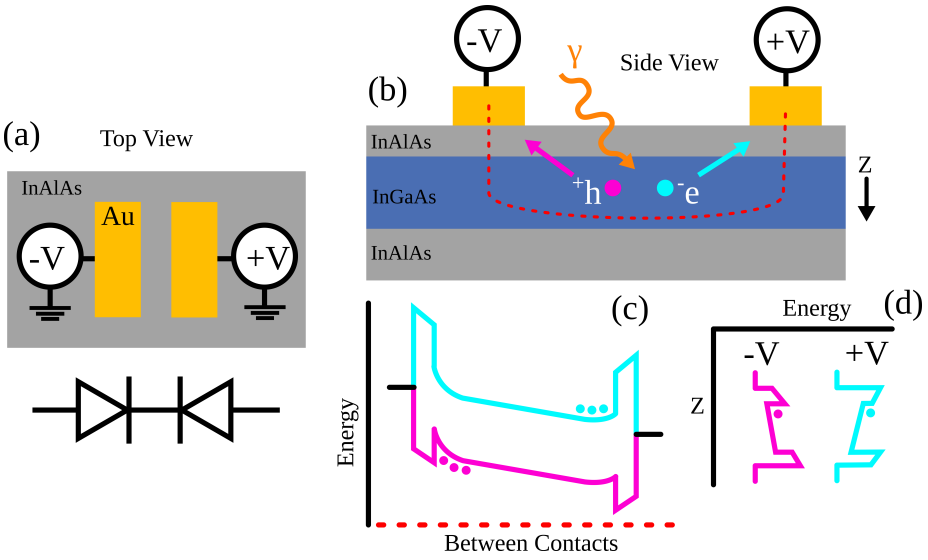


Figure 1.9: Common metal-semiconductor-metal (MSM) photodetector design (a) Metal contacts are deposited on a semiconductor (such as AlGaAs) producing a double Schottky barrier junction (b) MSM device along growth direction cross-section showing electron-hole pair generation in an InGaAs absorption layer (c) Bandedge diagram along electrode contact axis (d) Bandedge diagram along growth axis.

The responsivity of a photodetector, defined as the generated photocurrent per unit

incident optical power, varies as a function of wavelength due to the material's absorption characteristics and the efficiency of carrier extraction. In general, photodetectors exhibit a peak responsivity within the spectral range where the semiconductor's bandgap allows efficient photon absorption, with a sharp cutoff at longer wavelengths when the photon energy falls below the bandgap, shown in Figure 1.10. At shorter wavelengths, responsivity may also decrease due to increased surface recombination and absorption losses in the contact layers. The exact shape of the responsivity curve depends on factors such as the semiconductor composition, device architecture, and the presence of optical enhancement mechanisms like anti-reflection coatings or plasmonic structures. By engineering these factors, the spectral response can be tuned for specific applications, from ultraviolet to infrared detection.

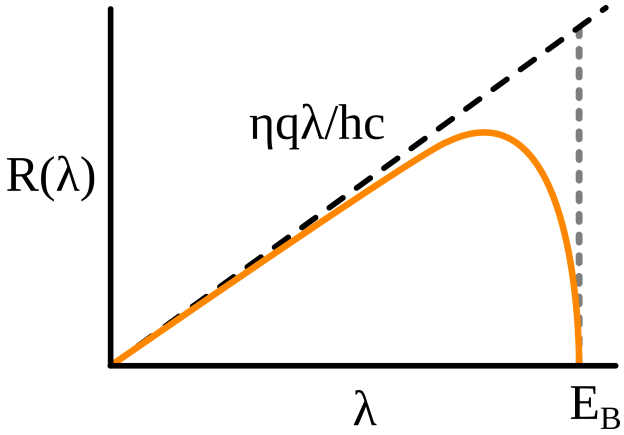


Figure 1.10: The responsivity of a general semiconductor photodetector with bandgap energy cutoff E_B is given by $R(\lambda) = \frac{\eta q \lambda}{hc}$, where η is the quantum efficiency, q is the electron charge, h is Planck's constant, and c is the speed of light. In general, the penetration depth of photons decreases with decreasing wavelength, i.e., the absorption coefficient increases, leading to greater surface recombination of electron-hole pairs and a reduction in photon-to-current conversion efficiency. Wavelengths beyond the bandgap cutoff do not possess enough energy to generate electron-hole pairs, resulting in zero response from the photodetector.

Localized Surface Plasmonic Resonance The LSPR phenomenon is physically observed when free electrons in the metallic nanoparticles oscillate collectively in response to incident light, creating resonant oscillations that significantly enhance the electromagnetic field at the nanoparticle surface, as shown in Figure 1.11. This resonance occurs at specific wavelengths determined by the size, shape, and material properties of the nanoparticles,

and it leads to a dramatic increase in local electric fields in the vicinity of the particles. The enhanced electric fields can be directly observed through the scattering or absorption of light by the nanoparticles, typically resulting in a strong color shift or intense peaks in the absorption spectra. Additionally, LSPR can be detected via changes in the extinction spectra, which correspond to shifts in the resonance frequency when the surrounding dielectric environment or particle geometry is altered.

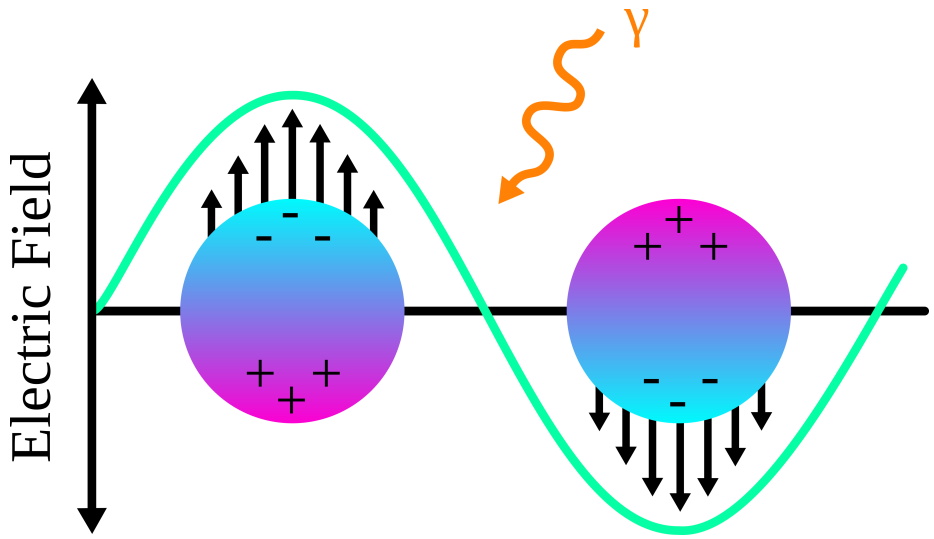


Figure 1.11: Sub-wavelength nano-particle structures exhibit enhanced electric fields locally from resonant charge fluctuations driven by external electro-magnetic field excitations.

Chapter 2

Quantum Dot Spin Qubit Simulator in Python

2.1 Introduction

Quantum dots (QDs) are a leading platform for scalable scalable quantum computing (QC). Their appeal lies in their long coherence times [97, 98], fast gate operations [91, 98], and compatibility with existing semiconductor fabrication technologies [46,99,100]. Spin-based QDs enable high-fidelity quantum gate operations through precise control of spin dynamics and tunable exchange interactions, which facilitate electrically controlled single- and two-qubit gates; an essential requirement for universal quantum computation. The small footprint of spin qubits in QDs compared to superconducting qubits or ion trap qubits is advantageous for creating high-qubit-density compact processors. Recent advances in isotopically purified materials [78,101], high-fidelity single- and two-qubit gates [78,79,91,92], "hot" qubit operation (i.e., operation above dilution refrigerator base temperatures) [62,63], and error mitigation schemes [78, 92, 102] have significantly improved coherence and control fidelity, bringing semiconductor qubits closer to fault-tolerant quantum computing. Despite these advances, scaling to large qubit arrays presents key challenges, including variability in qubit properties, crosstalk, and control complexity. Addressing these challenges will require improvements in qubit uniformity and the development of fast, tunable couplings to mitigate variability and crosstalk in large arrays. In parallel, integration with cryogenic complementary metal-oxide-semiconductor (CMOS) control electronics will be essential for scalable and efficient qubit control in practical QD-based quantum processors.

Various implementations of qubits rely on electrostatically confined charges, including

single-spin qubits [5,31,47], singlet-triplet qubits [48–50], exchange-only qubits [51–53], and donor spin qubits [54–56]. This research focuses specifically on single-electron spin qubits due to their scalability, relatively simple control requirements, and compatibility with standard semiconductor fabrication techniques. The fabrication of Quantum Processing Units (QPUs) of this kind involves two primary steps. First, semiconductor and dielectric layers are grown on a substrate using techniques such as chemical vapor deposition or atomic layer deposition to form heterostructures or quantum wells. At cryogenic temperatures (i.e., $\lesssim$ 100mK), these structures confine charges into two-dimensional electron (2-Dimensional Electron Gas (2DEG)) or hole gases (2-Dimensional Hole Gas (2DHG)), typically formed in material systems such as Si/SiGe, Si/SiO_2, GaAs/AlGaAs. Second, metal electrodes are patterned via photolithography and electron-beam lithography, used to apply external voltage that locally induces or depletes carriers to form isolated charge islands (i.e., QDs) and tune them into the few-charge-particle regime. These lateral gates typically have feature sizes on the order of tens of nanometers, highlighting the precision required in device fabrication. Research efforts have explored various QD material systems and electrode geometries, such as AlGaAs/GaAs hole/electron QDs [103], (CMOS)-compatible silicon electron QDs [72], and Si/SiGe electron/hole QDs [97], among others. Researchers originally investigated AlGaAs/GaAs QD devices due to the low lattice mismatch between AlGaAs and GaAs, which enables the growth of high-quality, low-disorder heterojunctions. However, the presence of non-zero nuclear spins in both materials leads to hyperfine interactions that cause unwanted qubit decoherence, i.e., inhomogeneous dephasing, T_2^*, on the order of $\sim$ 10 ns [49]. As fabrication processes have improved, researchers have shifted towards using enriched ^{28}Si for its zero nuclear spin, $T_2^* \sim 100$ μs [76], and compatibility with standard CMOS fabrication steps to enable large-scale processors. This shift has enabled more stable spin coherence and integration with industrial process flows. These device architectures have demonstrated the ability to initialize qubits, perform high-fidelity gate operations, and enable qubit readout [76, 79, 93, 94]. Hitherto, QD devices require highly skilled researchers to manually tune qubits, often over hours or days, for initialization, manipulation, and readout. Advances in fabrication have enabled QD arrays consisting of up to 16 qubits in a 2×2 arrangement [65] and the potential for three-dimensional arrays of coupled QDs [104]. The days of laboriously tuning QD devices may be nearing an end as companies like Intel have demonstrated 12-qubit QD arrays with embedded charge sensors, which enable fast, high-fidelity charge-state readout and pave the way for autonomous device tuning using real-time feedback, leveraging CMOS-compatible fabrication processes [46]. The development of automated tuning and calibration protocols, coupled with the potential for reproducible behavior across fabrication runs, could enable more efficient tuning protocols for future QPU devices. As qubit numbers increase, accurate predictions of device performance and control become a necessity.

QD spin qubits are formed by applying external electrode voltages to tune the QD's chemical potential, allowing for controlled addition or removal of electrons. A sufficient energy separation between the excited state ($|\uparrow\rangle$) and ground state ($|\downarrow\rangle$) is achieved by applying an external static Zeeman magnetic field, lifting spin degeneracy to enable spin-state manipulation. Once a spin qubit is initialized on a QD, its state can be manipulated by applying an external, resonant Radio Frequency (RF) magnetic field. The external RF magnetic field can be directly applied perpendicular to the Zeeman field, or enhanced spin-orbit coupling can be induced that enables RF electric fields from nearby electrodes to drive spin-state transitions. Qubit control is achieved through electron spin resonance (ESR) using global [74] or local microstrip lines [71–73], or via Electron Dipole Spin Resonance (EDSR) using micromagnets [46, 67, 70], which generate local magnetic field gradients for selective qubit addressing. While global ESR scales efficiently with fewer control lines, EDSR is typically more suitable for individual qubit addressability in dense arrays due to its localized control capabilities. The choice of control mechanism impacts scalability, fidelity, and coherence, guiding the optimization of QD-based quantum processors. In this thesis, we focus on spin qubit manipulation via a global microwave magnetic field that is capable of driving ESR transitions for all qubits in the processor.

As QD-based quantum processors scale, the increasing complexity of qubit control, calibration, and error mitigation necessitates a strong foundation in theoretical modeling and simulation tools [105–107]. Accurate theoretical models–such as Poisson–Schrödinger, Hubbard, or Full Configuration Interaction (FCI)–are essential for predicting physical behavior, guiding device design, and optimizing qubit operation by providing insights into decoherence mechanisms, charge noise effects, and exchange interactions. These models form the basis for numerical simulations that enable detailed studies of qubit dynamics, gate fidelities, and system-level performance under realistic conditions. Beyond fundamental modeling [108–114], specialized simulation tools are needed to study qubit evolution [115] within quantum circuits, allowing validation of quantum algorithms and refinement of error correction protocols [116, 117] tailored for QD architectures. Additionally, as experimental setups grow increasingly complex, advanced simulations can assist in real-time hardware control [116] by predicting optimal tuning parameters and automating calibration [95, 96, 118].In practical implementations, this is often achieved through embedded FPGAs and fast feedback loops that interface directly with measurement hardware to enable low-latency adaptive control. A crucial extension of these capabilities involves generating datasets through physics-based simulations [119–123], which can be leveraged for training machine learning (ML) models to automate qubit initialization, manipulation, and readout. This hybrid approach enables both predictive control and adaptive calibration across fabrication runs, bridging the gap between theoretical modeling and experimental

implementation. By integrating theoretical modeling with simulation-driven experimentation and ML-assisted control, researchers can accelerate the development of scalable, high-fidelity quantum processors while mitigating the challenges associated with qubit variability, decoherence from charge noise, and manual tuning.

Spin qubits in semiconductor QDs provide a promising route to scalable, fault-tolerant quantum computing. Despite these advantages, the development of large-scale spin-based QPUs remains hindered by significant engineering challenges, including precise device geometry design and optimal tuning of spin and charge states. To address these challenges, we develop a simulation tool that accelerates quantum device design iterations before fabrication. By leveraging three-dimensional Poisson simulations, we extract electrostatic potential landscapes of isolated QDs to compute spin and Hubbard Hamiltonian parameters, enabling efficient modeling of linear QD arrays. The simulator also supports the inclusion of disorder, charge traps, and realistic noise models, allowing for more accurate and robust predictions of device performance under experimental conditions. Precise spin qubit control requires mapping experimental parameters, such as electrode voltages, to effective qubit properties, including the electronic g-factor, exchange energy, and chemical potential. This mapping facilitates the implementation of optimal qubit control strategies, such as Gradient Ascent Pulse Engineering (GRAPE) or a constrained pulse shape engineering approach developed by Bohdan Khromets [1]–which determines theoretically perfect voltage control pulses compared to GRAPE. Our simulation framework enables the design of experimental voltage pulses to control Hamiltonian parameters, ensuring that the simulated results are physically accurate. These results serve as key figures of merit for device characterization and the implementation of single- and two-qubit gate operations, which form a universal gate set for QC. Such operations are essential for implementing general quantum algorithms and can be applied to construct entangled states in node-based quantum networks to execute surface code error correction protocols. The simulation framework developed in this thesis serves as a versatile design and validation platform, a "playground" for optimizing device architectures, testing multi-qubit control schemes, and informing the development of scalable models of spin-based quantum processors. Uniquely, the simulator operates in terms of actual gate voltages applied to realistic device geometries, in contrast to approaches that rely on idealized or analytically simplified potentials. The following chapter presents the construction and capabilities of this framework, and demonstrates its use in exploring both near-term device control and long-term architectural strategies.

2.2 Quantum Dot Spin Qubit Simulator

An important component for classical control of qubits in a QD system is the precise tunability of the QD device's underlying electrostatic potential using external experimental controls, such as electrode voltages. A priori knowledge of the potential landscape as a function of these voltages enables the extraction of effective parameters for the system Hamiltonian prior to device fabrication and characterization. This capability is critical for developing control methods and predicting device performance, thereby reducing experimental overhead and accelerating the design cycle. To facilitate processing of electrostatic potential datasets, qubit control method development, and general QC implementations using spin qubits in QDs, a Python-based QuDiPy package has been developed, which contains several modules for Poisson solvers, Hamiltonian parameter extraction, and control optimization. QuDiPy addresses critical gaps in quantum device engineering by unifying electrostatic landscape reconstruction, Hamiltonian parameter extraction, and control pulse optimization into a single simulation framework, capabilities that previously required disjointed toolchains [106, 115, 116, 124, 125]. Its automated voltage-to-Hamiltonian mapping enables rapid exploration of high-dimensional gate voltage spaces, which is essential for mitigating crosstalk in dense qubit arrays. As the first software package to combine realistic device electrostatics with full-stack qubit control simulations–encompassing everything from low-level voltage tuning to high-level gate fidelity analysis–QuDiPy significantly accelerates the transition from theoretical device designs to experimentally viable quantum processors.

In general, the underlying electrostatic potential for a specific QD device design may be determined numerically by solving both Poisson's and Schrödinger's equations self-consistently for a specific charge density distribution and set of applied electrode voltages. Self-consistency is essential because the charge distribution influences the electrostatic potential, which in turn modifies the wavefunction and thus the charge distribution itself. To precisely determine the potential landscape requires calculating the many-particle wavefunction under various voltage configurations, which proves to be computationally resource-intensive. To mitigate computational resource demand, one commonly uses a single-particle wavefunction and a mean-field potential [126] to approximate the multi-particle wavefunction. Such approximations fail to accurately represent the electron behavior in QD devices since numerical solutions of the electron density are not quantized, due to the ignored multi-particle Coulomb repulsion. Ignoring multi-particle interactions leads to unrealistic continuous charge densities under various voltage configurations and leads to incorrect electrostatic potentials. To address this, we define pseudo-materials to prevent electron population over experimental voltage ranges. Alternatively, we introduce electron doping

profiles at the heterojunction to approximate a quantized electron density distribution and estimate the underlying 3D potential landscape of a QD device. We focused on the 2D behavior of electrons confined in QDs due to the strong confinement at the heterojunction along the growth axis of the substrate. The 2D electrostatic potentials are determined at the expected 2DEG location along the growth axis from simulated 3D potentials calculated via the classical Poisson finite-element solver `nextnano++` [126]. The 2D potential datasets are generated for a range of control voltage configurations, $\{\vec{\mathcal{V}}\}$, where each control vector, $\vec{\mathcal{V}}$, consists of plunger gate voltages, $\vec{V}$, and tunnel barrier voltages, $\vec{W}$, and is defined as,

$$\vec{\mathcal{V}} \coloneqq \vec{V} \cup \vec{W} \equiv [V_1, W_1, \cdots, W_{N-1}, V_N],$$

for a device consisting of N QDs.

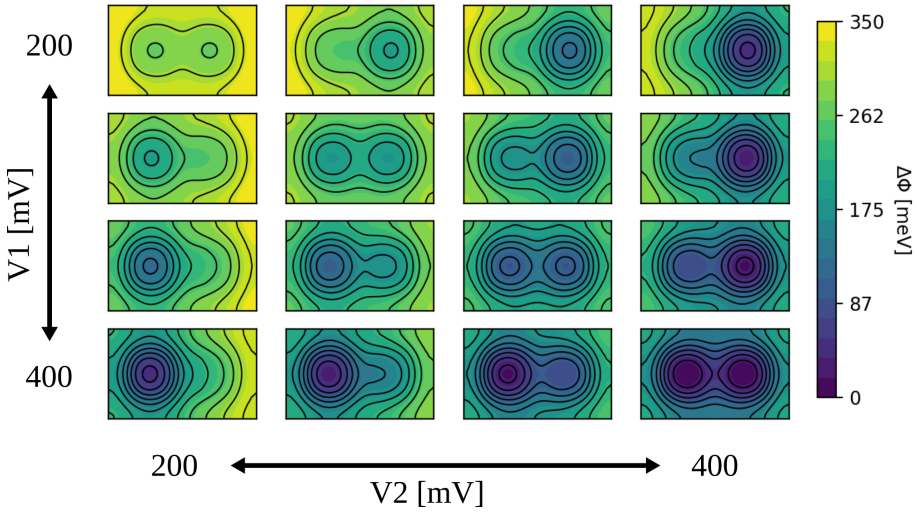


Figure 2.1: Mosaic of simulated electrostatic potential landscapes for a silicon, MOSFET style, double QD device as a function of the applied plunger gate voltages. Moving along the diagonal, top-left to bottom-right, shows the potential well depth increases without any detuning between the QDs. Conversely, the anti-diagonal, bottom-left to top-right, shows how to deepest potential well depth changes from the left to the right QD as the detuning voltage $\mathrm{V}_{\mathrm{detuning}} = \mathrm{V}_1 - \mathrm{V}_2$ is symmetrically varied from -200mV to 200mV.

The simulator processes the finite number of 2D potentials, $\Phi(\vec{r}, \vec{\mathcal{V}})$, simulated for a set of voltage configurations $\{\vec{\mathcal{V}}\}$ and performs a multi-variable interpolation for spatial and voltage coordinates to generate 2D interpolation functions for both the 2D potential, $\tilde{\Phi}(\vec{r}, \vec{\mathcal{V}})$, and the electric field along the growth axis, $\tilde{\mathcal{E}}(\vec{r}, \vec{\mathcal{V}})$. As seen in figure 2.1, cross-sections of

the potential interpolation objects $\tilde{\Phi}(\vec{r}, \vec{\mathcal{V}})$ are plotted over a range of plunger gate voltages for a CMOS style double QD device.

The interpolated functions $\tilde{\Phi}(\vec{r}, \vec{\mathcal{V}})$ and $\tilde{\mathcal{E}}(\vec{r}, \vec{\mathcal{V}})$ provide a direct mapping of the external control voltage inputs to the QD potential and electric field environment. These functions are inputs to the QuDiPy package, which enables a user to design a semiconductor QD device to be fabricated and estimate expected qubit dynamics. The general use of QuDiPy flows is as follows:

1. Design a 3D semiconductor QD device. Figure 2.2(a) shows a top-down view cross-section for an example double QD device with a single electron transistor for readout.

2. Solve 3D Poisson's equation for a range of control voltage configurations expected during experimental operation.

3. Process the 3D potentials to extract the 2D interpolation functions $\tilde{\Phi}(\vec{r}, \vec{\mathcal{V}})$ and $\tilde{\mathcal{E}}(\vec{r}, \vec{\mathcal{V}})$ for input to other QuDiPy modules.

4. Calculate the Single Particle Ground State Wavefunctions (SPGSWs) for all voltage configurations, as seen in figure 2.2(b).

5. Use the interpolation functions and SPGSWs to calculate relevant effective Hamiltonian parameters, design an experiment or quantum circuit to be simulated, and evolve the system density matrix under time-dependent external experiment controls, as seen in figure 2.2(c).

6. Predict the time evolution of a spin qubit processor; an example of a Hadamard gate applied to the first qubit while the second qubit idles is seen in figure 2.2(d).

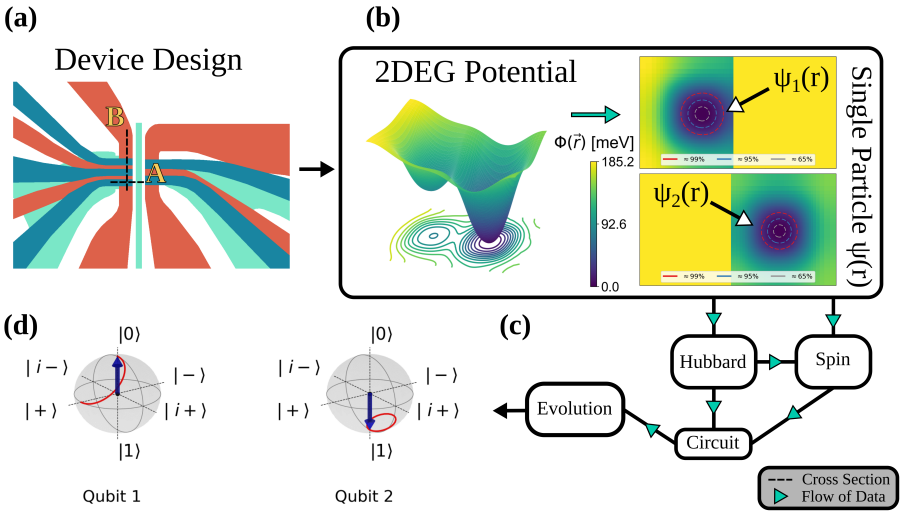


Figure 2.2: High level representation of data processing in the QuDiPy simulator for a double QD, i.e. 2 spin qubit, example (a) User designs a layered metal/semiconductor device and uses finite-element Poisson solutions to determine 3D electrostatic potential landscape for electrode voltage configurations in the range of expected experimental operation (b) The simulator extracts 2D electrostatic potential at the position of the 2DEG and calculates single particle ground state wave functions, i.e. $\psi_1(r)$ and $\psi_2(r)$, for isolated QD potentials at each simulated voltage configuration (see Section 2.2.3 for further discussion) (c) Python modules construct spin and Hubbard Hamiltonians allowing the user to initialize a given input density matrix, set of experimental gate operations, and construct a desired quantum circuit (d) The evolution module contains tools to visualize quantum gate operations.

2.2.1 Modeling Electrostatic Potentials

A fabricated spin qubit QD device consists of many plunger, barrier, and screening electrodes to control the QD confinement potential shape and location, as in figure 2.2(a). However, for efficient simulation of the electrostatic potential landscape, the device geometry used for solving the 3D finite-element Poisson solutions is simplified by only considering the electrode geometry near the regions where QDs are expected to form. The simplified device geometry used in this study is shown in Figure 2.3. Figure 2.3(a) shows the side cross-section of the QD device where a 2DEG is formed in the silicon substrate at the SiO_2/silicon heterojunction. Figure 2.3(b) shows the potential cross-section showing where electrons can accumulate when a positive voltage is applied to shift the conduction band

below the Fermi level, inducing a 2DEG which can be tuned into the few-electron regime.

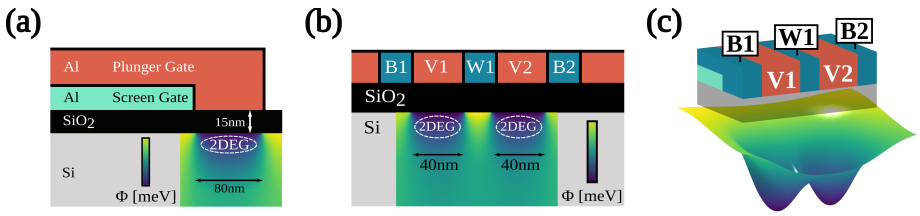


Figure 2.3: Cross-sections from figure 2.2 along lines (black dashed lines) (a) Cross-section perpendicular to QD array. (b) Cross-section along QD array. (c) Reduced 3D model geometry used for finite-element Poisson calculations of the electrostatic potential landscape in the plane of the induced 2DEGs.

2.2.2 Solving Time-Independent Schrödinger Equation

To numerically solve the Time Independent Schrödinger Equation (TISE) we must map the TISE,

$$-\frac{\hbar^2}{2m^*}\nabla^2\psi + V\psi = E\psi, \tag{2.1}$$

to a eigenvalue problem of the form $H\vec{\psi} = \lambda\vec{\psi}$, where $\vec{\psi}$ is a vector representing the wavefunction ψ at all spatial points on a mesh grid. This first step is to approximate the Laplacian, ∇^2, on a finite coordinate system.

Non-Uniform Mesh Grid Spacing

Derivatives can be approximated using finite difference methods, which are derived using Taylor series expansions of the wavefunction ψ. An example of a single variable wavefunction is,

$$\psi(x_i) + \frac{d\psi(x_i)}{dx}\Delta x_i + \frac{d^2\psi(x_i)}{dx^2}\frac{(\Delta x_i)^2}{2!} + \ldots + \frac{d^n\psi(x_i)}{dx^n}\frac{(\Delta x_i)^n}{n!}, \tag{2.2}$$

where $\Delta x_i = x_{i+1} + x_i$ is the 1D mesh grid step size.

1D TISE Eigenvalue Problem

The 1D Schrödinger equation is written as follows,

$$-\frac{\hbar^2}{2m^*}\frac{d^2\psi(x)}{dx^2} + V(x)\psi(x) = E\psi(x). \tag{2.3}$$

To solve this Ordinary Differential Equation (ODE), the first step is to approximate the first and second derivatives. The first derivatives can be approximated on a general 1D mesh grid as follows:

$$\left(\frac{d\psi}{dx}\right)_{i+1/2} \approx \frac{\psi(x+\Delta x_i) - \psi(x)}{\Delta x_i} + O\left({\Delta x_i}^2\right), \tag{2.4}$$

$$\left(\frac{d\psi}{dx}\right)_{i-1/2} \approx \frac{\psi(x) - \psi(x-\Delta x_{i-1})}{\Delta x_{i-1}} + O\left({\Delta x_{i-1}}^2\right). \tag{2.5}$$

The second derivative can then be approximated as,

$$\begin{aligned}
\left(\frac{d\psi^2}{dx^2}\right)_i &\approx \frac{2}{x_{i+1} - x_{i-1}}\left[\left(\frac{d\psi}{dx}\right)_{i-1/2} - \left(\frac{d\psi}{dx}\right)_{i+1/2}\right], \\
&= \frac{2}{x_{i+1} - x_i + x_i - x_{i-1}}\left[\left(\frac{d\psi}{dx}\right)_{i-1/2} - \left(\frac{d\psi}{dx}\right)_{i+1/2}\right], \\
&= \frac{2}{\Delta x_i - \Delta x_{i-1}}\left[\left(\frac{d\psi}{dx}\right)_{i+1/2} - \left(\frac{d\psi}{dx}\right)_{i-1/2}\right], \\
&= \frac{2}{\Delta x_i - \Delta x_{i-1}}\left(\frac{\psi(x+\Delta x_i) - \psi(x)}{\Delta x_i} - \frac{\psi(x) - \psi(x-\Delta x_{i-1})}{\Delta x_{i-1}}\right).
\end{aligned} \tag{2.6}$$

Let $L_i^2 = \frac{1}{2}(\Delta x_i - \Delta x_{i-1})$ [127] and $\gamma = -\frac{\hbar^2}{2m^*}$, then the Schrödinger equation becomes,

$$\begin{aligned}
\frac{\gamma}{L_i^2}\left[\left(\frac{\psi(x_i+\Delta x_i) - \psi(x_i)}{\Delta x_i}\right) - \left(\frac{\psi(x_i) - \psi(x_i - \Delta x_{i-1})}{\Delta x_{i-1}}\right)\right] + V(x_i)\psi(x_i) &= E\psi(x_i), \\
\frac{\gamma}{L_i^2}\left[\left(\frac{\psi_{i+1} - \psi_i}{\Delta x_i}\right) - \left(\frac{\psi_i - \psi_{i+1})}{\Delta x_{i-1}}\right)\right] + V_i\psi_i &= E\psi_i, \\
\frac{\gamma}{L_i^2}\left[\frac{\psi_{i+1}}{\Delta x_i} + \frac{\psi_{i-1}}{\Delta x_{i-1}}\right] + \left[-\frac{\gamma}{L_i^2}\left(\frac{1}{\Delta x_{i-1}} + \frac{1}{\Delta x_i}\right) + V_i\right]\psi_i &= E\psi_i.
\end{aligned} \tag{2.7}$$

Now the state vector $\vec{\psi}$ can be defined which describes the 1D wavefunction at all discrete x-coordinates,

$$\vec{\psi} = \begin{bmatrix} \psi_2 \\ \psi_3 \\ \vdots \\ \psi_{N-1} \end{bmatrix}. \tag{2.8}$$

Note, at the boundaries of the spatial region under consideration, the wavefunction at x_1 and x_N are set to zero, i.e. $\psi_1 = \psi_N = 0$. Having defined the state vector and necessary boundary conditions allows the eigenvectors and values to be found for the eigenvalue problem $H\vec{\psi} = \lambda\vec{\psi}$ by using equation 2.7 to write H as,

$$H_{ij} = \begin{cases} \frac{1}{L_i^2 \Delta x_i}, & \text{if } j = i+1, \\ \frac{1}{L_i^2 \Delta x_{i-1}}, & \text{if } j = i-1, \\ -\frac{1}{L_i^2}\left(\frac{1}{\Delta x_{i-1}} + \frac{1}{\Delta x_i}\right) + \frac{V_i}{\gamma}, & \text{if } j = i, \\ 0 & \text{otherwise} \end{cases} \tag{2.9}$$

where $\lambda = \frac{E}{\gamma}$. It is instructive to partially write elements of H in matrix form and, for compactness, define $\eta_{i-1,i} = -\left(\frac{1}{\Delta x_{i-1}} + \frac{1}{\Delta x_i}\right)$. Therefore, H takes the form,

$$H = \begin{bmatrix} \frac{1}{L_2^2}\eta_{12} + \frac{V_2}{\gamma} & \frac{1}{L_2^2 \Delta x_2} & 0 & \cdots & 0 \\ \frac{1}{L_3^2 \Delta x_2} & \frac{1}{L_3^2}\eta_{23} + \frac{V_3}{\gamma} & \frac{1}{L_3^2 \Delta x_3} & \ddots & \vdots \\ 0 & \frac{1}{L_4^2 \Delta x_3} & \frac{1}{L_4^2}\eta_{34} + \frac{V_4}{\gamma} & \ddots & 0 \\ \vdots & \ddots & \ddots & \ddots & \frac{1}{L_{N-2}^2 \Delta x_{N-2}} \\ 0 & \cdots & 0 & \frac{1}{L_{N-2}^2 \Delta x_{N-2}} & \frac{1}{L_{N-1}^2}\eta_{N-2,N-1} + \frac{V_{N-1}}{\gamma} \end{bmatrix} \tag{2.10}$$

The Hamiltonian H is sparse and tridiagonal, however, non-symmetric. To accurately and efficiently solve the computational eigenvalue problem for orthogonal eigenvectors $\vec{\psi}$, we transform the matrix H into a symmetric matrix [127,128]. This is achieved by taking note that each row of H is multiplied by L_i^{-2}, therefore, defining a diagonal matrix $M \coloneqq LL$ with diagonal elements L_i^2 and taking the product with H produces a symmetric matrix

S,

$$S = MH = \begin{bmatrix} \eta_{12} + \frac{V_2}{\gamma} & \frac{1}{\Delta x_2} & 0 & \cdots & 0 \\ \frac{1}{\Delta x_2} & \eta_{23} + \frac{V_3}{\gamma} & \frac{1}{\Delta x_3} & \ddots & \vdots \\ 0 & \frac{1}{\Delta x_3} & \eta_{34} + \frac{V_4}{\gamma} & \ddots & 0 \\ \vdots & \ddots & \ddots & \ddots & \frac{1}{\Delta x_{N-2}} \\ 0 & \cdots & 0 & \frac{1}{\Delta x_{N-2}} & \eta_{N-2,N-1} + \frac{V_{N-1}}{\gamma} \end{bmatrix}. \tag{2.11}$$

The original eigenvalue problem is transformed by first multiplying M to both sides and using the diagonal matrix L^{-1}, which has diagonal elements $L_i^{-1} = \sqrt{\frac{2}{\Delta x_i - \Delta x_{i-1}}}$,

$$\begin{aligned} S\vec{\psi} = MH\vec{\psi} &= \lambda M\vec{\psi}, \\ \left(L^{-1}SL^{-1}\right) L\vec{\psi} &= \lambda L^{-1}M\vec{\psi} = \lambda L\vec{\psi}, \\ H_{sys}\vec{\Psi} &= \lambda\vec{\Psi}. \end{aligned} \tag{2.12}$$

The transformed eigenvalue problem gives eigenvalues λ for transformed wavefunction eigenvectors $\vec{\Psi}$. To find the eigen energies, E, and true state vectors, $\vec{\psi}$, simply transform the quantities as follows, $E = \gamma\lambda$ and $\vec{\psi} = L^{-1}\vec{\Psi}$.

2D TISE Eigenvalue Problem

The 2D Schrödinger equation is written as follows,

$$-\frac{\hbar^2}{2m^*}\left(\frac{\partial^2\psi(x,y)}{\partial x^2} + \frac{\partial^2\psi(x,y)}{\partial y^2}\right) + V(x,y)\psi(x,y) = E\psi(x,y) \tag{2.13}$$

The continuous 2D TISE in the above equation 2.13 can be discretized using the 1D finite difference second derivative from equation 2.6 as,

$$\begin{aligned} \gamma\Bigg[\frac{2}{\Delta x_i + \Delta x_{i-1}}\left(\frac{\psi(x+\Delta x_i, y) - \psi(x,y)}{\Delta x_i} - \frac{\psi(x,y) - \psi(x-\Delta x_{i-1}, y)}{\Delta x_{i-1}}\right) + \\ \frac{2}{\Delta y_j + \Delta y_{j-1}}\left(\frac{\psi(x, y+\Delta y_j) - \psi(x,y)}{\Delta y_j} - \frac{\psi(x,y) - \psi(x, y-\Delta y_{j-1})}{\Delta y_{j-1}}\right)\Bigg] + \\ V(x,y)\psi(x,y) = E\psi(x,y) \end{aligned} \tag{2.14}$$

Which is simplified using index notation as,

$$\gamma\left[\frac{2}{\Delta x_i+\Delta x_{i-1}}\left(\frac{\psi_{i+1,j}-\psi_{ij}}{\Delta x_i}-\frac{\psi_{ij}-\psi_{i-1,j}}{\Delta x_{i-1}}\right)+\right.$$
$$\left.\frac{2}{\Delta y_j+\Delta y_{j-1}}\left(\frac{\psi_{i,j+1}-\psi_{ij}}{\Delta y_j}-\frac{\psi_{ij}-\psi_{i,j-1}}{\Delta y_{j-1}}\right)\right]+$$
$$V_{ij}\psi_{ij}=E\psi_{ij} \tag{2.15}$$

To better understand how to solve the eigenvalue problem in two dimensions, equation 2.15 is written in operator form as,

$$\begin{aligned}\left[\gamma\left(D_y\otimes I_x+I_y\otimes D_x\right)+W\right]\vec{\phi}&=E\vec{\phi}\\ \left[\gamma\left(D_y\oplus D_x\right)+W\right]\vec{\phi}&=E\vec{\phi}\end{aligned} \tag{2.16}$$

Where the 2D state vector takes the form,

$$\vec{\phi}=\begin{bmatrix}\vec{\psi}_{(2\longrightarrow N-1),2}\\ \vec{\psi}_{(2\longrightarrow N-1),3}\\ \vdots\\ \vec{\psi}_{(2\longrightarrow N-1),(N-1)}\end{bmatrix} \tag{2.17}$$

Where $\vec{\psi}_{(2\longrightarrow N-1),j}$ is defined as follows.

$$\vec{\psi}_{(2\longrightarrow N-1),j}=\begin{bmatrix}\psi_{2j}\\ \psi_{3j}\\ \vdots\\ \psi_{N-1,j}\end{bmatrix} \tag{2.18}$$

The left side of equation 2.16 is a sparse banded tri-diagonal matrix which is better seen by writing the tensor products $D_y\otimes I_x$ and $I_y\otimes D_x$, as well as W explicitly. The tensor

product $D_y \otimes I_x$ is a block tridiagonal matrix as shown below,

$$I_y \otimes D_x = I_y \otimes \begin{bmatrix} \frac{1}{L_2^2}\eta_{12} & \frac{1}{L_2^2\Delta x_2} & 0 & \cdots & 0 \\ \frac{1}{L_3^2\Delta x_2} & \frac{1}{L_3^2}\eta_{23} & \frac{1}{L_3^2\Delta x_3} & \ddots & \vdots \\ 0 & \frac{1}{L_4^2\Delta x_3} & \frac{1}{L_4^2}\eta_{34} & \ddots & 0 \\ \vdots & \ddots & \ddots & \ddots & \frac{1}{L_{N-2}^2\Delta x_{N-2}} \\ 0 & \cdots & 0 & \frac{1}{L_{N-2}^2\Delta x_{N-2}} & \frac{1}{L_{N-1}^2}\eta_{N-2,N-1} \end{bmatrix} \tag{2.19}$$

$$= \begin{bmatrix} D_x & 0 & 0 & \cdots & 0 \\ 0 & D_x & 0 & \ddots & \vdots \\ 0 & 0 & D_x & \ddots & 0 \\ \vdots & \ddots & \ddots & \ddots & 0 \\ 0 & \cdots & 0 & 0 & D_x \end{bmatrix} \tag{2.20}$$

Similarly, the tensor product $D_y \otimes I_x$ is a "banded" block diagonal matrix as shown below,

$$D_y \otimes I_x = \begin{bmatrix} \frac{1}{L_2^2}\eta_{12}I_x & \frac{1}{L_2^2\Delta x_2}I_x & 0 & \cdots & 0 \\ \frac{1}{L_3^2\Delta x_2}I_x & \frac{1}{L_3^2}\eta_{23}I_x & \frac{1}{L_3^2\Delta x_3}I_x & \ddots & \vdots \\ 0 & \frac{1}{L_4^2\Delta x_3}I_x & \frac{1}{L_4^2}\eta_{34}I_x & \ddots & 0 \\ \vdots & \ddots & \ddots & \ddots & \frac{1}{L_{N-2}^2\Delta x_{N-2}}I_x \\ 0 & \cdots & 0 & \frac{1}{L_{N-2}^2 I_x\Delta x_{N-2}}I_x & \frac{1}{L_{N-1}^2}\eta_{N-2,N-1}I_x \end{bmatrix} \tag{2.21}$$

The matrix W is a diagonal matrix of the potential that has been "unwrapped" to match the dimensions of the operator $D_y \oplus D_x$. The matrix elements are defined as,

$$W_{ij} = \langle i+j-1 | V_{ij} | i+j-1 \rangle \tag{2.22}$$

The eigenvalue problem posed by equation 2.16 can be rewritten after making use of the following operator definitions $M = LL$ and $N = KK$. Note that K is defined similarly to

L except that Δx is replaced by Δy.

$$\begin{aligned}
[\gamma\left(D_y \oplus D_x\right) + W]\,\vec{\phi} &= E\vec{\phi} \\
H\vec{\phi} &= E\vec{\phi} \\
\left(N \otimes M\right) H\vec{\phi} &= E\left(N \otimes M\right)\vec{\phi} \\
S\vec{\phi} &= E\left(N \otimes M\right)\vec{\phi} \\
\left(K^{-1} \otimes L^{-1}\right) S\left(K^{-1} \otimes L^{-1}\right)\vec{\phi} &= E\left(K \otimes L\right)\vec{\phi} \\
H_{sys}\vec{\Psi} &= \lambda\vec{\Psi}
\end{aligned} \tag{2.23}$$

The transformed eigenvalue problem gives eigenvalues λ for transformed wavefunction eigenvectors $\vec{\Psi}$. To find the eigen energies, E, and true state vectors, $\vec{\psi}$, simply transform the quantities as follows, $E = \gamma\lambda$ and $\vec{\psi} = \left(K^{-1} \otimes L^{-1}\right)\vec{\Psi}$.

2.2.3 Single-Particle Ground State Wavefunctions

To determine the SPGSWs for qubits isolated in each QD, as shown in Figure 2.2, we introduce a potential "masking" procedure to determine the isolated potentials for all QDs in a device. For each isolated QD potential, the 2D Schrödinger equation is solved to determine the SPGSW. If the SPGSW is calculated for the full QD device potential, any energy detuning between QDs causes it to localize in the lowest energy QD. However, this does not accurately represent electron behavior when multi-particle effects, such as Coulomb repulsion, are considered. Potential masking can be performed in several different ways, with primary methods consisting of 1) splitting the potential at the central coordinates of the user-designed tunnel barrier electrodes, 2) splitting the potential at the local maxima and performing either a harsh or Gaussian masking. Harsh masking simply assigns masked QDs with the max global potential, while Gaussian masking fits an inverted Gaussian function to the local minima of an isolated QD potential. Figure 2.4 is an example of a triple QD device potential, which is split along potential maxima between QDs with Gaussian masking applied. Regardless of the three masking procedures, no visible difference is observed in the Hamiltonian effective parameter calculations when comparing 1D voltage sweep plots. The invariance in effective parameter calculations across the various masking methods is attributed to the potential landscape not being significantly modified during masking in regions overlapping the calculated SPGSWs.

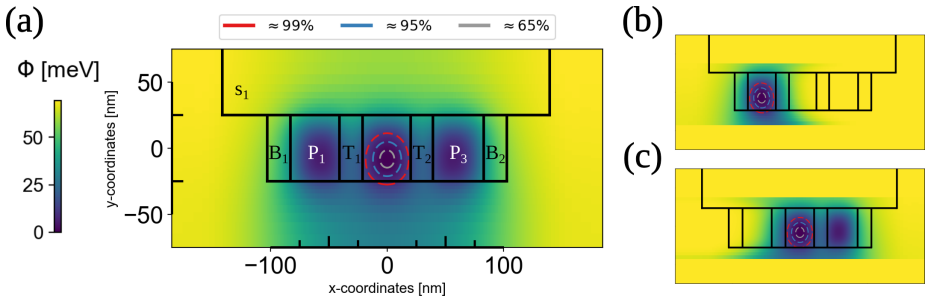


Figure 2.4: Example of a triple QD (a) Electrostatic potential in the plane of the 2DEG with regions showing $\approx 65\%$, $\approx 95\%$, and $\approx 99\%$ containment of the SPGSW (b) An example of potential masking for the left QD to determine the SPGSWs in that region (c) An example potential masking for the right QD pair used to determine the exchange energies. Both masking procedures in (b)-(c) show an example of Gaussian masking, which performs a fit of an inverted Gaussian function to local minima for QDs or QD pairs; however, other masking routines can be specified by the user.

2.2.4 Spin interactions in a semiconductor quantum processor

In an external magnetic field, $\vec{B}$, the electron spin Hamiltonian for a system of N electron spins is understood in general as,

$$H = \sum_{i}^{N} \frac{g_i \mu_B}{\hbar} \vec{B} \cdot \vec{S}_i = \frac{\mu_B}{2} \sum_{i}^{N} g_i \vec{B} \cdot \vec{\sigma}_i, \tag{2.24}$$

where g_i is the electron g-factor of the i^{th} electron, μ_B is the Bohr magneton, $\vec{S}_i$ is the spin operator of the i^{th} electron, and $\vec{\sigma}_i$ is the vector of Pauli operators, i.e., $\sigma_i \in \{X_i, Y_i, Z_i\}$. The static Zeeman field, B_0, defining the z-axis, produces spin precession around the z-axis for all electrons in the system. An additional RF magnetic field, $B_{\text{ESR}}(t)$, is applied perpendicular to B_0, enabling coherent spin rotations about the x- and y-axes in the rotating frame.

In addition to interactions with external magnetic fields, neighboring electrons are coupled through the exchange interaction, $J_{i,i+1}$, which arises from the overlap of their wavefunctions and is mediated by the Pauli exclusion principle. This interaction is described by the Hamiltonian term,

$$H_J = \frac{1}{4} \sum_{i=1}^{N-1} J_{i,i+1}(t) \vec{\sigma}_i \cdot \vec{\sigma}_{i+1}, \tag{2.25}$$

where $J_{i,i+1}(t)$ is the exchange coupling strength between the i^{th} and $(i+1)^{\text{th}}$ electrons. The exchange interaction is externally controlled via gate voltages that modulate the inter-dot barrier height and detuning.

Collecting all spin interaction Hamiltonian terms, the system Hamiltonian for N electrons in an array of QDs, in the laboratory reference frame, is given by

$$H_{\text{Lab}} = \frac{\mu_B B_0}{2} \sum_i^N \underbrace{g_i^{zz}(t) Z_i}_{\text{Zeeman}} + \frac{1}{4} \sum_{i=1}^{N-1} \underbrace{J_{i,i+1}(t) \vec{\sigma}_i \cdot \vec{\sigma}_{i+1}}_{\text{Exchange}}$$
$$+ \mu_B B_{RF}(t) \sum_i^N \underbrace{[g_i^{xx} X_i \cos(\omega_{\text{RF}} t + \phi(t)) + g_i^{yy} Y_i \sin(\omega_{\text{RF}} t + \phi(t))]}_{\text{ESR}}, \tag{2.26}$$

where $B_{RF}(t)$ represents the envelope amplitude of the applied RF field, $\omega_{\text{RF}} = 2\pi f_{RF}$ is the driving angular frequency, $\phi(t)$ is the RF field phase, and g_i^{jj} are components of the electronic g-factor tensor out-of-plane, $g_i^{xx(yy)} \coloneqq g_i^{(\perp)}$, or in plane, $g_i^{zz} \coloneqq g_i^{(\parallel)}$ with respect to the Zeeman field for the electron in the i^{th} QD. The Zeeman field is the dominant energy defining the quantization axis and is applied perpendicular to the substrate growth axis; $B_{RF}(t)$ is applied perpendicular to the Zeeman field axis. Note that off-diagonal tensor elements are negligible in silicon and diagonal components are $g^{(\parallel)} \approx g^{(\perp)} \approx 2$. The ESR field frequency is set to be in resonance with the Zeeman splitting, such that $\omega_{\text{RF}} \approx g^{(\parallel)} \mu_B B_0 / \hbar$, and under the assumption that $g^{(\parallel)}$ is the same for all electrons. Using the rotation operator $R = \exp\left(\frac{i}{2} \int_0^t \omega_{\text{rf}}(t') \text{d}t' \sum_{j=1}^N Z_j\right)$, the Hamiltonian for N electron spins in the laboratory reference frame is transformed using the following equation, $H_{\text{Rot}} = R H_{\text{Lab}} R^\dagger + i\hbar \dot{R} R^\dagger$, into the rotating reference frame,

$$H_{\text{Rot}} = \frac{\hbar}{2} \sum_{i=1}^N \left[\frac{\mu_{\text{B}} B_z g_i^{(\parallel)}(t)}{\hbar} - \omega_{\text{RF}}(t) \right] Z_i + \frac{1}{4} \sum_{i=1}^{N-1} J_{i,i+1}(t) \vec{\sigma}_i \cdot \vec{\sigma}_{i+1}$$
$$+ \mu_{\text{B}} B_{\text{RF}}(t) g^{(\perp)} \sum_{i=1}^N \left[\cos\phi(t)\ X_i + \sin\phi(t)\ Y_i \right], \tag{2.27}$$

It is instructive to rewrite the Hamiltonian in Equation 2.27 in terms of voltage induced g-factor deviation $\delta g(\vec{\mathcal{V}}(t))$, i.e. Stark shift, which is defined as $g_i^{(\parallel)}(\vec{\mathcal{V}}(t)) \coloneqq g_i^{(\parallel)}(\vec{\mathcal{V}}(0)) + \delta g_i(\vec{\mathcal{V}}(t))$ for each electron. Here $\vec{\mathcal{V}}(0)$ is the externally applied voltage from gate electrodes at time zero. Using the new definition for $g_i^{(\parallel)}$ and normalizing the Hamiltonian by $\hbar$ yields

the following,

$$\mathcal{H}_{\text{Rot}} = \frac{1}{2}\sum_{i=1}^{N}\left[\left(1+\frac{\delta g_i(\vec{\mathcal{V}}(t))}{g_i^{(\parallel)}(\vec{\mathcal{V}}(0))}\right)\omega_i - \omega_{\text{rf}}(t)\right]Z_i + \frac{1}{4\hbar}\sum_{i=1}^{N-1}J_{i,i+1}(\vec{\mathcal{V}}(t))\vec{\sigma}_i\cdot\vec{\sigma}_{i+1} + \frac{\Omega(t)}{2}\sum_{i=1}^{N}\left[\cos\phi(t)\ X_i + \sin\phi(t)\ Y_i\right], \tag{2.28}$$

where $\omega_i = \mu_B B_0 g_i^{(\parallel)}(\vec{\mathcal{V}}(0))/\hbar$ is the Larmor frequency, $\Omega(t) = g^{(\perp)}\mu_B B_{RF}(t)/\hbar$ is the Rabi frequency of the applied RF field, and $g_i^{(\parallel)}(\vec{\mathcal{V}}(0))$ is the initial g-factor of each electron. The time-dependent experimental inputs to the normalized Hamiltonian consist of the control voltage vector, $\vec{\mathcal{V}}(t)$, as well as the global ESR angular frequency, $\omega_{RF}(t)$, phase $\phi(t)$, and field envelope, $B_{RF}(t)$. The effective spin couplings in the Hamiltonian consist of: 1) Larmor frequency control through voltage-induced g-factor deviations, $\delta g(\vec{\mathcal{V}})$, 2) Voltage-controlled exchange interaction, $J_{i,i+1}$, between the i$^{\text{th}}$ and i+1$^{\text{th}}$ electrons, and 3) time-dependent global ESR field.

From the weak spin-orbit interaction in silicon, a Stark shift to the electron g-factor is primarily controlled by the plunger gate voltage directly over the QD and vary on the order of $\delta g \sim 10^{-5} - 10^{-3}$ [76, 129]. The Stark shift δg is observed in figure 2.5(a-c) for a triple QD device, where δg has been calculated from the out-of-plane electric field interpolation object $\tilde{\mathcal{E}}(\vec{r},\vec{\mathcal{V}})$ (cf. Section 2.2) and the formula,

$$\delta g_i(\vec{\mathcal{V}}) = \eta g_i(\vec{\mathcal{V}}(0))\langle|\tilde{\mathcal{E}}_i(\vec{\mathcal{V}})|^2\rangle, \tag{2.29}$$

where η is the quadratic Stark shift fit parameter estimated by Veldhorst et al. [76] to be $\approx 2.2\left(\frac{nm}{V}\right)^2$. It is observed that the dominant control of the electron g-factor is from the plunger gate directly above a given electron; however, non-negligible shifts in the g-factor occur from electrical cross-talk of neighboring plunger/barrier electrodes.

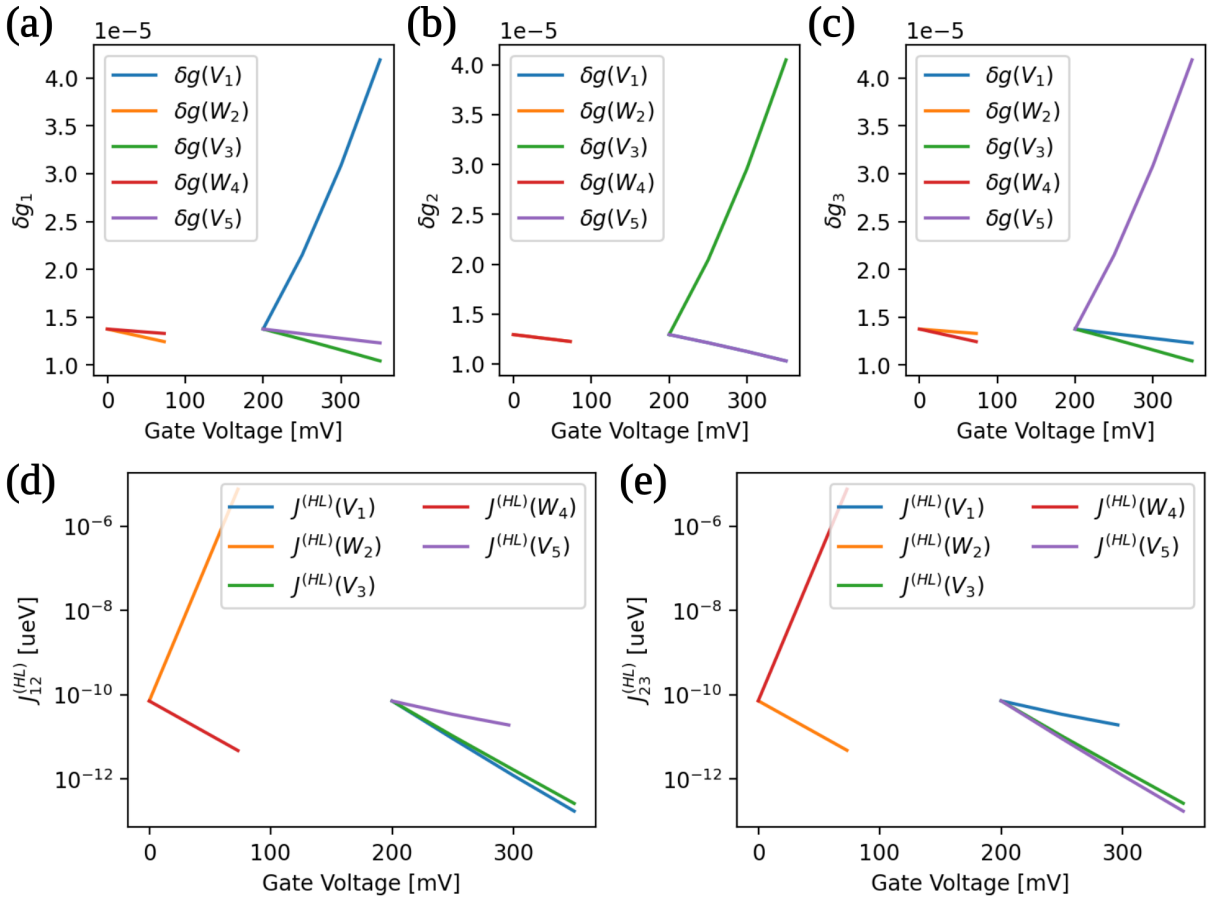
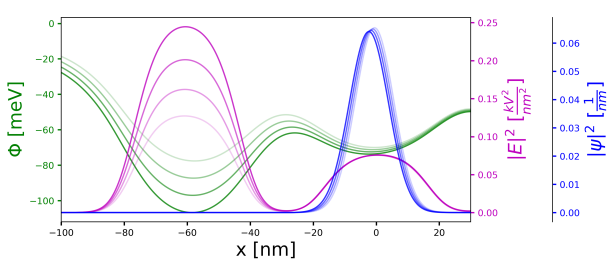
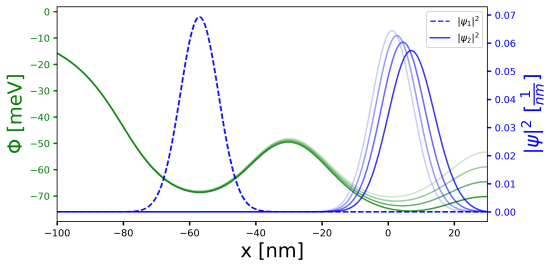


Figure 2.5: Effective parameters of the spin Hamiltonian calculated from Equation 2.29 and formulas discussed in Section 2.3 for a triple QD system. (a-c) g-factor deviation, i.e. $\delta g(\vec{V})$, for electrons in all three QDs as a function of plunger or tunnel barrier gate voltage. (d-e) exchange energy calculation using a Hund-Mulliken exchange approximation (cf. Section 2.3) for each pair of QDs as a function of plunger or tunnel barrier gate voltage.

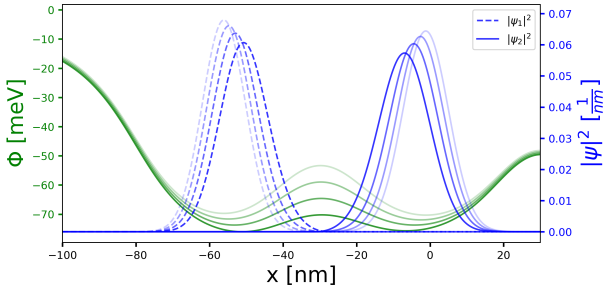
As will be discussed in Section 2.3, the exchange interaction is calculated from the numerical integration of the potential interpolation objects, $\tilde{\Phi}(\vec{r}, \vec{\mathcal{V}})$, for the Heitler-London (HL) or Hund-Mulliken (HM) exchange integral using SPGSWs basis functions as seen in Figure 2.5(d-e). The exchange interaction is able to be selectively turned on/off purely from electrostatic controls and changes exponentially for barrier electrodes between pairs of QDs [47, 72, 78, 91].



(a) Left QD potential and out-of-plane electric field vs left V_1 plunger gate sweep from 0.2-0.4 V.



(b) SPGSW orbitals in left/middle QD as a neighboring plunger gate, V_3, voltage is swept from 0.2-0.4 V.



(c) SPGSW orbitals overlap in left/middle QD as the tunnel gate, W_1, voltage is swept from -0.1 to 0.1 V.

Figure 2.6: Examples of wave function (blue) behavior under varying potential (green) and out-of-plane electric field (magenta) landscapes in a triple QD system when the voltage is swept for individual gates. The plots are zoomed in on the left and middle QD region.

The effective parameter behavior can be understood by studying the SPGSW orbital behavior in a triple QD system under various voltage configurations, as seen in Figure 2.6. For example, Stark shift of the g-factor is best explained for the triple QD system shown in Figure 2.6a. If a neighboring tunnel or plunger gate voltage is applied close to the middle QD, the middle QD potential delocalizes and shifts in the direction of the neighboring gate. This causes the SPGSW orbital to be less localized and shifted with regard to the out-of-plane electric field peak, causing $\langle|\tilde{\mathcal{E}}_i(\vec{\mathcal{V}})|^2\rangle$ to decrease. Instead, if the plunger gate voltage directly above the QD is increased, the potential well depth and the out-of-plane electric field increase substantially, increasing confinement, Stark shift, and ultimately δg, in agreement with the results observed in Figure 2.5.

The trends in exchange interaction in Figure 2.5(d-e) are best illustrated in Figures

2.6c-2.6b. Similarly to the observed behavior of δg, as the neighboring gate voltage is applied, the behavior of the exchange energy as a function of the gate voltage is controlled by the localization of the SPGSWs and their respective overlap with one another. Figure 2.6c shows how the SPGW in the middle QD delocalizes and is shifted to the right, decreasing the exchange energy, while the SPGSW for the electron in the left QD is negligibly impacted. Increasing the voltage of the tunnel gate significantly changes the height of the tunnel barrier between adjacent QDs, causing the SPGSWs in the left and middle QDs to overlap significantly, as seen in Figure 2.6b. Increasing the voltage of the tunnel gate lowers the barrier height, leading to the observed exponential increase in the exchange energy, as seen in Figure 2.5.

2.2.5 Predicting Spin Qubit Dynamics

Having defined the spin Hamiltonian for electron spins confined in an array of QDs, we can now predict the behavior under various device design considerations or external inputs. To simulate the system's spin state evolution, the Lindblad master equation formalism [130, 131] is used in place of the Liuoville-von Neumann master equation $\frac{d\rho}{dt} = -\frac{i}{\hbar}[H, \rho]$. This formalism models certain types of interaction between the qubits and the environment. The Lindblad equation is an example of a Markovian master equation, meaning it assumes the environment has no memory. It may be suitable for describing qubit interactions like charge noise, but it is not suitable for modeling decoherence due to nuclear spins, for example, since a nuclear spin system has a long memory. The Lindblad master equation is written as,

$$\frac{d\rho}{dt} = -\frac{i}{\hbar}[H, \rho] + 2\sum_{j=1}^{N}\sum_{\alpha=1}^{3}\left(L_{\alpha,j}\rho L_{\alpha,j}^{\dagger} - \frac{1}{2}\{L_{\alpha,j}L_{\alpha,j}^{\dagger}, \rho\}\right), \tag{2.30}$$

where $L_{\alpha,j}$ are the Lindblad operators [1, 132],

$$L_{1,j} = \sqrt{\frac{p_i}{2T_1}}\sigma_{+,j}, \quad L_{2,j} = \sqrt{\frac{1-p_i}{2T_1}}\sigma_{-,j}, \quad L_{3,j} = \frac{1}{2\sqrt{T_2}}Z_j,$$

where T_1 the characteristic time for the spin to relax to its ground state, i.e., aligned with external Zeeman field, T_2 is the characteristic time for spin dephasing, and p_i is the probability of the i$^{\text{th}}$ electron spin to be excited $|\downarrow\rangle$ at a given electron temperature, governed by the Boltzmann distribution. The operators $\sigma_{\pm,j}$ are the raising/lower operators

applied to the j$^{\text{th}}$ qubit which represent the operators:

$$\sigma_{\pm,j} = \left(\bigotimes_{i=1}^{j-1} I_i \right) \otimes \sigma_{\pm} \otimes \left(\bigotimes_{i=j+1}^{N} I_i \right),$$

where I_i is the identity matrix for the i$^{\text{th}}$ spin.

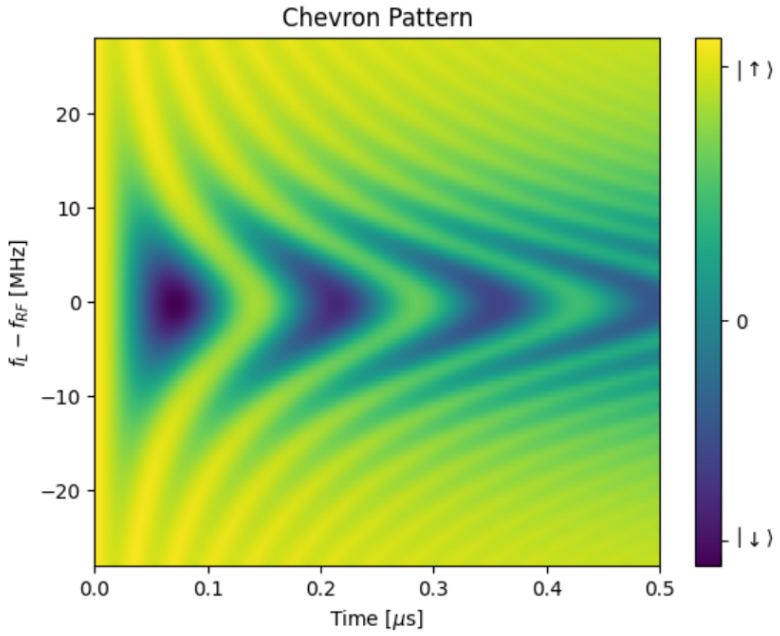
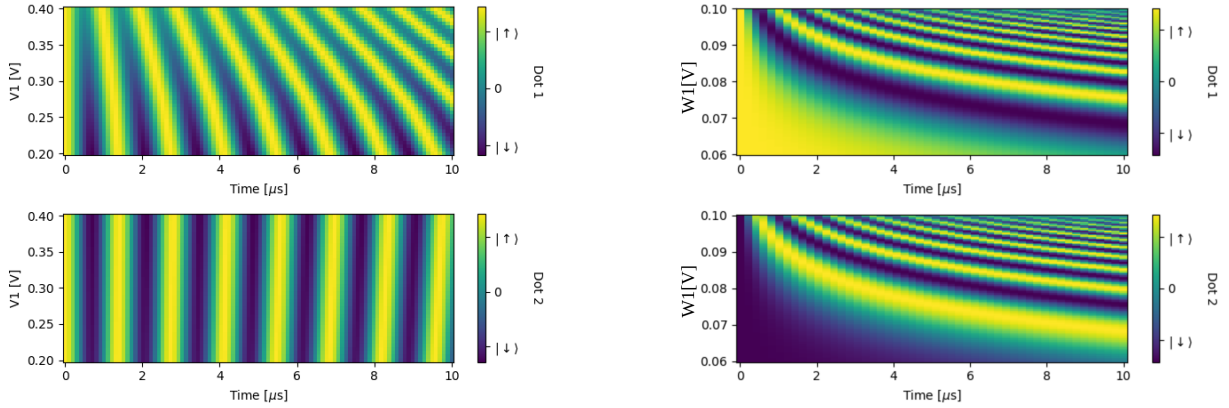


Figure 2.7: Simulated single QD Rabi-chevron map showing qubit spin-up probability as a function of ESR detuning frequency, $f_L - f_{RF}$, and ESR pulse time. A Zeeman field of $\approx 1T$ is applied, causing a Larmor frequency ≈ 28 GHz.

The first step in simulating an array of spin qubits under external experimental controls is to simulate the spin dynamics for a single qubit by explicit control of the effective parameters in the Hamiltonian. For example, the qubit in Figure 2.7 is initialized in the ground state, $|\uparrow\rangle$, then the evolution of the qubit's spin state is simulated by solving the ordinary differential equation defined in Equation 2.30 during an applied ESR field. By varying the Larmor frequency on/off resonance with a constant amplitude ESR field, with phase $\phi = 0$, the qubit undergoes rotations about an axis (in the rotating frame) in the x-z plane that depends on the resonance detuning. When the qubit is on resonance, $f_L - f_{RF} = 0$, solely x-axis rotation is observed, but detuning the qubit off resonance, $|f_L - f_{RF}| > 0$,

tilts the rotation axis away from the x-axis causing higher frequency “flopping" between the component of the spin state projections onto $|\uparrow\rangle$ and $|\downarrow\rangle$, as seen in Figure 2.7. What we also observe is that the visibility of the Rabi oscillations decreases due to interaction with the environment, causing decoherence, when $T_1 = \infty$ and $T_2 \approx 0.25\mu s$ are used as inputs to the simulation.



(a) Double QD Chevron pattern

(b) Double QD exchange oscillations

Figure 2.8: Examples of (a) Chevron patterns for a double QD device when g-factor detuning is induced by varying the plunger gate voltage, V_1, on QD 1. (b) Exchange oscillations between two electrons in a double QD pair when varying tunnel gate voltage, W_1.

Although it is instructive to simulate the spin state evolution of a single-qubit system, our goal is to predict the spin qubit dynamics for multi-qubit systems under the influence of external controls that can be applied experimentally. We now consider a two-qubit system formed in a double QD device geometry, similar to the one shown in Figure 2.3. The effective parameters, such as the g-factor and exchange coupling, are now controlled by external gate voltages, which dictate the underlying potential landscape of the QD device.

The first characterization of a QD device we perform is to determine the Rabi and exchange oscillations under various gate voltage conditions. In Figure 2.8a, the g-factor for both spin qubits is initially tuned to resonance with a constant amplitude ESR field. The plunger gate voltage of the left QD is varied, leading to a noticeable detuning from resonance in the left QD's electron Larmor frequency. This detuning causes Rabi oscillations with a higher frequency and lower visibility, as expected. Due to crosstalk, the right QD spin qubit experiences a slight detuning with the ESR field frequency, as seen in Figure

2.8a.

Another crucial characterization step is to assess the sensitivity of gate voltage controls on the exchange coupling between neighboring spin qubits. This is achieved by monitoring the $|\uparrow\rangle$ and $|\downarrow\rangle$ spin state projections of a double QD, initialized in a $|\uparrow\downarrow\rangle$ spin state, while the tunnel gate voltage modifies the tunnel barrier between the two QDs. The resultant exchange oscillations are observed in Figure 2.8b. As the tunnel gate voltage becomes increasingly positive, the tunnel barrier is lowered between the two QDs, inducing more rapid oscillations between the $|\uparrow\downarrow\rangle$ and $|\downarrow\uparrow\rangle$ states. Note, this is consistent with an exponential turn-on of exchange with respect to the tunnel gate voltage.

2.3 Double Quantum Dot Exchange Interaction

In semiconductor QD systems, the exchange interaction plays a crucial role in determining the spin dynamics of confined electrons. The exchange coupling arises due to the interplay between the Coulomb interaction and the Pauli exclusion principle, leading to an energy difference between symmetric (triplet $|T\rangle$) and antisymmetric (singlet $|S\rangle$) spin states. To analyze this effect, we start with the second-quantized Hamiltonian describing interacting electrons in a QD system:

$$H = \sum_i \epsilon_i c_i^\dagger c_i + \frac{e^2}{4\pi\epsilon_0\epsilon_r} \sum_{ijkl} \langle ij| \frac{1}{|\boldsymbol{r}_1 - \boldsymbol{r}_2|} |kl\rangle c_i^\dagger c_j^\dagger c_k c_l. \tag{2.31}$$

Here, ϵ_i represents the single-particle energy levels of the QD, while $c_i^\dagger$ and c_i are the fermionic creation and annihilation operators, respectively. The first term describes the non-interacting electron energy levels determined by confinement potentials in the dot. The second term accounts for the Coulomb interaction between electrons, where $\langle ij| \frac{1}{|\boldsymbol{r}_1 - \boldsymbol{r}_2|} |kl\rangle$ is the two-electron Coulomb integral, describing the electrostatic repulsion between electrons in orbitals i and j scattering into states k and l.

To extract the exchange interaction, we consider a two-electron system confined in a double QD potential. The exchange energy J is obtained from the difference in energy between the symmetric and antisymmetric spatial wavefunctions, which determine the symmetry of the spin wavefunctions. This energy splitting is given by:

$$J = \langle \psi_T | H | \psi_T \rangle - \langle \psi_S | H | \psi_S \rangle, \tag{2.32}$$

where $|\psi_T\rangle$ and $|\psi_S\rangle$ denote the spin-symmetric and spin-antisymmetric wavefunctions, respectively.

To calculate exchange numerically, we start by defining the Coulomb interaction as $H^{(c)}_{ijkl} \coloneqq \frac{e^2}{4\pi\epsilon_0\epsilon_r}\langle ij|\frac{1}{|\boldsymbol{r}_1-\boldsymbol{r}_2|}|kl\rangle$ and expressing it in integral form,

$$H^{(c)}_{ijkl} = \frac{e^2}{4\pi\epsilon_0\epsilon_r}\int_{-\infty}^{\infty}\int_{-\infty}^{\infty}\phi_i^*(\boldsymbol{r}_1)\phi_j^*(\boldsymbol{r}_2)\frac{1}{|\boldsymbol{r}_1-\boldsymbol{r}_2|}\phi_k(\boldsymbol{r}_1)\phi_l(\boldsymbol{r}_2)d\boldsymbol{r}_1 d\boldsymbol{r}_2, \tag{2.33}$$

Note that the Coulomb integral is singular when $\boldsymbol{r}_1 = \boldsymbol{r}_2$ making it potentially challenging to evaluate. However, a change of variable, $\boldsymbol{r} = \boldsymbol{r}_1 - \boldsymbol{r}_2$, eliminates this challenge by letting $\boldsymbol{r}_1 = \boldsymbol{r} + \boldsymbol{r}_2$, the Jacobian reads,

$$\begin{vmatrix} \frac{\partial \boldsymbol{r}_1}{\partial \boldsymbol{r}} & \frac{\partial \boldsymbol{r}_1}{\partial \boldsymbol{r}_2} \\ \frac{\partial \boldsymbol{r}_2}{\partial \boldsymbol{r}} & \frac{\partial \boldsymbol{r}_2}{\partial \boldsymbol{r}_2} \end{vmatrix} = \begin{vmatrix} 1 & 1 \\ 0 & 1 \end{vmatrix} = 1,$$

So Equation 2.33 now becomes,

$$H^{(c)}_{ijkl} = \frac{e^2}{4\pi\epsilon_0\epsilon_r}\int_{-\infty}^{\infty}\int_{0}^{2\pi}\int_{0}^{\infty}\phi_i^*\left((|\boldsymbol{r}|\cos\theta, |\boldsymbol{r}|\sin\theta) + \boldsymbol{r}_2\right)\phi_j^*(\boldsymbol{r}_2) \times \phi_k(\boldsymbol{r}_2)\phi_l\left((|\boldsymbol{r}|\cos\theta, |\boldsymbol{r}|\sin\theta) + \boldsymbol{r}_2\right)d|\boldsymbol{r}|d\theta d\boldsymbol{r}_2, \tag{2.34}$$

where the integration in Equation 2.34 of $\boldsymbol{r}$ is now carried out in polar coordinates, $d\boldsymbol{r} \equiv dxdy \rightarrow |\boldsymbol{r}|d|\boldsymbol{r}|d\theta$, to remove the $\frac{1}{|\boldsymbol{r}|}$ dependence in the integrand which could lead to a divergent integral. An integral of this form is a straightforward computational task when leveraging interpolation object basis functions over a mesh grid of coordinates and Simpson's rules for definite integration.

Calculating exchange energy requires evaluating a series of Coulomb-like integrals (equation 2.34) using a two-particle wave function that describes the two-electron state in a double-QD system, rather than the single-particle wavefunctions, $\phi(\boldsymbol{r})$, previously discussed. Exactly solving for the exchange energy would require constructing the exact two-particle wavefunctions from Slater determinants using an infinite set of single-particle orbital wavefunctions, which is computationally infeasible. To address this, several approximate methods have been developed that use a truncated set of single-particle orbital wavefunctions as a basis. Examples include full-configuration interaction (FCI), multi-configurational self-consistent field (MCSCF), density matrix renormalization group (DMRG), and quantum Monte Carlo (QMC). While the FCI method can converge to an exact solution, it requires diagonalizing the many-body Hamiltonian, whose size grows combinatorially with the number of single-particle orbitals and electrons, making it computationally expensive. Other methods aim to reduce computational overhead, often at the cost of accuracy or increased implementation complexity. For this thesis and lightweight

simulation, the Hund-Mulliken and Heitler-London exchange approximations offer a computationally efficient approach, as they simplify the treatment of electron-electron interactions by assuming separable exchange integrals and weak inter-electron correlation. These methods aim to balance accuracy and efficiency, making them well-suited for use in the QuDiPy simulator.

2.3.1 Heitler-London Exchange Energy

The HL exchange approximation is a widely used method in quantum mechanics to describe the exchange interaction between two electrons in a system, particularly in two-electron systems such as QD. Based on the Pauli exclusion principle and the symmetry of the two-particle wave function, the HL approximation simplifies the electron-electron repulsion by assuming that the two electrons are in a $|S\rangle$ or $|T\rangle$ state with a maximum spatial separation. In this approach, the exchange energy is derived from the overlap of the two-electron wavefunctions, specifically by calculating the exchange integrals that result from the interaction of the wavefunctions of individual particles. The HL approximation assumes a weak coupling between the electrons, meaning that their interactions are simplified to an effective two-body interaction, making the computation of the exchange energy analytically manageable. While this approximation is highly efficient and computationally feasible, especially for systems with well-separated QDs, it may not fully capture the complexities of electron correlation and may be less accurate in systems where electron-electron interactions are more significant. Nevertheless, the HL approximation remains a valuable tool for gaining quick insights into exchange effects in many-body quantum systems and applications to QD systems.

The HL approximation assumes that the the symmetric and antisymmetric orbital state wavefunctions $|\Psi_S\rangle$ and $|\Psi_T\rangle$ are constructed from SPGSWs [133] as,

$$\left|\Psi_{S/T}\right\rangle = \frac{\varphi_{-d}(\boldsymbol{r}_1)\varphi_{+d}(\boldsymbol{r}_2) \pm \varphi_{-d}(\boldsymbol{r}_2)\varphi_{+d}(\boldsymbol{r}_1)}{\sqrt{2(1 \pm S^2)}}, \tag{2.35}$$

Where $\varphi_{\pm d} \coloneqq \varphi(\boldsymbol{r}, \pm d)$ are the SPGSWs for an electron confined in the left or right QD of a QD pair separated by $2d$ and $S \coloneqq \langle \varphi_{\pm d} | \varphi_{\mp d} \rangle$ is the overlap of the orbital wavefunctions for the two SPGSWs. The approximate two-particle wave function from Equation 2.35 allows for the exchange energy to be calculated from Equation 2.32 once the SPGSWs are known.

Analytic Solution To determine the exchange coupling, one approach is to assume that the underlying double-QD potential resembles a biquadratic or quartic function [133–135].

In this thesis, we focus on estimating the double-QD potential using an analytic quartic function of the form,

$$\Phi(x,y) = \frac{m^*\omega_0^2}{2}\left(\frac{(x^2-d^2)^2}{4d^2} + y^2\right) + eEx, \tag{2.36}$$

where m^* is the electron effective mass, ω_0 determines the effective width of the quantum dots, given by $\sqrt{\hbar/m^*\omega_0}$, $2d$ is the QD separation, and E is the electric field along the x-axis, i.e., the major axis connecting the two dots. Next, the SPGSWs are assumed to be the wavefunctions of electrons confined in two dimensions for a harmonic oscillator, shifted by $\pm d$. This leads to SPGSWs in the form of Fock-Darwin states, shifted by $\pm d$:

$$\varphi_{\pm d}(x \pm d, y) = \sqrt{\frac{m\omega}{\pi\hbar}} e^{-m\omega((x\pm d)^2+y^2)}. \tag{2.37}$$

Plugging Equations 2.35-2.37 into 2.32 gives the following analytic expression for exchange energy at zero out-of-plane magnetic field,

$$J_{HL}(B=0) = \frac{\hbar\omega_0}{\sinh 2(d/a_b)^2}\left[c\left(e^{-(d/a_b)^2} I_0((d/a_b)^2) - I_0(0) + \frac{3}{4}(1+(d/a_b)^2)\right) + \frac{3}{2d^2}\left(\frac{eEd}{\hbar\omega_0}\right)^2\right], \tag{2.38}$$

where $c = \sqrt{\pi/2}\frac{e^2}{4\pi\epsilon_0\epsilon_r a_b}\frac{1}{\hbar\omega}$ and I_0 is the zeroth-order modified Bessel function of the first kind.

To calculate the exchange energy for QD device potentials using potential interpolation functions, a quartic potential of the form in equation 2.36 is fit to the local minima of the double-QD potential to estimate ω_0, d, and E in equation 2.38. The same procedure is applied for the biquadratic approximations. However, due to the barrier height dependence of both biquadratic and quadratic potentials, an accurate fit is not always guaranteed to exist.

In real QD devices, the barrier height between two QDs is typically controlled by a tunnel gate independent of QD separation. The analytic approximations and fitting routine provide a convenient method for quickly estimating exchange energy in QD devices within a specific domain of gate voltages. However, a more general approach is required to calculate exchange energy over the full range of possible gate voltage inputs.

Direct Integration Rather than assuming the analytical expression for SPGSWs, we instead use the 2D potential landscape extracted by QuDiPy beneath the SiO_2/Si interface, where a 2DEG is expected to form, to calculate the SPGSWs for each QD's local potential. Each QD's local potential is approximated by masking the double-QD potential, as shown in figures 2.9c-2.9d and described in Section 2.2.3.

Since the Hamiltonian contains both the single-electron kinetic energy and two-electron potential terms, it can be defined as $H \coloneqq H_1 + H_2$, where H_1 contains the kinetic energy operators $-\frac{\hbar^2}{2m^*}\nabla_i^2$ and H_2 represents the Coulomb interaction term, $H_2 \propto \frac{1}{|\boldsymbol{r}_1 - \boldsymbol{r}_2|}$. The SPGSWs are then used in equations 2.32 and 2.35 to evaluate the relevant Coulomb and exchange-like integrals.

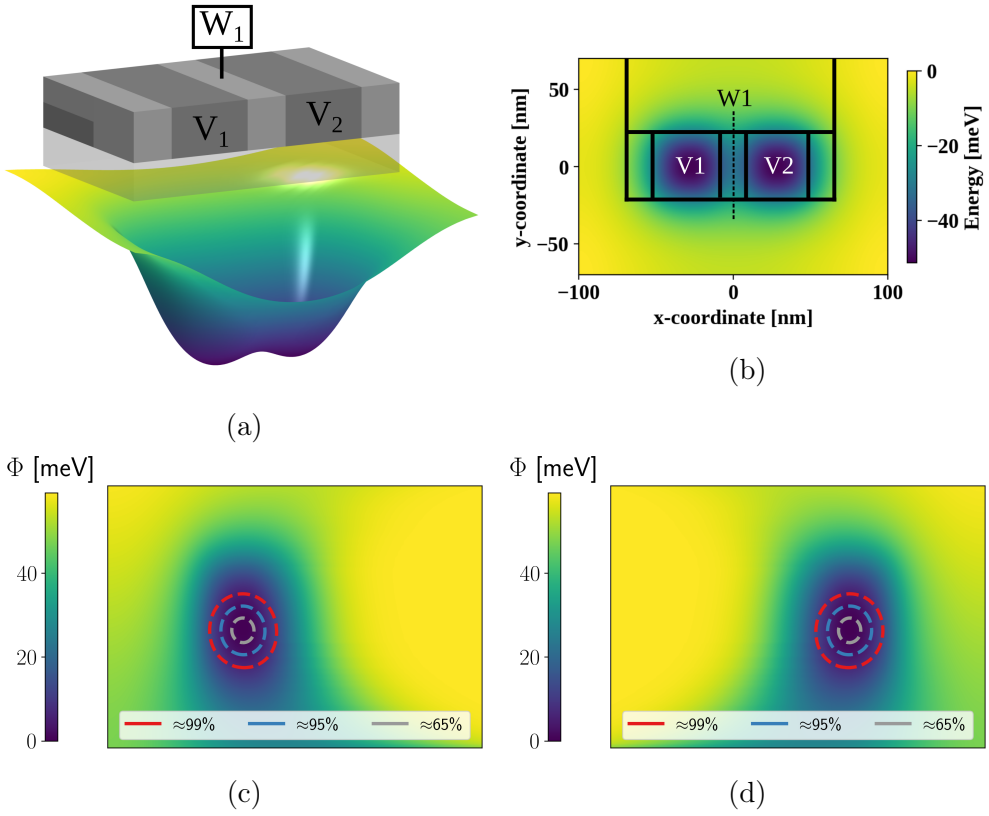


Figure 2.9: A schematic MOSFET double QD device in Si: (b) Top-view cross-section showing the double well confining potential formed by the plunger (V_1, V_2) and tunnel (W_1) electrodes. The electrostatic potential energy at the SiO_2/Si interface is calculated by a finite element Poisson solver based on a 3D device model. (a) Contour plot of the potential energy landscape in (b). Zoomed in electrostatic potential energy, Φ, regions for: (c) left single QD and masked right QD (d) right single QD and masked left QD. Regions are encircled where there is a $\approx 99\%$, $\approx 95\%$, and $\approx 65\%$ probability of finding an electron.

We begin with the given expression for the triplet state energy,

$$\begin{aligned}\langle\psi_T|H|\psi_T\rangle =& E_T + \frac{1}{8\pi\epsilon_0\epsilon_r}\iint\left[\varphi^*_{-d}(\boldsymbol{r}_1)\varphi^*_{+d}(\boldsymbol{r}_2) - \varphi^*_{-d}(\boldsymbol{r}_2)\varphi^*_{+d}(\boldsymbol{r}_1)\right] \\ &\times \frac{1}{|\boldsymbol{r}_1 - \boldsymbol{r}_2|}\left[\varphi_{-d}(\boldsymbol{r}_1)\varphi_{+d}(\boldsymbol{r}_2) - \varphi_{-d}(\boldsymbol{r}_2)\varphi_{+d}(\boldsymbol{r}_1)\right] d\boldsymbol{r}_1 d\boldsymbol{r}_2, \end{aligned} \tag{2.39}$$

where E_T is the kinetic energy of the two-electron system and simplifies to,

$$\begin{aligned}\langle\psi_T|H|\psi_T\rangle = E_T + \frac{1}{8\pi\epsilon_0\epsilon_r}\iint\frac{1}{|\boldsymbol{r}_1-\boldsymbol{r}_2|}\Big(&\varphi^*_{-d}(\boldsymbol{r}_1)\varphi^*_{+d}(\boldsymbol{r}_2)\varphi_{-d}(\boldsymbol{r}_1)\varphi_{+d}(\boldsymbol{r}_2)\\ &-\varphi^*_{-d}(\boldsymbol{r}_1)\varphi^*_{+d}(\boldsymbol{r}_2)\varphi_{-d}(\boldsymbol{r}_2)\varphi_{+d}(\boldsymbol{r}_1)\\ &-\varphi^*_{-d}(\boldsymbol{r}_2)\varphi^*_{+d}(\boldsymbol{r}_1)\varphi_{-d}(\boldsymbol{r}_1)\varphi_{+d}(\boldsymbol{r}_2)\\ &+\varphi^*_{-d}(\boldsymbol{r}_2)\varphi^*_{+d}(\boldsymbol{r}_1)\varphi_{-d}(\boldsymbol{r}_2)\varphi_{+d}(\boldsymbol{r}_1)\Big)d\boldsymbol{r}_1 d\boldsymbol{r}_2.\end{aligned}$$

Recognizing that the four terms in the integrand correspond to Coulomb C and exchange J_{ex} integrals, we can define,

$$C = \iint\frac{\varphi^*_{-d}(\boldsymbol{r}_1)\varphi^*_{+d}(\boldsymbol{r}_2)\varphi_{-d}(\boldsymbol{r}_1)\varphi_{+d}(\boldsymbol{r}_2)}{|\boldsymbol{r}_1-\boldsymbol{r}_2|}d\boldsymbol{r}_1 d\boldsymbol{r}_2, \text{ and} \tag{2.40}$$

$$J_{ex} = \iint\frac{\varphi^*_{-d}(\boldsymbol{r}_1)\varphi^*_{+d}(\boldsymbol{r}_2)\varphi_{-d}(\boldsymbol{r}_2)\varphi_{+d}(\boldsymbol{r}_1)}{|\boldsymbol{r}_1-\boldsymbol{r}_2|}d\boldsymbol{r}_1 d\boldsymbol{r}_2, \tag{2.41}$$

Since the integrals are symmetric, the second and third terms are equal to J_{ex}, while the first and fourth terms are equal to C. Thus, the entire expression simplifies to,

$$\begin{aligned}\langle\psi_T|H|\psi_T\rangle &= E_T + \frac{1}{8\pi\epsilon_0\epsilon_r}\frac{2C-2J_{ex}}{1-S^2}\\ &= E_T + \frac{1}{4\pi\epsilon_0\epsilon_r}\frac{C-J_{ex}}{1-S^2}.\end{aligned} \tag{2.42}$$

Similar to the derivation of Equation 2.42, the singlet energy is calculated as,

$$\langle\psi_S|H|\psi_S\rangle = E_S + \frac{1}{4\pi\epsilon_0\epsilon_r}\frac{C+J_{ex}}{1+S^2}, \tag{2.43}$$

and, since $E_S = E_T$, Equation 2.32 is written in terms of Coulomb, exchange, and overlap integrals as,

$$J_{HL} = \frac{1}{4\pi\epsilon_0\epsilon_r}\frac{S^2C-J_{ex}}{1-S^4}. \tag{2.44}$$

2.3.2 Hund-Mulliken Exchange Energy

Instead of the HL exchange energy approximation, which treats spatially isolated and weakly interacting electrons, we introduce the HM method of molecular orbits, which

extends the HL method by including the doubly occupied singlet states. This makes it a more accurate method than HL for describing systems with intermediate to strong electron-electron interactions, while still maintaining manageable computational complexity. Although the HM approximation does not capture all the subtleties of the full many-body wavefunction, it strikes a balance between accuracy and computational efficiency.

This new choice of molecular orbitals extends the Hilbert space from two to four dimensions and requires the creation of new single-particle orbitals, which must be orthonormalized [133, 134]. These new basis functions are,

$$\Phi_{\pm d}(\boldsymbol{r}) \coloneqq \Phi(\boldsymbol{r}, \pm d) = \frac{\varphi_{\pm d}(\boldsymbol{r}) + G\varphi_{\mp d}(\boldsymbol{r})}{\sqrt{1 - 2SG + G^2}}, \tag{2.45}$$

where, $S = \langle \varphi_{-d} | \varphi_{+d} \rangle$ and $G = (1 - \sqrt{1 - S^2})/S$ and the addition two-particle orbital basis functions for the doubly occupied singlet states are,

$$\Psi^D_{\pm d}(\boldsymbol{r}_1, \boldsymbol{r}_2) = \Phi_{\pm d}(\boldsymbol{r}_1)\Phi_{\pm d}(\boldsymbol{r}_2), \tag{2.46}$$

with a two-particle orbital basis function of a similar form to Equation 2.35 for the spatially separated singlet and triplet states,

$$\Psi^S_{\pm d}(\boldsymbol{r}_1, \boldsymbol{r}_2) = \frac{1}{\sqrt{2}} \left[\Phi_{+d}(\boldsymbol{r}_1)\Phi_{-d}(\boldsymbol{r}_2) \pm \Phi_{-d}(\boldsymbol{r}_1)\Phi_{+d}(\boldsymbol{r}_2) \right]. \tag{2.47}$$

Using this basis leads to the exchange energy calculation $J_{HM} = V - U_r/2 + \frac{1}{2}\sqrt{U_r^2 + 16t_r^2}$ with the following required integrals [133]:

$$V = V_- - V_+ = \left\langle \Psi^S_- \right| C \left| \Psi^S_- \right\rangle - \left\langle \Psi^S_+ \right| C \left| \Psi^S_+ \right\rangle \tag{2.48}$$

$$t_r = t - w = \langle \Phi_{\pm d} | \, h \, | \Phi_{\mp d} \rangle - \frac{1}{\sqrt{2}} \left\langle \Psi^S_+ \right| C \left| \Psi^D_{\pm d} \right\rangle \tag{2.49}$$

$$\begin{aligned} U_r &= U - V_+ + X \\ &= \left\langle \Psi^D_{\pm d} \right| C \left| \Psi^D_{\pm d} \right\rangle - \left\langle \Psi^S_+ \right| C \left| \Psi^S_+ \right\rangle + \left\langle \Psi^D_{\pm d} \right| C \left| \Psi^D_{\mp d} \right\rangle \end{aligned} \tag{2.50}$$

where X is similar to an inter-dot Coulomb exchange integral, U is the on-site (Hubbard) Coulomb repulsion, V_+ and V_- are the Coulomb energies for the (1,1) singlet and triplet states, with Ψ(1,1) S/T built out of orthogonalized single-electron orbitals, and t is the inter-dot tunneling matrix element modified by the Coulomb matrix element w (t is the bare tunneling).

Analytic Solution Similar to Section 2.3.1, the analytic form of exchange energy can be determined from Equations 2.48-2.50 assuming the quartic potential (2.36) and shifted Fock-Darwin SPGSWs (2.35). This leads to the following analytic forms for Equations 2.48-2.50 [133],

$$
\begin{aligned}
t &= \frac{3}{8}\frac{S}{1-S^2}\left(1+d^2\right) \\
V_+ &= N^4\left(4g^2(1+S^2)F_1 + (1+g^2)^2F_2 + 4g^2F_3 - 16g^2F_4\right) \\
V_- &= N^4(1-g^2)^2\left(F_2 - S^2F_3\right) \\
U &= N^4\left((1+g^4+2g^2S^2)F_1 + 2g^2F_2 + 2g^2S^2F_3 - 8g^2F_4\right) \\
X &= N^4\left[\left((1+g^4)S^2+2g^2\right)F_1 + 2g^2F_2 + 2g^2S^2F_3 - 8g^2F_4\right] \\
w &= N^4\left(-g(1+g^2)(1+S^2)F_1 - g(1+g^2)F_2 - g(1+g^2)S^2F_3 + (1+6g^2+g^4)SF_4\right)
\end{aligned}
$$

where the functions F_i [133] are defined as,

$$
\begin{aligned}
F_1 &= c \\
F_2 &= ce^{-d^2}I_0(d^2) \\
F_3 &= cI_0(0) \\
F_4 &= ce^{-d^2/4}\sum_{k=-\infty}^{\infty}(-1)^k I_{2k}\left(\frac{d^2}{4}\right)I_{2k}\left(-\frac{d^2}{2}\right)
\end{aligned}
$$

with I_n being the n-th order modified Bessel function of the first kind.

Direct Integration Similar to Section 2.3.1, instead of assuming the SPGSWs, we use the 2D potential landscape extracted by QuDiPy beneath the SiO_2/Si interface, where a 2DEG is expected to form, to calculate the SPGSWs for each QD's local potential. Each QD's local potential is approximated by masking the double-QD potential, as shown in figures 2.9c-2.9d and described in Section 2.2.3.

$$
\begin{aligned}
V_- = \left\langle \Psi_-^S \right| C \left| \Psi_-^S \right\rangle &= \frac{e^2}{4\pi\epsilon_r} \int\int \Psi_-^S(\boldsymbol{r}_1, \boldsymbol{r}_2)^* \frac{1}{|\boldsymbol{r}_1 - \boldsymbol{r}_2|} \Psi_-^S(\boldsymbol{r}_1, \boldsymbol{r}_2) d\boldsymbol{r}_1 d\boldsymbol{r}_2 \\
&= \frac{e^2}{8\pi\epsilon_r} [\\
&\int\int \Phi_{+d}(\boldsymbol{r}_1)^* \Phi_{-d}(\boldsymbol{r}_2)^* \frac{1}{|\boldsymbol{r}_1 - \boldsymbol{r}_2|} \Phi_{+d}(\boldsymbol{r}_1) \Phi_{-d}(\boldsymbol{r}_2) d\boldsymbol{r}_1 d\boldsymbol{r}_2 \\
&- \int\int \Phi_{-d}(\boldsymbol{r}_1)^* \Phi_{+d}(\boldsymbol{r}_2)^* \frac{1}{|\boldsymbol{r}_1 - \boldsymbol{r}_2|} \Phi_{+d}(\boldsymbol{r}_1) \Phi_{-d}(\boldsymbol{r}_2) d\boldsymbol{r}_1 d\boldsymbol{r}_2 \\
&- \int\int \Phi_{+d}(\boldsymbol{r}_1)^* \Phi_{-d}(\boldsymbol{r}_2)^* \frac{1}{|\boldsymbol{r}_1 - \boldsymbol{r}_2|} \Phi_{-d}(\boldsymbol{r}_1) \Phi_{+d}(\boldsymbol{r}_2) d\boldsymbol{r}_1 d\boldsymbol{r}_2 \\
&+ \int\int \Phi_{-d}(\boldsymbol{r}_1)^* \Phi_{+d}(\boldsymbol{r}_2)^* \frac{1}{|\boldsymbol{r}_1 - \boldsymbol{r}_2|} \Phi_{-d}(\boldsymbol{r}_1) \Phi_{+d}(\boldsymbol{r}_2) d\boldsymbol{r}_1 d\boldsymbol{r}_2] \qquad (2.51)
\end{aligned}
$$

$$
\begin{aligned}
V_+ = \left\langle \Psi_+^S \right| C \left| \Psi_+^S \right\rangle &= \frac{e^2}{4\pi\epsilon_0\epsilon_r} \int\int \Psi_+^S(\boldsymbol{r}_1, \boldsymbol{r}_2)^* \frac{1}{|\boldsymbol{r}_1 - \boldsymbol{r}_2|} \Psi_+^S(\boldsymbol{r}_1, \boldsymbol{r}_2) d\boldsymbol{r}_1 d\boldsymbol{r}_2 \\
&= \frac{e^2}{8\pi\epsilon_0\epsilon_r} [\\
&\int\int \Phi_{+d}(\boldsymbol{r}_1)^* \Phi_{-d}(\boldsymbol{r}_2)^* \frac{1}{|\boldsymbol{r}_1 - \boldsymbol{r}_2|} \Phi_{+d}(\boldsymbol{r}_1) \Phi_{-d}(\boldsymbol{r}_2) d\boldsymbol{r}_1 d\boldsymbol{r}_2 \\
&+ \int\int \Phi_{-d}(\boldsymbol{r}_1)^* \Phi_{+d}(\boldsymbol{r}_2)^* \frac{1}{|\boldsymbol{r}_1 - \boldsymbol{r}_2|} \Phi_{+d}(\boldsymbol{r}_1) \Phi_{-d}(\boldsymbol{r}_2) d\boldsymbol{r}_1 d\boldsymbol{r}_2 \\
&+ \int\int \Phi_{+d}(\boldsymbol{r}_1)^* \Phi_{-d}(\boldsymbol{r}_2)^* \frac{1}{|\boldsymbol{r}_1 - \boldsymbol{r}_2|} \Phi_{-d}(\boldsymbol{r}_1) \Phi_{+d}(\boldsymbol{r}_2) d\boldsymbol{r}_1 d\boldsymbol{r}_2 \\
&+ \int\int \Phi_{-d}(\boldsymbol{r}_1)^* \Phi_{+d}(\boldsymbol{r}_2)^* \frac{1}{|\boldsymbol{r}_1 - \boldsymbol{r}_2|} \Phi_{-d}(\boldsymbol{r}_1) \Phi_{+d}(\boldsymbol{r}_2) d\boldsymbol{r}_1 d\boldsymbol{r}_2] \qquad (2.52)
\end{aligned}
$$

Therefore, $V = V_- - V_+$ is simplified too:

$$
\begin{aligned}
V = &- \frac{e^2}{4\pi\epsilon_0\epsilon_r} [\\
&\int\int \Phi_{-d}(\boldsymbol{r}_1)^* \Phi_{+d}(\boldsymbol{r}_2)^* \frac{1}{|\boldsymbol{r}_1 - \boldsymbol{r}_2|} \Phi_{+d}(\boldsymbol{r}_1) \Phi_{-d}(\boldsymbol{r}_2) d\boldsymbol{r}_1 d\boldsymbol{r}_2 \\
&+ \int\int \Phi_{+d}(\boldsymbol{r}_1)^* \Phi_{-d}(\boldsymbol{r}_2)^* \frac{1}{|\boldsymbol{r}_1 - \boldsymbol{r}_2|} \Phi_{-d}(\boldsymbol{r}_1) \Phi_{+d}(\boldsymbol{r}_2) d\boldsymbol{r}_1 d\boldsymbol{r}_2] \qquad (2.53)
\end{aligned}
$$

$$t = \langle \Phi_{\pm d} | \, h_{\pm d} \, | \Phi_{\mp d} \rangle = \frac{e^2}{8\pi\epsilon_0\epsilon_r} \int\int \Phi_{\pm d}(\boldsymbol{r}_2)^* \frac{1}{|\boldsymbol{r}_1 - \boldsymbol{r}_2|} \Phi_{\mp d}(\boldsymbol{r}_1) d\boldsymbol{r}_1 d\boldsymbol{r}_2 \tag{2.54}$$

$$\begin{aligned} w = \left\langle \Psi^S_+ \right| C \left| \Psi^D_{\pm d} \right\rangle &= \frac{e^2}{4\pi\epsilon_0\epsilon_r} \int\int \Psi^S_+(\boldsymbol{r}_1, \boldsymbol{r}_2)^* \frac{1}{|\boldsymbol{r}_1 - \boldsymbol{r}_2|} \Psi^D_{\pm d}(\boldsymbol{r}_1, \boldsymbol{r}_2) d\boldsymbol{r}_1 d\boldsymbol{r}_2 \\ &= \frac{e^2}{8\pi\epsilon_0\epsilon_r} [\\ &\int\int \Phi_{+d}(\boldsymbol{r}_1)^* \Phi_{-d}(\boldsymbol{r}_2)^* \frac{1}{|\boldsymbol{r}_1 - \boldsymbol{r}_2|} \Phi_{\pm d}(\boldsymbol{r}_1) \Phi_{\pm d}(\boldsymbol{r}_2) d\boldsymbol{r}_1 d\boldsymbol{r}_2 \\ &+ \int\int \Phi_{-d}(\boldsymbol{r}_1)^* \Phi_{+d}(\boldsymbol{r}_2)^* \frac{1}{|\boldsymbol{r}_1 - \boldsymbol{r}_2|} \Phi_{\pm d}(\boldsymbol{r}_1) \Phi_{\pm d}(\boldsymbol{r}_2) d\boldsymbol{r}_1 d\boldsymbol{r}_2] \end{aligned} \tag{2.55}$$

$$\begin{aligned} X = \left\langle \Psi^D_{\pm d} \right| C \left| \Psi^D_{\pm d} \right\rangle &= \frac{e^2}{4\pi\epsilon_0\epsilon_r} \int\int \Psi^D_{\pm d}(\boldsymbol{r}_1, \boldsymbol{r}_2)^* \frac{1}{|\boldsymbol{r}_1 - \boldsymbol{r}_2|} \Psi^D_{\pm d}(\boldsymbol{r}_1, \boldsymbol{r}_2) d\boldsymbol{r}_1 d\boldsymbol{r}_2 \\ &= \frac{e^2}{8\pi\epsilon_0\epsilon_r} \int\int \Phi_{\pm d}(\boldsymbol{r}_1)^* \Phi_{\pm d}(\boldsymbol{r}_2)^* \frac{1}{|\boldsymbol{r}_1 - \boldsymbol{r}_2|} \Phi_{\pm d}(\boldsymbol{r}_1) \Phi_{\pm d}(\boldsymbol{r}_2) d\boldsymbol{r}_1 d\boldsymbol{r}_2 \end{aligned} \tag{2.56}$$

$$U = \left\langle \Psi^D_{\pm d} \right| C \left| \Psi^D_{\mp d} \right\rangle = \frac{e^2}{4\pi\epsilon_0\epsilon_r} \int\int \Psi^D_{\pm d}(\boldsymbol{r}_1, \boldsymbol{r}_2)^* \frac{1}{|\boldsymbol{r}_1 - \boldsymbol{r}_2|} \Psi^D_{\pm d}(\boldsymbol{r}_1, \boldsymbol{r}_2) d\boldsymbol{r}_1 d\boldsymbol{r}_2 \tag{2.57}$$

$$= \frac{e^2}{8\pi\epsilon_0\epsilon_r} \int\int \Phi_{\pm d}(\boldsymbol{r}_1)^* \Phi_{\pm d}(\boldsymbol{r}_2)^* \frac{1}{|\boldsymbol{r}_1 - \boldsymbol{r}_2|} \Phi_{\mp d}(\boldsymbol{r}_1) \Phi_{\mp d}(\boldsymbol{r}_2) d\boldsymbol{r}_1 d\boldsymbol{r}_2 \tag{2.58}$$

The integrals in Equation 2.44 from Section 2.3.1 and integrals in Equations 2.48-2.57 are numerically integrated using Equation 2.34 and evaluating the function on a cartesian and polar coordinate mesh grid for specific integrands, while S is calculated as the dot product between arrays representing 2D wavefunctions.

2.3.3 Results

To determine the validity of the numerical integration routines for the exchange calculations in Sections 2.3.1 and 2.3.2, exchange calculations were performed using the shifted Fock-Darwin basis functions and compared to the analytic solutions for the exchange energy

under the assumption that the potentials are biquadratic and quartic. Excellent agreement between the analytic solutions for exchange energy and the numerically integrated calculations was obtained.

Having confirmed the accuracy of the numerical integration methods, we now turn to calculating exchange energy by determining the SPGSWs from solving the Schrödinger equation on simulated single-QD potentials processed by QuDiPy. Figure 2.10(a) shows the comparison of the exchange energy calculated for both the HL and HM methods using analytic solutions with a quartic potential fit and the solutions for numerical direct integration. In general, HM estimates higher exchange compared to HL, caused by the inter-dot delocalization of the electron wavefunctions when using the four HM basis functions from Equations 2.46 and 2.47. Direct integration methods estimate exchange orders of magnitude stronger than analytic solutions due to both over-confinement of electrons when assuming a quartic potential compared to the true QD potential and overestimating the tunnel barrier energy when fitting the quartic potential to a more realistic QD potential as seen in Figure 2.10(b).

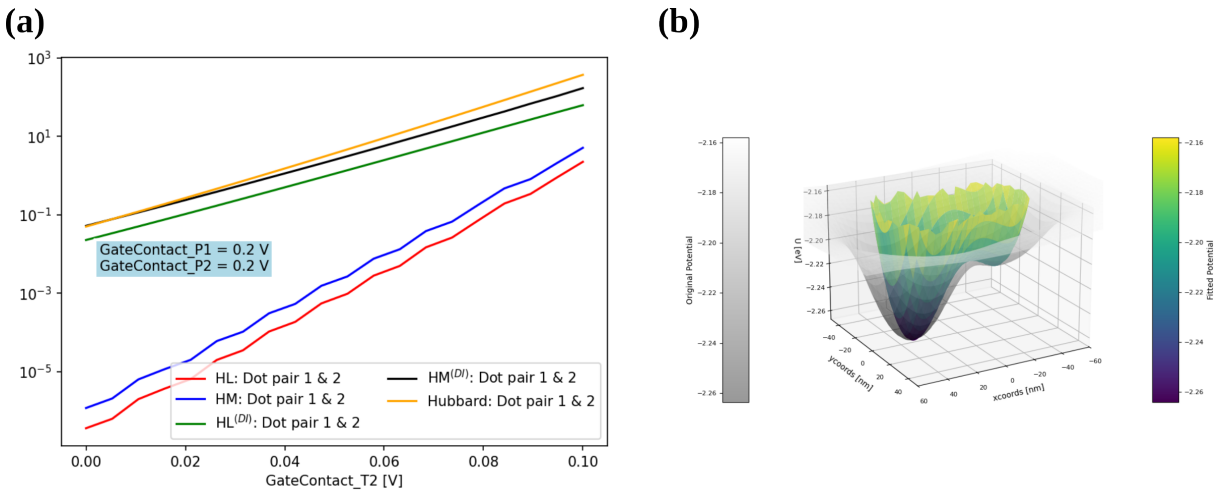


Figure 2.10: Exchange energy as a function of barrier voltage, W_1. All exchange calculations exhibit an exponential relationship of exchange energy vs W_1.

We go further than just comparing the direct integration and analytical fit methods by comparing the exchange energy results to Hubbard model calculations of the tunnel coupling, t, on-site energy, U_i, and detuning energy, ϵ, where the exchange interaction is

calculated from [81],

$$J_H = \frac{2t^2}{U_1 - \epsilon} + \frac{2t^2}{U_2 + \epsilon}, \tag{2.59}$$

to compare the spin and Hubbard model numerical methods. The exchange calculated from Hubbard parameters is comparable to the HM exchange calculated from direct integration, as seen in Figure 2.10(a).

2.4 Quantum Dot Hubbard Model

The Charge Stability Diagram (CSD) is a fundamental characterization tool for gate-defined QDs that elucidates regions of Coulomb blockade under various device operating conditions. Accurately simulating CSDs allows for estimating voltage ranges suitable for initialization and readout experiments, as well as defining boundaries for voltage controls in spin qubit gate operations.

The simplest model for CSDs is the constant interaction model [33], as described in Section 1.2.1. This model treats each QD as a classical system with an integer number of charges, capacitively coupled to neighboring QDs and/or reservoirs. As a result, the CSD exhibits periodicity in the voltage domain, with electron additions occurring at regular voltage intervals that shift the QD's chemical potential by the charging energy. Although this model provides a good approximation in many cases, it breaks down in regimes where quantum effects become significant—particularly under strong tunnel coupling. In this regime, charge transition lines near the triple points in the CSD become rounded, a phenomenon that the constant interaction model cannot fully capture.

To account for these quantum effects, we construct the Hamiltonian matrix elements using the Hubbard model, which enables the generation of CSDs that incorporate strong tunnel coupling effects. Another key distinction between the two models is that specific parameters in the Hubbard model can be directly calculated from the underlying potential of a given QD device. This allows the calculation of CSDs solely from the changing potential landscape as input control voltages vary. In contrast, the constant interaction model requires prior knowledge of capacitances between QDs and all other charge carriers (e.g., reservoirs, gates), which can be challenging to determine experimentally. Additionally, the Hubbard model allows for a priori determination of electron CSDs for a given device design before conducting any experiments, which is something that the constant interaction model is not capable of.

Thus, incorporating the Hubbard model into the QuDiPy simulator provides a more comprehensive and predictive framework for analyzing CSDs, particularly in regimes where quantum effects cannot be neglected.

2.4.1 Hamiltonian

A generalized Hubbard Hamiltonian developed by [136, 137] for electrostatically defined QD systems is composed of,

$$H(\vec{\mathcal{V}}) = H_\mu(\vec{\mathcal{V}}) + H_t(\vec{\mathcal{V}}) + H_U(\vec{\mathcal{V}}) + H_J(\vec{\mathcal{V}}), \tag{2.60}$$

Where terms describing the chemical potential, H_μ, tunnel coupling, H_t, Coulomb repulsion, H_U, and spin exchange, H_J, are included. The first term, H_μ, represents the occupation of spin states in an array of N quantum dots:

$$H_\mu(\vec{\mathcal{V}}) = -\sum_{\sigma=\uparrow,\downarrow}\left[\sum_{i=1}^{N}\mu_i(\vec{\mathcal{V}},\gamma)\hat{n}_{i,\sigma}\right], \tag{2.61}$$

Here, i is the index of each QD in a linear array of N QDs, μ_i are their chemical potentials, $\sigma \in \{\uparrow,\downarrow\}$ is the spin state, and $\hat{n}_{i,\sigma}$ is the electron number operator for the spin state σ of the i^{th} QD. The number operator is defined as $\hat{n}_{i,\sigma} = \hat{c}^\dagger_{i,\sigma}\hat{c}_{i,\sigma}$, where $\hat{c}^\dagger_{i,\sigma}$ ($\hat{c}_{i,\sigma}$) are the usual creation (annihilation) operators. The chemical potential, μ_i, for the i$^{\text{th}}$ QD is found by isolating the single QDs potential and calculating the SPGSW eigenenergy. The formula for the chemical potential in each QD reads $\mu_i = \varepsilon_i + \gamma_i$, where γ_i is a constant energy shift to match the chemical potential to experiment [136].

The second term, H_t, represents the tunnel couplings between QDs where an electron with spin state σ is allowed to tunnel to an adjacent QD,

$$H_t(\vec{\mathcal{V}}) = -\sum_{\sigma=\uparrow,\downarrow}\left[\sum_{j=1}^{N-1}t_{j,j+1}(\vec{\mathcal{V}})\left(\hat{c}^\dagger_{j,\sigma}\hat{c}_{j+1,\sigma} + \hat{c}^\dagger_{j+1,\sigma}\hat{c}_{j,\sigma}\right)\right], \tag{2.62}$$

Here, $t_{j,j+1}$ is the tunnel coupling, or inter-site hopping terms for adjacent QDs. The operators $\hat{c}^\dagger_{j,\sigma}\hat{c}_{j+1,\sigma}$, $\left(\hat{c}^\dagger_{j+1,\sigma}\hat{c}_{j,\sigma}\right)$, account for $j \to (j+1)$, $(j \leftarrow (j+1))$, tunneling events. The tunnel coupling term $t_{j,j+1}$ between the j^{th} and $(j+1)^{\text{th}}$ QD is calculated assuming a double QD Hamiltonian of the form [1, 35],

$$H_{j,j+1}(\vec{\mathcal{V}}) = \begin{bmatrix} \bar{\varepsilon}_{j,j+1}(\vec{\mathcal{V}}) + \frac{\Delta\epsilon_{j,j+1}(\vec{\mathcal{V}})}{2} & t_{j,j+1}(\vec{\mathcal{V}}) \\ t_{j,j+1}(\vec{\mathcal{V}}) & \bar{\varepsilon}_{j,j+1}(\vec{\mathcal{V}}) + \frac{\Delta\epsilon_{j,j+1}(\vec{\mathcal{V}})}{2} \end{bmatrix},$$

where $\bar{\varepsilon}_{j,j+1} = (\varepsilon_j + \varepsilon_{j+1})/2$ is the average energy, and $\Delta\epsilon_{j,j+1} = |\epsilon_j - \epsilon_{j+1}|$ is the detuning energy between the QD pair. The eigenenergies of this Hamiltonian are,

$$E^{(e/g)}_{j,j+1} = \bar{\varepsilon}_{j,j+1} \pm \sqrt{\Delta\epsilon^2_{j,j+1} + 4t^2_{j,j+1}},$$

and taking the difference between the ground and first excited state energies of the QD pair system, $E^{(e)}_{j,j+1} - E^{(g)}_{j,j+1}$, leads to a tunnel coupling of the form [1, 35],

$$t_{j,j+1}(\vec{\mathcal{V}}) = \frac{1}{2}\sqrt{\left(E^{(e)}_{j,j+1}(\vec{\mathcal{V}}) - E^{(g)}_{j,j+1}(\vec{\mathcal{V}})\right)^2 - \left(\varepsilon^{(g)}_j(\vec{\mathcal{V}}) - \varepsilon^{(g)}_{j+1}(\vec{\mathcal{V}})\right)^2}.$$

The single QD ground state energies, $\varepsilon^{(g)}_j$, are obtained by solving the 2D Schrödinger equation for the isolated single QD potential, while the double QD energies, $E^{(g)}_{j,j+1}$, are calculated using the isolated QD potential of the double QD system.

The third term, $H_U(\vec{\mathcal{V}})$, is the Coulomb repulsion between all electron pairs,

$$H_U(\vec{\mathcal{V}}) = \sum_{i=1}^{N} U_i(\vec{\mathcal{V}})\hat{n}_{i,\uparrow}\hat{n}_{i,\downarrow} + \sum_{\sigma_1,\sigma_2\in\{\uparrow,\downarrow\}}\left[\sum_{j=1}^{N-1} U_{j,j+1}(\vec{\mathcal{V}})\hat{n}_{j,\sigma_1}\hat{n}_{j+1,\sigma_2}\right],$$

The intra-Coulomb (onsite) energy, $U_i(\vec{\mathcal{V}})$, represents the Coulomb repulsion energy of electrons within the same QD, while the inter-Coulomb energy, $U_{j,j+1}(\vec{\mathcal{V}})$, accounts for the Coulomb interaction between electrons in adjacent QDs. In general, the inter-Coulomb energy includes contributions from all pairs of electrons in different QDs; however, in this work, only nearest-neighbor interactions are considered. The onsite energy energy is calculated using the developed numerical integration method described prior in Section 2.3 applied to the following integral form,

$$U_i = \int\int |\varphi_i(\boldsymbol{r_1})|^2 |\varphi_i(\boldsymbol{r_2})|^2 \frac{e^2}{4\pi\epsilon_0\epsilon_r |\boldsymbol{r_1} - \boldsymbol{r_2}|} d\boldsymbol{r_1} d\boldsymbol{r_2}, \tag{2.63}$$

where φ_i is the SPGSW in the i$^{\text{th}}$ QD, e is the charge of the electron, ϵ_0 is the vacuum permittivity, and ϵ_r is the relative permittivity. The inter-Coulomb repulsion term is calculated similarly,

$$U_{j,j+1} = \int\int |\varphi_j(\boldsymbol{r_1})|^2 |\varphi_{j+1}(\boldsymbol{r_2})|^2 \frac{e^2}{4\pi\epsilon_0\epsilon_r |\boldsymbol{r_1} - \boldsymbol{r_2}|} d\boldsymbol{r_1} d\boldsymbol{r_2}, \tag{2.64}$$

where φ_j and φ_{j+1} are the SPGSWs in the j^{th} or $(\mathrm{j}+1)^{\mathrm{th}}$ QD. Note that for the last term H_J in the Hamiltonian from Equation 2.60 represents the exchange interaction. Generally there will be a difference in Coulomb repulsion for the states with spin pairs that are aligned (triplet state) and anti-aligned (singlet state) due to the exchange interaction H_J. However, this effect is small in comparison to the inter-Coulomb energy and is ignored in the Hubbard model we utilize.

2.4.2 Example: Double QD System with 2 electrons

With a complete description of the Hamiltonian established, we now construct it explicitly to facilitate calculations and implementation in code. One approach would be to use Jordan-Wigner transformations to define the creation and annihilation operators explicitly. However, we adopt a method in which matrix elements are computed for a given basis [138]. This simplifies the task to generating a sufficient number of basis states and evaluating inner products, both of which are straightforward.

As an illustrative example, we construct the Hamiltonian for a two-site, two-electron system. The first step is to define the basis, which consists of all possible ways to distribute two electrons across two QD sites while respecting the Pauli exclusion principle. In this case, there are six possible states. Although the ordering of basis states is arbitrary, we follow the convention used in Ref. [139] to ensure consistency and facilitate verification. Thus, the six basis states are:

$$
\begin{aligned}
|a\rangle &= c^\dagger_{1,\uparrow} c^\dagger_{2,\uparrow} |0,0\rangle = |\uparrow,\uparrow\rangle = |0011\rangle \\
|b\rangle &= c^\dagger_{2,\downarrow} c^\dagger_{2,\uparrow} |0,0\rangle = |0,\uparrow\downarrow\rangle = |0101\rangle \\
|c\rangle &= c^\dagger_{1,\downarrow} c^\dagger_{2,\uparrow} |0,0\rangle = |\downarrow,\uparrow\rangle = |1001\rangle \\
|d\rangle &= c^\dagger_{2,\downarrow} c^\dagger_{1,\uparrow} |0,0\rangle = |\uparrow,\downarrow\rangle = |0110\rangle \\
|e\rangle &= c^\dagger_{1,\downarrow} c^\dagger_{1,\uparrow} |0,0\rangle = |\uparrow\downarrow,0\rangle = |1010\rangle \\
|f\rangle &= c^\dagger_{1,\downarrow} c^\dagger_{2,\downarrow} |0,0\rangle = |\downarrow,\downarrow\rangle = |1100\rangle \,.
\end{aligned}
$$

The last equality for each basis state expresses the occupation of all $|\downarrow\rangle$ or $|\uparrow\rangle$ states for each QD site:

$$
|\psi\rangle \coloneqq |n_1 n_2\rangle_\downarrow \, |n_1 n_2\rangle_\uparrow = |n_{1,\downarrow} n_{2,\downarrow} n_{1,\uparrow} n_{2,\uparrow}\rangle \,,
$$

where $|\psi\rangle$ represents a specific charge state, and $n_{i,(\uparrow/\downarrow)} \in \{0,1\}$ denotes the occupancy of a given QD site. This notation will be useful when constructing a CSD that maps to specific charge state configurations.

With the basis defined, we now construct the Hamiltonian. Starting from Equation 2.60 and neglecting the small H_J term, we obtain:

$$H = H_\mu + H_t + H_U. \tag{2.65}$$

We analyze each term individually, beginning with the chemical potential term:

$$\langle m| H_\mu |n\rangle = -\sum_{i=1,\sigma}^{2} \mu_i \langle m| n_{i,\sigma} |n\rangle . \tag{2.66}$$

Since the number operator $n_{i,\sigma}$ does not redistribute states, the inner product is zero for $m \neq n$, ensuring that this term is diagonal. For the diagonal elements, we count the number of electrons on each dot to determine the total energy contribution from the chemical potential:

$$H_\mu = \begin{bmatrix} -(\mu_1+\mu_2) & 0 & 0 & 0 & 0 & 0 \\ 0 & -2\mu_2 & 0 & 0 & 0 & 0 \\ 0 & 0 & -(\mu_1+\mu_2) & 0 & 0 & 0 \\ 0 & 0 & 0 & -(\mu_1+\mu_2) & 0 & 0 \\ 0 & 0 & 0 & 0 & -2\mu_1 & 0 \\ 0 & 0 & 0 & 0 & 0 & -(\mu_1+\mu_2) \end{bmatrix}. \tag{2.67}$$

Here, we assume the absence of a magnetic field, meaning spin states with different orientations have the same chemical potential. To incorporate a magnetic field, we would introduce an additional term corresponding to the Zeeman splitting, which can be conveniently included in Equation 2.65.

The tunnel coupling term for the Hamiltonian is the most difficult to calculate since all the other terms are diagonal, whereas this term is manifestly off-diagonal as it couples pairs of different states. To determine which terms of the tunnel coupling are non-zero, we need to identify which pairs of basis states are one-electron “hops" away from each other — that is, states where moving one spin from one site to the other transforms one basis state into another. There are four such allowed “hops":

$$\begin{aligned} |0,\uparrow\downarrow\rangle &\Leftrightarrow |\downarrow,\uparrow\rangle \quad (|b\rangle \Leftrightarrow |c\rangle) \\ |0,\uparrow\downarrow\rangle &\Leftrightarrow |\uparrow,\downarrow\rangle \quad (|b\rangle \Leftrightarrow |d\rangle) \\ |\uparrow\downarrow,0\rangle &\Leftrightarrow |\downarrow,\uparrow\rangle \quad (|e\rangle \Leftrightarrow |c\rangle) \\ |\uparrow\downarrow,0\rangle &\Leftrightarrow |\uparrow,\downarrow\rangle \quad (|e\rangle \Leftrightarrow |d\rangle) \end{aligned}$$

Thus, we only need to compute four inner products for this Hamiltonian. Although there will be eight non-zero terms in the Hamiltonian (one for each direction of the four tunnel couplings), we can use the fact that the Hamiltonian is Hermitian. Therefore, we can simply take the conjugate transpose of each element to account for the other direction of the hopping. The two spin states where both spins are aligned in the same orientation are isolated because they both require a spin flip in order to connect with any other basis state.

Now, let us compute one of the terms,

$$\begin{aligned}
\langle b|\, H_t\, |c\rangle &= -\sum_{\sigma} t_{bc} \langle b| \left(c^{\dagger}_{0,\sigma} c_{1,\sigma} + c^{\dagger}_{1,\sigma} c_{0,\sigma} \right) |c\rangle \\
&= -t_{bc} \langle 0, \uparrow\downarrow| \left(c^{\dagger}_{0,\uparrow} c_{1,\uparrow} + \cancel{c^{\dagger}_{1,\uparrow} c_{0,\uparrow}} + \cancel{c^{\dagger}_{0,\downarrow} c_{1,\downarrow}} + c^{\dagger}_{1,\downarrow} c_{0,\downarrow} \right) |\downarrow, \uparrow\rangle \\
&= -t_{bc} \left(\langle 0, \uparrow\downarrow|\, c^{\dagger}_{0,\uparrow} \,|\downarrow, 0\rangle + \langle 0, \uparrow\downarrow|\, c^{\dagger}_{1,\downarrow} \,|0, \uparrow\rangle \right) \\
&= -t_{bc} \left(\cancel{\langle 0, \uparrow\downarrow| \uparrow\downarrow, 0\rangle} + \langle 0, \uparrow\downarrow|\, 0, \uparrow\downarrow\rangle \right) \\
&= -t_{bc}.
\end{aligned}$$

All other non-zero terms are evaluated the same way. Therefore, the final Hamiltonian we end up with is:

$$H_t = \begin{bmatrix} 0 & 0 & 0 & 0 & 0 & 0 \\ 0 & 0 & -t_{bc} & -t_{bd} & 0 & 0 \\ 0 & -t_{bc} & 0 & 0 & -t_{ec} & 0 \\ 0 & -t_{bd} & 0 & 0 & -t_{ed} & 0 \\ 0 & 0 & -t_{ec} & -t_{ed} & 0 & 0 \\ 0 & 0 & 0 & 0 & 0 & 0 \end{bmatrix}. \tag{2.68}$$

In this particular example, we assume all the tunnel coupling rates to be different between different pairs of states. However, one approximation that simplifies this would be to assume they are all the same and have a common tunnel coupling t.

Matrix elements for the Coulomb repulsion terms H_U in the Hamiltonian are calculated similar to Equation 2.66 as,

$$\begin{aligned}
\langle m|\, H_U\, |n\rangle =& \langle m| U_1 n_{1,\uparrow} n_{1,\downarrow} + U_2 n_{2,\uparrow} n_{2,\downarrow} |n\rangle \\
&+ \langle m| U_{12} \left(n_{1,\uparrow} n_{2,\downarrow} + n_{1,\downarrow} n_{2,\uparrow} + n_{1,\uparrow} n_{2,\uparrow} + n_{1,\downarrow} n_{2,\downarrow} \right) |n\rangle.
\end{aligned} \tag{2.69}$$

Since the number operator does not redistribute states, this term of the Hamiltonian must be diagonal. Additionally, each pair will contribute only one term, where both sets of the

number operator do not yield zero. Therefore, the Hamiltonian is:

$$H_U = \begin{bmatrix} U_{12} & 0 & 0 & 0 & 0 & 0 \\ 0 & U_2 & 0 & 0 & 0 & 0 \\ 0 & 0 & U_{12} & 0 & 0 & 0 \\ 0 & 0 & 0 & U_{12} & 0 & 0 \\ 0 & 0 & 0 & 0 & U_1 & 0 \\ 0 & 0 & 0 & 0 & 0 & U_{12} \end{bmatrix}. \tag{2.70}$$

Putting everything together, we end up with the following Hamiltonian:

$$H = \begin{bmatrix} -(\mu_1+\mu_2)+U_{12} & 0 & 0 & 0 & 0 & 0 \\ 0 & -2\mu_2+U_2 & -t_{bc} & -t_{bd} & 0 & 0 \\ 0 & -t_{bc} & -(\mu_1+\mu_2)+U_{12} & 0 & -t_{ec} & 0 \\ 0 & -t_{bd} & 0 & -(\mu_1+\mu_2)+U_{12} & -t_{ed} & 0 \\ 0 & 0 & -t_{ec} & -t_{ed} & -2\mu_1+U_1 & 0 \\ 0 & 0 & 0 & 0 & 0 & -(\mu_1+\mu_2)+U_{12} \end{bmatrix} \tag{2.71}$$

In order to construct a CSD, the Hamiltonian matrix in Equation 2.71 must be diagonalized, and the eigenvector corresponding to the lowest eigenvalue must be determined for each voltage configuration.

2.4.3 Generalization: Many QD System

Now that we have worked through a specific example, we can generalize the method to n electrons in m sites.

In the previous example, we considered a system with exactly 2 electrons. However, we now want to be able to vary the number of electrons in the system (as is needed for a CSD). To achieve this, we extend the basis states to include configurations with different numbers of electrons. For each non-negative integer l where $0 \leq l < n$, we generate all possible states with l electrons distributed across m sites, initially ignoring other degrees of freedom. Then, for each possible configuration, we assign spin states to the electrons, ensuring that we discard any configurations that violate the Pauli exclusion principle. Since states with different numbers of electrons do not couple in the Hamiltonian, this results in a block-diagonal matrix.

One important consideration with this model is that placing more than 2 electrons on a single site becomes complex. This is because the orbital energy spacing must be

known in order to determine the energy of adding a third (or fourth, fifth, etc.) electron to a site. Therefore, when generating basis states, we limit ourselves to a maximum of 2 electrons per site, which ensures that $n \leq 2m$. In QuDiPy simulations, we do not exceed 2 electrons per site, so this limitation should not be restrictive for most of the QD spin qubit QC experiments that we wish to perform. To ensure compliance with the Pauli exclusion principle, the QuDiPy implements a combined site and spin index, restricting each index to contain either 0 or 1 electron. This guarantees that no site is doubly occupied by electrons with the same spin.

Once the basis states are generated, we construct the Hamiltonian matrix by applying the general forms of the various Hamiltonian components. Although in the previous example, we simplified the process by exploiting our understanding of the system, performing the full calculation in a computational framework yields the same results. To this end, we created a simple implementation that includes the creation, annihilation, and number operators, as well as an inner product calculator.

2.4.4 Regions of Charge Stability

Given the Hamiltonian components defined in Equations 2.61 through 2.63, the effective parameters $\mu_i(\vec{\mathcal{V}})$, $U_i(\vec{\mathcal{V}})$, $U_{i,i+1}(\vec{\mathcal{V}})$, and $t_{i,i+1}(\vec{\mathcal{V}})$ are pre-calculated for all voltage configurations, $\vec{\mathcal{V}}$, and saved as interpolation objects. The resulting behavior of each Hubbard effective parameter is shown in Figure 2.11(a) for a 2D sweep of plunger gate voltages, with a fixed barrier voltage of -0.4V, for a double QD device. The $\vec{\mathcal{V}}$-dependent effective parameter objects enable QuDiPy to efficiently construct and diagonalize the Hamiltonian in Equation 2.60, thereby determining the lowest energy charge state base vector, which produces the CSD observed in Figure 2.11(b).

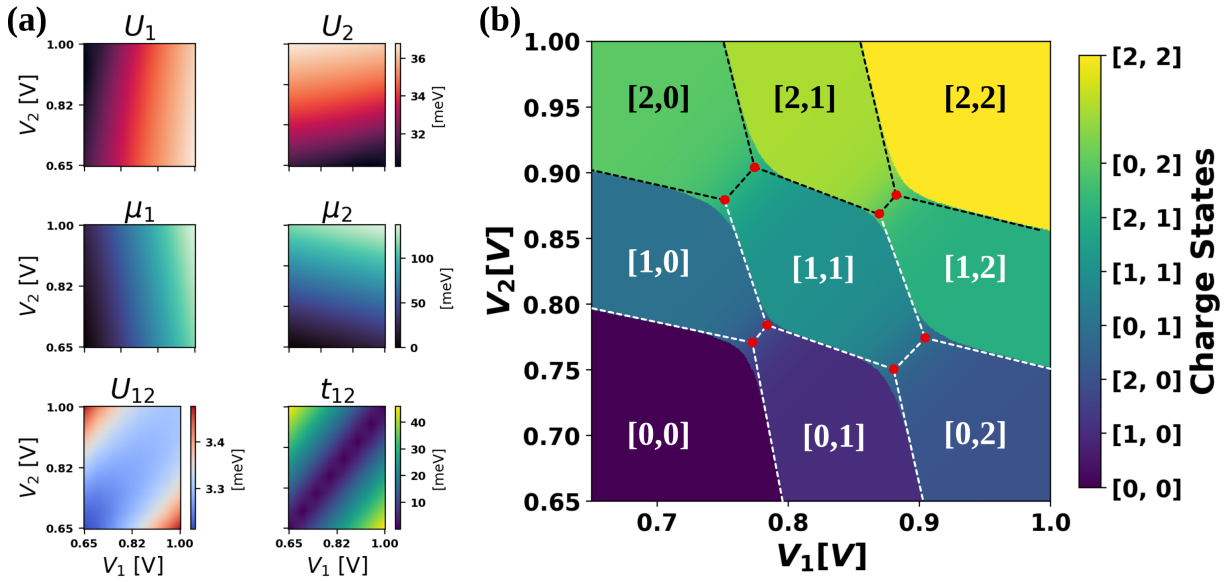


Figure 2.11: (a) Calculated effective parameters of the Hubbard Hamiltonian for a double QD system. Hubbard parameters are a function of $\vec{\mathcal{V}} = [V_1, W_1, V_2]$, however, W_1 has been chosen to be in the low tunnel barrier regime of -0.4V for the sweep of the plunger gates. (b) CSD resulting from exact diagonalization of the Hubbard Hamiltonian constructed with the Hubbard effective parameters in subfigure (a) with a constant tunnel coupling set to 3 meV.

2.4.5 Automated Extraction of Capacitance Matrix

The ability to efficiently and accurately determine the capacitive couplings between the charge on the QD and the gate electrodes is invaluable to the experimental control of spin qubits in QDs. Extracting the capacitance between all QD-electrode and $\text{QD}_{i,i+1}$ pairs allows for virtual gates to be created, enabling easier qubit control, and for Hubbard parameters such as charging energy to me estimated. The two capacitance matrices of interest, and in our ability to estimate with only unbiased CSDs, are the following,

$$C_d = \begin{bmatrix} C_1 & C_m \\ C_m & C2 \end{bmatrix}, \quad Cg = \begin{bmatrix} C_{g1d1} & C_{g1d2} \\ C_{g2d1} & C_{g2d2} \end{bmatrix} \tag{2.72}$$

Where C_d is the capacitance matrix associated with the only QD charges, i.e. $C_1(2) \equiv$ total capacitance on $\text{QD}_{1(2)}$ and $C_m \equiv$ mutual capacitance between QD_1 and QD_2. Similarly, C_g is the capacitance matrix associated with the QD charge and gate electrodes,

i.e. $C_{g1(2)d1(2)} \equiv$ capacitance between $\mathrm{QD}_{1(2)}$ and gate $\mathrm{V}_{1(2)}$ and $C_{g1(2)d2(1)} \equiv$ capacitance between $\mathrm{QD}_{1(2)}$ and gate $\mathrm{V}_{2(1)}$. The total capacitance on each QD is the sum of all QD and electrode capacitances, including source/drain leads, and is written as $C_{1(2)} = C_{L(R)} + C_{g1(2)d1(2)} + C_{g2(1)d1(2)} + C_m$ with $C_{L(R)} \equiv$ capacitance between $\mathrm{QD}_{1(2)}$ and $\mathrm{V}_{\mathrm{source(drain)}}$.

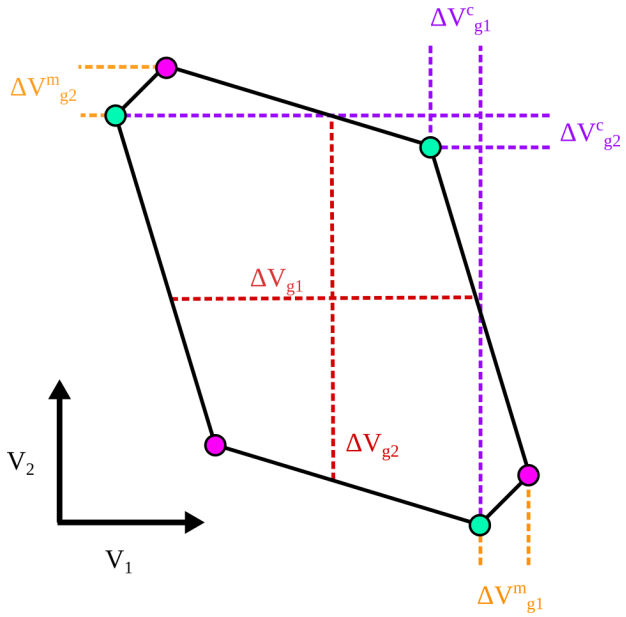


Figure 2.12: Honeycomb region for an example double QD showing a single charge state with along with the electron-hole triple point pairs. The voltage spacings between electron-hole, electron-electron, and hole-hole triple point pairs allows capacitance matrix estimates to be made using the constant interaction model.

Using the constant interaction model, and following references [33, 45], we derive the following expressions for the capacitance matrix elements from voltage spacings as shown in Figure 2.12,

$$C_{g1} = \frac{|e|}{\Delta V_{g1}}, \quad C_{g2} = \frac{|e|}{\Delta V_{g2}}, \quad C_m = \frac{\Delta V^m_{g1}}{\Delta V_{g1}} C_2 = \frac{\Delta V^m_{g2}}{\Delta V_{g2}} C_1, \tag{2.73}$$

$$C_{g1(2)d1(2)} = \frac{|e|\Delta V_{g2(1)}}{\Delta V_{g1}\Delta V_{g2} - \Delta V^c_{g1}\Delta V^c_{g2}}, \quad C_{g1(2)d2(1)} = \frac{|e|\Delta V^c_{g2(1)}}{\Delta V_{g1}\Delta V_{g2} - \Delta V^c_{g1}\Delta V^c_{g2}}, \tag{2.74}$$

$$\frac{C_{1(2)}}{C_m} = \frac{|e|}{C_{g2(1)d2(1)}\Delta V^m_{g2(1)}} - \frac{C_{g2(1)d1(2)}}{C_{g2(1)d2(1)}}. \tag{2.75}$$

Note though, that without biased CSD measurements, which produce bias triangle features, all capacitance matrix elements can be estimated expect for $C_{1(2)}$ and C_m; only the ratio $\frac{C_{1(2)}}{C_m}$ can be estimated. However, assuming that $C_{L(R)} \approx C_{g1(2)d1(2)}$ simplifies the expression for $C_{1(2)} \approx 2C_{g1(2)d1(2)} + C_{g2(1)d1(2)} + C_m$ such that the ratio $\frac{C_{1(2)}}{C_m}$ calculated from Equations 2.73 enables us to find the mutual capacitance and fully estimate both capacitance matrices. This approximation is in line with recent reported values in literature [140] and leads to an expression for the mutual capacitance as,

$$C_m = \left(C_{g1(2)d1(2)} + C_{g2(1)d1(2)}\right)\left[\frac{|e|}{C_{g1(2)d1(2)}\Delta V^m_{g2(1)}} - \frac{C_{g2(1)d1(2)}}{C_{g1(2)d1(2)}} - 1\right]^{-1} \tag{2.76}$$

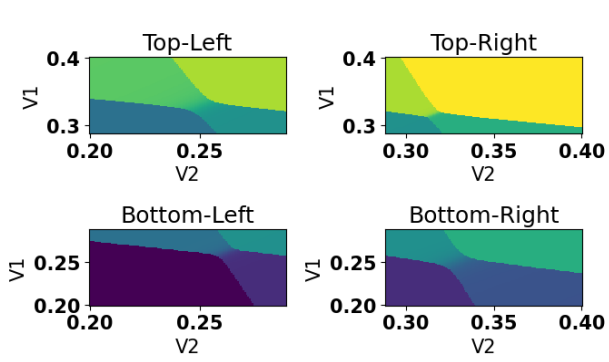
Given a CSD, we wish to extract estimates for the voltage coordinates for all visible triple point pairs. Once extracted the triple point coordinates trivially estimate the required voltage spaces used in Equations 2.73. For this reason, a QuDiPy module was developed to process CSDs, an example of a double QD CSD is shown in Figure 2.13, where the module: (2.13a) splits the charge stability regions on perceived centroids into quadrants (2.13b) performs a spiraling search, i.e. “snake" search to identify charge transition lines and their slopes (2.13c) find the charge transition line intersections to estimate triple point pair voltage coordinates (2.13d) perform the triple point pair coordinate extraction on all sub-CSD regions.

Inputting the extracted triple point pair coordinates into Equations 2.73 yields the following estimates for the capacitance and lever arm matrices,

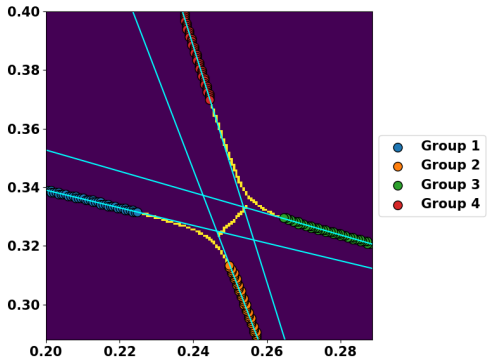
$$C_d = \begin{bmatrix} 2.399\text{ aF} & 0.837\text{ aF} \\ 0.837\text{ aF} & 2.685\text{ aF} \end{bmatrix}, \quad C_g = \begin{bmatrix} 2.482\text{ aF} & 0.481\text{ aF} \\ 0.483\text{ aF} & 2.778\text{ aF} \end{bmatrix}, \tag{2.77}$$

$$\alpha = \begin{bmatrix} \alpha_{g1d1} & \alpha_{g1d2} \\ \alpha_{g2d1} & \alpha_{g2d2} \end{bmatrix} = \begin{bmatrix} 0.402 & 0.069 \\ 0.069 & 0.397 \end{bmatrix} \tag{2.78}$$

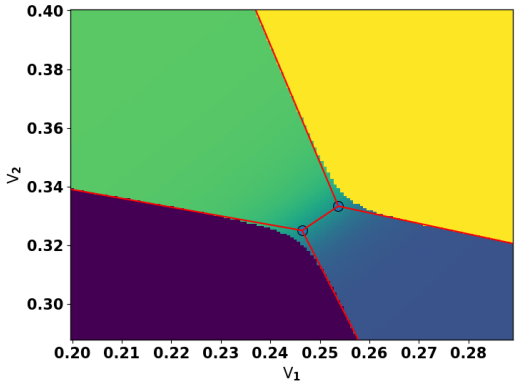
Which is in good agreement with values reported in [140].



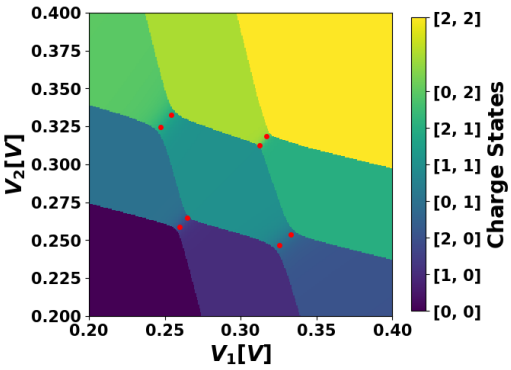
(a) CSD similar to Figure 2.11 split into quadrants.



(b) Snake search algorithm detects transition line slopes.



(c) Triple point pairs are determined from transition line slopes.



(d) Triple point voltage coordinates extracted from all quadrants.

Figure 2.13: Figure showing the automated extraction of triple point pairs used to determine capacitance and lever arm matrices.

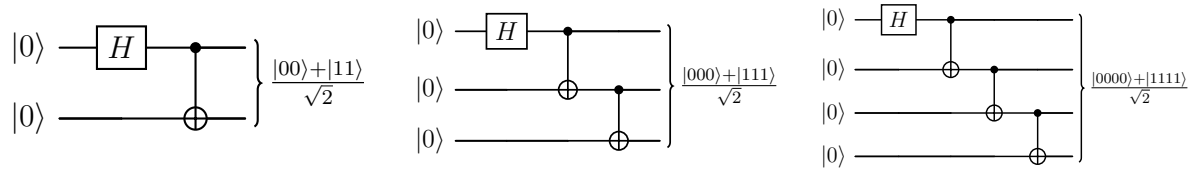
2.5 Node Network

The realization of large-scale, fault-tolerant quantum computing requires architectures that can efficiently implement quantum error correction while maintaining scalability and high-fidelity qubit operations. Among various qubit implementations, spin qubits in semiconductor QDs offer a compelling pathway due to their potential for high-density integration, long coherence times, and compatibility with existing semiconductor fabrication technologies. However, scaling up QD-based processors to a practical size presents numerous chal-

lenges, including qubit connectivity, control wiring constraints, and the need for reliable entanglement distribution.

A promising approach to addressing these challenges is the use of a node-based network architecture for spin qubit quantum computing. This architecture, as proposed by Buonacorsi et al. [64], employs a distributed network of QD nodes connected via electron shuttling pathways. Each minimal node consists of a small number of QDs, comprising one data qubit, two ancilla qubits, and additional shuttle QDs that collectively perform stabilizer operations for quantum error correction. The nodes are arranged in a scalable 2D network, with entanglement distributed through the coherent transport of electron spins between adjacent nodes.

A key feature of this architecture is its ability to implement surface code quantum error correction with minimal hardware overhead. Instead of relying on direct physical coupling between distant qubits, entanglement is established through spin singlet states that are spatially separated via controlled electron shuttling. This approach effectively mitigates cross-talk and interference issues that arise in densely packed qubit arrays while enabling high-fidelity quantum gate operations. Moreover, the micron-scale separation between nodes allows for practical integration of classical control electronics, which is essential for large-scale implementations.



(a) Two qubits

(b) Three qubits

(c) Four qubits

Figure 2.14: Quantum circuits for generating maximally entangled GHZ states. The examples assume entanglement creation in separate QD nodes if two-qubit gate operations can be applied between node pairs.

In principle, creating entangled states between qubits in different QD nodes can be achieved by applying a series of single- and two-qubit gates as shown in Figure 2.14. However, non-local two-qubit gates must be applied directly between QD nodes, which is not possible in the node network proposal. To avoid this limitation, entanglement distribution is shared by shuttling individual electrons from a singlet pair to specific QDs on nodes in the network. A series of gate operations and qubit measurements are then

applied locally to specific QDs and specific nodes to realize a 4-qubit GHZ state that is leveraged for surface code stabilizer operations.

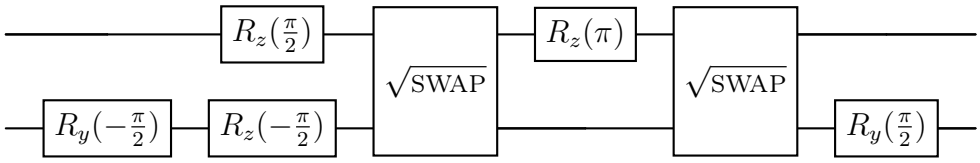


Figure 2.15: Series of single- and two-qubit gate operations to achieve a two-qubit CNOT gate. The top wire represents the control qubit channel, while the bottom is the target channel.

The set of required local gate operations to implement the node network surface code is shown in Figure 3.1, where the quantum circuit's net effect is performing a CNOT gate. The single-qubit gates are operators $R_{\hat{n}}(\theta)$ which perform single-qubit rotations about an axis $\hat{n}$ by an angle θ, and are realized through voltage controlled g-factor variation, $R_z(\theta)$, or applied ESR pulses, $R_y(\theta)$. Two-qubit $\sqrt{SWAP}$ gates are achieved through the voltage-controlled exchange interaction. QuDiPy can generate control pulses for general single-qubit, $R_{\hat{n}}(\theta)$, and two-qubit, $SWAP^k$, gate operations, as well as simulate the evolution of a multi-qubit spin system. This enables small-scale simulation of the node network proposal.

As discussed in Section 1.2.2, singlet generation in QDs is a simple and efficient method to generate entanglement. A singlet state is generated by loading two electrons into a QD by proper alignment of the reservoir and QD chemical potentials. The electron pair forms the singlet state, then can be separated by coherently shuttling the electrons to different QDs in nodes across the network. The distributed entanglement is utilized as a resource to create new entangled states between nodes in the network, effectively creating non-local two-qubit gate operations.

2.5.1 2 Node Bell State Preparation

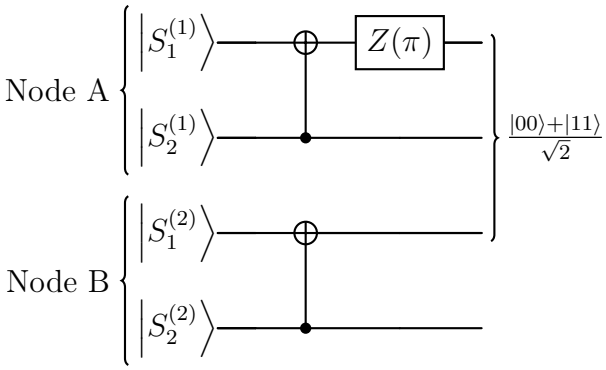


Figure 2.16: Quantum circuit diagram illustrating distributed entanglement between QD nodes A and B by preparing a two-qubit maximally entangled Bell state. Singlet states S_1 and S_2 are shared between QDs 1 and 2 in both node A and B. CNOT gates are applied to each node separately and a single $Z(\pi)$ rotation gate is applied to the qubit in A_1 which forms a Bell state between qubits in A_1 and B_1.

To demonstrate non-local entanglement generation, we start with a simple double QD two-node example, as shown in Figure 2.16. We define the state of networked nodes A and B to be the following,

$$|\Psi\rangle \coloneqq |A_1 A_2, B_1 B_2\rangle\,, \tag{2.79}$$

where A_n and B_n are considered to be ancilla qubit states in individual QDs for each respective node. In the absence of a qubit in one of the node's QDs, we define an empty QD state to be $|\emptyset\rangle$, e.g., empty QDs representing ancillas A_2 and B_2 would read $|\Psi\rangle = |A_1\emptyset, B_1\emptyset\rangle$. If a singlet, $|S\rangle = \frac{1}{\sqrt{2}}\left[|\uparrow\downarrow\rangle - |\downarrow\uparrow\rangle\right] = \frac{1}{\sqrt{2}}\left[|01\rangle - |10\rangle\right]$, is generated and shared between A_1-B_2 and A_2-B_1 then the state becomes,

$$\begin{aligned}
|\Psi\rangle &= \frac{1}{\sqrt{2}}\left(|01\rangle - |10\rangle\right)_{A_1B_1} \otimes \frac{1}{\sqrt{2}}\left(|01\rangle - |10\rangle\right)_{A_2B_2}\,,\\
&\coloneqq \frac{1}{2}\left(|0\emptyset, 1\emptyset\rangle - |1\emptyset, 0\emptyset\rangle\right) \otimes \left(|\emptyset 0, \emptyset 1\rangle - |\emptyset 1, \emptyset 0\rangle\right)\,,\\
&= \frac{1}{2}\left(|00, 11\rangle - |10, 01\rangle - |01, 10\rangle + |11, 00\rangle\right)\,,
\end{aligned} \tag{2.80}$$

Applying CNOT gates between ancillas A_1-B_2 and A_2-B_1 creates the following state,

$$\begin{aligned} CNOT_{A_2A_1}\left|\Psi\right\rangle &= \frac{1}{2}\left(\left|00,11\right\rangle - \left|10,01\right\rangle - \left|11,10\right\rangle + \left|01,00\right\rangle\right), \\ CNOT_{B_2B_1}CNOT_{A_2A_1}\left|\Psi\right\rangle &= \frac{1}{2}\left(\left|00,01\right\rangle - \left|10,11\right\rangle - \left|11,10\right\rangle + \left|01,00\right\rangle\right), \\ &\coloneqq \frac{1}{2}(\left|00\right\rangle_{a1}\left|01\right\rangle_{a2} - \left|11\right\rangle_{a1}\left|01\right\rangle_{a2} \\ &\quad - \left|11\right\rangle_{a1}\left|10\right\rangle_{a2} + \left|00\right\rangle_{a1}\left|10\right\rangle_{a2}), \end{aligned} \tag{2.81}$$

where the states $\left|\right\rangle_{a1(2)}$ have been defined as the state between ancilla qubits in QDs $A_{1(2)}$ and $B_{1(2)}$. Now we consider a $Z(\pi) \coloneqq ROT(\pi, \hat{z}) = \exp\{(-i\frac{\pi}{2}\hat{\sigma}_3)\}$ which simplifies to,

$$\begin{aligned} e^{-i\frac{\pi}{2}\hat{\sigma}_3} &= \cos\left(\frac{\pi}{2}\right)\hat{\sigma}_0 - i\cos\left(\frac{\pi}{2}\right)\hat{\sigma}_3 \\ &= e^{-i\frac{\pi}{2}}\hat{\sigma}_3 \end{aligned} \tag{2.82}$$

Applying the $Z(\pi)$ gate to the first ancilla produces the following final state,

$$\begin{aligned} Z_{A_1}(\pi)_{A_1}CNOT_{B_2B_1}CNOT_{A_2A_1}\left|\Psi\right\rangle &= \frac{e^{-i\frac{\pi}{2}}}{2}(\left|00\right\rangle_{a1}\left|01\right\rangle_{a2} + \left|11\right\rangle_{a1}\left|01\right\rangle_{a2} \\ &\quad + \left|11\right\rangle_{a1}\left|10\right\rangle_{a2} + \left|00\right\rangle_{a1}\left|10\right\rangle_{a2}), \\ &= \frac{e^{-i\frac{\pi}{2}}}{2}[\,\left|00\right\rangle_{a1}(\left|01\right\rangle_{a2} + \left|10\right\rangle_{a2}) \\ &\quad + \left|11\right\rangle_{a1}(\left|01\right\rangle_{a2} + \left|10\right\rangle_{a2})\,], \\ &= e^{-i\frac{\pi}{2}}\underbrace{\frac{1}{\sqrt{2}}(\left|00\right\rangle_{a1} + \left|11\right\rangle_{a1})}_{\text{Bell State}} \times \frac{1}{\sqrt{2}}(\left|01\right\rangle_{a2} + \left|10\right\rangle_{a2}). \end{aligned} \tag{2.83}$$

Note that the state between the ancilla qubits in both nodes, $\left|\psi_{a1}\right\rangle$, produces a maximally entangled Bell state, $\left|\psi_{a1}\right\rangle = (\left|00\right\rangle_{a1} + \left|11\right\rangle_{a1})/\sqrt{2}$ with a global phase factor $e^{-i\frac{\pi}{2}}$.

2.5.2 3 Node GHZ State Preparation

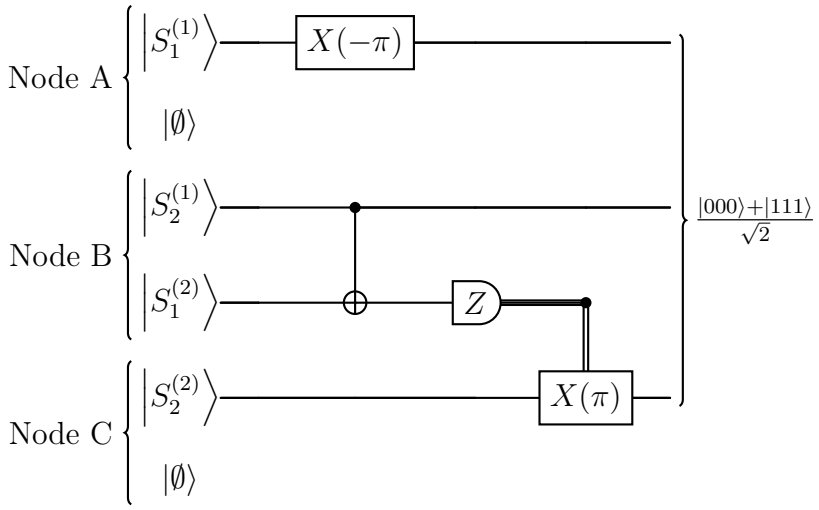


Figure 2.17: Quantum circuit diagram illustrating distributed entanglement between QD nodes A, B, and C by preparing a three-qubit maximally entangled GHZ state. Singlet states S_1 and S_2 are shared between QDs in nodes A, B, and C. A X($-\pi$) gate is applied to ancilla 1 in node A, in parallel with a CNOT gate between ancilla qubits in node B. A conditional X(π) gate is applied to ancilla one in node C after a Z-basis measurement of the second ancilla qubit in node B, forming a GHZ state between the first ancilla qubits across all three nodes.

As another illustrative example, we show how non-local entanglement can be generated for a 3-qubit state for a system of double QDs across three nodes. We define the state of networked nodes A, B and C to be the following,

$$|\Psi\rangle \coloneqq |A_1A_2, B_1B_2, C_1C_2\rangle\,, \tag{2.84}$$

where A_n, B_n, and C_n are considered to be ancilla qubit states in individual QDs for each respective node. If a singlet, $|S\rangle = \frac{1}{\sqrt{2}}\left[|\uparrow\downarrow\rangle - |\downarrow\uparrow\rangle\right] = \frac{1}{\sqrt{2}}\left[|01\rangle - |10\rangle\right]$, is generated and

shared between A_1-B_1 and B_1-C_1 then the state becomes,

$$\begin{aligned}|\Psi\rangle &= \frac{1}{\sqrt{2}}\left(|01\rangle - |10\rangle\right)_{A_1B_1} \otimes \frac{1}{\sqrt{2}}\left(|01\rangle - |10\rangle\right)_{B_2C_1}, \\ &\coloneqq \frac{1}{2}\left(|0\emptyset, 1\emptyset, \emptyset\emptyset\rangle - |1\emptyset, 0\emptyset, \emptyset\emptyset\rangle\right) \otimes \left(|\emptyset\emptyset, \emptyset 0, 1\emptyset\rangle - |\emptyset\emptyset, \emptyset 1, 0\emptyset\rangle\right), \\ &= \frac{1}{2}\left(|0\emptyset, 10, 1\emptyset\rangle - |1\emptyset, 00, 1\emptyset\rangle - |0\emptyset, 11, 0\emptyset\rangle + |1\emptyset, 01, 0\emptyset\rangle\right), \end{aligned} \tag{2.85}$$

For clarity, we ignore empty ancilla qubits in the second QD for each node, i.e.,

$$|A_1, \emptyset, B_1B_2, C_1, \emptyset\rangle \coloneqq |A_1, B_1B_2, C_1\rangle .$$

Applying a CNOT gate between ancillas B_1-B_2 creates the following state,

$$CNOT_{B_1B_2}|\Psi\rangle = \frac{1}{2}\left(|0, 11, 1\rangle - |1, 00, 1\rangle - |0, 10, 0\rangle + |1, 01, 0\rangle\right). \tag{2.86}$$

A $X(-\pi)$ gate can be applied in parallel to the $CNOT_{B_1B_2}$ gate, but for illustrative purposes, we apply the $X(-\pi)$ gate after the CNOT operation, which produces the following state,

$$\begin{aligned}X_{A_1}(-\pi)CNOT_{B_1B_2}|\Psi\rangle &= \frac{1}{2}\left(-|1, 11, 1\rangle + |0, 00, 1\rangle + |1, 10, 0\rangle - |0, 01, 0\rangle\right), \\ &\coloneqq \frac{1}{2}(-|111\rangle_{a1}|\emptyset 1\emptyset\rangle_{a2} + |001\rangle_{a1}|\emptyset 0\emptyset\rangle_{a2} \\ &\quad + |110\rangle_{a1}|\emptyset 0\emptyset\rangle_{a2} - |000\rangle_{a1}|\emptyset 1\emptyset\rangle_{a2}). \end{aligned} \tag{2.87}$$

Measuring the B_2 ancilla qubit in the Z-basis yields the following two observed states,

$${}_{a2}\langle\emptyset 0\emptyset|\psi_{a2}\rangle = |\emptyset 0\emptyset\rangle_{a2} \rightarrow \frac{1}{2}\left(|001\rangle_{a1} + |110\rangle_{a1}\right), \tag{2.88}$$

$${}_{a2}\langle\emptyset 1\emptyset|\psi_{a2}\rangle = |\emptyset 1\emptyset\rangle_{a2} \rightarrow -\frac{1}{2}\left(|111\rangle_{a1} + |000\rangle_{a1}\right). \tag{2.89}$$

When the measurement produces $|0\rangle_{B2}$, i.e., ${}_{a2}\langle\emptyset 0\emptyset|\psi_{a2}\rangle = |\emptyset 0\emptyset\rangle_{a2}$, a $X(\pi)$ is applied to ancilla qubit C_1, producing a 3-qubit GHZ state across the first ancilla qubits for all three nodes A, B, and C with 100% probability,

$$\left|\psi_{a1}^{(\text{final})}\right\rangle = \frac{1}{\sqrt{2}}\left(|000\rangle_{a1} + |111\rangle_{a1}\right), \tag{2.90}$$

while ignoring a global phase factor of $e^{i\pi} = -1$.

2.5.3 4 Node GHZ State Preparation

The previous two examples demonstrate how non-local entanglement generation is possible when electron singlet pairs are used as a resource and distributed across a network of QD nodes. However, to perform the surface code for fault-tolerant error correction, QC, non-local 4-qubit entangled states are required, along with the necessary experimental control inputs to realize such states.

To this end, QuDiPy has been designed to be lightweight to simulate nodes up to four QDs. An example 4-qubit GHZ state is prepared from a series of Hadamard and CZ gates for a four QD device, as shown in Figure 2.18. The initialized state of the qubit system is all set to the $|0\rangle$ state, and the gate voltages are tuned such that the g-factor of each electron is the same across all four qubits. QuDiPy determines the effective parameter evolution required to implement Hadamard or CZ gates for various qubits or qubit pairs and calculates the estimated voltage and ESR field pulses to achieve them [1, 141].

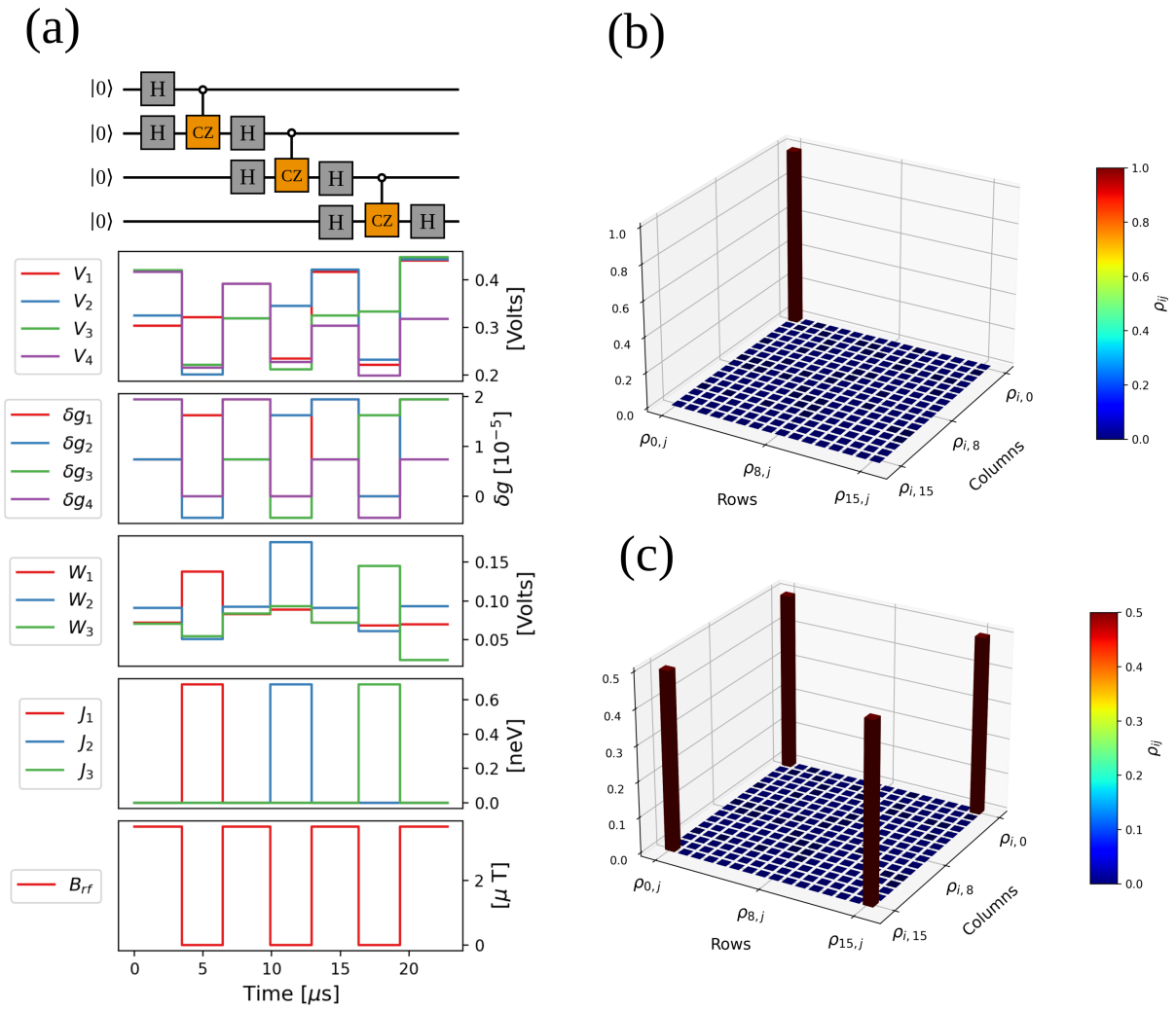


Figure 2.18: 4-qubit maximally entangled GHZ preparation from a series of Hadamard and CZ gate operations. CZ gate is realized as a CPHASE(π) gate operation in QuDiPy. The required effective parameter evolution (g-factor and exchange J) is determined, and the resultant experimental control pulses (plunger gate V, tunnel gate W, and ESR field B_{RF}) are plotted.

While the node network proposal presents a QD node device consisting of four QDs, to simulate the surface code in QuDiPy, only requires a triple QD node, which consists of a data qubit and two ancilla qubits. Simulating an error correction stabilizer step requires four nodes and entanglement distribution from three singlets. The singlet sharing, gate

operation, and measurement protocol are shown in Figure 2.19, which generates a 4-qubit maximally entangled GHZ state between four nodes and performs either a Z or X stabilizer operation.

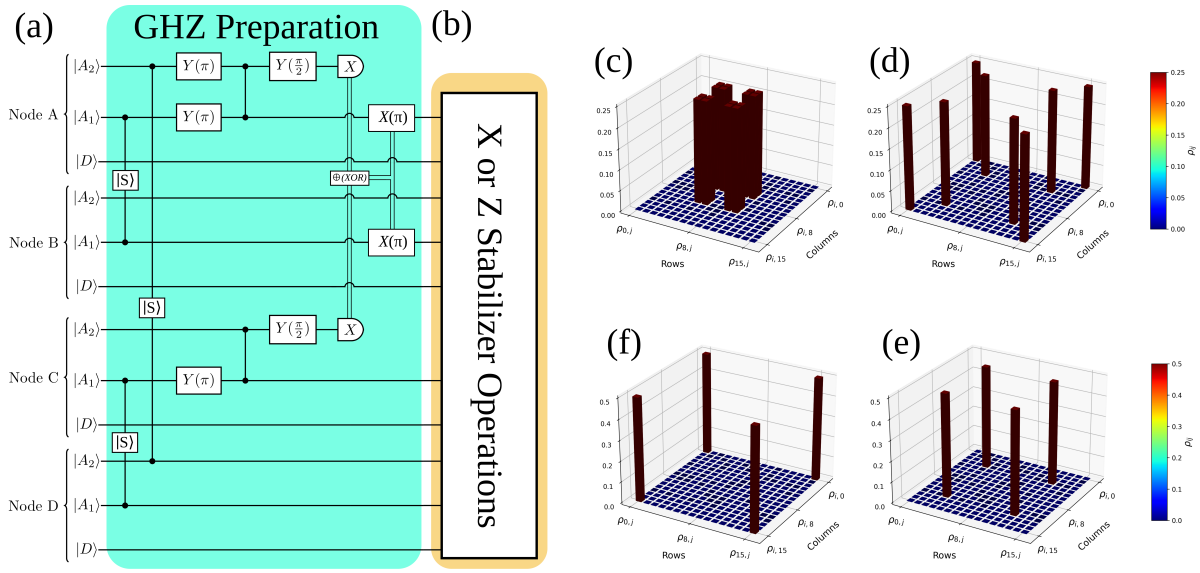


Figure 2.19: (a) Triple QD and four-node GHZ preparation and X/Z surface code stabilizer operation. Singlet states $|S\rangle$ are distributed between ancilla 1 in nodes A-B, ancilla 1 in nodes C-D, and ancilla 2 in nodes A-D. Single- and two-qubit gates are performed, X-basis measurement on ancilla qubits 2 in nodes A and C, and conditional $X(\pi)$ gates on ancilla qubits 1 in nodes A and B to form a GHZ state across all ancilla 1 qubits. (b) Additional gates are conditionally applied to achieve an X or Z stabilizer operation. (c-f) Show the resultant density matrix elements for the qubit state across ancillas A_1, B_1, C_1, and D_1. Density matrix elements ar show at intermediate steps when preparing the 4-qubit GHZ state: (c) initial state after singlet distribution, (d) state after single- and two-qubit rotation gates, (f) state after an X-basis measurement is applied to ancilla qubits A_2 and C_2 (measuring odd parity), and (e) the final GHZ state after corrective $X(\pi)$ gates are applied for an odd parity measurement between A_2 and C_2.

2.6 Conclusions

This chapter introduced QuDiPy, a lightweight Python-based simulation tool designed to model quantum dot spin qubit systems, supporting device design and the investigation of spin qubit control and error correction protocols. The simulator enables memory-efficient handling of electrostatic potential interpolation functions and fast calculations of single-particle wavefunctions, Coulomb-like integrals in exchange energy, and Hubbard model applications, as well as effective Hamiltonian parameters. Multi-variant interpolation functions enable efficient simulation of a QD device's spin state under control signal inputs and estimation of its charge state using a control-voltage-dependent Hubbard model.

To maintain efficiency without compromising accuracy, QuDiPy incorporates strategic approximations, such as isolating single and double QD potentials via a masking routine and computing exchange energy with a finite orbital basis set. These simplifications enable the simulator to capture spin qubit dynamics with sufficient detail for investigating general qubit control and quantum error correction protocols.

Additionally, we demonstrated QuDiPy's capability to simulate multi-qubit interactions, particularly in generating entangled states such as Bell and GHZ states across QD arrays. Validation against experimentally relevant parameters confirmed its utility for both theoretical investigations and practical quantum computing applications. Future enhancements, including noise modeling, adaptive control schemes, and a QD-specific multi-electron solver, will further expand its role in designing scalable quantum processors.

Chapter 3

Spin Qubit Compact Model for Control Electronic Design

3.1 Introduction

Chapter 2 focused on the development of the QuDiPy simulator to aid in QD device design, spin qubit control, and the investigation of QD physical models. The work in Chapter 2 assumes the ability to generate highly precise voltage and magnetic field signals experimentally, which presents a significant technical challenge worthy of dedicated investigation. While the prior work assumed the ability to generate arbitrarily precise control signals, QuDiPy is capable of processing real control signals created by experimental Digital to analog converter (DAC) signal generators. While this is useful for investigating the physical impacts of bandwidth-limited or noisy signals, it poses a design bottleneck for electrical engineers who need to iterate through various DAC specifications and other control electronics for specific spin qubit experiments or quantum computations. The restriction on design iteration time necessitates the creation of a classical compact model that can simulate qubit behavior under classical control electronic input signals while allowing a classical circuit simulator, such as SPICE [3] and ADS [4], to perform the calculations entirely within the respective software package.

In recent years, several spin qubit compact models have been proposed [142–147], which have shown progress towards building compact models to aid qubit control electronic design. However, these methods generally require the spin Hamiltonian to be simulated outside of the classical circuit solver or use approximations that introduce additional error. The goal of this chapter is to take a given Hamiltonian and map the Liouville-von

Neumann and Lindblad master equations to a model that can represent the quantum system state evolution as a classical circuit compact model. This model is be able to take experimental control signal inputs to a qubit system, simulate the state evolution under a desired unitary, and output the resultant state of the system for modeling in software systems e.g. [3, 4] with minimal reduction in fidelity from the theoretically perfect unitary gates generated by QuDiPy.

To study control electronic signal impacts on qubit state evolution, a master state equation, such as the Liouville-von Neumann master equation $i\hbar\frac{d\rho}{dt} = [H, \rho]$, must be solved for each matrix element of the density matrix. The following equations can be written as $\frac{d\rho_i}{dt} = \sum_{j=1} G_{ij}\rho_j$, resemble Kirchhoff's current law, and can be solved by proper creation of a classical circuit. With the aid of QuDiPy, voltage and ESR field control pulses can be simulated for spin qubit gate operations, and an analytic functional map can be constructed through an optimization protocol to create a spin qubit compact model using the Varilog-A programming language. The methodology for constructing a compact model is a follows:

1. Define a set of universal gate operations or a specific desired unitary along with experimental controls, i.e. $R(\vec{\mathcal{V}}(t), B_{RF}(t), \phi(t), \omega_{RF}, \theta, \hat{n}) \in X, Y, Z$, $SWAP^k(\vec{\mathcal{V}}(t))$, $U(\vec{\mathcal{V}}(t), B_{RF}(t), \phi(t), \omega_{RF})$.

2. Generate experimental controls pulses: gates, $\vec{\mathcal{V}}(t)$, ($\vec{V}(t) \coloneqq$ Plunger, $\vec{W}(t) \coloneqq$ Barrier) voltage and global ESR, $B_{RF}(t), \phi(t), \omega_{RF}$ ($B_{RF}(t) =$ amplitude, $\phi(t) =$ phase, and $\omega_{RF} =$ angular frequency).

3. Map experimental controls to system effective parameters i.e. $g(t) = F_g(\vec{\mathcal{V}}(t))$ and $J(t) = F_J(\vec{\mathcal{V}}(t))$

4. Create Verilog-A compact model in classic circuit software package and hard-code experiment-to-effective parameter functions.

5. Simulate quantum system evolution for QuDiPy-generated ideal control pulses and compare against pulses generated by DACs.

Without the experimental-to-effective parameter mappings, this methodology would require a simulation package like SPICE/ADS to generate experimental control pulses, export them to QuDiPy for processing, and import the system state evolution after simulation. It is advantageous to skip the export/import step with SPICE/ADS and have a

self-contained, compact model. To this end, the effective parameter g-factor is assumed to have an approximately quadratic relationship to electrode voltages [76] of the form,

$$g_m(\vec{\mathcal{V}}(t), A^{(m)}, B^{(m)}) \coloneqq \sum_{i}^{n} \left(\sum_{p=0}^{2} A_{ip}^{(m)} V_i^p(t) \right) + \sum_{j}^{n-1} \left(\sum_{p=0}^{2} B_{ip}^{(m)} W_i^p(t) \right), \tag{3.1}$$

where $A^{(m)}$ and $B^{(m)}$ are matrices containing fit coefficients for the quartic functions mapping plunger, V_i, and tunnel, W_i, gate voltages to the electron g-factor along the growth axis in the $m^{\text{th}} \in [1, \cdots, n]$ QD. Each row in A or B corresponds to the coefficients for a degree-2 polynomial for a specific plunger or tunnel gate. Similarly, exchange energy between adjacent pairs of QDs is assumed to have an exponential or polynomial relationship to gate voltage. It is assumed that exchange changes exponentially for tunnel gate electrodes between the QD pair and has a polynomial relationship for all other electrons, which leads to the functional form,

$$\begin{aligned} J_{m,m+1}(\vec{\mathcal{V}}(t), C^{(m)}, D^{(m)}, \vec{\alpha}^{(m)}) \coloneqq & \sum_{i}^{n} \left(\sum_{p=0}^{5} C_{ip}^{(m)} V_i^p(t) \right) + \sum_{j \neq n}^{n-1} \left(\sum_{p=0}^{5} D_{ip}^{(m)} W_i^p(t) \right) \\ & + \alpha_1^{(m)} \exp\Big\{ \alpha_2^{(m)} W_n(t) \Big\}, \end{aligned} \tag{3.2}$$

where $C^{(m)}$ and $D^{(m)}$ are matrices containing fit coefficients for the degree-5 polynomial functions mapping plunger, V_i, and tunnel, W_i, gate voltages to exchange energy for the $(m, m+1)^{\text{th}}$ pair$\in [1, \cdots, n-1]$ of QDs. The other function parameter, $\vec{\alpha}^{(m)}$, is a vector of fit coefficients for the exponential function mapping exchange to the tunnel gate voltage for the tunnel gate between $(m, m+1)^{\text{th}}$ pair of QDs.

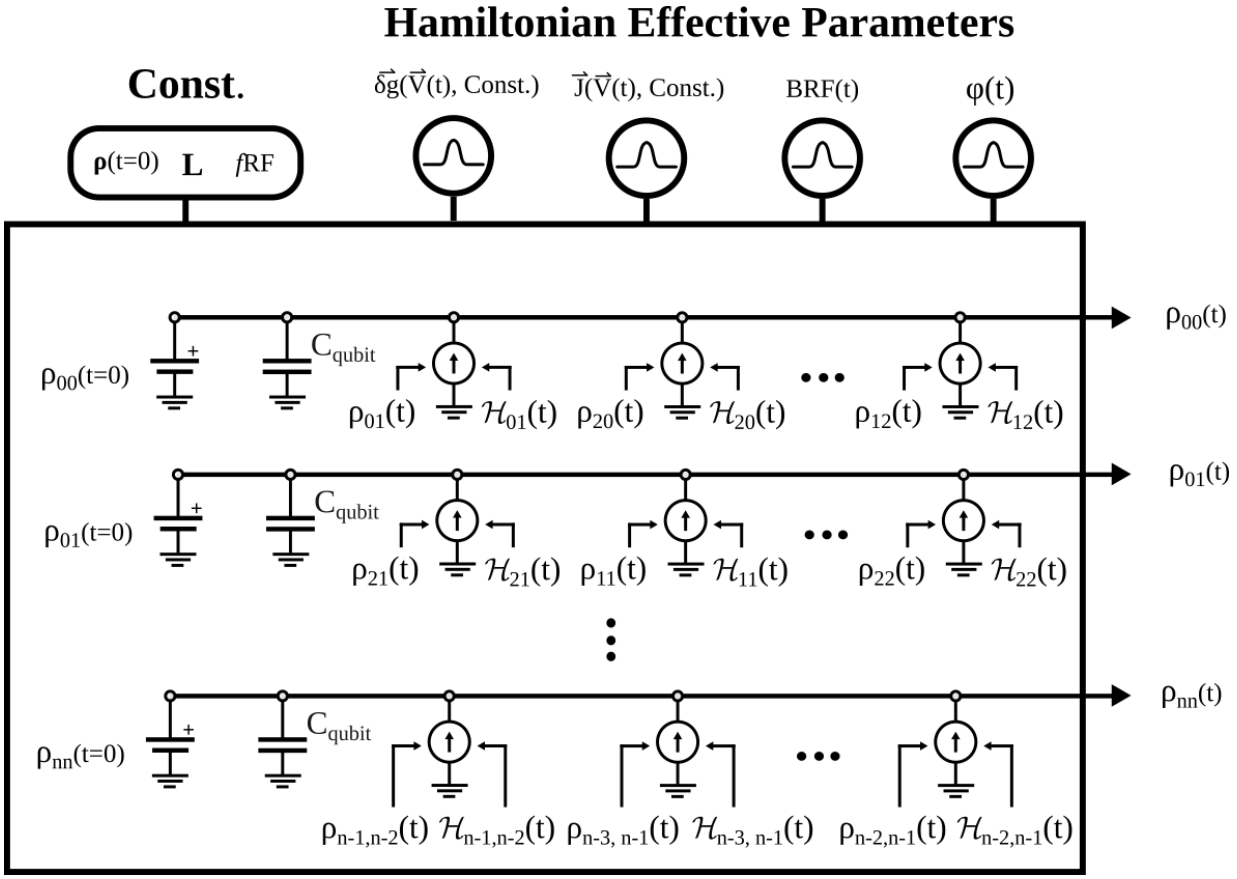


Figure 3.1: An abstract circuit representation of a qubit compact model. The voltage across each capacitor, C_{qubit}, represents the quantum state density matrix elements as the system evolves under experimental control inputs. Voltage-controlled current sources vary the voltage across the capacitors as the density matrix elements and system Hamiltonian evolve under experimental input controls.

The voltage across each capacitor, C_{qubit}, of the circuit in Figure 3.1 solves each coupled ordinary differential equation that represents a density matrix element for the master equation, which describes the evolution of the quantum state. The exact system Hamiltonian used in the master equation dictates which voltage outputs for each row are feedback into other rows to control voltage-controlled current sources connected to each capacitor. The quantum state is initialized by applying a voltage at time $t = 0$ to each capacitor for a desired starting density matrix. After time $t = 0$, the voltage sources used to initialize the charge on each capacitor are disconnected, and the current is allowed to flow under

the influence of the current-controlled voltage sources. Current-controlled voltage sources are governed by the instantaneous voltage across other capacitors and Hamiltonian matrix element inputs as experimental control pulses are applied.

3.2 Single Spin Qubit Compact Model

Let's assume a single qubit state, $|\psi\rangle$, for a system Hamiltonian, H, and density operator, ρ. The operators can be written in matrix form in the following general form,

$$H = \begin{bmatrix} H_{00} & H_{01} \\ H_{10} & H_{11} \end{bmatrix}, \quad \rho = |\psi\rangle \langle\psi| = \begin{bmatrix} \rho_{00} & \rho_{01} \\ \rho_{10} & \rho_{11} \end{bmatrix}, \tag{3.3}$$

Where the single qubit spin Hamiltonian in the rotating frame is,

$$H = \frac{\hbar}{2}\left[\left(1 + \frac{\delta g_1^z(t)}{2}\right)\omega - \omega_{RF}\right] Z_1 + \Omega(t)\left(X_1 \cos(\phi(t)) + Y_1 \sin(\phi(t))\right).$$

3.2.1 System Master Equation

As an illustrative example, we treat a simple closed quantum system, i.e., no decoherence, whose system evolution can be modeled by the Liouville-von Neumann master equation $i\hbar\frac{d\rho}{dt} = [H, \rho]$:

$$i\hbar\frac{d\rho_{00}}{dt} = H_{01}\rho_{10} - \rho_{01}H_{10} \tag{3.4}$$

$$i\hbar\frac{d\rho_{01}}{dt} = H_{00}\rho_{01} + H_{01}\rho_{11} - \rho_{00}H_{01} - \rho_{01}H_{11} \tag{3.5}$$

$$i\hbar\frac{d\rho_{10}}{dt} = H_{10}\rho_{00} + H_{11}\rho_{10} - \rho_{10}H_{00} - \rho_{11}H_{10} \tag{3.6}$$

$$i\hbar\frac{d\rho_{11}}{dt} = H_{10}\rho_{01} - \rho_{10}H_{01} \tag{3.7}$$

Since density matrix and Hamiltonian elements are mapped to voltage inputs in the compact model, the real and imaginary components of the master equation must be solved separately. Defining the real and complex components of the Hamiltonian and density operator as $H_{ij} \coloneqq H_{ij}^R + iH_{ij}^I$ and $\rho_{ij} \coloneqq \rho_{ij}^R + i\rho_{ij}^I$ transforms the above equations:

$$\hbar\frac{d(\rho_{00}^R + i\rho_{00}^I)}{dt} = H_{01}^I\rho_{10}^R - H_{10}^I\rho_{01}^R + H_{01}^R\rho_{10}^I - H_{10}^R\rho_{01}^I$$

$$
\begin{aligned}
&+ i\left(H_{01}^{I}\rho_{10}^{I} - H_{10}^{I}\rho_{01}^{I} - H_{01}^{R}\rho_{10}^{R} + H_{10}^{R}\rho_{01}^{R}\right) \\
\hbar\frac{d(\rho_{01}^{R}+i\rho_{01}^{I})}{dt} &= H_{00}^{I}\rho_{01}^{R} - H_{01}^{I}\rho_{00}^{R} + H_{01}^{I}\rho_{11}^{R} - H_{11}^{I}\rho_{01}^{R} + H_{00}^{R}\rho_{01}^{I} - H_{01}^{R}\rho_{00}^{I} + H_{01}^{R}\rho_{11}^{I} - H_{11}^{R}\rho_{01}^{I} \\
&+ i\left(H_{00}^{I}\rho_{01}^{I} - H_{01}^{I}\rho_{00}^{I} + H_{01}^{I}\rho_{11}^{I} - H_{11}^{I}\rho_{01}^{I} - H_{00}^{R}\rho_{01}^{R} + H_{01}^{R}\rho_{00}^{R} - H_{01}^{R}\rho_{11}^{R} + H_{11}^{R}\rho_{01}^{R}\right) \\
\hbar\frac{d(\rho_{10}^{R}+i\rho_{10}^{I})}{dt} &= -H_{00}^{I}\rho_{10}^{R} + H_{10}^{I}\rho_{00}^{R} - H_{10}^{I}\rho_{11}^{R} + H_{11}^{I}\rho_{10}^{R} - H_{00}^{R}\rho_{10}^{I} + H_{10}^{R}\rho_{00}^{I} - H_{10}^{R}\rho_{11}^{I} + H_{11}^{R}\rho_{10}^{I} \\
&+ i\left(-H_{00}^{I}\rho_{10}^{I} + H_{10}^{I}\rho_{00}^{I} - H_{10}^{I}\rho_{11}^{I} + H_{11}^{I}\rho_{10}^{I} + H_{00}^{R}\rho_{10}^{R} - H_{10}^{R}\rho_{00}^{R} + H_{10}^{R}\rho_{11}^{R} - H_{11}^{R}\rho_{10}^{R}\right) \\
\hbar\frac{d(\rho_{11}^{R}+i\rho_{11}^{I})}{dt} &= -H_{01}^{I}\rho_{10}^{R} + H_{10}^{I}\rho_{01}^{R} - H_{01}^{R}\rho_{10}^{I} + H_{10}^{R}\rho_{01}^{I} \\
&+ i\left(-H_{01}^{I}\rho_{10}^{I} + H_{10}^{I}\rho_{01}^{I} + H_{01}^{R}\rho_{10}^{R} - H_{10}^{R}\rho_{01}^{R}\right)
\end{aligned}
$$

Both operators are Hermitian, i.e., $\rho = \rho^{\dagger}$ and $H = H^{\dagger}$; therefore, each real and imaginary matrix element is related to its transpose by: $\rho_{ij}^{R} = \rho_{ji}^{R}$, $\rho_{ij}^{I} = -\rho_{ji}^{I}$, $H_{ij}^{R} = H_{ji}^{R}$, and $H_{ij}^{I} = -H_{ji}^{I}$. Using the Hermiticity of the operators simplifies the previous master state equations and reduces the total number of equations required when simulating the spin qubit compact model by two; only diagonal and lower or upper triangular matrix elements are required. The reduced set of simplified master state equations then reads:

$$
\begin{aligned}
\hbar\frac{d(\rho_{00}^{R}+i\rho_{00}^{I})}{dt} &= 2(H_{01}^{I}\rho_{01}^{R} - H_{01}^{R}\rho_{01}^{I}) \\
\hbar\frac{d(\rho_{01}^{R}+i\rho_{01}^{I})}{dt} &= \hbar\frac{d(\rho_{10}^{R}-i\rho_{10}^{I})}{dt} \\
&= H_{00}^{I}\rho_{01}^{R} - H_{01}^{I}\rho_{00}^{R} + H_{01}^{I}\rho_{11}^{R} - H_{11}^{I}\rho_{01}^{R} + H_{00}^{R}\rho_{01}^{I} - H_{01}^{R}\rho_{00}^{I} + H_{01}^{R}\rho_{11}^{I} - H_{11}^{R}\rho_{01}^{I} \\
&+ i\left(H_{00}^{I}\rho_{01}^{I} - H_{01}^{I}\rho_{00}^{I} + H_{01}^{I}\rho_{11}^{I} - H_{11}^{I}\rho_{01}^{I} - H_{00}^{R}\rho_{01}^{R} + H_{01}^{R}\rho_{00}^{R} - H_{01}^{R}\rho_{11}^{R} + H_{11}^{R}\rho_{01}^{R}\right) \\
\hbar\frac{d(\rho_{11}^{R}+i\rho_{11}^{I})}{dt} &= -2(H_{01}^{I}\rho_{01}^{R} + H_{01}^{R}\rho_{01}^{I})
\end{aligned}
$$

Note that the equations for $\frac{d(\rho_{01}^{R}+i\rho_{01}^{I})}{dt}$ were omitted since they are determined from the Hermiticity condition. These equations describe the state evolution of a closed quantum system for a single spin qubit. This information is useful; however, we wish to capture decoherence effects from interaction with the environment. For this reason, the Lindblad master equation formalism described in Section 2.2.5, by Equation 2.30, is used in place of the Liouville-von Neumann master equation.

Given the following Hamiltonian for a single spin qubit subject to a global electron spin

resonant magnetic field in the rotating frame and normalized by $\mathscr{H} = \mathrm{H}/\hbar$:

$$\mathscr{H}(\delta g_1(t), \Omega(t), \phi(t), \{\omega, \omega_{RF}\}) = \begin{bmatrix} \frac{\omega\left(\frac{\delta g_1(t)}{2}+1\right)}{2} - \frac{\omega_{RF}}{2} & \frac{(-i\sin(\phi(t))+\cos(\phi(t)))\Omega(t)}{2} \\ \frac{(i\sin(\phi(t))+\cos(\phi(t)))\Omega(t)}{2} & -\frac{\omega\left(\frac{\delta g_1(t)}{2}+1\right)}{2} + \frac{\omega_{RF}}{2} \end{bmatrix} \tag{3.8}$$

Where $\omega(t) = \frac{2\mu_B B_0}{\hbar}$ is the Larmor frequency and $\Omega(t) = \frac{2\mu_B B_{RF}(t)}{\hbar}$ is the Rabi frequency. Given the single qubit Hamiltonian from equation 3.2.1, the above Lindblad master equations become:

$$\begin{aligned}
\frac{d\rho_{00}^R}{dt} &= \frac{\left(-\rho_{01}^I \cos(\phi(t)) - \rho_{01}^R \sin(\phi(t))\right)\Omega(t)}{2} \\
&\quad - \frac{\left(\rho_{01}^I \cos(\phi(t)) + \rho_{01}^R \sin(\phi(t))\right)\Omega(t)}{2} - \frac{\rho_{00}^R a_1}{T_1} + \frac{\rho_{11}^R p_1}{T_1} \\
\frac{d\rho_{00}^I}{dt} &= -\frac{\rho_{00}^I a_1}{T_1} + \frac{\rho_{11}^I p_1}{T_1} \\
\frac{d\rho_{01}^R}{dt} &= 2\rho_{01}^I \left(\frac{\omega\left(\frac{\delta g_1(t)}{2}+1\right)}{2} - \frac{\omega_{RF}}{2}\right) - \frac{\left(\rho_{00}^I \cos(\phi(t)) - \rho_{00}^R \sin(\phi(t))\right)\Omega(t)}{2} \\
&\quad + \frac{\left(\rho_{11}^I \cos(\phi(t)) - \rho_{11}^R \sin(\phi(t))\right)\Omega(t)}{2} - \frac{\rho_{01}^R}{T_2} - \frac{\rho_{01}^R a_1}{2T_1} - \frac{\rho_{01}^R p_1}{2T_1} \\
\frac{d\rho_{01}^I}{dt} &= -2\rho_{01}^R \left(\frac{\omega\left(\frac{\delta g_1(t)}{2}+1\right)}{2} - \frac{\omega_{RF}}{2}\right) + \frac{\left(\rho_{00}^I \sin(\phi(t)) + \rho_{00}^R \cos(\phi(t))\right)\Omega(t)}{2} \\
&\quad - \frac{\left(\rho_{11}^I \sin(\phi(t)) + \rho_{11}^R \cos(\phi(t))\right)\Omega(t)}{2} - \frac{\rho_{01}^I}{T_2} - \frac{\rho_{01}^I a_1}{2T_1} - \frac{\rho_{01}^I p_1}{2T_1} \\
\frac{d\rho_{11}^R}{dt} &= -\frac{\left(\rho_{01}^I \cos(\phi(t)) + \rho_{01}^R \sin(\phi(t))\right)\Omega(t)}{2} \\
&\quad + \frac{\left(\rho_{01}^I \cos(\phi(t)) + \rho_{01}^R \sin(\phi(t))\right)\Omega(t)}{2} + \frac{\rho_{00}^R a_1}{T_1} - \frac{\rho_{11}^R p_1}{T_1} \\
\frac{d\rho_{11}^I}{dt} &= \frac{\rho_{00}^I a_1}{T_1} - \frac{\rho_{11}^I p_1}{T_1}
\end{aligned}$$

To ensure the validity of the equations derived above, we consider the generalized Bloch

sphere state vector,

$$|\psi\rangle = \cos\left(\frac{\theta}{2}\right)|0\rangle + e^{i\phi}\sin\left(\frac{\theta}{2}\right)|1\rangle,$$

Where $\phi = 0$ and $\theta = \frac{\pi}{2}$ define an initial state vector making a 45° angle with the $|0\rangle$-axis in the $|0\rangle/|+\rangle$-plane.

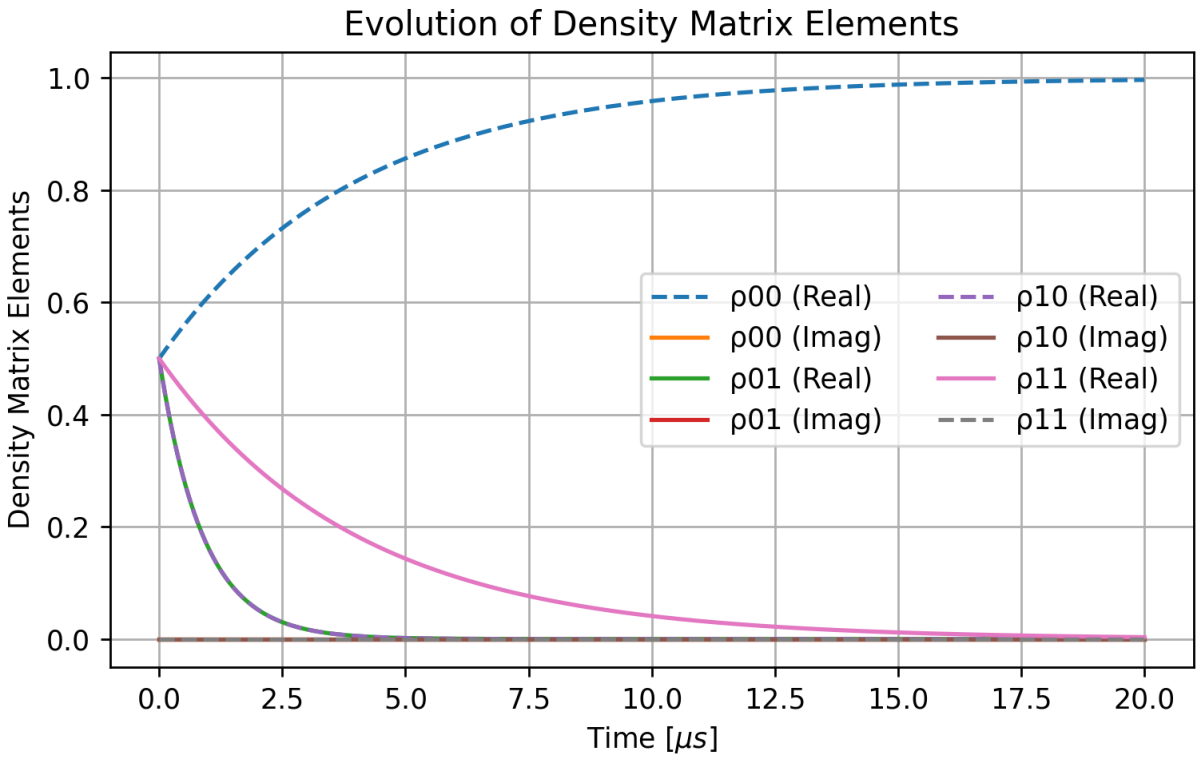


Figure 3.2: Numerical solutions for the Lindblad master equation with an initial state vector defined by $\phi = 0$ and $\theta = \frac{\pi}{2}$. Off-diagonal elements rapidly decay to 0 from dephasing, while the $\mathrm{Re}\{\rho_{00}\}$ converges to 1 from spin relaxation to the external Zeeman field.

Numerically solving the above master equations for the initial state under relaxation time $T_1 = 40\mu s$, dephasing time $T_2 = 10\mu s$, and over a duration of $20\mu s$, yields the density matrix element evolution shown in Figure 3.2. As expected, the off-diagonal density matrix elements quickly decay to 0 from the dephasing while the on-diagonal elements slowly relax to either 1 or 0, exhibiting spin alignment with the external Zeeman field. The resultant

evolution of the voltage across each capacitor when simulated in the compact model is in good agreement with the numerically obtained results after normalizing the voltage outputs of the model to map to the true density matrix values.

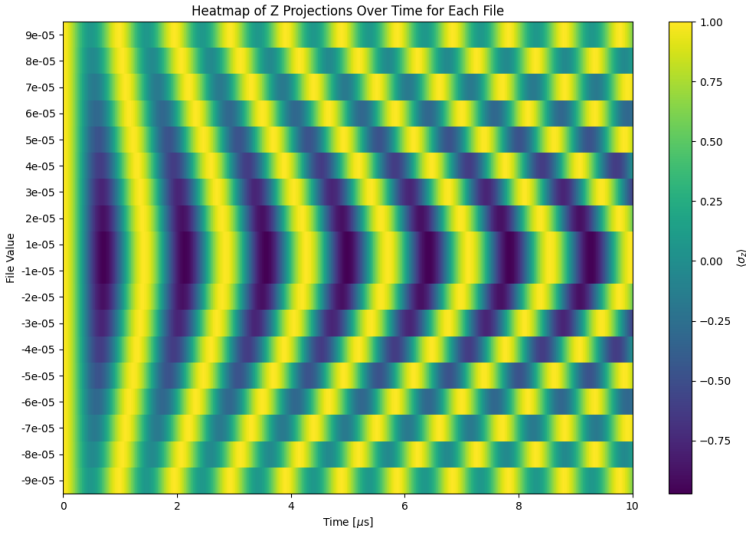


Figure 3.3: Simulated Rabi oscillations as a function of qubit g-factor detuning generated by a single qubit compact model.

After defining the compact model circuit in the ADS circuit solver using Verilog-A, the Lindblad master equation is solved for a qubit in the initial state $|\uparrow\rangle$ with spin relaxation and dephasing "turned off", i.e., $T_1 = T_2 = \infty$. A series of simulations were performed for various g-factor detunings to observe Rabi oscillation decrease as the detuning is increased; generating a prototypical chevron pattern. Figure 3.3 shows the resultant Rabi oscillation frequency as a function of experimentally realized g-factor detuning for a silicon single QD device; visual artifacts on the right of the figure are caused by a finite number of compact model simulations.

3.2.2 Mapping Voltage to δg

After confirming the validity of the derived master equation in section 3.2.1, a quadratic fit must be found that maps input plunger gate voltage to g-factor deviation, δg, to allow for

a self-contained single qubit compact. A fit with an $R^2 = 0.9996$ is trivially obtained and is displayed in Figure 3.4. For this simple example, equation 3.1 simplifies to $\delta g_1(V_1, A^{(1)}) = A_{11}^{(1)} V^2(t) + A_{12}^{(1)} V(t) + A_{13}^{(1)}$ where $A_1 = [3.396 \cdot 10^{-4}, 3.787 \cdot 10^{-5}, -1.453 \cdot 10^{-06}]$.

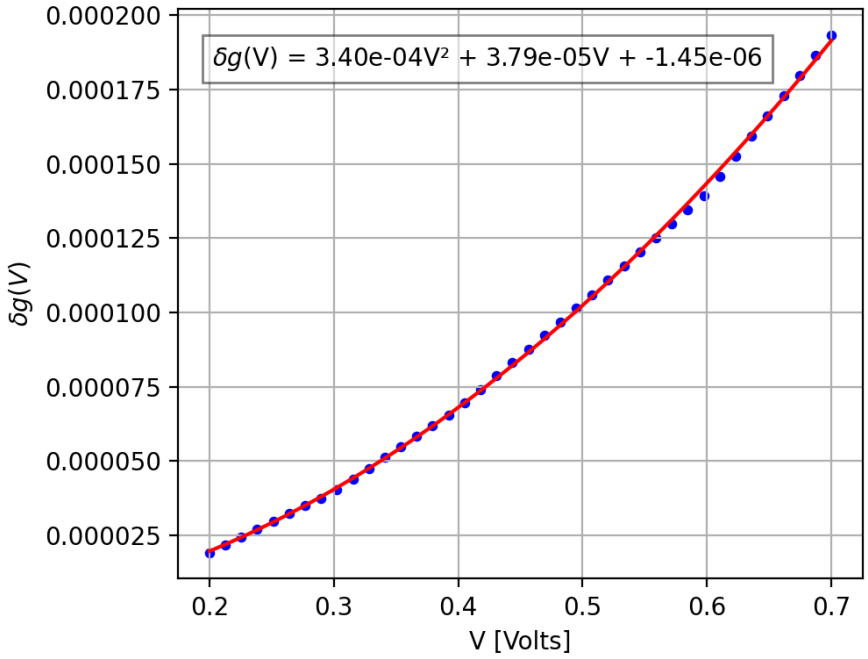


Figure 3.4: Quadratic fit for δg-factor as a function of plunger gate voltage with an $R^2 = 0.9996$.

Given the analytic functional map of plunger gate voltage, V_1, to g-factor deviation, δg_1, enables the function to be hard-coded in a self-contained single qubit compact model. For example, it may be desired to implement a single qubit gate which requires specific ESR field and voltage control pulses, which must be generated by DACs and other control electronics. To determine the exact design criteria to limit impacts on gate fidelity, a set of control pulses should be benchmarked on the compact model. To illustrate this procedure, a set of control pulses was generated by QuDiPy for a $X_1\left(\frac{\pi}{2}\right)|\uparrow\rangle = |i\rangle$ gate operation and imported to the compact model. The resultant state evolution of the single qubit system is shown in Figure 3.5, where Bloch sphere projections are plotted along the principle axes to observe the $|\uparrow\rangle$ state evolve to the expected $|i\rangle$ after the application of ESR field and voltage pulses. The control pulse QuDiPy determines to produce perfect infidelity

of $\sim 10^{-12}$ is reduced to $\sim 10^{-7}$ after simulation in the compact model. The increase in infidelity is attributed to the time step size in the ADS circuit solver and can be improved to limit the increase in infidelity at the expense of computational cost.

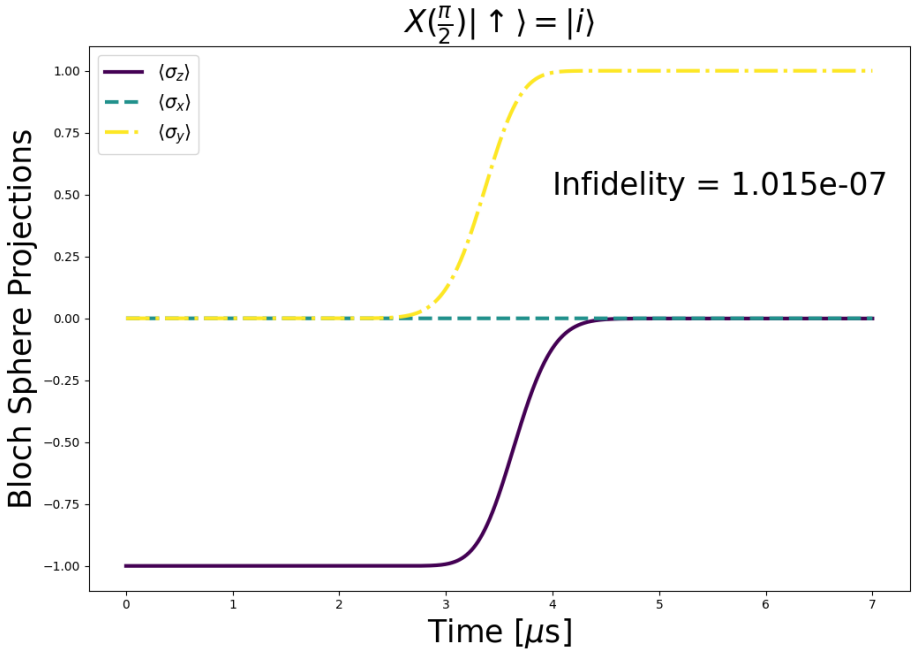


Figure 3.5: Simulated state evolution of a qubit under ESR field and voltage pulses to realize a $\mathrm{X}\left(\frac{\pi}{2}\right)$. ESR and voltage pulses were determined by QuDiPy's optimal control module.

3.3 Two Spin Qubit Compact Model

Considering a two-qubit system becomes noticeably more interesting to simulate, as there are now two plunger gates for each qubit, each isolated in its respective quantum dot potential well, as well as one barrier gate used to control the tunnel coupling or mitigate capacitive cross-talk between neighboring qubits. The two-qubit Hamiltonian is defined similarly to before but now includes additional operators:

$$H = \sum_{i=1}^{2} \left\{ \frac{\hbar}{2} \left[\left(1 + \frac{\delta g_i^z(t)}{2} \right) \omega - \omega_{RF} \right] Z_i + \Omega(t) \left(X_i \cos(\phi(t)) + Y_i \sin(\phi(t)) \right) \right\}$$

$$+\frac{J_{12}(t)}{4}\left[X_1\otimes X_2+Y_1\otimes Y_2+Z_1\otimes Z_2\right] \tag{3.9}$$

Where each Pauli operator, $\sigma_n \in \{X, Y, Z\}$ for $n \in \{1, 2, 3\}$, is defined as

$$\sigma_{n,j} = \left(\bigotimes_{i=1}^{j-1} I_i\right) \otimes \sigma_n \otimes \left(\bigotimes_{i=j+1}^{N} I_i\right), \tag{3.10}$$

and there are additional operators related to the exchange energy between qubits in the two QDs, i.e., $\sigma_n \otimes \sigma_n$. All two-qubit operators are displayed in Table 3.1 below. The

$X_1 \otimes I$	$I \otimes X_2$	$X_1 \otimes X_2$
$\begin{bmatrix} 0 & 1 & 0 & 0 \\ 1 & 0 & 0 & 0 \\ 0 & 0 & 0 & 1 \\ 0 & 0 & 1 & 0 \end{bmatrix}$	$\begin{bmatrix} 0 & 0 & 1 & 0 \\ 0 & 0 & 0 & 1 \\ 1 & 0 & 0 & 0 \\ 0 & 1 & 0 & 0 \end{bmatrix}$	$\begin{bmatrix} 0 & 0 & 0 & 1 \\ 0 & 0 & 1 & 0 \\ 0 & 1 & 0 & 0 \\ 1 & 0 & 0 & 0 \end{bmatrix}$
$Y_1 \otimes I$	$I \otimes Y_2$	$Y_1 \otimes Y_2$
$\begin{bmatrix} 0 & -i & 0 & 0 \\ i & 0 & 0 & 0 \\ 0 & 0 & 0 & -i \\ 0 & 0 & i & 0 \end{bmatrix}$	$\begin{bmatrix} 0 & 0 & -i & 0 \\ 0 & 0 & 0 & -i \\ i & 0 & 0 & 0 \\ 0 & i & 0 & 0 \end{bmatrix}$	$\begin{bmatrix} 0 & 0 & 0 & -1 \\ 0 & 0 & 1 & 0 \\ 0 & 1 & 0 & 0 \\ -1 & 0 & 0 & 0 \end{bmatrix}$
$Z_1 \otimes I$	$I \otimes Z_2$	$Z_1 \otimes Z_2$
$\begin{bmatrix} 1 & 0 & 0 & 0 \\ 0 & 1 & 0 & 0 \\ 0 & 0 & -1 & 0 \\ 0 & 0 & 0 & -1 \end{bmatrix}$	$\begin{bmatrix} 1 & 0 & 0 & 0 \\ 0 & -1 & 0 & 0 \\ 0 & 0 & 1 & 0 \\ 0 & 0 & 0 & -1 \end{bmatrix}$	$\begin{bmatrix} 1 & 0 & 0 & 0 \\ 0 & -1 & 0 & 0 \\ 0 & 0 & -1 & 0 \\ 0 & 0 & 0 & 1 \end{bmatrix}$

Table 3.1: Two-qubit Pauli operator matrices.

total number of master equations that must be added to the compact model, in general, is 2^{2N+1} but is reduced to $2^{2N} + 2N$ when the Hermiticity of ρ and H is taken into account.

Therefore, in the two-qubit case, the $2^5 = 32$ master equations can be fully simulated with a subset of $2^4 + 4 = 20$. The fully derived master equations for the two-qubit Hamiltonian, using equation 3.9, are given in Appendix A.1.

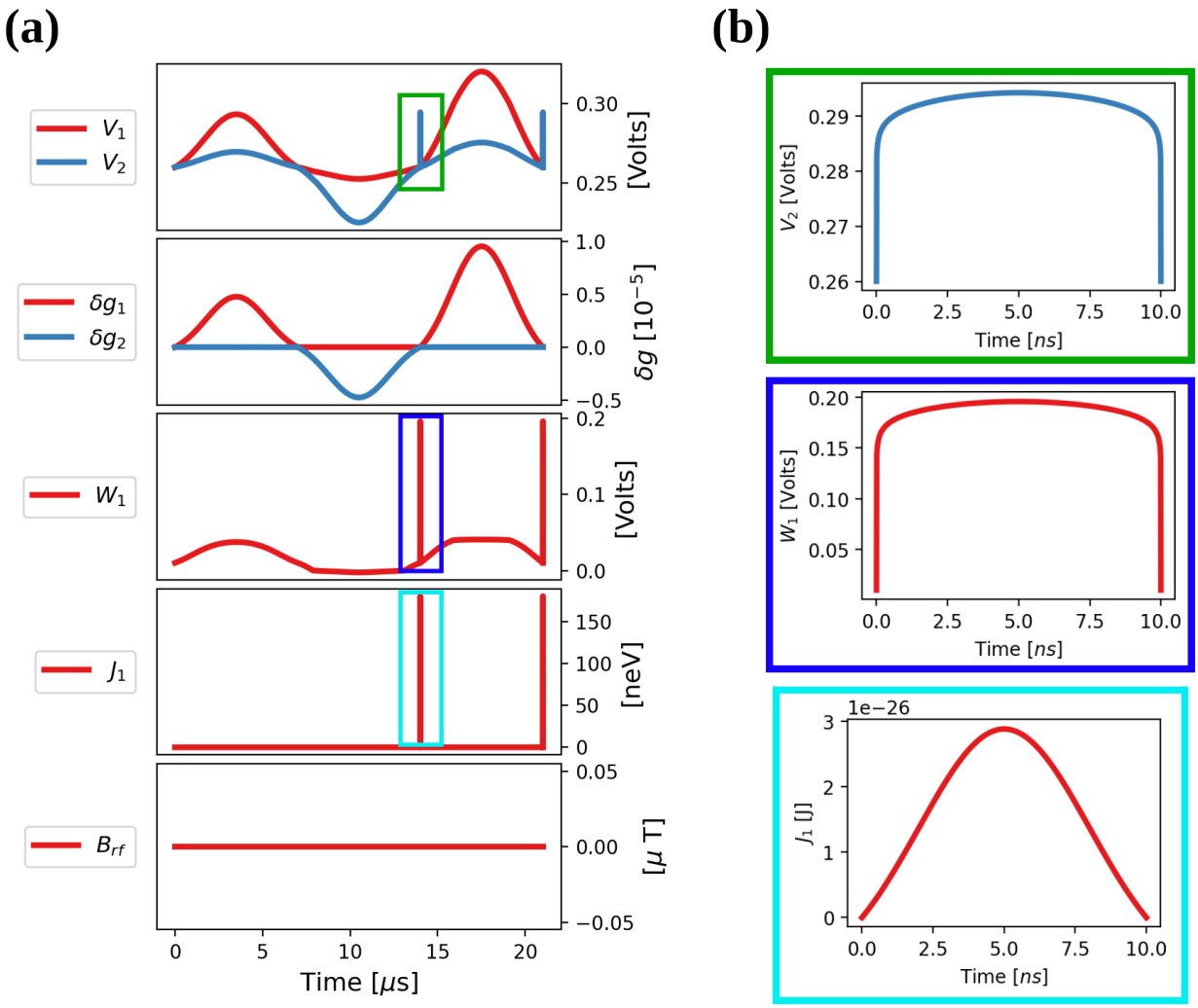


Figure 3.6: (a) Experimental control pulses to realize a CZ gate from a sequence of single and two-qubit gate operations generated by QuDiPy. (b) Zoomed-in figures showing experimental input pulses for a $\sqrt{SWAP}$ gate.

Previously in Sections 2.5.1-2.5.3, a node network architecture was proposed for a scalable fault-tolerant quantum computing application. To realize the surface code error cor-

rection protocol, a sequence of single- and two-qubit gates must be implemented experimentally with DACs and other control electronics. The twenty master equations required to simulate the two-qubit system were hard-coded into a Verilog-A compact model and simulated in ADS for various qubit gate operations by using the Hamiltonian effective parameter pulses as inputs. This is the first step for testing the validity of the compact model prior to finding a voltage-to-effective parameter functional mapping. As shown in Figure 3.6, QuDiPy is leveraged to generate a series of control voltage and effective parameter pulses, simulating both singe-/two-qubit gates, to realize a control-Z, CZ, gate operation.

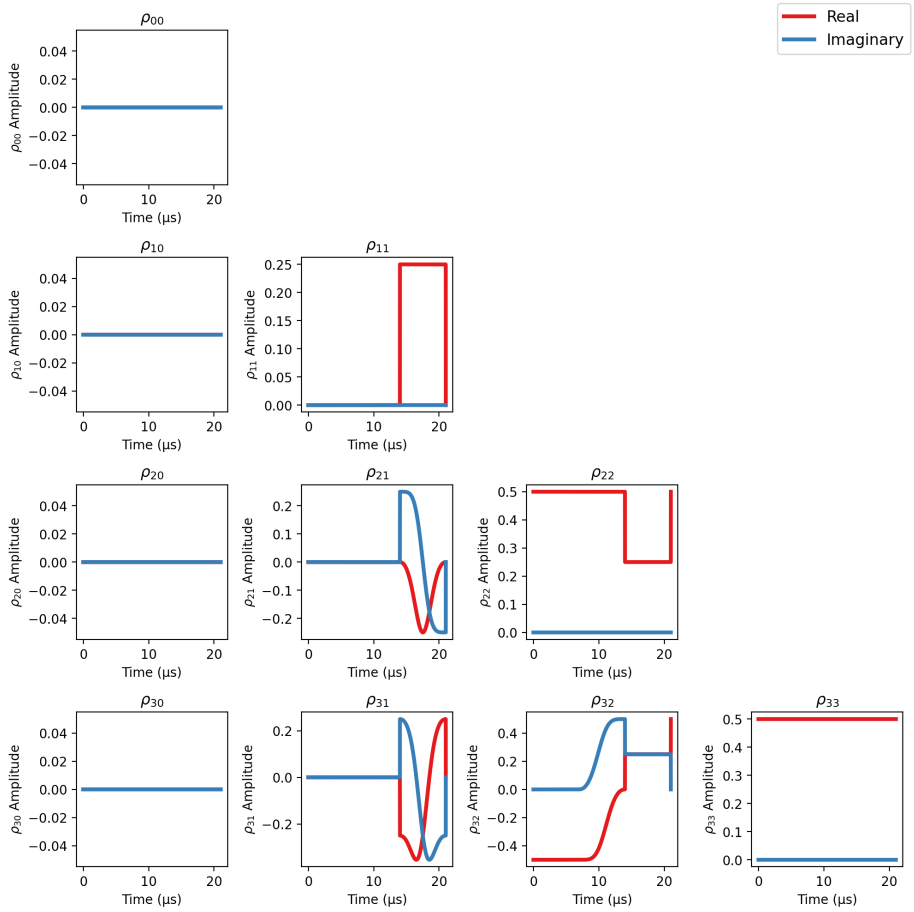


Figure 3.7: simulated Density matrix element evolution under ESR field and voltage pulses generated by QuDiPy and consistent with the two-qubit compact model results.

As shown in Figure 3.7, the twenty density matrix elements for the diagonal and lower

triangular density matrix elements evolve properly for a two-qubit CZ gate and initial state $CZ_{12}\,|\downarrow -\rangle = |\downarrow +\rangle$. The results generated by QuDiPy are consistent with the two-qubit compact model; however, a time step of dt $\approx$ ps is required for the compact model numerical integration routine. This leads in the simulation of the circuit taking a few hours to produce the state evolution results, which is less than desired but can be mitigated by simulating individual single- and two-qubit gates as separate smaller compact model circuit elements and defining a unique time step size for each circuit element; larger time steps can be set for single qubit gate operations since their pulse duration is limited for a few μs.

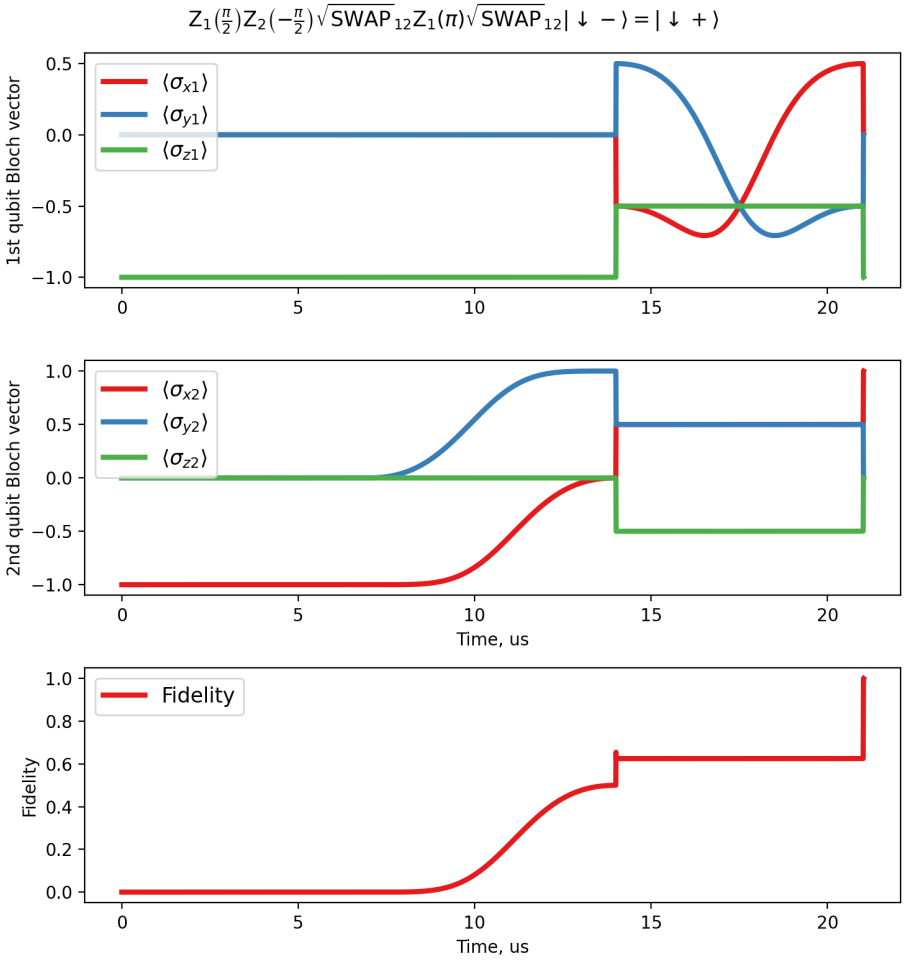
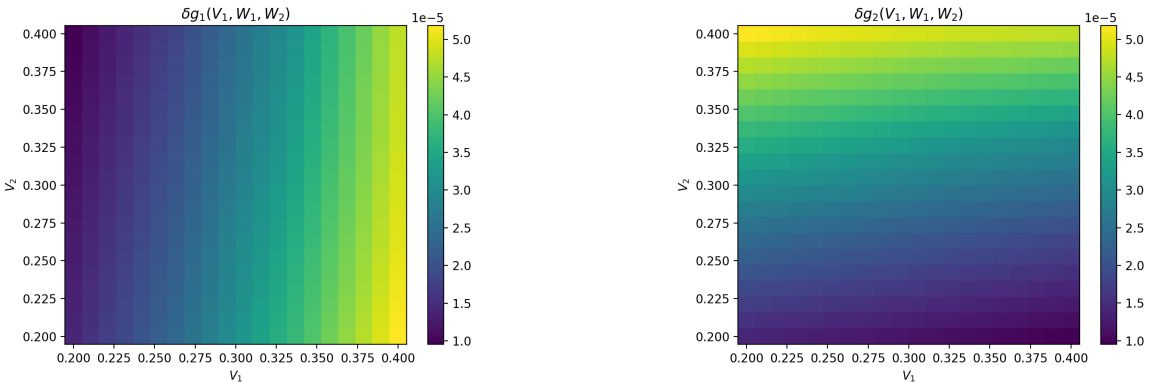


Figure 3.8: Bloch sphere projections of a two-qubit CZ gate operation consistent with the two-qubit compact model.

Figure 3.8 shows the single-qubit Bloch sphere projections constructed from the two-qubit density matrix elements after a series of single- and two-qubit gates are applied to realize a CZ_{12} gate, along with the fidelity after subsequent gate operations. As in Figure 3.6, the apparent discontinuities near 14μs and 21μs in Figure 3.8 are nanosecond time-scale $\sqrt{SWAP}$ gate operations.

3.3.1 Mapping Voltage to δg and Exchange

Finding an analytic function mapping of plunger gate voltage to g-factor for the single qubit case in section 3.2.2 is quite straightforward. However, the problem of analytic function fitting becomes significantly more challenging as the effective parameters become multi-variable functions of plunger and tunnel gate voltage, i.e., $\delta g_m(\vec{\mathcal{V}}(t))$ and $J_{m,m+1}(\vec{\mathcal{V}}(t))$.



(a) $\delta g_1(V_1, V_2)$ (b) $\delta g_2(V_1, V_2)$

Figure 3.9: QuDiPy interpolated function for δg_n plotted as a function of the two plunger gates with $W_1 = -0.1V$.

Figures 3.9a-3.9b show example 2D cross-sections of δg for a fixed tunnel gate voltage of $W_1 = -0.1V$ generated from QuDiPy calculations. To determine analytic functional maps of voltage-to-effective parameters for a two-qubit system, the following analytic functions must be fit to the multi-variant effective parameter data,

$$g_m(\vec{\mathcal{V}}(t), A^{(m)}, B^{(m)}) = \sum_{p=0}^{2} A_{1p}^{(m)} V_i^p(t) + \sum_{p=0}^{2} A_{2p}^{(m)} V_i^p(t) + \sum_{p=0}^{2} B_{ip}^{(m)} w_i^p(t), \tag{3.11}$$

$$J_{12}(\vec{\mathcal{V}}(t), C^{(m)}, \vec{\alpha}^{(m)}) = \sum_{p=0}^{5} C_{1p}^{(m)} V_i^p(t) + \sum_{p=0}^{5} C_{2p}^{(m)} V_i^p(t) + \alpha_1^{(m)} \exp\Big\{\alpha_2^{(m)} W_1(t)\Big\}. \tag{3.12}$$

The coefficient matrices and vector in Equations 3.3.1 and 3.3.1 can be estimated through various optimization techniques, but for the initial investigation, nonlinear regression from Python's SciPy optimization package is used.

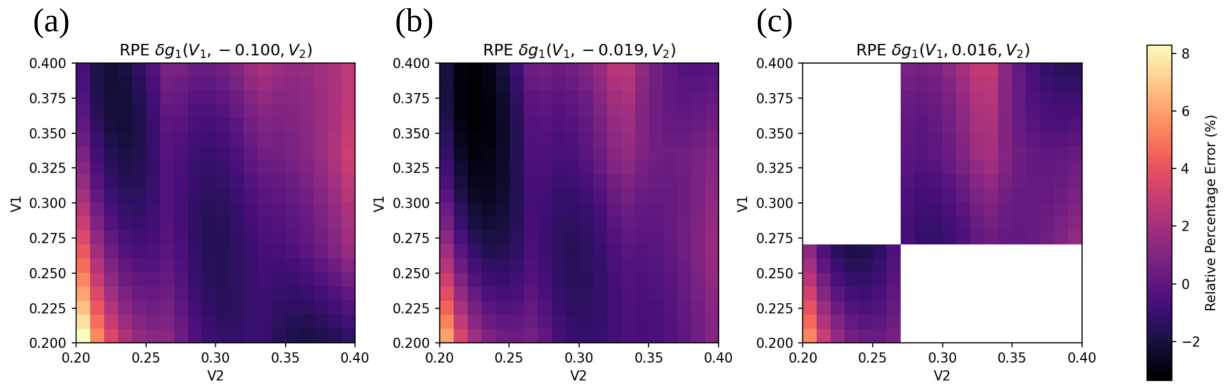


Figure 3.10: Percent relative error for the δg_1 and the fitted analytic function for various W_1 cross-sections (a) $W_1 = -0.1V$ (b) $W_1 = -0.019V$ (c) $W_1 = 0.016V$. The missing data points in (c) are from NaNs in the δg interpolation, caused intentionally after a dot merging event occurs.

After determining the fit coefficients the percent relative error (PRE) is calculated using,

$$PRE(f, \vec{\mathcal{V}}) = 100\% \times \frac{f^{(fit)}(\vec{\mathcal{V}}) - f^{(QuDiPy)}(\vec{\mathcal{V}})}{f^{(QuDiPy)}(\vec{\mathcal{V}})}$$

To determine whether the fitting procedure and functional form agree with the effective parameter interpolation function produced by QuDiPy, Figure 3.10 shows examples of several 2D cross-sections of PRE calculations for δg_1 at various tunnel gate voltages. The analytic functions generally exhibit a few percent error compared to the expected effective parameter interpolation function, which is not suitable for use in the two-qubit compact model. Small errors in exchange would lead to artificially large errors in the compact model results due to the exponential/polynomial behavior of exchange versus voltage, and even moderate errors in the g-factor would lead to artificial off-resonance rotations. For this reason, an alternative approach is leveraged.

Attempting to fit the analytic effective parameter functions from Equations 3.3.1-3.3.1 over the full domain of voltage inputs proves inadequate for application to the compact model. A fit over the full domain of voltage inputs would enable a single general compact model that would have the ability to simulate any desired single- or two-qubit unitary operations, regardless of the desired gate voltage pulses.

Gate	Initial State	Final State	Model	Optimized Parameters	Infidelity	
					Theory	**Fit**
$\sqrt{\text{SWAP}}$	$\|\uparrow\downarrow\rangle$	$\frac{1+i}{2}\|\uparrow\downarrow\rangle + \frac{1-i}{2}\|\downarrow\uparrow\rangle$	$J_{12} = \exp(v_1 a_1 + a_2 w + v_2 a_3 + a_4)$ $g_1 =$ Simulated ≈ 0 $g_2 =$ Simulated ≈ 0	$a_1 = -203.64 \quad a_3 = -436.89$ $a_2 = 236.62 \quad a_4 = 82.35$	1.253×10^{-8}	8.506×10^{-4}
$Y_2(\pm\frac{\pi}{2})$	$\|\uparrow\uparrow\rangle$	$\|\uparrow \pm\rangle$	$g_1 = a_1 v_1^2 + a_2 w^2 + a_3 v_2^2 + a_4 v_1 w + a_5 v_1 v_2 + a_6 w v_2 + a_7 v_1 + a_8 w + a_9 v_2 + a_{10}$ $g_2 =$ Simulated ≈ 0 $J_{12} =$ Simulated ≈ 0	$a_1 = 1.0116\times10^{-4} \quad a_6 = -1.1019\times10^{-5}$ $a_2 = -2.3135\times10^{-6} \quad a_7 = 1.1972\times10^{-4}$ $a_3 = 5.7297\times10^{-6} \quad a_8 = -4.0347\times10^{-5}$ $a_4 = -1.1271\times10^{-5} \quad a_9 = 6.6604\times10^{-6}$ $a_5 = 4.0049\times10^{-5} \quad a_{10} = -2.1653\times10^{-5}$	8.822×10^{-12}	3.826×10^{-4}
$Z_1(\frac{\pi}{2})$	$\|+\uparrow\rangle$	$\|i\uparrow\rangle$	$g_1 = a_1 v_1^2 + a_2 w^2 + a_3 v_2^2 + a_4 v_1 w + a_5 v_1 v_2 + a_6 w v_2 + a_7 v_1 + a_8 w + a_9 v_2 + a_{10}$ $g_2 =$ Simulated ≈ 0 $J_{12} =$ Simulated ≈ 0	$a_1 = 4.6047\times10^{-5} \quad a_6 = 9.3208\times10^{-6}$ $a_2 = 1.8456\times10^{-6} \quad a_7 = 7.6951\times10^{-5}$ $a_3 = 9.9127\times10^{-6} \quad a_8 = 3.2566\times10^{-5}$ $a_4 = 1.1870\times10^{-5} \quad a_9 = 1.7147\times10^{-5}$ $a_5 = 2.6485\times10^{-5} \quad a_{10} = -9.5753\times10^{-6}$	5.007×10^{-14}	1.234×10^{-3}
$Z_2(-\frac{\pi}{2})$	$\|\uparrow+\rangle$	$\|\uparrow -i\rangle$	$g_2 = a_1 v_1^2 + a_2 v_1 + a_4 w + a_5 v_2^2 + a_6 v_2 + a_7$ $g_1 =$ Simulated ≈ 0 $J_{12} =$ Simulated ≈ 0	$a_1 = 8.2771\times10^{-7} \quad a_4 = -7.7241\times10^{-7}$ $a_2 = 4.1076\times10^{-6} \quad a_5 = 4.6797\times10^{-7}$ $a_3 = -1.3012\times10^{-6} \quad a_6 = 1.9562\times10^{-5}$	1.772×10^{-8}	3.193×10^{-6}
$Z_1(\pi)$	$\|+\uparrow\rangle$	$\|-\uparrow\rangle$	$g_1 = a_1 v_1^2 + a_2 w^2 + a_3 v_2^2 + a_4 v_1 w + a_5 v_1 v_2 + a_6 w v_2 + a_7 v_1 + a_8 w + a_9 v_2 + a_{10}$ $g_2 =$ Simulated ≈ 0 $J_{12} =$ Simulated ≈ 0	$a_1 = 6.9755\times10^{-5} \quad a_6 = 2.1591\times10^{-6}$ $a_2 = 3.2327\times10^{-7} \quad a_7 = 1.0312\times10^{-4}$ $a_3 = 1.0645\times10^{-5} \quad a_8 = 5.1035\times10^{-6}$ $a_4 = 5.4619\times10^{-6} \quad a_9 = 1.6738\times10^{-5}$ $a_5 = 3.5645\times10^{-5} \quad a_{10} = -1.8366\times10^{-5}$	1.790×10^{-12}	4.535×10^{-5}

Table 3.2: Summary of gate operations, input/output test states, analytic fit models with simulated g_1, g_2, and J_{12} behavior, optimized parameters determined by Nelder-Mead optimization using L^2 regularization with a scale factor of $10^{-3} - 10^{-6}$, and infidelity values. Note that the initial cost function uses mean square error (MSE) to compare theoretical gate pulses as a function of voltage to the proposed analytic models, then the L^2 norm of the fit coefficients is added to help reduce infidelities.

Rather than fitting the function to the full domain of possible input voltages, a set of specific unitary gate operations is instead generated, in QuDiPy, to form a universal set of quantum gates for QC. Each generated gate object contains information about the effective parameter pulses over time that realize the respective unitary. A Nelder-Mead optimization routine is then employed to find the fit coefficient matrices and vector for the effective parameter pulses for each unitary in the set. Restricting the voltage domain for each unitary effective parameter fitting enables single- and two-qubit unitary gate infidelities ranging from $\sim 10^{-3}$ to $\sim 10^{-6}$. The resultant effective parameter analytic models, respective optimized fit parameters, and theoretical versus fitted voltage pulse gate infidelities are presented in Table 3.2. The above set of gates was selected to construct a CNOT gate in the compact model simulations to test DAC voltage pulses. Since each gate from the set only has one non-zero effective parameter varying in time, we only perform a single analytic model fit for the non-zero effective parameter and use the theoretically exact effective parameter pulses for nearly zero effective parameters. Performing the model fits enables the compact model to be self-contained in the classical circuit solver, with no additional need to calculate the spin dynamics under voltage pulses in QuDiPy.

3.4 Conclusions

In summary, a methodology has been developed for constructing spin-qubit compact models in single- and two-qubit systems that generalizes to large qubit systems. The method enables self-contained quantum system simulations within classical circuit solver packages to support control electronics design. Using QuDiPy simulations of effective parameter relationships $\delta g_m(\vec{\mathcal{V}})$ and $J_{m,m+1}(\vec{\mathcal{V}})$ as a function of input gate voltages, $\vec{\mathcal{V}}$, we can construct analytic functions which can be hard-coded into Verilog-A to create a self-contained compact model. We overcome the limitation of reduced accuracy in analytic function fitting to the full domain of input voltages by restricting the domain for desired single- and two-qubit unitary operations and constructing separate gate compact model modules. This creates more work by constructing multiple compact models, but with the trade-off of reduced simulation time for faster design prototyping. Future work includes exploring alternative analytic function anzatzs to accurately fit to the effective parameter functions over the full voltage domain, as well as investigating noise impacts for various DAC specifications.

Chapter 4

Metal-Semiconductor-Metal InGaAs Photodetector Enhancement

4.1 Introduction

Light detection in the NIR and IR wavelength ranges has numerous applications in fields such as biomedical imaging and sensing, thermal imaging, and telecommunications [40,148–152]. Initially, mesoscopic-scale inorganic semiconducting materials were the primary candidates for developing faster, smaller, and more sensitive detectors. However, recent efforts have shifted towards engineering inorganic, organic, and hybrid inorganic/organic semiconducting nanostructures to significantly enhance performance, reduce device size, and create flexible form factor devices for industrial applications [42,152,153]. Promising approaches include designing III-V semiconductor nanowires, in situ-grown metal/semiconductor nanoparticles, and utilizing chemical vapor deposition or exfoliation techniques to produce 2D inorganic graphene/perovskite structures for optoelectronic devices [153–155].

During the past few decades, interest in the physics and applications of IR photodetectors with a tunable band gap for telecommunication wavelengths ($\sim 1.2 - 1.7$ μm) has grown, especially those based on III-V semiconductors such as InGaAs [156, 157]. Several InGaAs photodetector designs are commonly studied, such as PN or PIN junctions, avalanche, and MSM photodetectors [157]. MSM detectors are desirable for telecommunication applications due to their fast response times and ease of fabrication and integration with other electronics [158–163].

A standard MSM photodetector consists of interdigitated metallic electrodes deposited on an active layer, such as InGaAs, forming two Schottky junctions in series. A finger

electrode design is often chosen for simplicity of the device, both in terms of fabrication and characterization. MSM detectors can suffer from large dark currents due to relatively low Schottky barriers, however, this can be mitigated by introducing a lattice-matched InAlAs top layer to increase the barrier height. Performance improvements have been achieved through band gap tuning via $In_xGa_{1-x}As$ alloy concentration, Schottky barrier enhancement, and superlattice structures [157, 161, 164]. In this paper, we explore the use of plasmonic semiconductor nanocrystals to enhance the optical-to-electrical conversion efficiency of InGaAs MSM photodetectors, as measured by responsivity in the wavelength range of $1 - 1.7$ μm.

Plasmonics primarily focuses on the generation, propagation, and detection of plasmonic waves, which are collective electronic excitations resulting from the interaction between an electromagnetic (EM) field and a metal/dielectric interface [165–167]. When EM waves interact with a metallic surface, a coherent charge density oscillation coupled to the EM field arises, known as a surface plasmon. Strong nanoscale confinement leads to LSPR, characterized by discrete optical absorption bands and electric fields orders of magnitude larger than those associated with free space EM waves. Given their nanoscale dimensions, integration of plasmonic nanostructures with micro- and nanoelectronic devices is possible, and holds the potential to enhance device performance or realize novel functionalities.

Conductors with sub-wavelength dimensions support LSPRs, whose resonance frequencies depend on the geometry and free carrier density of the nanostructure, as well as its orientation with respect to the polarization of the EM field. Depending on the material, LSPRs can span from the ultraviolet (UV) to the far-infrared. Upon illumination, nanoscale regions of strong EM field enhancement, referred to as hot-spots, are generated at the surface of the structure. Plasmonics have been widely used to enhance the performance of photodetector and photovoltaic devices [168–174]. The enhanced EM field surrounding nanostructures can be harnessed in optoelectronic devices by generating LSPRs to improve responsivity across a broad range of frequencies. LSPR mechanisms that contribute to enhanced responsivity include: 1) increased concentration of the incident EM field and extended optical path length within the semiconductor, thereby enhancing photon absorption, and 2) plasmonic energy transfer from the nanostructure to the semiconductor through direct electron transfer [175]. Because of these broadband optical properties, plasmonic nanostructures have found use in a variety of applications including catalysis, medicine, surface chemistry, solar cells, and sensing [165–167, 176–182].

Typically, Au and Ag nanoparticles (NPs) exhibit strong LSPRs and are used as plasmonic materials in the visible [183] or UV [184–186] spectral ranges. An emerging area of interest focuses on identifying high-performance plasmonic materials compatible with other frequency ranges of interest, from NIR to terahertz [187–190]. Fundamentally, the

physics of LSPR does not change in the IR compared to the visible region, but the material requirements are dramatically different. The optical resonances in Au and Ag can be tuned to a degree by changing the size and shape of nanostructures, but the charge carrier densities ($\sim 10^{22}$ cm^{-3}) that primarily determine the plasmonic frequency response are fixed. NIR applications require materials with lower carrier concentrations compared to metals, such as degenerately doped or non-stoichiometric semiconductors [191–194]. There have been several reports on the use of materials such as transition metal oxides [195, 196], nitrides [197], and doped semiconductors [198] for IR plasmonic photodetectors.

Two candidate materials for IR plasmonics are WO_{3-x} [189] and Cs_yWO_{3-x} [190] NCs. Compared to commonly used plasmonic Au/Ag nanostructures exhibiting LSPR in the UV-visible region, both WO_{3-x} and Cs_yWO_{3-x} possess visible-NIR LSPR due to their lower carrier densities, in the range of 10^{18}-10^{22} cm^{-3}. These materials are known to have optical absorption in the NIR, but their effectiveness as plasmonic materials for enhancement of responsivity in a photodetector has not yet been thoroughly investigated; only one recent study has investigated photodetector enhancement in the visible light range using WO_{3-x} nanowire arrays [189]. The carrier densities of these materials can also be tuned via the chemical synthesis procedure (e.g., extrinsic doping). However, a potential challenge when using WO_{3-x} and Cs_yWO_{3-x} NCs, despite being environmentally benign, is their rate of oxidation in air. Oxidation degrades the carrier concentration over time or with exposure to higher temperatures, which may lead to changes in crystal structure by reducing the oxygen vacancy concentration, and thus the carrier density.

In this paper, we characterize the performance of InGaAs MSM photodetectors operating in the NIR modified by drop-cast WO_{3-x} nanorods and Cs_yWO_{3-x} hexagonal prisms. Clear enhancements of responsivity by up to a factor $\sim$2.5, broadly consistent with the plasmonic absorption spectra of the NCs, are observed. These results indicate that suitably prepared conductive metal oxide NCs are a promising family of materials for IR plasmonic applications.

4.2 Materials and Methods

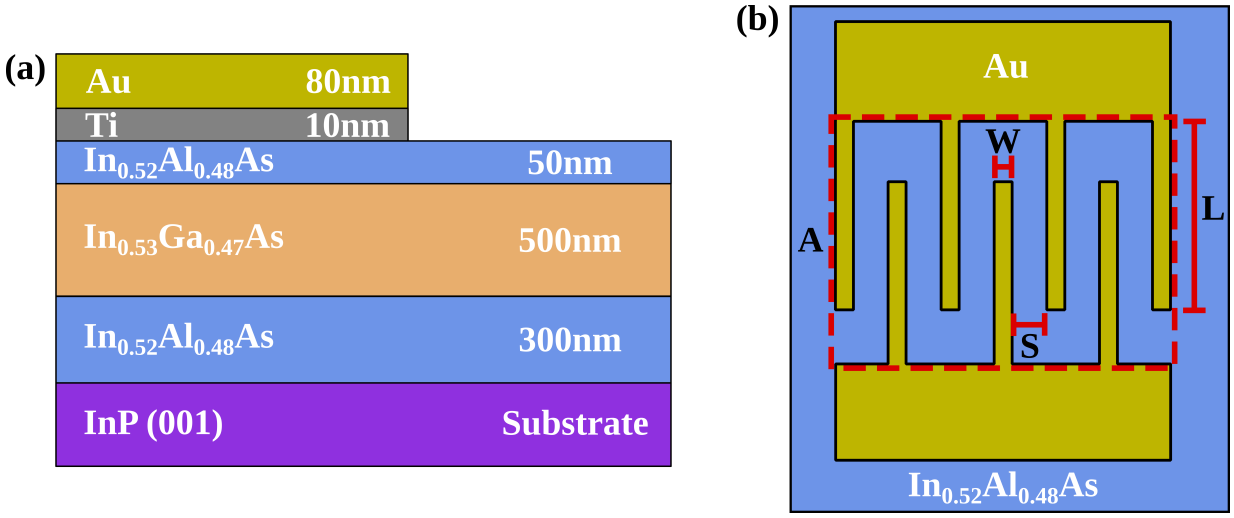


Figure 4.1: Structure of the IR metal-semiconductor-metal (MSM) photodetectors. (a) Semiconductor heterostructure layers grown by molecular beam epitaxy. The $In_{0.53}Ga_{0.47}As$ active region is grown between $In_{0.52}Al_{0.48}As$ barriers on an InP substrate. (b) Top view schematic of the interdigitated metal electrode geometry, where design parameters are electrode width (W $\sim$ 10 μm), spacing (S $\sim$ few μm), length (L $\sim$ 500 μm), and active area (A $\sim$ 500 μm $\times$ 540 μm) indicated by dashed red box.

4.2.1 Molecular Beam Epitaxy of InGaAs Heterostructures

The InGaAs heterostructure shown in Figure 4.1(a) was grown by molecular beam epitaxy (MBE). Prior to growth, a 2", semi-insulating (Fe-doped), double-side polished InP(001) substrate was heated to 520 °C for approximately 10 minutes to desorb surface oxides. Epitaxy of the InAlAs/InGaAs/InAlAs layers was carried out at a substrate temperature of 470 $\pm$10 °C. Both the $In_{0.53}Ga_{0.47}As$ and $In_{0.52}Al_{0.48}As$ layers were grown at a rate of 2.5 Å/s.

4.2.2 Nanocrystal Synthesis

Materials

All chemicals were used as received, with no further purification. $W(CO)_6$ (97 %) and HPLC-grade tetrachloroethylene (TCE) ($\geq$ 99.5 %) were purchased from Thermo Scientific, WCl_4 (95 %), CsCl (95 %) from Kodak, technical-grade oleic acid (OlAc, 90 %) and oleylamine (OlAm, 70 %), HPLC-grade acetone ($\geq$ 99.9 %), toluene ($\geq$ 99.9 %), and hexane ($\geq$ 98.5 %) were all purchased from Sigma Aldrich.

Synthesis of WO_{3-x}

Substoichiometric tungsten oxide (WO_{3-x}) NCs were synthesized following the thermal decomposition synthesis procedure for tungsten NPs reported by Sahoo et al. [199], with minor modifications as previously reported [200]. Briefly, 7.626 g of OlAc, 2.415 g of OlAm, and 1.057 g of $W(CO)_6$ precursor were mixed inside a reaction vessel and degassed for 30 minutes. Using a standard Schlenk line technique, the vessel was purged with nitrogen gas, then the reaction mixture was heated to 300 °C at a rate of 0.5 °C/s. After 2 hours at 300 °C, the vessel was removed from the heating mantle and naturally cooled to room temperature. The blue-color reaction mixture, indicating the presence of WO_{3-x} NCs, was purified three times using toluene and ethanol in a 1:1 volumetric ratio. After each washing cycle, the samples were centrifuged at 3000 RPM for 5 min at room temperature. After final purification, the WO_{3-x} NCs were dispersed in 5 mL of toluene. For the optical extinction measurements, 1 mL of the toluene dispersion was precipitated once again using the above method and redispersed in 1 mL of TCE. All the colloidal dispersions were stored under N_2 atmosphere until further use.

Synthesis of Cs_yWO_{3-x}

Hexagonal Cs_yWO_{3-x} NCs were synthesized using the synthesis method reported by Mattox et al. [201] with minor modifications. The solid precursors (0.20 mmol of WCl_4 and 0.12 mmol of CsCl) were added into a mixture of OlAc (8.95 g) and OlAm (0.267 g), which was then degassed for approximately 20 min at 120 °C. The reaction mixture was then heated to 300 °C and kept at that temperature. After 2 hours, the reaction mixture was cooled down to room temperature, and the dark blue product obtained was pipetted into centrifuge tubes. NCs were washed with toluene and acetone in approximately 1:1 volumetric ratio, applying vortex mixing for 5 minutes, then the sample was centrifuged at 7830

RPM for 5 min to separate the NCs from the supernatant. Similar to the WO_{3-x} NCs, the as-prepared Cs_yWO_{3-x} NCs were suspended in toluene or TCE for optical measurements and stored under N_2 atmosphere until further use.

4.2.3 Photodetector Fabrication

A 2 cm × 2 cm die from the as-grown InGaAs heterostructure wafer was cleaned by sonication in acetone and isopropyl alcohol (IPA) for 2 minutes each. Polydimethylglutarimide polymer (PMGI) and Shipley 1813 positive photoresists were deposited by spin coating at 5000 RPM for 60 seconds to create a homogeneous bilayer approximately 1.3 μm thick. The resist is baked at 120°C for 90 seconds, followed by optical lithography performed using a Heidelberg Instruments MLA150 maskless aligner to pattern the interdigitated electrodes and bond pads. The patterned resist was developed in a metal-free optical developer (MF-319) for 100 seconds, followed by a 20 second plasma ash to remove traces of resist residue from the exposed areas. A 1 minute HF etch was performed to remove surface oxides prior to deposition of 20/80nm of Ti/Au via electron beam evaporation. Metal liftoff was performed by leaving the sample overnight in Remover PG, followed by rinsing in acetone and IPA. A schematic of the interdigitated electrode geometry is shown in Figure 4.1(b).

4.2.4 Characterization of Nanocrystals

X-ray diffractometry (XRD) was performed to study the crystallinity and phase of the synthesized NCs using a Rigaku MiniFlex II Diffractometer equipped with a Cu Kα1 radiation source (λ = 1.54056 Å). Transmission electron microscopy (TEM) measurements were performed to investigate the NC morphology using a JEOL-2010F instrument operating at 200 kV. The optical extinction spectra of the colloidal NC dispersions in TCE or NC thin films were performed to characterize the resonant wavelengths, absorption peak widths, and overall spectral shape using a Varian Cary 5000 UV-vis-NIR spectrophotometer. The synthesis and optical properties of the WO_{3-x} and Cs_yWO_{3-x} NCs in this work were found to be highly reproducible (see Figures S4-S5 in Supplementary Information).

4.2.5 Photocurrent Measurement Setup

Photodetectors are characterized using a custom setup that enables photocurrent measurements as a function of bias voltage and incident wavelength of light from the visible to the

near-IR. The setup also enables characterization of the power spectrum of the light source, which is necessary for proper normalization of the measured photodetector responsivity. A schematic of the setup is shown in Figure 4.2.

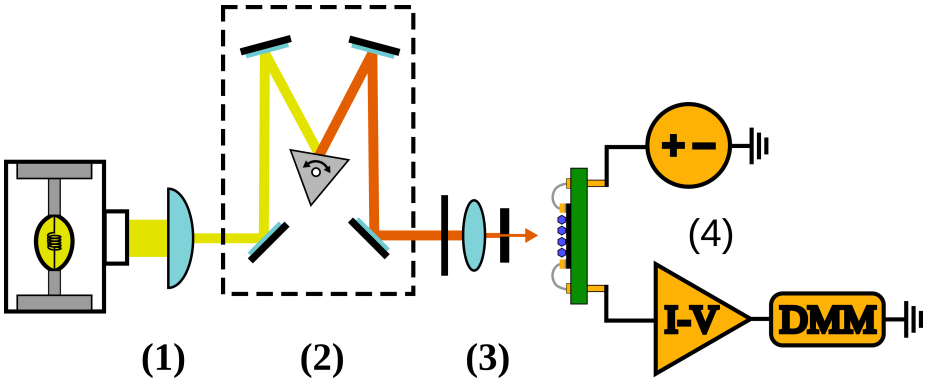


Figure 4.2: Measurement setup for characterizing photodetector responsivity. (1) The broadband light source generates a beam that is collimated and then focused on the monochromator entrance slit; (2) wavelengths are selected by mechanical positioning of diffraction gratings; (3) the monochromator output is filtered and focused onto the wire-bonded MSM device; (4) a bias voltage is applied to the device and the photocurrent is measured using a current-voltage (I-V) amplifier. The output of the I-V amplifier is read out with a digital multimeter (DMM). Responsivity is determined from the DMM output and incident beam power measurements.

A Thorlabs SLS402 Mercury-Xenon short-arc light source generates a broadband spectrum ranging from 240 nm-2.4 μm that is collimated and focused using a Thorlabs LA4464-f = 60.0 mm UV fused plano-convex uncoated lens into the 2 mm aperture entrance slit of a Sciencetech monochromator. A desired wavelength is selected by choosing one of the three Blaze gratings inside the monochromator and rotating the grating into to proper position with respect to the incident beam. The wavelength ranges for each of the three gratings are 100-700 nm, 700-1500 nm, and 1500-3500 nm. The diffracted beam for a selected wavelength then passes through a 2 mm aperture exit slit, FEL1400 or FEL0750 longpass filters to prevent higher-order diffracted wavelength modes, and is then focused using a Thorlabs LA5370-f = 40.0 nm CaF_2 plano-convex uncoated lens through a post-mounted iris diaphragm onto the sample focal plane.

Photodetector devices are attached to a printed circuit board and wire bonded to Au-plated pins that connect to an external circuit through a custom socket. The sample mount is fixed to a lateral (XY) translation stage assembled from Thorlabs single-axis PT1 and PT

series components to facilitate alignment of a chosen detector with the beam. A Keithley 230 programmable voltage source supplies a bias voltage to the source/drain electrodes of a detector. Current is measured using a DL Instruments 1212 current-voltage amplifier, with the output signal fed into an Agilent 34401A digital multimeter. The monochromator and the voltage source are computer-controlled using a custom-written LabVIEW program.

Responsivity Measurement Protocol

The broadband light source is switched on for 1 hour to reach a stable operating temperature and ensure stability of the output spectrum. Prior to measuring the photodetector spectral responsivity, a Thorlabs 700-1800 nm, 50 nW-40 mW Ge photodiode power sensor is used to obtain the power spectrum of the light source. The power sensor is placed in the focal plane behind the post-mounted iris diaphragm, and the FEL0750 filter is placed between the monochromator and the LA5370 focusing lens. The power spectrum is measured over the wavelength range 750-1400 nm, with data points acquired at 5 nm intervals. In the 1400-1800 nm range, the FEL1400 filter is used.

Once the source power spectrum is acquired, the power sensor is replaced by a chosen photodetector, which is then positioned using the XY translation stage to maximize the photocurrent detected at a reference wavelength of 550 nm. The photodetector dark current is recorded over a bias voltage range of +1 V to -1 V with the iris closed. The photocurrent versus bias voltage is then measured across the same wavelength values as the power spectrum to obtain the spectral responsivity of the device. All such measurements were carried out after covering the optical table with a piece of nylon blackout fabric to shield the detector from ambient light.

4.2.6 Nanocrystal Drop-Casts

Nanocrystals are deposited onto the active area of the photodetectors by drop-casting, using diluted suspensions of the WO_{3-x} or Cs_yWO_{3-x} NCs. Each colloidal NC suspension is diluted with hexane using a VWR single-channel pipette. Approximately 0.255 g of the original 190 g/L suspension of Cs_yWO_{3-x} NCs was measured on a digital scale, and then diluted with 340 μL of hexane, yielding a concentration of 152 g/L. Similarly, a WO_{3-x} colloidal NC suspension was diluted to yield a concentration of 100 g/L. The dilute suspensions are then drop-cast onto the active areas of photodetectors using a 0.5 μL volume, and subsequently dried with nitrogen gas.

4.3 Results

4.3.1 Nanocrystal Characterization

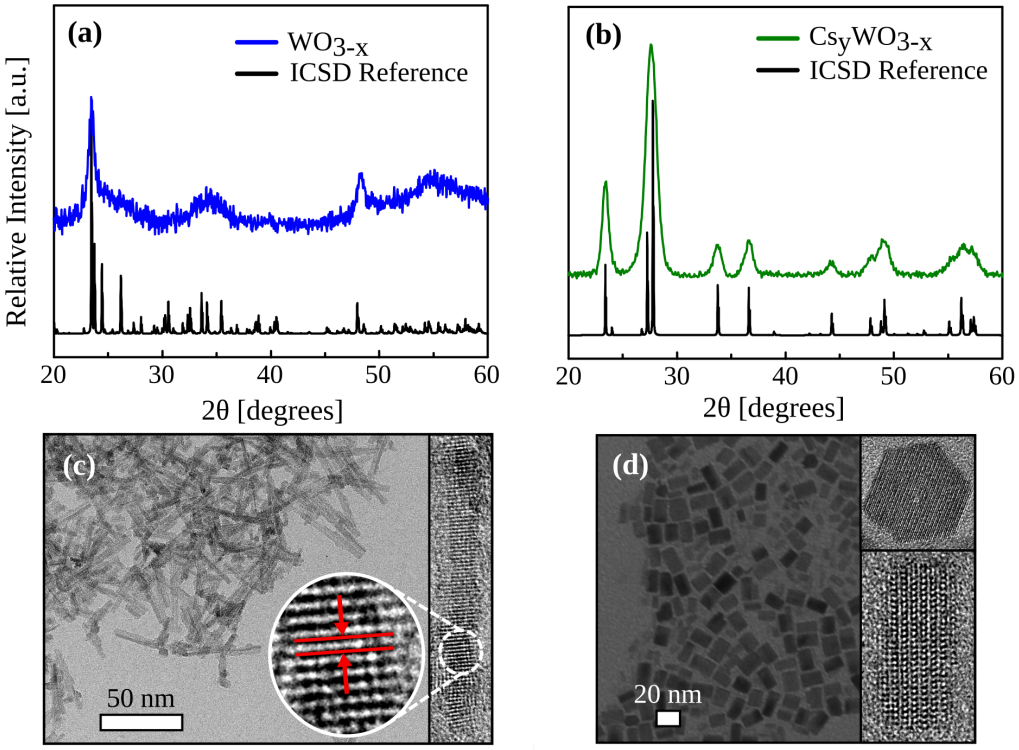


Figure 4.3: Characterization of crystalline structure and morphology of the synthesized NCs. (a-b) X-ray diffraction (XRD) spectra of WO_{3-x} and Cs_yWO_{3-x} NCs with background signal subtracted. Reference spectra of the bulk materials are reproduced from ICSD no. 24731 and no. 56223. (c) TEM images of drop-cast WO_{3-x} nanorods; (right inset) lateral cross-section of a single nanorod; (magnified inset) lattice spacing along $\langle 010 \rangle$ direction. (d) TEM images of drop-cast Cs_yWO_{3-x} NCs; (top right inset) end cross-section of a single NC; (bottom right inset) lateral cross-section image of a single NC.

Depending on the specific W/O atomic ratio, substoichiometric tungsten (VI) oxide (WO_{3-x}) can adopt different crystal structures, known as Magneli phases [202]. In the present study, colloidally synthezised WO_{3-x} NCs crystallized in the monoclinic phase, as suggested by

the excellent match of the experimental X-ray diffractogram (figure 4.3(b), blue trace) with the simulated XRD pattern (black trace) of bulk monoclinic $WO_{2.72}$. The two dominant peaks in the XRD pattern of the WO_{3-x} NCs appearing at approximately 23.5° and 48.3° can be assigned to (010) and (020) planes, respectively, suggesting the oriented growth of the NCs along the ⟨010⟩ direction. This observation was confirmed by the TEM micrographs seen in figure 4.3(c) showing the presence of elongated NCs (nanorods) with a mean length of 32.1 ± 7.8 nm and a diameter of 4.3 ± 1.4 nm (for further details see Supplementary Information). The inset of figure 4.3(c) displays a high-resolution TEM micrograph of a WO_{3-x} nanorod having a mean lattice spacing of 3.7 Å along the ⟨010⟩ direction indicated by the red lines/arrows. In undoped non-stoichiometric plasmonic metal oxides, oxygen vacancies can introduce at most two electrons per vacancy ($V_o^{\bullet\bullet}$) into the crystal to maintain charge neutrality [203], which can subsequently lead to the reduction of nearby metal ions in the lattice (*e.g.*, $2W^{6+} + V_o^{\bullet\bullet} \rightarrow 2W^{5+} + V_o$). To investigate the electronic structure and tungsten speciation in the WO_{3-x} nanorods, X-ray photoelectron spectroscopy (XPS) measurements were performed, the results of which were presented in our earlier report [200]. The W 4f XPS spectra suggested approximately 6% W^{5+} to be present in the WO_{3-x} nanorods. In the optical extinction spectrum of the colloidal (black trace) and drop-cast (blue trace) WO_{3-x} NCs shown in figure 4.4(a), a characteristic broad band starting in the visible region near 490 nm and extending into the NIR region can be observed. Based on the earlier report [200], the optical absorption in the visible region originates from intra-ionic (d-d) transitions, whereas the absorption at lower energies in the NIR region is assigned to LSPR originating from the collective oscillation of oxygen-vacancy-induced free electrons in the conduction band. The intense absorption in the UV region with an onset starting near 480 nm is assigned to the excitonic (band-to-band) transition of the semiconducting WO_{3-x} nanorods [200].

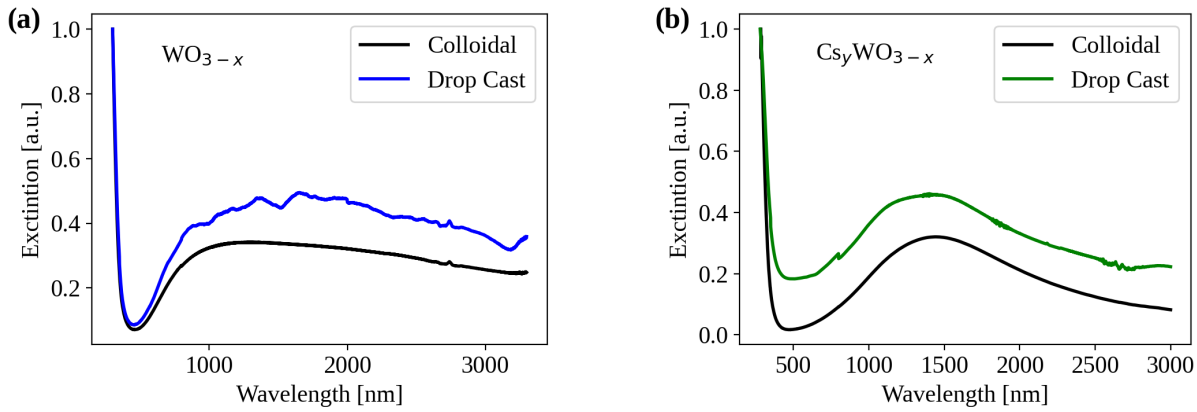


Figure 4.4: (a-b) Optical extinction spectra measured for colloidal solutions and drop-cast WO_{3-x}/Cs_yWO_{3-x} NCs showing plasmonic resonance in the NIR-IR wavelength range. Colloidal solutions were prepared using tetrachloroethylene (TCE). Spectra are normalized by the peak extinction and vertically shifted for comparison.

When tungsten oxide is doped with metal ions, a family of non-stoichiometric compounds of the general formula M_yWO_3 (M is usually an alkali metal ion) is formed, called tungsten bronzes [204]. Depending on the type and radius of the dopant ion, the crystal structure as well as the free carrier concentration, and thus the metallic conductivity, can be modulated in tungsten bronzes. The X-ray diffractogram seen in figure 4.3(b) reveals that as-synthesized Cs_yWO_{3-x} NCs are of high purity and crystallized in the hexagonal phase, indicated by the excellent match between the experimental data and the simulated XRD pattern of the hexagonal-phase $Cs_{0.29}WO_3$. The two most intense peaks near 23.3° and 27.7° originate from the (002) prismatic and (200) basal planes, respectively. The TEM images shown in Figure 4.3(d) reveal a rod-like morphology for as-synthesized Cs_yWO_{3-x} NCs and a mean length and height of 17.8 nm and 10.4 nm (aspect ratio 1.7), respectively (see Figure S2 of the Supplementary Information). The high-resolution TEM micrographs in Figure 4.3(d) display an inset image of a basal plane (top) and the prismatic plane (bottom) of a Cs_yWO_{3-x} NC along the $\langle 002 \rangle$ direction. In tungsten bronzes, the electric charge introduced by the dopant ion results in an increase in the number of free electrons in the conduction band, leading to an increase in electrical conductivity. Therefore, besides the oxygen vacancies, the other source of free carriers in Cs_yWO_{3-x} NCs is the cesium dopant ion. In the optical extinction spectra shown in Figure 4.4(b), the sharply increasing UV signal originates from the bandgap absorption, similar to WO_{3-x} NCs. The broad vis-NIR absorption band of Cs_yWO_{3-x} nanorods has been reported in the literature to originate

from two resonance (transverse and longitudinal) modes as a result of strong crystalline and shape anisotropy [205, 206], with an additional polaronic band in the visible region [207]. Given the geometric parameters of the as-synthesized Cs_yWO_{3-x} NCs (aspect ratio 1.7), the longitudinal and transverse LSPR modes nearly overlap, resulting in the broadened single-peak absorption band seen in Figure 4(b) [205, 206].

4.3.2 Photodetector Characterization

An array of 16 MSM photodetectors with varying electrode geometries was characterized using an Agilent E5262A source/measure unit probe station. The typical device resistances were measured under white light illumination (R_{light}) and in the dark (R_{dark}). Figure 4.5(a) shows an optical microscope image of a photodetector device with a geometry similar to those used in this study. The interdigitated finger electrode structure allows colloidally suspended NCs to be readily drop-cast, as discussed previously in section 4.2.6.

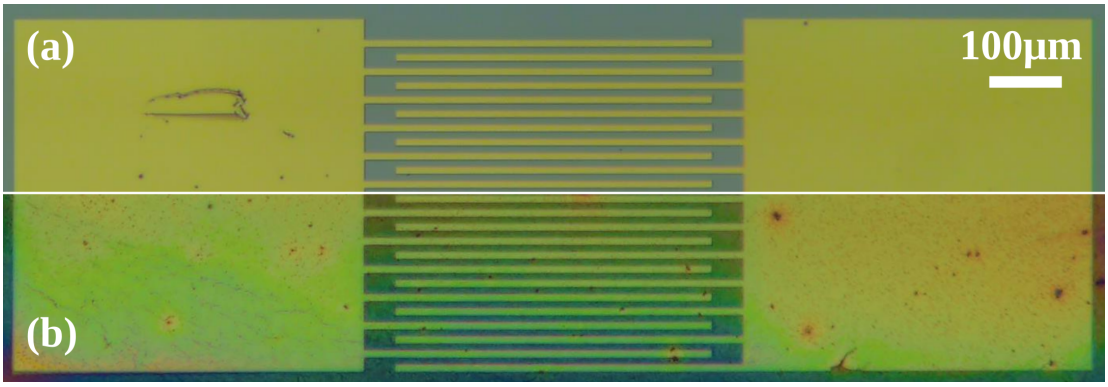


Figure 4.5: Optical microscope images of a MSM photodetector with a similar geometry to the photodetectors measured in this study: a) Upper half of the MSM device with no NCs, b) lower half of the MSM device after drop-casting Cs_yWO_{3-x} NCs from a 150 g/L solution. The lower image indicates a relatively uniform distribution of NCs.

Table 4.1 summarizes the resistance values measured with applied bias -10 mV to +10 mV, including the mean and standard deviation values for the entire array. Two devices, referred to as A and B, showed relatively large increases in conductivity under illumination and were selected for further measurements.

The spectral responsivities of devices A and B were measured using the setup described in Figure 4.2. These photodetectors share the same geometry, with active area 500 μm $\times$

Device	$R_{\text{dark}}[M\Omega]$	$R_{\text{light}}[M\Omega]$	$\Delta R[\%]$
$\mu \pm \sigma$ All	4.24 ± 2.44	0.144 ± 0.0950	-96.6
A	0.200	0.0183	-90.8
B	4.55	0.181	-96.0

Table 4.1: Resistance values for as-fabricated photodetectors measured on a probe station with (R_{light}) and without (R_{dark}) illumination under a white light source to characterize photodetector performance. The applied bias ranged from -10 mV to +10 mV. The optical power was approximately 18 $\frac{\mu W}{mm^2}$ with the probe station lamp on and 32 $\frac{nW}{mm^2}$ with the lamp turned off (ambient light). Devices A and B were chosen for the plasmonic enhancement study because they exhibited significant decreases in resistance under illumination and had the same electrode geometry. ΔR refers to the percentage change in resistance under illumination. The mean resistance (μ) and standard deviation (σ) across the array of 16 detectors are also indicated.

540 μm, and finger width, spacing, and length of 10 μm, 3 μm, and 500 μm, respectively. The photoresponse versus bias voltage obtained at a wavelength of 1550 nm is shown in Figure 4.6. A relatively large dark current was observed compared to similar InGaAs MSM photodetectors reported in the literature (∼nA [158, 161]), even with the InAlAs barrier layer present. We attribute this to a pitting surface defect density of $\sim 10^6$ cm^{-2} in the InAlAs/InGaAs wafer material that leads to regions with lowered Schottky barriers and deviations from typical thermionic emission behavior [208, 209]. Using a double Schottky barrier model described in [210], the dark current through the MSM device can be modeled as

$$J(V) = \frac{2J_S(\Phi_1)J_S(\Phi_2)\sinh\left(\frac{\beta V}{2n}\right)}{J_S(\Phi_1)\exp\left(\frac{\beta V}{2n}\right) + J_S(\Phi_2)\exp\left(\frac{-\beta V}{2n}\right)} \tag{4.1}$$

where $\beta = 1/(k_B T)$, $\Phi_{1/2}$ is the Schottky barrier for either contact, n is the ideality factor assumed to be the same for both contacts, and $J_S(\Phi_{1/2})$ are the thermionic saturation current densities for either contact. From the double Schottky barrier model, the average barrier heights between MSM contacts were estimated to be $\langle\Phi_A\rangle \approx 0.53$ eV and $\langle\Phi_B\rangle \approx 0.50$ eV for both devices A and B, compared to the theoretically expected 0.7 eV [209]. These results are also consistent with earlier theoretical predictions [161]. See the Supplementary Information for characterization of wafer morphology and details of the dark current model.

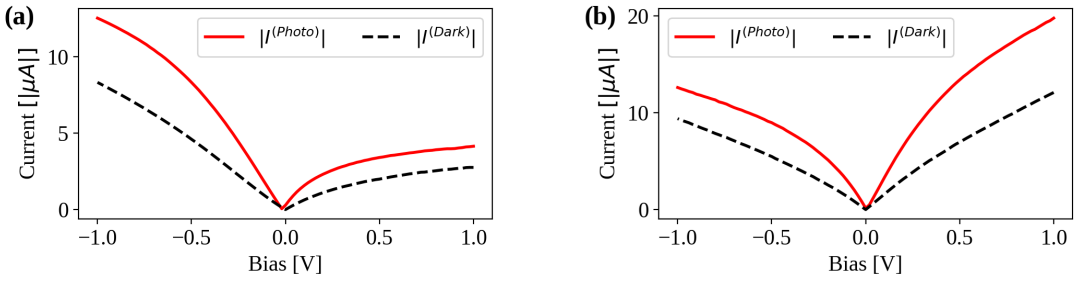


Figure 4.6: Characterization of photodetector performance versus bias voltage and illumination. Dark current and photocurrent for the as-fabricated InGaAs photodetectors A (a) and B (b) used in this study. Photocurrent was acquired at a wavelength of 1550 nm with an incident beam power of 176 $\frac{\mu W}{mm^2}$ over the photodetector active area.

4.3.3 Enhancement of Photodetector Spectral Responsivity

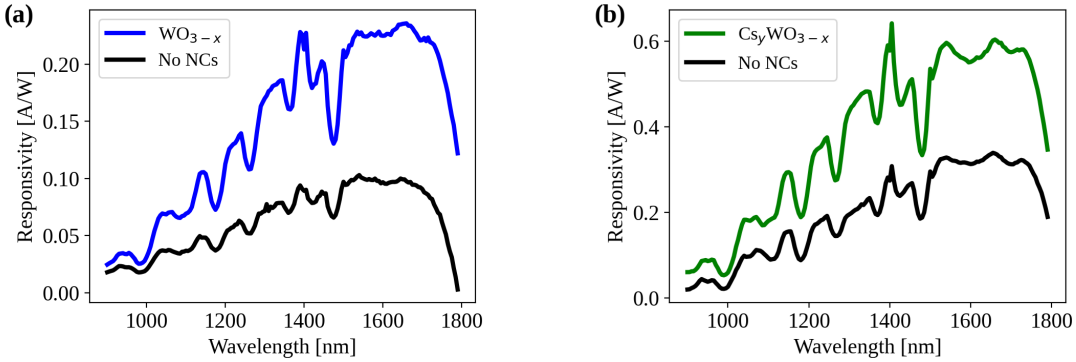


Figure 4.7: Responsivity measured at a bias voltage -1 V with and without (a) WO_{3-x} NCs (device A) and (b) Cs_yWO_{3-x} NCs (device B). Significant increases in responsivity are observed for both types of NC. Responsivity is determined by subtracting the dark current and normalizing the photocurrent with respect to the measured power spectrum of the light source. Note that the fluctuations in responsivity versus wavelength are reproducible and not due to measurement noise (uncertainty due to noise is smaller than the plot line width). These fluctuations may arise from sharp features in the broadband light source spectrum that are not fully removed by our normalization protocol (see Supplementary Information) or by wave interference due to the electrode geometry.

Spectral responsivity is defined as the ratio of the output photocurrent to the incident optical power, and it measures the optical-to-electrical conversion efficiency of the photodetector. The spectral responsivities of the as-fabricated photodetectors were first determined by measuring the dark current, photocurrent, and power spectrum of the light source. A fixed bias voltage of -1 V was used for both devices. Note that the light source power spectrum was appropriately scaled to account for the differing areas between the photodiode detector and the MSM photodetectors, as well as variations in the beam profile. Also, measurement artifacts from switching between two gratings during the spectral sweep were removed (see Supplementary Information). Next, diluted solutions of WO_{3-x} (100 g/L) and Cs_yWO_{3-x} (152 g/L) NCs were drop-cast onto the active area of each photodetector and dried. The optical microscope image in figure 4.5(b) shows an example of drop-cast Cs_yWO_{3-x} NCs. Similar drop-casts are obtained for WO_{3-x} NCs, although there can be significant variability in the quality of the drop-cast (see Supplementary Information). The responsivity measurements were then repeated in order to quantify the effect of having NCs present.

Figure 4.7 shows the responsivities with and without NCs for devices A and B. Device A (B) had WO_{3-x} (Cs_yWO_{3-x}) NCs drop-cast. Before NC deposition, both devices show a wavelength-dependent responsivity characteristic of MSM photodetectors with an InGaAs active layer [211, 212]. Using the responsivity, the specific detectivity for both devices is calculated as:

$$D^* = \sqrt{\frac{A}{2q_e I_{dark}}} \times R(\lambda) \tag{4.2}$$

Where A is the electrode contact area, q_e is the elementary electron charge, I_{dark} is the average dark current, and $R(\lambda)$ is the wavelength-dependent responsivity. Peak detectivities of $D^*_A \sim 10^9$ Jones and $D^*_B \sim 10^{10}$ Jones are observed for devices A and B, respectively, which are comparable to other NIR photodetectors [155, 174, 213] that typically range from $D^* \sim 10^8 - 10^{14}$ Jones. Furthermore, MSM InAlAs/InGaAs photodetector detectivities up to $D^* \sim 10^{11}$ Jones can be achieved with improved substrate quality [163]. Significantly increased responsivity is observed for the addition of both WO_{3-x} and Cs_yWO_{3-x} NCs to the active regions of the photodetectors.

Relative Enhancement

It is of interest to examine the relative enhancement of responsivity as a function of wavelength and compare it with the optical extinction measurements of the drop-cast NCs. The

relative percent difference (RPD) is defined as:

$$RPD(\lambda) = \frac{R_{NC}(\lambda) - R_0(\lambda)}{R_0(\lambda)} \times 100\% \tag{4.3}$$

where λ is wavelength, and $R_{NC}(\lambda)$ and $R_0(\lambda)$ are the responsivities with and without NCs, respectively.

The RPD is plotted in Figure 4.8, with the NC optical extinction measurements overlaid. The RPD calculated from equation 4.3 is in the range of 60-150% and 58-125% for devices A and B, respectively, demonstrating a strong overall enhancement of the responsivity with the addition of both NC types.

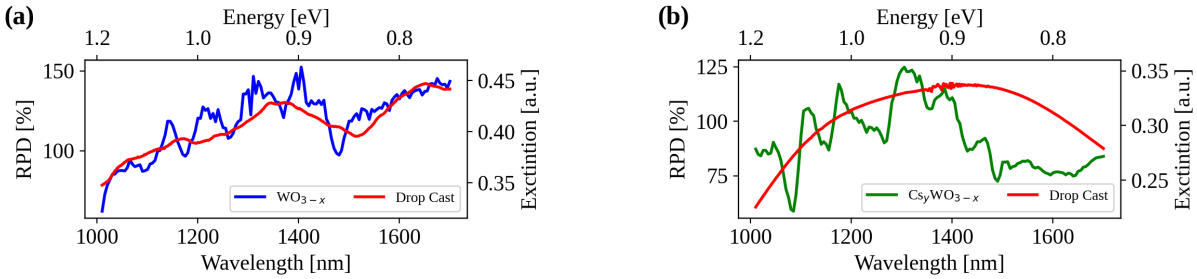


Figure 4.8: Relative percent change in responsivity (RPD) as a function of wavelength due to the addition of (a) WO_{3-x} and (b) Cs_yWO_{3-x} NCs. The optical extinction measurement for drop-cast NCs (red line), plotted on the right vertical axis in each plot, shows overall agreement with the RPD. Note that the relative scaling of the two vertical axes is arbitrary.

Broad agreement between the RPD and the NC extinction spectra is observed in Figure 4.8, indicating that the plasmonic responses of the NCs likely play a role in the enhanced photoresponse of the MSM detectors. Better agreement between the RPD and the NC extinction spectra was observed for WO_{3-x} NCs compared to the case of Cs_yWO_{3-x} NCs. The details of the spectral responses are expected to depend strongly on aggregation effects and film thickness, both of which can vary significantly between drop-casts (see Supplementary Information).

External Quantum Efficiency

The ability of a photodetector to convert incident photons to charges collected in the electrodes is quantified by the external quantum efficiency (EQE) as a function of wave-

length [41]:

$$EQE(\lambda) = \frac{R(\lambda)hc}{q_e\lambda} \times 100\% \tag{4.4}$$

where h is Planck's constant and c is the speed of light. Figure 4.9 shows the EQE for both photodetectors with and without NCs, calculated based on the data shown in Figure 4.7. The highest EQEs are observed in the wavelength range 1400-1600 nm for both devices.

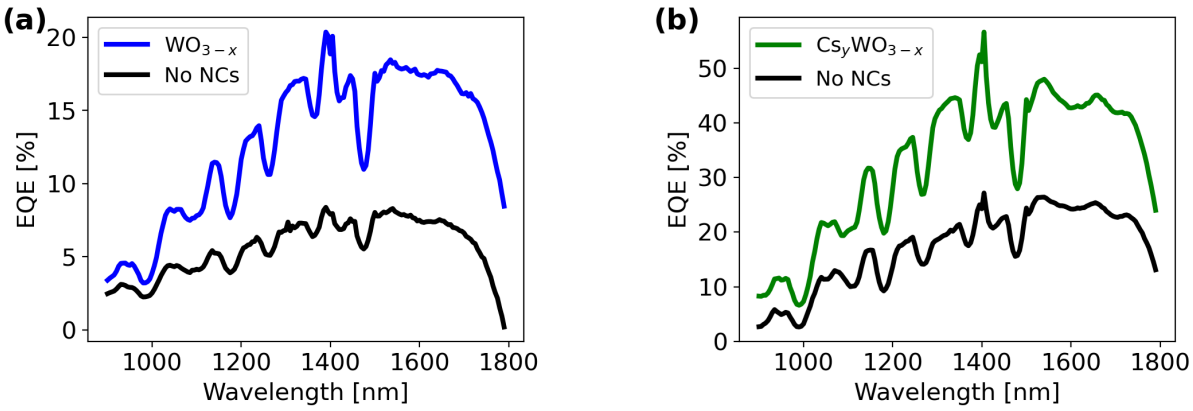


Figure 4.9: External quantum efficiency (EQE) of each photodetector with and without the addition of (a) WO_{3-x} and (b) Cs_yWO_{3-x} NCs. EQEs based on the data shown in Figure 4.7 demonstrate improved photodetector optical-to-electrical conversion efficiency for both NC types.

The EQE increases from approximately 7% to 20% for device A and approximately 25% to 60% for device B at a wavelength of 1400 nm, indicating that ∼2-3 times as many charge carriers are generated or collected after the addition of the WO_{3-x} and Cs_yWO_{3-x} NCs. The EQEs before the addition of NCs are comparable to those reported for other NIR photodetectors [214] and are enhanced by the addition of NCs.

4.4 Discussion

Mechanisms for plasmonic response giving rise to increased photodetector EQEs have been debated in recent years. Possible mechanisms to explain our observations include:

1. LSPR modes of the NCs [205, 206] create stronger electric fields in the InGaAs layer of the MSM photodetector, generating charge carriers at a higher rate [215].

2. Plasmon-induced hot carriers are injected from the NCs into the bulk semiconductor [15, 174, 216–218].

3. Photon collection from scattering is increased due to the NC films forming an anti-reflective (AR) coating [175, 219, 220].

It is not clear from the present data which of these mechanisms are present or dominant in our devices. However, recent work has demonstrated that injection of plasmonically-excited carriers can play a primary role in enhanced photodetection [174, 214]. Evidence that hot carrier injection is the primary mechanism for WO_{3-x} nanorod photodetectors has been demonstrated [189]. The plasmonic absorption band for our NCs ranges over 0.7-1.2 eV. Depending on the work function of the NCs, a Schottky barrier could form that would be low enough to inject energetic carriers into the bulk semiconductor, generating a photocurrent under an applied bias. To test this hypothesis, carrier injection could be suppressed by depositing a thin, wide-bandgap insulating layer between the NCs and the InAlAs surface. The influence of hot carrier injection on photodetector responsivity could be studied by varying the doping concentration of the NCs, where a higher doping concentration would be expected to yield a stronger increase in responsivity. Additionally, LSPR-generated EM fields can be orders of magnitude stronger than the incident field. A stronger EM field in the InGaAs active layer would generate electron-hole pairs at a higher rate. Here, the enhancement in photodetection would be governed by the thickness of the InAlAs buffer layer, since the electric field generated at the NC surface drops off as $|E| \propto 1/r^2$ [215]. This mechanism can be tested by varying the thickness of the InAlAs layer.

The magnitude and distribution of the EM field are determined by the NC morphology, which governs the packing behavior of the NCs and the dominant LSPR mode [206]. The optimal morphology for increased density of EM field hot spots in the active region could be investigated using finite-difference time-domain EM simulations [205, 206], and correlated with responsivity measurements for different NC morphologies.

Finally, enhancement in EQE from the NCs acting as an AR coating could be potentially challenging to separate from other LSPR effects. Plasmonic nanostructures have been used for AR coatings [221], alongside commonly used dielectric nanoparticles. A systematic study of the reflectivity of transition metal oxide NC films on various surfaces could clarify the significance of this effect.

Future work will aim to clarify the dominant mechanisms for enhancement and improve performance through the following approaches:

1. Synthesizing Cs_yWO_{3-x} NCs with varied aspect ratios and carrier concentrations to elucidate the role of LSPR;
2. Characterizing performance improvements using non-plasmonic dielectric AR coatings;
3. Improving sensitivity by using higher-quality substrates for MBE growth to reduce dark current. In addition, incorporating control devices with variable-thickness dielectric barriers between the NCs and the InAlAs surface to test the hot carrier injection hypothesis;
4. Applying NCs via cold vacuum aerosol deposition, or spin coating with NCs embedded in a silica matrix, in order to improve the reproducibility and quality of NC coverage.

4.5 Conclusion

In this study, we have demonstrated that easy-to-fabricate MSM photodetectors can exhibit improved performance in the NIR with the addition of semiconducting WO_{3-x} or Cs_yWO_{3-x} NCs to the active area. This shows the potential of both non-stoichiometric and doped transition metal oxide plasmonic nanomaterials for various IR optoelectronics applications, such as enhanced speed and sensitivity of receivers in optical fiber communications or increased range and reliability of Light Detection and Ranging (LiDAR) systems for autonomous vehicles. The ease of deposition by drop-casting is convenient for rapid prototyping of modified MSM detectors, but lacks the consistency needed for industrial scaling.

In future work, the mechanisms for plasmonic enhancement of photodetection can be distinguished by systematic experiments, as previously discussed, along with comparison to finite-difference time-domain EM simulations. Other directions for improvement include the use of higher quality substrates for MBE growth (reduced dark current), the use of more sophisticated NC deposition methods for reproducibility and consistency, and the use of a transparent conductive material (such as indium tin oxide) for the electrodes.

Chapter 5

Conclusions

In conclusion, we explored key advancements in the simulation and modeling of QD spin qubits, compact models for qubit control electronic design, and LSPR enhancements in photodetectors. Chapter 1 introduces QD device electron transport behavior and examines regions of charge stability under the assumption of a semi-classical constant interaction model. The chapter also discusses electron spin qubit initialization and manipulation, concluding with an overview of photodetectors and plasmonic principles. Through the development of computational tools, theoretical models, and experimental validation, this work has contributed to a deeper understanding of QD spin qubit device behavior and semiconductor photodetection enhancements.

Chapter 2 focuses on the development of QuDiPy, a simulation framework for QD spin qubits. By efficiently computing electrostatic potentials, charge stability, and spin interactions, QuDiPy provides an essential tool for bridging theoretical modeling with experimental optimization. Its ability to estimate charge stability regions, extract capacitance matrix elements, and simulate entangled state preparation in a network of quantum dot nodes underscores the simulator's importance in guiding QD device design and experimental spin qubit control. Future work will focus on the incorporation of experimental feedback loops that make corrective changes to the effective parameter behavior. This will aim to improve the simple, idealized spin and Hubbard models, as well as characterize potential defect features or noise sources. Among the next steps, we will note the creation of large datasets for effective parameter and charge stability diagram variation for 1,2,3, and 4 QD devices. The different device geometries will be simulated with various charge defects so that machine learning models can be trained for noise source classification and autonomous device control. Building on this foundation, several promising directions remain for extending QuDiPy's functionality and impact: 1) constraining spin Hamiltonian

optimal control strategy's voltage pulses using CSD information from the Hubbard model, 2) improving the accuracy of exchange calculations using a many-body solver, e.g., using a linear combination of harmonic orbitals (LCHO) approach previously developed [222], 3) extend the simulator's capability to handle 3D potentials, opposed to 2D potential cross-section, 4) develop a self-consistent Poisson-Schrödinger-many-body solver for electrons in QDs, 5) extend capabilities of the simulator for hole calculations and EDSR control, 6) incorporate a spin-valley Hamiltonian, and 7) develop a module to investigate charge shuttling between QD nodes.

Chapter 3 introduces a compact modeling approach that incorporates spin qubit dynamics into classical circuit simulations, enabling its application to qubit control electronics design. By mapping qubit Hamiltonians to electrical circuit representations, this model efficiently simulates qubit evolution under realistic control signals generated by classical electronics. Furthermore, since the approach is fully integrated within classical circuit simulation software, it facilitates rapid prototyping of control electronic design parameters to mitigate the impacts of control signal noise on spin qubit gate operations. This modeling framework provides a practical pathway for designing and optimizing quantum processors in conjunction with conventional electronics. Future work will focus on improving the analytical functional forms that are fit to simulated multi-variant effective parameter data. This will be achieved by using spectral analysis on the effective parameter data and selecting an appropriate basis function to reconstruct the effective parameter-to-voltage relationships. Additional future work will consist of simulating the qubit evolution for control signals generated by DAC circuitry and characterizing the design parameters that significantly impact qubit gate fidelity.

Chapter 4 investigates plasmonic enhancements in MSM photodetectors by the addition of NCs to the photodetector's active area via drop casting. By leveraging LSPR effects through engineered NCs, we demonstrated significant improvements in photocurrent generation and spectral responsivity, achieving enhancements in external quantum efficiency and specific detectivity. These results highlight the potential for cost-effective, scalable improvements in semiconductor photodetector performance. Future work will focus on improving the NC application protocol to improve reproducibility and stability, such as using a silica gel to uniformly distribute the NCs across the photodetector surface and slow the rate of oxidation. Additional experiments will be conducted to elucidate the precise mechanisms leading to the observed increase in spectral responsivity.

References

[1] Bohdan Khromets. Heterostructure development and quantum control for semiconductor qubits. *University of Waterloo*, 2022.

[2] Paurevic Andrija. Automated tuning and optimal control of spin qubits in quantum dot devices. *University of Waterloo*, 2024.

[3] Cadence Spectre Circuit Simulator. Version 2023.

[4] Advanced Design System (ADS). Version 2023.

[5] J. M. Elzerman, R. Hanson, L. H. Willems van Beveren, B. Witkamp, L. M. K. Vandersypen, and L. P. Kouwenhoven. Single-shot read-out of an individual electron spin in a quantum dot. *Nature*, 430(6998):431–435, July 2004.

[6] J. Bardeen and W. H. Brattain. The transistor, a semi-conductor triode. *Physical Review*, 74(2):230–231, July 1948.

[7] T. H. Maiman. Stimulated optical radiation in ruby. *Nature*, 187(4736):493–494, August 1960.

[8] P. C. Lauterbur. Image formation by induced local interactions: Examples employing nuclear magnetic resonance. *Nature*, 242(5394):190–191, March 1973.

[9] K. W. J. Barnham and G. Duggan. A new approach to high-efficiency multi-band-gap solar cells. *Journal of Applied Physics*, 67(7):3490–3493, April 1990.

[10] Vittorio Giovannetti, Seth Lloyd, and Lorenzo Maccone. Advances in quantum metrology. *Nature Photonics*, 5(4):222–229, March 2011.

[11] Jonathan P. Dowling and Kaushik P. Seshadreesan. Quantum optical technologies for metrology, sensing, and imaging. *Journal of Lightwave Technology*, 33(12):2359–2370, June 2015.

[12] S. Pirandola, B. R. Bardhan, T. Gehring, C. Weedbrook, and S. Lloyd. Advances in photonic quantum sensing. *Nature Photonics*, 12(12):724–733, November 2018.

[13] Nabeel Aslam, Hengyun Zhou, Elana K. Urbach, Matthew J. Turner, Ronald L. Walsworth, Mikhail D. Lukin, and Hongkun Park. Quantum sensors for biomedical applications. *Nature Reviews Physics*, 5(3):157–169, February 2023.

[14] Nicolas Gisin and Rob Thew. Quantum communication. *Nature Photonics*, 1(3):165–171, March 2007.

[15] Jian Luo, Qile Wu, Lin Zhou, Weixi Lu, Wenxing Yang, and Jia Zhu. Plasmon-induced hot carrier dynamics and utilization. *Photonics Insights*, 2(4):R08, 2023.

[16] Paul Benioff. The computer as a physical system: A microscopic quantum mechanical hamiltonian model of computers as represented by turing machines. *Journal of Statistical Physics*, 22(5):563–591, May 1980.

[17] Richard P. Feynman. Simulating physics with computers. *International Journal of Theoretical Physics*, 21(6–7):467–488, June 1982.

[18] Ashley Montanaro. Quantum algorithms: an overview. *npj Quantum Information*, 2(1), January 2016.

[19] A. P. Lund, Michael J. Bremner, and T. C. Ralph. Quantum sampling problems, bosonsampling and quantum supremacy. *npj Quantum Information*, 3(1), April 2017.

[20] Colin D. Bruzewicz, John Chiaverini, Robert McConnell, and Jeremy M. Sage. Trapped-ion quantum computing: Progress and challenges. *Applied Physics Reviews*, 6(2), May 2019.

[21] John Clarke and Frank K. Wilhelm. Superconducting quantum bits. *Nature*, 453(7198):1031–1042, June 2008.

[22] Jay M. Gambetta, Jerry M. Chow, and Matthias Steffen. Building logical qubits in a superconducting quantum computing system. *npj Quantum Information*, 3(1), January 2017.

[23] Jeremy L. O'Brien. Optical quantum computing. *Science*, 318(5856):1567–1570, December 2007.

[24] Peter L. McMahon. The physics of optical computing. *Nature Reviews Physics*, 5(12):717–734, October 2023.

[25] Chetan Nayak, Steven H. Simon, Ady Stern, Michael Freedman, and Sankar Das Sarma. Non-abelian anyons and topological quantum computation. *Reviews of Modern Physics*, 80(3):1083–1159, September 2008.

[26] Khashayar Khazen and Hans Jurgen von Bardeleben. Nv-centers in sic: A solution for quantum computing technology? *Frontiers in Quantum Science and Technology*, 2, January 2023.

[27] Guido Burkard, Thaddeus D. Ladd, Andrew Pan, John M. Nichol, and Jason R. Petta. Semiconductor spin qubits. *Reviews of Modern Physics*, 95(2):025003, June 2023.

[28] David P. DiVincenzo. Topics in quantum computers, 1996.

[29] Austin G. Fowler, Matteo Mariantoni, John M. Martinis, and Andrew N. Cleland. Surface codes: Towards practical large-scale quantum computation. *Physical Review A*, 86(3):032324, September 2012.

[30] John Preskill. *Fault-tolerant Quantum Computation*, pages 213–269. World Scientific, October 1998.

[31] Daniel Loss and David P. DiVincenzo. Quantum computation with quantum dots. *Physical Review A*, 57(1):120–126, January 1998.

[32] L P Kouwenhoven, D G Austing, and S Tarucha. Few-electron quantum dots. *Reports on Progress in Physics*, 64(6):701–736, May 2001.

[33] W. G. van der Wiel, S. De Franceschi, J. M. Elzerman, T. Fujisawa, S. Tarucha, and L. P. Kouwenhoven. Electron transport through double quantum dots. *Reviews of Modern Physics*, 75(1):1–22, December 2002.

[34] R. Hanson, L. P. Kouwenhoven, J. R. Petta, S. Tarucha, and L. M. K. Vandersypen. Spins in few-electron quantum dots. *Reviews of Modern Physics*, 79(4):1217–1265, October 2007.

[35] Thomas. Ihn. *Semiconductor nanostructures : quantum states and electronic transport*. Oxford University Press, Oxford ;, 2010.

[36] Christoph Kloeffel and Daniel Loss. Prospects for spin-based quantum computing in quantum dots. *Annual Review of Condensed Matter Physics*, 4(1):51–81, April 2013.

[37] Floris A. Zwanenburg, Andrew S. Dzurak, Andrea Morello, Michelle Y. Simmons, Lloyd C. L. Hollenberg, Gerhard Klimeck, Sven Rogge, Susan N. Coppersmith, and Mark A. Eriksson. Silicon quantum electronics. *Reviews of Modern Physics*, 85(3):961–1019, July 2013.

[38] Neil W. Ashcroft and N. David Mermin. *Solid state physics*. Holt, Rinehart and Winston,, New York, 1976.

[39] Stefan A Maier. *Plasmonics: Fundamentals and Applications: Fundamentals and Applications*. Springer Science + Business Media, New York, NY, 1. aufl. edition, 2007.

[40] Fuwei Zhuge, Zhi Zheng, Peng Luo, Liang Lv, Yu Huang, Huiqiao Li, and Tianyou Zhai. Nanostructured materials and architectures for advanced infrared photodetection. *Advanced Materials Technologies*, 2(8), May 2017.

[41] Linlin Shi, Keqiang Chen, Aiping Zhai, Guohui Li, Mingming Fan, Yuying Hao, Furong Zhu, Han Zhang, and Yanxia Cui. Status and outlook of metal–inorganic semiconductor–metal photodetectors. *Laser & Photonics Reviews*, 15(1), December 2020.

[42] Karthickraja Ramakrishnan, B. Ajitha, and Y. Ashok Kumar Reddy. Review on metal sulfide-based nanostructures for photodetectors: From ultraviolet to infrared regions. *Sensors and Actuators A: Physical*, 349:114051, January 2023.

[43] Brandon Buonacorsi. Quantum dot devices in silicon and dopant-free gaas/algaas heterostructures. *University of Waterloo*, 2021.

[44] Gregory Holloway. Electron transport in semiconducting nanowires and quantum dots. *University of Waterloo*, 2017.

[45] Z. V. Penfold-Fitch, F. Sfigakis, and M. R. Buitelaar. Microwave spectroscopy of a carbon nanotube charge qubit. *Physical Review Applied*, 7(5):054017, May 2017.

[46] Hubert C. George, Mateusz T. Mądzik, Eric M. Henry, Andrew J. Wagner, Mohammad M. Islam, Felix Borjans, Elliot J. Connors, J. Corrigan, Matthew Curry, Michael K. Harper, Daniel Keith, Lester Lampert, Florian Luthi, Fahd A. Mohiyaddin, Sandra Murcia, Rohit Nair, Rambert Nahm, Aditi Nethwewala, Samuel Neyens, Bishnu Patra, Roy D. Raharjo, Carly Rogan, Rostyslav Savytskyy, Thomas F. Watson, Josh Ziegler, Otto K. Zietz, Stefano Pellerano, Ravi Pillarisetty, Nathaniel C. Bishop, Stephanie A. Bojarski, Jeanette Roberts, and James S. Clarke.

12-spin-qubit arrays fabricated on a 300 mm semiconductor manufacturing line. *Nano Letters*, 25(2):793–799, December 2024.

[47] Adam R. Mills, Charles R. Guinn, Michael J. Gullans, Anthony J. Sigillito, Mayer M. Feldman, Erik Nielsen, and Jason R. Petta. Two-qubit silicon quantum processor with operation fidelity exceeding 99%. *Science Advances*, 8(14), apr 2022.

[48] Jeremy Levy. Universal quantum computation with spin-1/2pairs and heisenberg exchange. *Physical Review Letters*, 89(14):147902, September 2002.

[49] J. R. Petta, A. C. Johnson, J. M. Taylor, E. A. Laird, A. Yacoby, M. D. Lukin, C. M. Marcus, M. P. Hanson, and A. C. Gossard. Coherent manipulation of coupled electron spins in semiconductor quantum dots. *Science*, 309(5744):2180–2184, September 2005.

[50] Federico Fedele, Anasua Chatterjee, Saeed Fallahi, Geoffrey C. Gardner, Michael J. Manfra, and Ferdinand Kuemmeth. Simultaneous operations in a two-dimensional array of singlet-triplet qubits. *PRX Quantum*, 2(4):040306, October 2021.

[51] D. P. DiVincenzo, D. Bacon, J. Kempe, G. Burkard, and K. B. Whaley. Universal quantum computation with the exchange interaction. *Nature*, 408(6810):339–342, November 2000.

[52] J. Medford, J. Beil, J. M. Taylor, S. D. Bartlett, A. C. Doherty, E. I. Rashba, D. P. DiVincenzo, H. Lu, A. C. Gossard, and C. M. Marcus. Self-consistent measurement and state tomography of an exchange-only spin qubit. *Nature Nanotechnology*, 8(9):654–659, September 2013.

[53] Wonill Ha, Sieu D. Ha, Maxwell D. Choi, Yan Tang, Adele E. Schmitz, Mark P. Levendorf, Kangmu Lee, James M. Chappell, Tower S. Adams, Daniel R. Hulbert, Edwin Acuna, Ramsey S. Noah, Justine W. Matten, Michael P. Jura, Jeffrey A. Wright, Matthew T. Rakher, and Matthew G. Borselli. A flexible design platform for si/sige exchange-only qubits with low disorder. *Nano Letters*, 22(3):1443–1448, November 2021.

[54] B. E. Kane. A silicon-based nuclear spin quantum computer. *Nature*, 393(6681):133–137, May 1998.

[55] Andrea Morello, Jarryd J. Pla, Floris A. Zwanenburg, Kok W. Chan, Kuan Y. Tan, Hans Huebl, Mikko Möttönen, Christopher D. Nugroho, Changyi Yang, Jessica A. van Donkelaar, Andrew D. C. Alves, David N. Jamieson, Christopher C. Escott,

Lloyd C. L. Hollenberg, Robert G. Clark, and Andrew S. Dzurak. Single-shot readout of an electron spin in silicon. *Nature*, 467(7316):687–691, September 2010.

[56] Y. He, S. K. Gorman, D. Keith, L. Kranz, J. G. Keizer, and M. Y. Simmons. A two-qubit gate between phosphorus donor electrons in silicon. *Nature*, 571(7765):371–375, July 2019.

[57] L. M. K. Vandersypen, H. Bluhm, J. S. Clarke, A. S. Dzurak, R. Ishihara, A. Morello, D. J. Reilly, L. R. Schreiber, and M. Veldhorst. Interfacing spin qubits in quantum dots and donors—hot, dense, and coherent. *npj Quantum Information*, 3(1), September 2017.

[58] L. Petit, J. M. Boter, H. G. J. Eenink, G. Droulers, M. L. V. Tagliaferri, R. Li, D. P. Franke, K. J. Singh, J. S. Clarke, R. N. Schouten, V. V. Dobrovitski, L. M. K. Vandersypen, and M. Veldhorst. Spin lifetime and charge noise in hot silicon quantum dot qubits. *Physical Review Letters*, 121(7):076801, aug 2018.

[59] Keiji Ono, Takahiro Mori, and Satoshi Moriyama. High-temperature operation of a silicon qubit. *Scientific Reports*, 9(1), jan 2019.

[60] C. H. Yang, R. C. C. Leon, J. C. C. Hwang, A. Saraiva, T. Tanttu, W. Huang, J. Camirand Lemyre, K. W. Chan, K. Y. Tan, F. E. Hudson, K. M. Itoh, A. Morello, M. Pioro-Ladrière, A. Laucht, and A. S. Dzurak. Operation of a silicon quantum processor unit cell above one kelvin. *Nature*, 580(7803):350–354, April 2020.

[61] L. Petit, H. G. J. Eenink, M. Russ, W. I. L. Lawrie, N. W. Hendrickx, S. G. J. Philips, J. S. Clarke, L. M. K. Vandersypen, and M. Veldhorst. Universal quantum logic in hot silicon qubits. *Nature*, 580(7803):355–359, apr 2020.

[62] Luca Petit, Maximilian Russ, Gertjan H. G. J. Eenink, William I. L. Lawrie, James S. Clarke, Lieven M. K. Vandersypen, and Menno Veldhorst. Design and integration of single-qubit rotations and two-qubit gates in silicon above one kelvin. *Communications Materials*, 3(1), November 2022.

[63] Jonathan Y. Huang, Rocky Y. Su, Wee Han Lim, MengKe Feng, Barnaby van Straaten, Brandon Severin, Will Gilbert, Nard Dumoulin Stuyck, Tuomo Tanttu, Santiago Serrano, Jesus D. Cifuentes, Ingvild Hansen, Amanda E. Seedhouse, Ensar Vahapoglu, Ross C. C. Leon, Nikolay V. Abrosimov, Hans-Joachim Pohl, Michael L. W. Thewalt, Fay E. Hudson, Christopher C. Escott, Natalia Ares, Stephen D. Bartlett, Andrea Morello, Andre Saraiva, Arne Laucht, Andrew S. Dzurak, and

Chih Hwan Yang. High-fidelity spin qubit operation and algorithmic initialization above 1 k. *Nature*, 627(8005):772–777, March 2024.

[64] Brandon Buonacorsi, Zhenyu Cai, Eduardo B Ramirez, Kyle S Willick, Sean M Walker, Jiahao Li, Benjamin D Shaw, Xiaosi Xu, Simon C Benjamin, and Jonathan Baugh. Network architecture for a topological quantum computer in silicon. *Quantum Science and Technology*, 4(2):025003, January 2019.

[65] Francesco Borsoi, Nico W. Hendrickx, Valentin John, Marcel Meyer, Sayr Motz, Floor van Riggelen, Amir Sammak, Sander L. de Snoo, Giordano Scappucci, and Menno Veldhorst. Shared control of a 16 semiconductor quantum dot crossbar array. *Nature Nanotechnology*, 19(1):21–27, August 2023.

[66] Justyna P. Zwolak, Jacob M. Taylor, Reed W. Andrews, Jared Benson, Garnett W. Bryant, Donovan Buterakos, Anasua Chatterjee, Sankar Das Sarma, Mark A. Eriksson, Eliška Greplová, Michael J. Gullans, Fabian Hader, Tyler J. Kovach, Pranav S. Mundada, Mick Ramsey, Torbjørn Rasmussen, Brandon Severin, Anthony Sigillito, Brennan Undseth, and Brian Weber. Data needs and challenges for quantum dot devices automation. *npj Quantum Information*, 10(1), October 2024.

[67] Stephan G. J. Philips, Mateusz T. Mądzik, Sergey V. Amitonov, Sander L. de Snoo, Maximilian Russ, Nima Kalhor, Christian Volk, William I. L. Lawrie, Delphine Brousse, Larysa Tryputen, Brian Paquelet Wuetz, Amir Sammak, Menno Veldhorst, Giordano Scappucci, and Lieven M. K. Vandersypen. Universal control of a six-qubit quantum processor in silicon. *Nature*, 609(7929):919–924, September 2022.

[68] Irina Heinz and Guido Burkard. Crosstalk analysis for single-qubit and two-qubit gates in spin qubit arrays. *Physical Review B*, 104(4):045420, jul 2021.

[69] Justyna P. Zwolak and Jacob M. Taylor. Colloquium : Advances in automation of quantum dot devices control. *Reviews of Modern Physics*, 95(1):011006, February 2023.

[70] Brennan Undseth, Xiao Xue, Mohammad Mehmandoost, Maximilian Rimbach-Russ, Pieter T. Eendebak, Nodar Samkharadze, Amir Sammak, Viatcheslav V. Dobrovitski, Giordano Scappucci, and Lieven M.K. Vandersypen. Nonlinear response and crosstalk of electrically driven silicon spin qubits. *Physical Review Applied*, 19(4):044078, apr 2023.

[71] Jarryd J. Pla, Kuan Y. Tan, Juan P. Dehollain, Wee H. Lim, John J. L. Morton, David N. Jamieson, Andrew S. Dzurak, and Andrea Morello. A single-atom electron spin qubit in silicon. *Nature*, 489(7417):541–545, September 2012.

[72] M. Veldhorst, C. H. Yang, J. C. C. Hwang, W. Huang, J. P. Dehollain, J. T. Muhonen, S. Simmons, A. Laucht, F. E. Hudson, K. M. Itoh, A. Morello, and A. S. Dzurak. A two-qubit logic gate in silicon. *Nature*, 526(7573):410–414, October 2015.

[73] C. H. Yang, K. W. Chan, R. Harper, W. Huang, T. Evans, J. C. C. Hwang, B. Hensen, A. Laucht, T. Tanttu, F. E. Hudson, S. T. Flammia, K. M. Itoh, A. Morello, S. D. Bartlett, and A. S. Dzurak. Silicon qubit fidelities approaching incoherent noise limits via pulse engineering. *Nature Electronics*, 2(4):151–158, April 2019.

[74] Nir Dayan, Yakir Ishay, Yaron Artzi, David Cristea, Edward Reijerse, Periannan Kuppusamy, and Aharon Blank. Advanced surface resonators for electron spin resonance of single microcrystals. *Review of Scientific Instruments*, 89(12), December 2018.

[75] Cody Jones, Michael A. Fogarty, Andrea Morello, Mark F. Gyure, Andrew S. Dzurak, and Thaddeus D. Ladd. Logical qubit in a linear array of semiconductor quantum dots. *Physical Review X*, 8(2):021058, June 2018.

[76] M. Veldhorst, J. C. C. Hwang, C. H. Yang, A. W. Leenstra, B. de Ronde, J. P. Dehollain, J. T. Muhonen, F. E. Hudson, K. M. Itoh, A. Morello, and A. S. Dzurak. An addressable quantum dot qubit with fault-tolerant control-fidelity. *Nature Nanotechnology*, 9(12):981–985, October 2014.

[77] T. F. Watson, S. G. J. Philips, E. Kawakami, D. R. Ward, P. Scarlino, M. Veldhorst, D. E. Savage, M. G. Lagally, Mark Friesen, S. N. Coppersmith, M. A. Eriksson, and L. M. K. Vandersypen. A programmable two-qubit quantum processor in silicon. *Nature*, 555(7698):633–637, February 2018.

[78] Chia-Hsien Huang, Chih-Hwan Yang, Chien-Chang Chen, Andrew S. Dzurak, and Hsi-Sheng Goan. High-fidelity and robust two-qubit gates for quantum-dot spin qubits in silicon. *Physical Review A*, 99(4):042310, apr 2019.

[79] W. Huang, C. H. Yang, K. W. Chan, T. Tanttu, B. Hensen, R. C. C. Leon, M. A. Fogarty, J. C. C. Hwang, F. E. Hudson, K. M. Itoh, A. Morello, A. Laucht, and A. S. Dzurak. Fidelity benchmarks for two-qubit gates in silicon. *Nature*, 569(7757):532–536, May 2019.

[80] A. J. Sigillito, M. J. Gullans, L. F. Edge, M. Borselli, and J. R. Petta. Coherent transfer of quantum information in a silicon double quantum dot using resonant swap gates. *npj Quantum Information*, 5(1), November 2019.

[81] Utkan Güngördü and J. P. Kestner. Robust implementation of quantum gates despite always-on exchange coupling in silicon double quantum dots. *Physical Review B*, 101(15):155301, April 2020.

[82] B. M. Maune, M. G. Borselli, B. Huang, T. D. Ladd, P. W. Deelman, K. S. Holabird, A. A. Kiselev, I. Alvarado-Rodriguez, R. S. Ross, A. E. Schmitz, M. Sokolich, C. A. Watson, M. F. Gyure, and A. T. Hunter. Coherent singlet-triplet oscillations in a silicon-based double quantum dot. *Nature*, 481(7381):344–347, January 2012.

[83] H. W. Liu, T. Fujisawa, Y. Ono, H. Inokawa, A. Fujiwara, K. Takashina, and Y. Hirayama. Pauli-spin-blockade transport through a silicon double quantum dot. *Physical Review B*, 77(7):073310, February 2008.

[84] N. S. Lai, W. H. Lim, C. H. Yang, F. A. Zwanenburg, W. A. Coish, F. Qassemi, A. Morello, and A. S. Dzurak. Pauli spin blockade in a highly tunable silicon double quantum dot. *Scientific Reports*, 1(1), October 2011.

[85] Amanda E. Seedhouse, Tuomo Tanttu, Ross C.C. Leon, Ruichen Zhao, Kuan Yen Tan, Bas Hensen, Fay E. Hudson, Kohei M. Itoh, Jun Yoneda, Chih Hwan Yang, Andrea Morello, Arne Laucht, Susan N. Coppersmith, Andre Saraiva, and Andrew S. Dzurak. Pauli blockade in silicon quantum dots with spin-orbit control. *PRX Quantum*, 2(1):010303, jan 2021.

[86] David J. Niegemann, Victor El-Homsy, Baptiste Jadot, Martin Nurizzo, Bruna Cardoso-Paz, Emmanuel Chanrion, Matthieu Dartiailh, Bernhard Klemt, Vivien Thiney, Christopher Bäuerle, Pierre-André Mortemousque, Benoit Bertrand, Heimanu Niebojewski, Maud Vinet, Franck Balestro, Tristan Meunier, and Matias Urdampilleta. Parity and singlet-triplet high-fidelity readout in a silicon double quantum dot at 0.5 k. *PRX Quantum*, 3(4):040335, December 2022.

[87] A. Crippa, R. Ezzouch, A. Aprá, A. Amisse, R. Laviéville, L. Hutin, B. Bertrand, M. Vinet, M. Urdampilleta, T. Meunier, M. Sanquer, X. Jehl, R. Maurand, and S. De Franceschi. Gate-reflectometry dispersive readout and coherent control of a spin qubit in silicon. *Nature Communications*, 10(1), July 2019.

[88] Elliot J. Connors, JJ Nelson, and John M. Nichol. Rapid high-fidelity spin-state readout in si/si-ge quantum dots via rf reflectometry. *Physical Review Applied*, 13(2):024019, feb 2020.

[89] Y.-Y. Liu, S.G.J. Philips, L.A. Orona, N. Samkharadze, T. McJunkin, E.R. MacQuarrie, M.A. Eriksson, L.M.K. Vandersypen, and A. Yacoby. Radio-frequency reflectometry in silicon-based quantum dots. *Physical Review Applied*, 16(1):014057, July 2021.

[90] Florian Vigneau, Federico Fedele, Anasua Chatterjee, David Reilly, Ferdinand Kuemmeth, M. Fernando Gonzalez-Zalba, Edward Laird, and Natalia Ares. Probing quantum devices with radio-frequency reflectometry. *Applied Physics Reviews*, 10(2), February 2023.

[91] F. A. Calderon-Vargas, George S. Barron, Xiu-Hao Deng, A. J. Sigillito, Edwin Barnes, and Sophia E. Economou. Fast high-fidelity entangling gates for spin qubits in si double quantum dots. *Physical Review B*, 100(3):035304, jul 2019.

[92] Tuomo Tanttu, Wee Han Lim, Jonathan Y. Huang, Nard Dumoulin Stuyck, Will Gilbert, Rocky Y. Su, MengKe Feng, Jesus D. Cifuentes, Amanda E. Seedhouse, Stefan K. Seritan, Corey I. Ostrove, Kenneth M. Rudinger, Ross C. C. Leon, Wister Huang, Christopher C. Escott, Kohei M. Itoh, Nikolay V. Abrosimov, Hans-Joachim Pohl, Michael L. W. Thewalt, Fay E. Hudson, Robin Blume-Kohout, Stephen D. Bartlett, Andrea Morello, Arne Laucht, Chih Hwan Yang, Andre Saraiva, and Andrew S. Dzurak. Assessment of the errors of high-fidelity two-qubit gates in silicon quantum dots. *Nature Physics*, 20(11):1804–1809, August 2024.

[93] John M. Nichol, Lucas A. Orona, Shannon P. Harvey, Saeed Fallahi, Geoffrey C. Gardner, Michael J. Manfra, and Amir Yacoby. High-fidelity entangling gate for double-quantum-dot spin qubits. *npj Quantum Information*, 3(1), January 2017.

[94] Maximilian Russ, D. M. Zajac, A. J. Sigillito, F. Borjans, J. M. Taylor, J. R. Petta, and Guido Burkard. High-fidelity quantum gates in si/sige double quantum dots. *Physical Review B*, 97(8):085421, February 2018.

[95] Tyler J. Kovach, Daniel Schug, M. A. Wolfe, E. R. MacQuarrie, Patrick J. Walsh, Jared Benson, Mark Friesen, M. A. Eriksson, and Justyna P. Zwolak. Batis: Bootstrapping, autonomous testing, and initialization system for quantum dot devices, 2024.

[96] Anantha S. Rao, Donovan Buterakos, Barnaby van Straaten, Valentin John, Cécile X. Yu, Stefan D. Oosterhout, Lucas Stehouwer, Giordano Scappucci, Menno Veldhorst, Francesco Borsoi, and Justyna P. Zwolak. Mavis: Modular autonomous virtualization system for two-dimensional semiconductor quantum dot arrays, 2024.

[97] E. Kawakami, P. Scarlino, D. R. Ward, F. R. Braakman, D. E. Savage, M. G. Lagally, Mark Friesen, S. N. Coppersmith, M. A. Eriksson, and L. M. K. Vandersypen. Electrical control of a long-lived spin qubit in a si/sige quantum dot. *Nature Nanotechnology*, 9(9):666–670, August 2014.

[98] Jun Yoneda, Kenta Takeda, Tomohiro Otsuka, Takashi Nakajima, Matthieu R. Delbecq, Giles Allison, Takumu Honda, Tetsuo Kodera, Shunri Oda, Yusuke Hoshi, Noritaka Usami, Kohei M. Itoh, and Seigo Tarucha. A quantum-dot spin qubit with coherence limited by charge noise and fidelity higher than 99.9%. *Nature Nanotechnology*, 13(2):102–106, dec 2017.

[99] M. F. Gonzalez-Zalba, S. de Franceschi, E. Charbon, T. Meunier, M. Vinet, and A. S. Dzurak. Scaling silicon-based quantum computing using CMOS technology. *Nature Electronics*, 4(12):872–884, dec 2021.

[100] A. M. J. Zwerver, T. Krähenmann, T. F. Watson, L. Lampert, H. C. George, R. Pillarisetty, S. A. Bojarski, P. Amin, S. V. Amitonov, J. M. Boter, R. Caudillo, D. Correas-Serrano, J. P. Dehollain, G. Droulers, E. M. Henry, R. Kotlyar, M. Lodari, F. Lüthi, D. J. Michalak, B. K. Mueller, S. Neyens, J. Roberts, N. Samkharadze, G. Zheng, O. K. Zietz, G. Scappucci, M. Veldhorst, L. M. K. Vandersypen, and J. S. Clarke. Qubits made by advanced semiconductor manufacturing. *Nature Electronics*, 5(3):184–190, March 2022.

[101] A.R. Mills, C.R. Guinn, M.M. Feldman, A.J. Sigillito, M.J. Gullans, M.T. Rakher, J. Kerckhoff, C.A.C. Jackson, and J.R. Petta. High-fidelity state preparation, quantum control, and readout of an isotopically enriched silicon spin qubit. *Physical Review Applied*, 18(6):064028, December 2022.

[102] David W. Kanaar, Utkan Güngördü, and J. P. Kestner. Two-qubit controlled-z gates robust against charge noise in silicon while compensating for crosstalk using neural network. *Physical Review B*, 105(24):245308, jun 2022.

[103] M. D. Shulman, S. P. Harvey, J. M. Nichol, S. D. Bartlett, A. C. Doherty, V. Umansky, and A. Yacoby. Suppressing qubit dephasing using real-time hamiltonian estimation. *Nature Communications*, 5(1), October 2014.

[104] Alberto Tosato, Beatrice Ferrari, Amir Sammak, Alexander R. Hamilton, Menno Veldhorst, Michele Virgilio, and Giordano Scappucci. A high-mobility hole bilayer in a germanium double quantum well. *Advanced Quantum Technologies*, 5(5), March 2022.

[105] X. Gao, E. Nielsen, R. P. Muller, R. W. Young, A. G. Salinger, N. C. Bishop, M. P. Lilly, and M. S. Carroll. Quantum computer aided design simulation and optimization of semiconductor quantum dots. *Journal of Applied Physics*, 114(16), October 2013.

[106] Félix Beaudoin, Pericles Philippopoulos, Chenyi Zhou, Ioanna Kriekouki, Michel Pioro-Ladrière, Hong Guo, and Philippe Galy. Robust technology computer-aided design of gated quantum dots at cryogenic temperature. *Applied Physics Letters*, 120(26), June 2022.

[107] Hamza Jnane and Simon C Benjamin. Ab initio modelling of quantum dot qubits: Coupling, gate dynamics and robustness versus charge noise, 2024.

[108] S. Bednarek, B. Szafran, and J. Adamowski. Theoretical description of electronic properties of vertical gated quantum dots. *Physical Review B*, 64(19):195303, October 2001.

[109] T. Matsuse, T. Hama, H. Kaihatsu, N. Toyoda, and T. Takizawa. Electronic structures in coupled two quantum dots by 3d-mesh hartree-fock-kohn-sham calculation. *The European Physical Journal D*, 16(1):391–394, October 2001.

[110] S. Bednarek, B. Szafran, K. Lis, and J. Adamowski. Modeling of electronic properties of electrostatic quantum dots. *Physical Review B*, 68(15):155333, October 2003.

[111] Hong Jiang, Denis Ullmo, Weitao Yang, and Harold U. Baranger. Electron-electron interactions in isolated and realistic quantum dots: A density functional theory study. *Physical Review B*, 69(23):235326, June 2004.

[112] Ioanna Kriekouki, Félix Beaudoin, Pericles Philippopoulos, Chenyi Zhou, Julien Camirand Lemyre, Sophie Rochette, Salvador Mir, Manuel J. Barragan, Michel Pioro-Ladrière, and Philippe Galy. Interpretation of 28 nm fd-soi quantum dot transport data taken at 1.4 k using 3d quantum tcad simulations. *Solid-State Electronics*, 194:108355, August 2022.

[113] Ioanna Kriekouki, Félix Beaudoin, Pericles Philippopoulos, Chenyi Zhou, Julien Camirand Lemyre, Sophie Rochette, Claude Rohrbacher, Salvador Mir, Manuel J. Barragan, Michel Pioro-Ladrière, and Philippe Galy. Understanding conditions for

the single electron regime in 28 nm fd-soi quantum dots: Interpretation of experimental data with 3d quantum tcad simulations. *Solid-State Electronics*, 204:108626, June 2023.

[114] Jesús D. Cifuentes, Tuomo Tanttu, Will Gilbert, Jonathan Y. Huang, Ensar Vahapoglu, Ross C. C. Leon, Santiago Serrano, Dennis Otter, Daniel Dunmore, Philip Y. Mai, Frédéric Schlattner, MengKe Feng, Kohei Itoh, Nikolay Abrosimov, Hans-Joachim Pohl, Michael Thewalt, Arne Laucht, Chih Hwan Yang, Christopher C. Escott, Wee Han Lim, Fay E. Hudson, Rajib Rahman, Andrew S. Dzurak, and Andre Saraiva. Bounds to electron spin qubit variability for scalable cmos architectures. *Nature Communications*, 15(1), May 2024.

[115] Neill Lambert, Eric Giguère, Paul Menczel, Boxi Li, Patrick Hopf, Gerardo Suárez, Marc Gali, Jake Lishman, Rushiraj Gadhvi, Rochisha Agarwal, Asier Galicia, Nathan Shammah, Paul Nation, J. R. Johansson, Shahnawaz Ahmed, Simon Cross, Alexander Pitchford, and Franco Nori. Qutip 5: The quantum toolbox in python, 2024.

[116] David C. McKay, Thomas Alexander, Luciano Bello, Michael J. Biercuk, Lev Bishop, Jiayin Chen, Jerry M. Chow, Antonio D. Córcoles, Daniel Egger, Stefan Filipp, Juan Gomez, Michael Hush, Ali Javadi-Abhari, Diego Moreda, Paul Nation, Brent Paulovicks, Erick Winston, Christopher J. Wood, James Wootton, and Jay M. Gambetta. Qiskit backend specifications for openqasm and openpulse experiments, 2018.

[117] Matthew Amy and Vlad Gheorghiu. staq—a full-stack quantum processing toolkit. *Quantum Science and Technology*, 5(3):034016, June 2020.

[118] Anton Zubchenko, Danielle Middlebrooks, Torbjørn Rasmussen, Lara Lausen, Ferdinand Kuemmeth, Anasua Chatterjee, and Justyna P. Zwolak. Autonomous bootstrapping of quantum dot devices. *Physical Review Applied*, 23(1):014072, January 2025.

[119] Justyna P. Zwolak, Sandesh S. Kalantre, Xingyao Wu, Stephen Ragole, and Jacob M. Taylor. Qflow lite dataset: A machine-learning approach to the charge states in quantum dot experiments. *PLOS ONE*, 13(10):e0205844, October 2018.

[120] Justyna P. Zwolak, Joshua Ziegler, Sandesh S. Kalantre, and Jacob M. Taylor. Qflow 2.0: Quantum dot data for machine learning, 2022.

[121] Jan A. Krzywda, Weikun Liu, Evert van Nieuwenburg, and Oswin Krause. Qdarts: A quantum dot array transition simulator for finding charge transitions in the presence of finite tunnel couplings, non-constant charging energies and sensor dots, 2024.

[122] Valentina Gualtieri, Charles Renshaw-Whitman, Vinicius Hernandes, and Eliska Greplova. Qdsim: An user-friendly toolbox for simulating large-scale quantum dot device, 2024.

[123] Fabian Hader, Sarah Fleitmann, Jan Vogelbruch, Lotte Geck, and Stefan van Waasen. Simulation of charge stability diagrams for automated tuning solutions (simcats). *IEEE Transactions on Quantum Engineering*, 5:1–14, 2024.

[124] Raphaël J. Prentki, Felix Fehse, Pericles Philippopoulos, Chenyi Zhou, Hong Guo, Marek Korkusinski, and Félix Beaudoin. Robust sub-kelvin simulations of quantum dot charge sensing. In *2023 International Conference on Simulation of Semiconductor Processes and Devices (SISPAD)*, pages 349–352. IEEE, September 2023.

[125] Pericles Philippopoulos, Félix Beaudoin, and Philippe Galy. Analysis and 3d tcad simulations of single-qubit control in an industrially-compatible fd-soi device. *Solid-State Electronics*, 215:108883, May 2024.

[126] S. Birner, T. Zibold, T. Andlauer, T. Kubis, M. Sabathil, A. Trellakis, and P. Vogl. nextnano: General purpose 3-d simulations. *IEEE Transactions on Electron Devices*, 54(9):2137–2142, sep 2007.

[127] I-H. Tan, G. L. Snider, L. D. Chang, and E. L. Hu. A self-consistent solution of schrödinger–poisson equations using a nonuniform mesh. *Journal of Applied Physics*, 68(8):4071–4076, October 1990.

[128] Lloyd N. Trefethen. Pseudospectra of linear operators. *SIAM Review*, 39(3):383–406, January 1997.

[129] Rusko Ruskov, Menno Veldhorst, Andrew S. Dzurak, and Charles Tahan. Electron g -factor of valley states in realistic silicon quantum dots. *Physical Review B*, 98(24):245424, December 2018.

[130] A. Kossakowski. On quantum statistical mechanics of non-hamiltonian systems. *Reports on Mathematical Physics*, 3(4):247–274, December 1972.

[131] Daniel Manzano. A short introduction to the lindblad master equation. *AIP Advances*, 10(2), February 2020.

[132] Michael A. Nielsen and Isaac Chuang. Quantum computation and quantum information. *American Journal of Physics*, 70(5):558–559, 2002.

[133] Guido Burkard, Daniel Loss, and David P. DiVincenzo. Coupled quantum dots as quantum gates. *Physical Review B*, 59(3):2070–2078, January 1999.

[134] Jesper Pedersen, Christian Flindt, Niels Asger Mortensen, and Antti-Pekka Jauho. Failure of standard approximations of the exchange coupling in nanostructures. *Physical Review B*, 76(12):125323, September 2007.

[135] Qiuzi Li, Łukasz Cywiński, Dimitrie Culcer, Xuedong Hu, and S. Das Sarma. Exchange coupling in silicon quantum dots: Theoretical considerations for quantum computation. *Physical Review B*, 81(8):085313, feb 2010.

[136] S Das Sarma, Xin Wang, and Shuo Yang. Hubbard model description of silicon spin qubits: Charge stability diagram and tunnel coupling in si double quantum dots. *Physical Review B*, 83(23), 6 2011.

[137] Shuo Yang, Xin Wang, and S. Das Sarma. Generic hubbard model description of semiconductor quantum-dot spin qubits. *Physical Review B*, 83(16):161301, April 2011.

[138] Marek Korkusinski. *Correlations in semiconductor quantum dots*. PhD thesis, University of Ottawa, 2004.

[139] S. A. Jafari. Introduction to hubbard model and exact diagonalization. *arXiv*, 2008.

[140] Andrija Paurevic, Ali Sakr, Tanmay Joshi, Dennis van der Bovenkamp, Quim T. Nicolau, Floris A. Zwanenburg, and Jonathan Baugh. Automated tuning and characterization of a single-electron transistor charge sensor, 2025.

[141] Bohdan Khromets, Zach D. Merino, and Jonathan Baugh. Hamiltonian engineering with time-ordered evolution for unitary control of electron spins in semiconductor quantum dots, 2024.

[142] B. Gys, F. A. Mohiyaddin, R. Acharya, R. Li, K. De Greve, G. Gielen, B. Govoreanu, I. P. Radu, and F. Catthoor. Circuit model for the efficient co-simulation of spin qubits and their control & readout circuitry. In *ESSCIRC 2021 - IEEE 47th European Solid State Circuits Conference (ESSCIRC)*, volume 526, pages 63–66. IEEE, September 2021.

[143] Laurea Magistrale. Definition of compact models forthe simulation of spin qubits insemiconductor quantum dots. 2022.

[144] Mattia Borgarino. Circuit-based compact model of electron spin qubit. *Electronics*, 11(4):526, February 2022.

[145] Samantha van Rijs, Ilke Ercan, Andrei Vladimirescu, and Fabio Sebastiano. Single-electron-transistor compact model for spin-qubit readout. In *2023 19th International Conference on Synthesis, Modeling, Analysis and Simulation Methods and Applications to Circuit Design (SMACD)*, volume 1, pages 1–4. IEEE, July 2023.

[146] Elias A. Pérez-Rodríguez, María T. Orvañanos-Guerrero, and Tetsufumi Tanamoto. Spice compact model of controlling electrons of spin qubits using finfet. *Japanese Journal of Applied Physics*, 62(SC):SC1065, February 2023.

[147] L. Peri, M. Benito, C. J. B. Ford, and M. F. Gonzalez-Zalba. Unified linear response theory of quantum electronic circuits. *npj Quantum Information*, 10(1), November 2024.

[148] A. Rogalski, J. Antoszewski, and L. Faraone. Third-generation infrared photodetector arrays. *Journal of Applied Physics*, 105(9), May 2009.

[149] P. Martyniuk, J. Antoszewski, M. Martyniuk, L. Faraone, and A. Rogalski. New concepts in infrared photodetector designs. *Applied Physics Reviews*, 1(4):041102, December 2014.

[150] Sarath D. Gunapala, Sumith V. Bandara, John K. Liu, Jason M. Mumolo, Sir B. Rafol, David Z. Ting, Alexander Soibel, and Cory Hill. Quantum well infrared photodetector technology and applications. *IEEE Journal of Selected Topics in Quantum Electronics*, 20(6):154–165, November 2014.

[151] Zhi-Ming Zhong, Feng Peng, Lei Ying, Zhen-Qiang Huang, Wen-Kai Zhong, Gang Yu, Yong Cao, and Fei Huang. Infrared photodetectors and image arrays made with organic semiconductors. *Chinese Journal of Polymer Science*, 41(10):1629–1637, April 2023.

[152] Yu Zhu, Hongbin Chen, Ruiman Han, Hao Qin, Zhaoyang Yao, Hang Liu, Yanfeng Ma, Xiangjian Wan, Guanghui Li, and Yongsheng Chen. High-speed flexible near-infrared organic photodiode for optical communication. *National Science Review*, 11(3), December 2023.

[153] Ziyuan Li, Zeyu He, Chenyang Xi, Fanlu Zhang, Longsibo Huang, Yang Yu, Hark Hoe Tan, Chennupati Jagadish, and Lan Fu. Review on iii–v semiconductor nanowire array infrared photodetectors. *Advanced Materials Technologies*, 8(13), April 2023.

[154] Liming Wang, Bo Wang, Yichi Zhang, Lingyao Meng, Hao Sun, Tao Liu, Ningning Zhang, Zuimin Jiang, and Huiyong Hu. Infrared broadband enhancement of responsivity in ge photodetectors decorated with au nanoparticles. *Optics Express*, 29(9):12941, April 2021.

[155] Shonak Bansal. Long-wave bilayer graphene/hgcdte based gbp type-ii superlattice unipolar barrier infrared detector. *Results in Optics*, 12:100425, July 2023.

[156] Joost Brouckaert, Gunther Roelkens, Dries Van Thourhout, and Roel Baets. Compact inalas–ingaas metal– semiconductor– metal photodetectors integrated on silicon-on-insulator waveguides. *IEEE Photonics Technology Letters*, 19(19):1484–1486, October 2007.

[157] Dudu Hatice Unal and Ilkay Demir. Ingaas-based msm photodetector: Researching absorption layer, barrier layer, and digital graded superlattice layer with 3d simulation. *Results in Optics*, 13:100581, December 2023.

[158] J.B.D. Soole and H. Schumacher. Ingaas metal-semiconductor-metal photodetectors for long wavelength optical communications. *IEEE Journal of Quantum Electronics*, 27(3):737–752, March 1991.

[159] D. Kuhl, F. Hieronymi, E.H. Bottcher, T. Wolf, D. Bimberg, J. Kuhl, and M. Klingenstein. Influence of space charges on the impulse response of ingaas metal-semiconductor-metal photodetectors. *Journal of Lightwave Technology*, 10(6):753–759, June 1992.

[160] A.F. Salem and K.F. Brennan. Theoretical study of the response of ingaas metal-semiconductor-metal photodetectors. *IEEE Journal of Quantum Electronics*, 31(5):944–953, May 1995.

[161] W. A. Wohlmuth, M. Arafa, A. Mahajan, P. Fay, and I. Adesida. Ingaas metal-semiconductor-metal photodetectors with engineered schottky barrier heights. *Applied Physics Letters*, 69(23):3578–3580, December 1996.

[162] K. Aliberti, M. Wraback, M. Stead, P. Newman, and H. Shen. Measurements of ingaas metal–semiconductor–metal photodetectors under high-illumination conditions. *Applied Physics Letters*, 80(16):2848–2850, April 2002.

[163] J. Kim, W.B. Johnson, S. Kanakaraju, L.C. Calhoun, and C.H. Lee. Improvement of dark current using inp/ingaasp transition layer in large-area ingaas msm photodetectors. *IEEE Transactions on Electron Devices*, 51(3):351–356, March 2004.

[164] Badreddine Smiri, Marwa Ben Arbia, Demir Ilkay, Faouzi Saidi, Zied Othmen, Brahim Dkhil, Altuntas Ismail, Elagoz Sezai, Fredj Hassen, and Hassen Maaref. Optical and structural properties of in-rich inxga1−xas epitaxial layers on (1 0 0) inp for swir detectors. *Materials Science and Engineering: B*, 262:114769, December 2020.

[165] Pierre Berini. Surface plasmon photodetectors and their applications. *Laser & Photonics Reviews*, 8(2):197–220, June 2013.

[166] Alexander Dorodnyy, Yannick Salamin, Ping Ma, Jelena Vukajlovic Plestina, Nolan Lassaline, Dmitry Mikulik, Pablo Romero-Gomez, Anna Fontcuberta i Morral, and Juerg Leuthold. Plasmonic photodetectors. *IEEE Journal of Selected Topics in Quantum Electronics*, 24(6):1–13, November 2018.

[167] Junchang Zhang, Yawen Wang, Dong Li, Yinghui Sun, and Lin Jiang. Engineering surface plasmons in metal/nonmetal structures for highly desirable plasmonic photodetectors. *ACS Materials Letters*, 4(2):343–355, January 2022.

[168] Serkan Butun, Neval A Cinel, and Ekmel Ozbay. Lspr enhanced msm uv photodetectors. *Nanotechnology*, 23(44):444010, October 2012.

[169] K M Azizur-Rahman and R R LaPierre. Optical design of a mid-wavelength infrared insb nanowire photodetector. *Nanotechnology*, 27(31):315202, June 2016.

[170] Curtis J Goosney, Victoria M Jarvis, Debra P Wilson, Nebile I Goktas, and Ray R LaPierre. Insb nanowires for multispectral infrared detection. *Semiconductor Science and Technology*, 34(3):035023, February 2019.

[171] Tao Yang, Simon Hertenberger, Stefanie Morkötter, Gerhard Abstreiter, and Gregor Koblmüller. Size, composition, and doping effects on in(ga)as nanowire/si tunnel diodes probed by conductive atomic force microscopy. *Applied Physics Letters*, 101(23), December 2012.

[172] Yisong Zhu, Hongxing Xu, Peng Yu, and Zhiming Wang. Engineering plasmonic hot carrier dynamics toward efficient photodetection. *Applied Physics Reviews*, 8(2), April 2021.

[173] Naiquan Yan, Yanyan Qiu, Xubing He, Xin Tang, Qun Hao, and Menglu Chen. Plasmonic enhanced nanocrystal infrared photodetectors. *Materials*, 16(8):3216, April 2023.

[174] Won-Yong Lee, Junhee Lee, Hyuk-Jun Kwon, Kwangeun Kim, Hongki Kang, and Jaewon Jang. High-detectivity silver telluride nanoparticle-based near-infrared photodetectors functionalized with surface-plasmonic gold nanoparticles. *Applied Surface Science*, 654:159563, May 2024.

[175] S. K. Cushing and N. Wu. Plasmon-enhanced solar energy harvesting. *Interface magazine*, 22(2):63–67, January 2013.

[176] Jian-An Huang and Lin-Bao Luo. Low-dimensional plasmonic photodetectors: Recent progress and future opportunities. *Advanced Optical Materials*, 6(8), February 2018.

[177] Yanan Ji, Wen Xu, Dongyu Li, Donglei Zhou, Xu Chen, Nan Ding, Jing Li, Nan Wang, Xue Bai, and Hongwei Song. Semiconductor plasmon enhanced monolayer upconversion nanoparticles for high performance narrowband near-infrared photodetection. *Nano Energy*, 61:211–220, July 2019.

[178] Juan Li, Zaizhu Lou, and Baojun Li. Engineering plasmonic semiconductors for enhanced photocatalysis. *Journal of Materials Chemistry A*, 9(35):18818–18835, 2021.

[179] Anas A.M. Alqanoo, Naser M. Ahmed, M.R. Hashim, Munirah A. Almessiere, Sofyan A. Taya, and Samer H. Zyoud. Silver nanowires assisted porous silicon for high photodetector sensitivity using surface plasmonic phenomena. *Sensors and Actuators A: Physical*, 347:113942, November 2022.

[180] Rajshree Rajkumari, Chitralekha Ngangbam, and Naorem Khelchand Singh. High detectivity photodetector based on wo3 nanowires by the surface plasmonic effect of ag nanoparticles. *IEEE Electron Device Letters*, 43(3):470–473, March 2022.

[181] Luxia Zheng, Yang Yang, Chris R. Bowen, Lan Jiang, Zhan Shu, Yun He, Hongli Yang, Zongzhuo Xie, Taixu Lu, Feng Hu, and Weiyou Yang. A high-performance uv photodetector with superior responsivity enabled by a synergistic photo/thermal enhancement of localized surface plasmon resonance. *Journal of Materials Chemistry C*, 11(18):6227–6238, 2023.

[182] Sukhendu Maity, Krishnendu Sarkar, and Praveen Kumar. Wo3-np-activated ws2 layered heterostructures for efficient broadband (254 nm–940 nm) photodetection. *Nanoscale*, 15(39):16068–16079, 2023.

[183] Yuan Liu, Rui Cheng, Lei Liao, Hailong Zhou, Jingwei Bai, Gang Liu, Lixin Liu, Yu Huang, and Xiangfeng Duan. Plasmon resonance enhanced multicolour photodetection by graphene. *Nature Communications*, 2(1), December 2011.

[184] Tong Wu and Jing Guo. Computational assessment of silicon quantum gate based on detuning mechanism for quantum computing. *IEEE Transactions on Electron Devices*, 65(12):5530–5536, December 2018.

[185] Chunguang Tian, Dayong Jiang, Baozeng Li, Jingquan Lin, Yajun Zhao, Wenxiang Yuan, Jianxun Zhao, Qingcheng Liang, Shang Gao, Jianhua Hou, and Jieming Qin. Performance enhancement of zno uv photodetectors by surface plasmons. *ACS Applied Materials & Interfaces*, 6(3):2162–2166, January 2014.

[186] Sundar Kunwar, Sanchaya Pandit, Jae-Hun Jeong, and Jihoon Lee. Improved photoresponse of uv photodetectors by the incorporation of plasmonic nanoparticles on gan through the resonant coupling of localized surface plasmon resonance. *Nano-Micro Letters*, 12(1), April 2020.

[187] Pradeep Senanayake, Chung-Hong Hung, Joshua Shapiro, Andrew Lin, Baolai Liang, Benjamin S. Williams, and D. L. Huffaker. Surface plasmon-enhanced nanopillar photodetectors. *Nano Letters*, 11(12):5279–5283, November 2011.

[188] Keng-Te Lin, Han Lin, and Baohua Jia. Plasmonic nanostructures in photodetection, energy conversion and beyond. *Nanophotonics*, 9(10):3135–3163, June 2020.

[189] Yongan Zhu, Wei Lu, Tongtong Gu, Xin Gao, Naisen Yu, Sergey Yu. Ketkov, and Zhenyi Zhang. W18o49 nanowire arrays for plasmonic photodetector with electromediated broadband photoresponse. *ACS Applied Nano Materials*, 6(13):11104–11114, June 2023.

[190] Louise Daugas, Khalid Lahlil, Capucine Cleret de Langavant, Ileana Florea, Eric Larquet, Hervé Henry, Jongwook Kim, and Thierry Gacoin. Investigation of lspr coupling effects toward the rational design of csxwo3–δ based solar nir filtering coatings. *Advanced Functional Materials*, 33(43), June 2023.

[191] Tanjew Nütz, Ulf zum Felde, and Markus Haase. Wet-chemical synthesis of doped nanoparticles: Blue-colored colloids of n-doped sno2:sb. *The Journal of Chemical Physics*, 110(24):12142–12150, June 1999.

[192] Ting Wang and Pavle V. Radovanovic. Free electron concentration in colloidal indium tin oxide nanocrystals determined by their size and structure. *The Journal of Physical Chemistry C*, 115(2):406–413, December 2010.

[193] Joseph M. Luther, Prashant K. Jain, Trevor Ewers, and A. Paul Alivisatos. Localized surface plasmon resonances arising from free carriers in doped quantum dots. *Nature Materials*, 10(5):361–366, April 2011.

[194] Enrico Della Gaspera, Anthony S. R. Chesman, Joel van Embden, and Jacek J. Jasieniak. Non-injection synthesis of doped zinc oxide plasmonic nanocrystals. *ACS Nano*, 8(9):9154–9163, August 2014.

[195] Xing Dai, Maria Tchernycheva, and Cesare Soci. *Compound Semiconductor Nanowire Photodetectors*, pages 75–107. Elsevier, 2016.

[196] Hanbing Fang, Manu Hegde, Penghui Yin, and Pavle V. Radovanovic. Tuning plasmon resonance of in2o3 nanocrystals throughout the mid-infrared region by competition between electron activation and trapping. *Chemistry of Materials*, 29(11):4970–4979, May 2017.

[197] Arash Ahmadivand, Mustafa Karabiyik, and Nezih Pala. *Plasmonic photodetectors*, pages 157–193. Elsevier, 2016.

[198] Guanghong Bao, Dabing Li, Xiaojuan Sun, Mingming Jiang, Zhiming Li, Hang Song, Hong Jiang, Yiren Chen, Guoqing Miao, and Zhiwei Zhang. Enhanced spectral response of an algan-based solar-blind ultraviolet photodetector with al nanoparticles. *Optics Express*, 22(20):24286, September 2014.

[199] Prasanta Kumar Sahoo, S.S. Kalyan Kamal, M. Premkumar, T. Jagadeesh Kumar, B. Sreedhar, A.K. Singh, S.K. Srivastava, and K. Chandra Sekhar. Synthesis of tungsten nanoparticles by solvothermal decomposition of tungsten hexacarbonyl. *International Journal of Refractory Metals and Hard Materials*, 27(4):784–791, July 2009.

[200] Aaron Kenny-Wilby, Gyorgy Jaics, Chenwei Zhang, Penghui Yin, and Pavle V. Radovanovic. Revisiting plasmonic properties of complex semiconductor nanocrystals using magnetic circular dichroism spectroscopy: A cautionary tale. *The Journal of Physical Chemistry C*, 127(2):1087–1096, January 2023.

[201] Tracy M. Mattox, Amy Bergerud, Ankit Agrawal, and Delia J. Milliron. Influence of shape on the surface plasmon resonance of tungsten bronze nanocrystals. *Chemistry of Materials*, 26(5):1779–1784, February 2014.

[202] D. B. Migas, V. L. Shaposhnikov, and V. E. Borisenko. Tungsten oxides. ii. the metallic nature of magnéli phases. *Journal of Applied Physics*, 108(9), November 2010.

[203] Sebastien D. Lounis, Evan L. Runnerstrom, Anna Llordés, and Delia J. Milliron. Defect chemistry and plasmon physics of colloidal metal oxide nanocrystals. *The Journal of Physical Chemistry Letters*, 5(9):1564–1574, April 2014.

[204] Lawrence E Conroy and M. J Sienko. Magnetic susceptibility of the lithium tungsten bronzes. *Journal of the American Chemical Society*, 74(14):3520–3522, 1952.

[205] Yannis Cheref, Florian Lochon, Louise Daugas, Capucine Cleret de Langavant, Éric Larquet, Alexandre Baron, Thierry Gacoin, and Jongwook Kim. Dual-band lspr of tungsten bronze nanocrystals tunable over nir and swir ranges. *Chemistry of Materials*, 34(21):9795–9802, October 2022.

[206] Jongwook Kim, Ankit Agrawal, Franziska Krieg, Amy Bergerud, and Delia J. Milliron. The interplay of shape and crystalline anisotropies in plasmonic semiconductor nanocrystals. *Nano Letters*, 16(6):3879–3884, May 2016.

[207] Keisuke Machida, Mika Okada, and Kenji Adachi. Excitations of free and localized electrons at nearby energies in reduced cesium tungsten bronze nanocrystals. *Journal of Applied Physics*, 125(10), March 2019.

[208] O. Breitenstein, P. Altermatt, K. Ramspeck, M.A. Green, Jianhua Zhao, and A. Schenk. Interpretation of the commonly observed i-v characteristics of c-si cells having ideality factor larger than two. In *2006 IEEE 4th World Conference on Photovoltaic Energy Conference*. IEEE, 2006.

[209] I. B. Chistokhin, M. S. Aksenov, N. A. Valisheva, D. V. Dmitriev, I. V. Marchishin, A. I. Toropov, and K. S. Zhuravlev. The influence of the inalas layer surface morphology on the temperature dependence of parameters of au/ti/n-inalas(001) schottky diodes. *Technical Physics Letters*, 45(2):180–184, February 2019.

[210] Gourab Bhattacharya and A Venimadhav. An alternative approach to extract diode parameters from metal–semiconductor–metal asymmetric schottky diodes. *Journal of Physics D: Applied Physics*, 55(43):435101, August 2022.

[211] Jian Chen, Jiuxu Wang, Xin Li, Jin Chen, Feilong Yu, Jiale He, Jian Wang, Zengyue Zhao, Guanhai Li, Xiaoshuang Chen, and Wei Lu. Recent progress in improving

the performance of infrared photodetectors via optical field manipulations. *Sensors*, 22(2):677, January 2022.

[212] Xuanzhang Li, Junyang Zhang, Chen Yue, Xiansheng Tang, Zhendong Gao, Yang Jiang, Chunhua Du, Zhen Deng, Haiqiang Jia, Wenxin Wang, and Hong Chen. High performance visible-swir flexible photodetector based on large-area ingaas/inp pin structure. *Scientific Reports*, 12(1), May 2022.

[213] Shonak Bansal, Krishna Prakash, Kuldeep Sharma, Neha Sardana, Sanjeev Kumar, Neena Gupta, and Arun K Singh. A highly efficient bilayer graphene/zno/silicon nanowire based heterojunction photodetector with broadband spectral response. *Nanotechnology*, 31(40):405205, July 2020.

[214] Ran Duan, Weihong Qi, Panke Li, Kewei Tang, Guoliang Ru, and Weimin Liu. A high-performance mos 2 -based visible–near-infrared photodetector from gateless photogating effect induced by nickel nanoparticles. *Research*, 6, January 2023.

[215] Ibrahim Abdulhalim. Coupling configurations between extended surface electromagnetic waves and localized surface plasmons for ultrahigh field enhancement. *Nanophotonics*, 7(12):1891–1916, November 2018.

[216] Yang Tian and Tetsu Tatsuma. Mechanisms and applications of plasmon-induced charge separation at tio2 films loaded with gold nanoparticles. *Journal of the American Chemical Society*, 127(20):7632–7637, April 2005.

[217] Lingling Chu, Chao Xu, Duanwangde Liu, Chao Nie, and Liting Deng. Plasmon-induced hot-electron injection effect: mechanism of performance enhancement for zno msm hybrid photodetector by introducing ag nws and mxene. *Journal of Physics D: Applied Physics*, 57(4):045102, October 2023.

[218] César Clavero. Plasmon-induced hot-electron generation at nanoparticle/metal-oxide interfaces for photovoltaic and photocatalytic devices. *Nature Photonics*, 8(2):95–103, January 2014.

[219] Kiyofumi Katagiri, Shin-ichiro Yamazaki, Kei Inumaru, and Kunihito Koumoto. Anti-reflective coatings prepared via layer-by-layer assembly of mesoporous silica nanoparticles and polyelectrolytes. *Polymer Journal*, 47(2):190–194, November 2014.

[220] Shah Zeb, Guoxin Sun, Yong Nie, Huiyan Xu, Yu Cui, and Xuchuan Jiang. Advanced developments in nonstoichiometric tungsten oxides for electrochromic applications. *Materials Advances*, 2(21):6839–6884, 2021.

[221] Bhaskar Singh, Mohammed M. Shabat, and Daniel M. Schaadt. Large photocurrent density enhancement assisted by non-absorbing spherical dielectric nanoparticles in a gaas layer. *Scientific Reports*, 10(1), October 2020.

[222] Brandon Buonacorsi, Marek Korkusinski, Bohdan Khromets, and Jonathan Baugh. Optimizing lateral quantum dot geometries for reduced exchange noise, 2020.

APPENDICES

Appendix A

Compact Model Master Equations

A.1 2 Spin Qubit Hamiltonian to Circuit Representation

For the 2-qubit example from Equation 3.9, the normalized Hamiltonian components due to the Zeeman and ESR field terms read as follows,

$$\mathscr{H}_{\text{Zeeman}} + \mathscr{H}_{\text{ESR}} = \begin{bmatrix} \frac{\omega\left(\frac{\delta g_1(t)}{2}+1\right)}{2} + \frac{\omega\left(\frac{\delta g_2(t)}{2}+1\right)}{2} - \omega_{RF} & \frac{(-i\sin(\phi(t))+\cos(\phi(t)))\Omega(t)}{2} & \frac{(-i\sin(\phi(t))+\cos(\phi(t)))\Omega(t)}{2} & 0 \\ \frac{(i\sin(\phi(t))+\cos(\phi(t)))\Omega(t)}{2} & \frac{\omega\left(\frac{\delta g_1(t)}{2}+1\right)}{2} - \frac{\omega\left(\frac{\delta g_2(t)}{2}+1\right)}{2} & 0 & \frac{(-i\sin(\phi(t))+\cos(\phi(t)))\Omega(t)}{2} \\ \frac{(i\sin(\phi(t))+\cos(\phi(t)))\Omega(t)}{2} & 0 & -\frac{\omega\left(\frac{\delta g_1(t)}{2}+1\right)}{2} + \frac{\omega\left(\frac{\delta g_2(t)}{2}+1\right)}{2} & \frac{(-i\sin(\phi(t))+\cos(\phi(t)))\Omega(t)}{2} \\ 0 & \frac{(i\sin(\phi(t))+\cos(\phi(t)))\Omega(t)}{2} & \frac{(i\sin(\phi(t))+\cos(\phi(t)))\Omega(t)}{2} & -\frac{\omega\left(\frac{\delta g_1(t)}{2}+1\right)}{2} - \frac{\omega\left(\frac{\delta g_2(t)}{2}+1\right)}{2} + \omega_{RF} \end{bmatrix} \tag{A.1}$$

Accounting for the exchange interaction terms yields the following normalized Hamiltonian term:

$$\mathscr{H}_{\text{J}} = \begin{bmatrix} \frac{J_1(t)}{4\hbar} & 0 & 0 & 0 \\ 0 & \frac{-J_1(t)}{4\hbar} & \frac{J_1(t)}{2\hbar} & 0 \\ 0 & \frac{J_1(t)}{2\hbar} & \frac{-J_1(t)}{4\hbar} & 0 \\ 0 & 0 & 0 & \frac{J_1(t)}{4\hbar} \end{bmatrix} \tag{A.2}$$

Putting everything together, $\mathscr{H} = \mathscr{H}_{\text{Zeeman}} + \mathscr{H}_{\text{ESR}} + \mathscr{H}_{\text{J}}$ and defining,

$$\gamma_1 \coloneqq \frac{1}{2}\left[\left(1 + \frac{\delta g_1(t)}{2}\right)\omega - \omega_{RF}\right], \quad \gamma_2 \coloneqq \frac{1}{2}\left[\left(1 + \frac{\delta g_2(t)}{2}\right)\omega - \omega_{RF}\right], \quad \gamma_3 \coloneqq \frac{\Omega(t)}{2},$$

allows for the real and imaginary components of the master equation to be written as:

$$\frac{d\rho_{00}^R}{dt} = -2\rho_{01}^I\gamma_3(t) - 2\rho_{02}^I\gamma_3(t) - \frac{\rho_{00}^R a_1}{T_1} - \frac{\rho_{00}^R a_2}{T_1} + \frac{\rho_{11}^R p_2}{T_1} + \frac{\rho_{22}^R p_1}{T_1}$$

$$\frac{d\rho_{00}^I}{dt} = -\frac{\rho_{00}^I a_1}{T_1} - \frac{\rho_{00}^I a_2}{T_1} + \frac{\rho_{11}^I p_2}{T_1} + \frac{\rho_{22}^I p_1}{T_1}$$

$$\begin{aligned}\frac{d\rho_{10}^R}{dt} = {} & \rho_{00}^I\gamma_3(t) - \rho_{01}^I\left(-\gamma_1(t) - \gamma_2(t) - \frac{J_1(t)}{4\hbar}\right) - \rho_{01}^I\left(\gamma_1(t) - \gamma_2(t) - \frac{J_1(t)}{4\hbar}\right) - \frac{\rho_{02}^I J_1(t)}{2\hbar} \\ & - \rho_{03}^I\gamma_3(t) - \rho_{11}^I\gamma_3(t) - \rho_{12}^I\gamma_3(t) - \frac{\rho_{01}^R}{T_2} - \frac{\rho_{01}^R a_1}{T_1} - \frac{\rho_{01}^R a_2}{2T_1} - \frac{\rho_{01}^R p_2}{2T_1} + \frac{\rho_{23}^R p_1}{T_1}\end{aligned}$$

$$\begin{aligned}\frac{d\rho_{10}^I}{dt} = {} & -\rho_{00}^R\gamma_3(t) - \rho_{01}^R\left(-\gamma_1(t) - \gamma_2(t) - \frac{J_1(t)}{4\hbar}\right) - \rho_{01}^R\left(\gamma_1(t) - \gamma_2(t) - \frac{J_1(t)}{4\hbar}\right) - \frac{\rho_{02}^R J_1(t)}{2\hbar} \\ & - \rho_{03}^R\gamma_3(t) + \rho_{11}^R\gamma_3(t) + \rho_{12}^R\gamma_3(t) + \frac{\rho_{01}^I}{T_2} + \frac{\rho_{01}^I a_1}{T_1} + \frac{\rho_{01}^I a_2}{2T_1} + \frac{\rho_{01}^I p_2}{2T_1} - \frac{\rho_{23}^I p_1}{T_1}\end{aligned}$$

$$\frac{d\rho_{11}^R}{dt} = 2\rho_{01}^I\gamma_3(t) - \frac{\rho_{12}^I J_1(t)}{\hbar} - 2\rho_{13}^I\gamma_3(t) + \frac{\rho_{00}^R a_2}{T_1} - \frac{\rho_{11}^R a_1}{T_1} - \frac{\rho_{11}^R p_2}{T_1} + \frac{\rho_{33}^R p_1}{T_1}$$

$$\frac{d\rho_{11}^I}{dt} = \frac{\rho_{00}^I a_2}{T_1} - \frac{\rho_{11}^I a_1}{T_1} - \frac{\rho_{11}^I p_2}{T_1} + \frac{\rho_{33}^I p_1}{T_1}$$

$$\begin{aligned}\frac{d\rho_{20}^R}{dt} = {} & \rho_{00}^I\gamma_3(t) - \frac{\rho_{01}^I J_1(t)}{2\hbar} - \rho_{02}^I\left(-\gamma_1(t) - \gamma_2(t) - \frac{J_1(t)}{4\hbar}\right) - \rho_{02}^I\left(-\gamma_1(t) + \gamma_2(t) - \frac{J_1(t)}{4\hbar}\right) \\ & - \rho_{03}^I\gamma_3(t) + \rho_{12}^I\gamma_3(t) - \rho_{22}^I\gamma_3(t) - \frac{\rho_{02}^R}{T_2} - \frac{\rho_{02}^R a_1}{2T_1} - \frac{\rho_{02}^R a_2}{T_1} - \frac{\rho_{02}^R p_1}{2T_1} + \frac{\rho_{13}^R p_2}{T_1}\end{aligned}$$

$$\begin{aligned}\frac{d\rho_{20}^I}{dt} = {} & -\rho_{00}^R\gamma_3(t) - \frac{\rho_{01}^R J_1(t)}{2\hbar} - \rho_{02}^R\left(-\gamma_1(t) - \gamma_2(t) - \frac{J_1(t)}{4\hbar}\right) - \rho_{02}^R\left(-\gamma_1(t) + \gamma_2(t) - \frac{J_1(t)}{4\hbar}\right) \\ & - \rho_{03}^R\gamma_3(t) + \rho_{12}^R\gamma_3(t) + \rho_{22}^R\gamma_3(t) + \frac{\rho_{02}^I}{T_2} + \frac{\rho_{02}^I a_1}{2T_1} + \frac{\rho_{02}^I a_2}{T_1} + \frac{\rho_{02}^I p_1}{2T_1} - \frac{\rho_{13}^I p_2}{T_1}\end{aligned}$$

$$\frac{d\rho_{21}^R}{dt} = \rho_{01}^I\gamma_3(t) + \rho_{02}^I\gamma_3(t) + \frac{\rho_{11}^I J_1(t)}{2\hbar} - \rho_{12}^I\left(-\gamma_1(t) + \gamma_2(t) - \frac{J_1(t)}{4\hbar}\right) - \rho_{12}^I\left(-\gamma_1(t) + \gamma_2(t) + \frac{J_1(t)}{4\hbar}\right)$$
$$- \rho_{13}^I\gamma_3(t) - \frac{\rho_{22}^I J_1(t)}{2\hbar} - \rho_{23}^I\gamma_3(t) - \frac{2\rho_{12}^R}{T_2} - \frac{\rho_{12}^R a_1}{2T_1} - \frac{\rho_{12}^R a_2}{2T_1} - \frac{\rho_{12}^R p_1}{2T_1} - \frac{\rho_{12}^R p_2}{2T_1}$$

$$\frac{d\rho_{21}^I}{dt} = -\rho_{01}^R\gamma_3(t) + \rho_{02}^R\gamma_3(t) - \frac{\rho_{11}^R J_1(t)}{2\hbar} - \rho_{12}^R\left(-\gamma_1(t) + \gamma_2(t) - \frac{J_1(t)}{4\hbar}\right) - \rho_{12}^R\left(-\gamma_1(t) + \gamma_2(t) + \frac{J_1(t)}{4\hbar}\right)$$
$$- \rho_{13}^R\gamma_3(t) + \frac{\rho_{22}^R J_1(t)}{2\hbar} + \rho_{23}^R\gamma_3(t) + \frac{2\rho_{12}^I}{T_2} + \frac{\rho_{12}^I a_1}{2T_1} + \frac{\rho_{12}^I a_2}{2T_1} + \frac{\rho_{12}^I p_1}{2T_1} + \frac{\rho_{12}^I p_2}{2T_1}$$

$$\frac{d\rho_{22}^R}{dt} = 2\rho_{02}^I\gamma_3(t) + \frac{\rho_{12}^I J_1(t)}{\hbar} - 2\rho_{23}^I\gamma_3(t) + \frac{\rho_{00}^R a_1}{T_1} - \frac{\rho_{22}^R a_2}{T_1} - \frac{\rho_{22}^R p_1}{T_1} + \frac{\rho_{33}^R p_2}{T_1}$$

$$\frac{d\rho_{22}^I}{dt} = \frac{\rho_{00}^I a_1}{T_1} - \frac{\rho_{22}^I a_2}{T_1} - \frac{\rho_{22}^I p_1}{T_1} + \frac{\rho_{33}^I p_2}{T_1}$$

$$\frac{d\rho_{30}^R}{dt} = -\rho_{01}^I\gamma_3(t) - \rho_{02}^I\gamma_3(t) - \rho_{03}^I\left(-\gamma_1(t) - \gamma_2(t) - \frac{J_1(t)}{4\hbar}\right) - \rho_{03}^I\left(-\gamma_1(t) - \gamma_2(t) + \frac{J_1(t)}{4\hbar}\right)$$
$$+ \rho_{13}^I\gamma_3(t) + \rho_{23}^I\gamma_3(t) - \frac{2\rho_{03}^R}{T_2} - \frac{\rho_{03}^R a_1}{2T_1} - \frac{\rho_{03}^R a_2}{2T_1} - \frac{\rho_{03}^R p_1}{2T_1} - \frac{\rho_{03}^R p_2}{2T_1}$$

$$\frac{d\rho_{30}^I}{dt} = -\rho_{01}^R\gamma_3(t) - \rho_{02}^R\gamma_3(t) - \rho_{03}^R\left(-\gamma_1(t) - \gamma_2(t) - \frac{J_1(t)}{4\hbar}\right) - \rho_{03}^R\left(-\gamma_1(t) - \gamma_2(t) + \frac{J_1(t)}{4\hbar}\right)$$
$$+ \rho_{13}^R\gamma_3(t) + \rho_{23}^R\gamma_3(t) + \frac{2\rho_{03}^I}{T_2} + \frac{\rho_{03}^I a_1}{2T_1} + \frac{\rho_{03}^I a_2}{2T_1} + \frac{\rho_{03}^I p_1}{2T_1} + \frac{\rho_{03}^I p_2}{2T_1}$$

$$\frac{d\rho_{31}^R}{dt} = \rho_{03}^I\gamma_3(t) + \rho_{11}^I\gamma_3(t) - \rho_{12}^I\gamma_3(t) - \rho_{13}^I\left(-\gamma_1(t) - \gamma_2(t) + \frac{J_1(t)}{4\hbar}\right) - \rho_{13}^I\left(-\gamma_1(t) + \gamma_2(t) + \frac{J_1(t)}{4\hbar}\right)$$
$$+ \frac{\rho_{23}^I J_1(t)}{2\hbar} - \rho_{33}^I\gamma_3(t) - \frac{\rho_{13}^R}{T_2} + \frac{\rho_{02}^R a_2}{T_1} - \frac{\rho_{13}^R a_1}{2T_1} - \frac{\rho_{13}^R p_1}{2T_1} - \frac{\rho_{13}^R p_2}{T_1}$$

$$\frac{d\rho_{31}^I}{dt} = \rho_{03}^R\gamma_3(t) - \rho_{11}^R\gamma_3(t) - \rho_{12}^R\gamma_3(t) - \rho_{13}^R\left(-\gamma_1(t) - \gamma_2(t) + \frac{J_1(t)}{4\hbar}\right) - \rho_{13}^R\left(-\gamma_1(t) + \gamma_2(t) + \frac{J_1(t)}{4\hbar}\right) + \frac{\rho_{23}^R J_1(t)}{2\hbar} + \rho_{33}^R\gamma_3(t) + \frac{\rho_{13}^I}{T_2} - \frac{\rho_{02}^I a_2}{T_1} + \frac{\rho_{13}^I a_1}{2T_1} + \frac{\rho_{13}^I p_1}{2T_1} + \frac{\rho_{13}^I p_2}{T_1}$$

$$\frac{d\rho_{32}^R}{dt} = \rho_{03}^I\gamma_3(t) + \rho_{12}^I\gamma_3(t) + \frac{\rho_{13}^I J_1(t)}{2\hbar} + \rho_{22}^I\gamma_3(t) - \rho_{23}^I\left(-\gamma_1(t) - \gamma_2(t) + \frac{J_1(t)}{4\hbar}\right) - \rho_{23}^I\left(\gamma_1(t) - \gamma_2(t) + \frac{J_1(t)}{4\hbar}\right) - \rho_{33}^I\gamma_3(t) - \frac{\rho_{23}^R}{T_2} + \frac{\rho_{01}^R a_1}{T_1} - \frac{\rho_{23}^R a_2}{2T_1} - \frac{\rho_{23}^R p_1}{T_1} - \frac{\rho_{23}^R p_2}{2T_1}$$

$$\frac{d\rho_{32}^I}{dt} = \rho_{03}^R\gamma_3(t) - \rho_{12}^R\gamma_3(t) + \frac{\rho_{13}^R J_1(t)}{2\hbar} - \rho_{22}^R\gamma_3(t) - \rho_{23}^R\left(-\gamma_1(t) - \gamma_2(t) + \frac{J_1(t)}{4\hbar}\right) - \rho_{23}^R\left(\gamma_1(t) - \gamma_2(t) + \frac{J_1(t)}{4\hbar}\right) + \rho_{33}^R\gamma_3(t) + \frac{\rho_{23}^I}{T_2} - \frac{\rho_{01}^I a_1}{T_1} + \frac{\rho_{23}^I a_2}{2T_1} + \frac{\rho_{23}^I p_1}{T_1} + \frac{\rho_{23}^I p_2}{2T_1}$$

$$\frac{d\rho_{33}^R}{dt} = 2\rho_{13}^I\gamma_3(t) + 2\rho_{23}^I\gamma_3(t) + \frac{\rho_{11}^R a_1}{T_1} + \frac{\rho_{22}^R a_2}{T_1} - \frac{\rho_{33}^R p_1}{T_1} - \frac{\rho_{33}^R p_2}{T_1}$$

$$\frac{d\rho_{33}^I}{dt} = \frac{\rho_{11}^I a_1}{T_1} + \frac{\rho_{22}^I a_2}{T_1} - \frac{\rho_{33}^I p_1}{T_1} - \frac{\rho_{33}^I p_2}{T_1}$$

$$\frac{d\rho_{00}^R}{dt} = \frac{\left(-\rho_{01}^I\cos\left(\phi(t)\right) - \rho_{01}^R\sin\left(\phi(t)\right)\right)\Omega(t)}{2} - \frac{\left(\rho_{01}^I\cos\left(\phi(t)\right) + \rho_{01}^R\sin\left(\phi(t)\right)\right)\Omega(t)}{2} + \frac{\left(-\rho_{02}^I\cos\left(\phi(t)\right) - \rho_{02}^R\sin\left(\phi(t)\right)\right)\Omega(t)}{2} - \frac{\left(\rho_{02}^I\cos\left(\phi(t)\right) + \rho_{02}^R\sin\left(\phi(t)\right)\right)\Omega(t)}{2} - \frac{\rho_{00}^R a_1}{T_1} - \frac{\rho_{00}^R a_2}{T_1} + \frac{\rho_{11}^R p_2}{T_1} + \frac{\rho_{22}^R p_1}{T_1}$$

$$\frac{d\rho_{00}^I}{dt} = -\frac{\rho_{00}^I a_1}{T_1} - \frac{\rho_{00}^I a_2}{T_1} + \frac{\rho_{11}^I p_2}{T_1} + \frac{\rho_{22}^I p_1}{T_1}$$

$$\frac{d\rho_{10}^{R}}{dt} = -\rho_{01}^{I}\left(\frac{\omega\left(\frac{\delta g_1(t)}{2}+1\right)}{2} - \frac{\omega\left(\frac{\delta g_2(t)}{2}+1\right)}{2} - \frac{J_1(t)}{4}\right)$$
$$- \rho_{01}^{I}\left(-\frac{\omega\left(\frac{\delta g_1(t)}{2}+1\right)}{2} - \frac{\omega\left(\frac{\delta g_2(t)}{2}+1\right)}{2} + \omega_{RF} - \frac{J_1(t)}{4}\right) - \frac{\rho_{02}^{I}J_1(t)}{2}$$
$$+ \frac{\left(\rho_{00}^{I}\cos\left(\phi(t)\right) + \rho_{00}^{R}\sin\left(\phi(t)\right)\right)\Omega(t)}{2} + \frac{\left(-\rho_{03}^{I}\cos\left(\phi(t)\right) - \rho_{03}^{R}\sin\left(\phi(t)\right)\right)\Omega(t)}{2}$$
$$- \frac{\left(\rho_{11}^{I}\cos\left(\phi(t)\right) + \rho_{11}^{R}\sin\left(\phi(t)\right)\right)\Omega(t)}{2} - \frac{\left(\rho_{12}^{I}\cos\left(\phi(t)\right) + \rho_{12}^{R}\sin\left(\phi(t)\right)\right)\Omega(t)}{2}$$
$$- \frac{\rho_{01}^{R}}{T_2} - \frac{\rho_{01}^{R}a_1}{T_1} - \frac{\rho_{01}^{R}a_2}{2T_1} - \frac{\rho_{01}^{R}p_2}{2T_1} + \frac{\rho_{23}^{R}p_1}{T_1}$$

$$\frac{d\rho_{10}^{I}}{dt} = -\rho_{01}^{R}\left(\frac{\omega\left(\frac{\delta g_1(t)}{2}+1\right)}{2} - \frac{\omega\left(\frac{\delta g_2(t)}{2}+1\right)}{2} - \frac{J_1(t)}{4}\right)$$
$$- \rho_{01}^{R}\left(-\frac{\omega\left(\frac{\delta g_1(t)}{2}+1\right)}{2} - \frac{\omega\left(\frac{\delta g_2(t)}{2}+1\right)}{2} + \omega_{RF} - \frac{J_1(t)}{4}\right) - \frac{\rho_{02}^{R}J_1(t)}{2}$$
$$- \frac{\left(-\rho_{00}^{I}\sin\left(\phi(t)\right) + \rho_{00}^{R}\cos\left(\phi(t)\right)\right)\Omega(t)}{2} - \frac{\left(-\rho_{03}^{I}\sin\left(\phi(t)\right) + \rho_{03}^{R}\cos\left(\phi(t)\right)\right)\Omega(t)}{2}$$
$$+ \frac{\left(-\rho_{11}^{I}\sin\left(\phi(t)\right) + \rho_{11}^{R}\cos\left(\phi(t)\right)\right)\Omega(t)}{2} + \frac{\left(-\rho_{12}^{I}\sin\left(\phi(t)\right) + \rho_{12}^{R}\cos\left(\phi(t)\right)\right)\Omega(t)}{2}$$
$$+ \frac{\rho_{01}^{I}}{T_2} + \frac{\rho_{01}^{I}a_1}{T_1} + \frac{\rho_{01}^{I}a_2}{2T_1} + \frac{\rho_{01}^{I}p_2}{2T_1} - \frac{\rho_{23}^{I}p_1}{T_1}$$

$$\frac{d\rho_{11}^R}{dt} = -\rho_{12}^I J_1(t) - \frac{\left(-\rho_{01}^I \cos\left(\phi(t)\right) - \rho_{01}^R \sin\left(\phi(t)\right)\right)\Omega(t)}{2} + \frac{\left(\rho_{01}^I \cos\left(\phi(t)\right) + \rho_{01}^R \sin\left(\phi(t)\right)\right)\Omega(t)}{2}$$
$$+ \frac{\left(-\rho_{13}^I \cos\left(\phi(t)\right) - \rho_{13}^R \sin\left(\phi(t)\right)\right)\Omega(t)}{2} - \frac{\left(\rho_{13}^I \cos\left(\phi(t)\right) + \rho_{13}^R \sin\left(\phi(t)\right)\right)\Omega(t)}{2}$$
$$+ \frac{\rho_{00}^R a_2}{T_1} - \frac{\rho_{11}^R a_1}{T_1} - \frac{\rho_{11}^R p_2}{T_1} + \frac{\rho_{33}^R p_1}{T_1}$$

$$\frac{d\rho_{11}^I}{dt} = \frac{\rho_{00}^I a_2}{T_1} - \frac{\rho_{11}^I a_1}{T_1} - \frac{\rho_{11}^I p_2}{T_1} + \frac{\rho_{33}^I p_1}{T_1}$$

$$\frac{d\rho_{20}^R}{dt} = -\frac{\rho_{01}^I J_1(t)}{2} - \rho_{02}^I \left(-\frac{\omega\left(\frac{\delta g_1(t)}{2} + 1\right)}{2} + \frac{\omega\left(\frac{\delta g_2(t)}{2} + 1\right)}{2} - \frac{J_1(t)}{4} \right)$$
$$- \rho_{02}^I \left(-\frac{\omega\left(\frac{\delta g_1(t)}{2} + 1\right)}{2} - \frac{\omega\left(\frac{\delta g_2(t)}{2} + 1\right)}{2} + \omega_{RF} - \frac{J_1(t)}{4} \right) + \frac{\left(\rho_{00}^I \cos\left(\phi(t)\right) + \rho_{00}^R \sin\left(\phi(t)\right)\right)\Omega(t)}{2}$$
$$+ \frac{\left(-\rho_{03}^I \cos\left(\phi(t)\right) - \rho_{03}^R \sin\left(\phi(t)\right)\right)\Omega(t)}{2} - \frac{\left(-\rho_{12}^I \cos\left(\phi(t)\right) + \rho_{12}^R \sin\left(\phi(t)\right)\right)\Omega(t)}{2}$$
$$- \frac{\left(\rho_{22}^I \cos\left(\phi(t)\right) + \rho_{22}^R \sin\left(\phi(t)\right)\right)\Omega(t)}{2} - \frac{\rho_{02}^R}{T_2} - \frac{\rho_{02}^R a_1}{2T_1} - \frac{\rho_{02}^R a_2}{T_1} - \frac{\rho_{02}^R p_1}{2T_1} + \frac{\rho_{13}^R p_2}{T_1}$$

$$\frac{d\rho_{20}^{I}}{dt} = -\frac{\rho_{01}^{R} J_1(t)}{2} - \rho_{02}^{R}\left(-\frac{\omega\left(\frac{\delta g_1(t)}{2}+1\right)}{2} + \frac{\omega\left(\frac{\delta g_2(t)}{2}+1\right)}{2} - \frac{J_1(t)}{4}\right)$$
$$- \rho_{02}^{R}\left(-\frac{\omega\left(\frac{\delta g_1(t)}{2}+1\right)}{2} - \frac{\omega\left(\frac{\delta g_2(t)}{2}+1\right)}{2} + \omega_{RF} - \frac{J_1(t)}{4}\right) - \frac{\left(-\rho_{00}^{I}\sin\left(\phi(t)\right) + \rho_{00}^{R}\cos\left(\phi(t)\right)\right)\Omega(t)}{2}$$
$$- \frac{\left(-\rho_{03}^{I}\sin\left(\phi(t)\right) + \rho_{03}^{R}\cos\left(\phi(t)\right)\right)\Omega(t)}{2} + \frac{\left(\rho_{12}^{I}\sin\left(\phi(t)\right) + \rho_{12}^{R}\cos\left(\phi(t)\right)\right)\Omega(t)}{2}$$
$$+ \frac{\left(-\rho_{22}^{I}\sin\left(\phi(t)\right) + \rho_{22}^{R}\cos\left(\phi(t)\right)\right)\Omega(t)}{2} + \frac{\rho_{02}^{I}}{T_2} + \frac{\rho_{02}^{I}a_1}{2T_1} + \frac{\rho_{02}^{I}a_2}{T_1} + \frac{\rho_{02}^{I}p_1}{2T_1} - \frac{\rho_{13}^{I}p_2}{T_1}$$

$$\frac{d\rho_{21}^{R}}{dt} = \frac{\rho_{11}^{I} J_1(t)}{2} - \rho_{12}^{I}\left(-\frac{\omega\left(\frac{\delta g_1(t)}{2}+1\right)}{2} + \frac{\omega\left(\frac{\delta g_2(t)}{2}+1\right)}{2} - \frac{J_1(t)}{4}\right)$$
$$- \rho_{12}^{I}\left(-\frac{\omega\left(\frac{\delta g_1(t)}{2}+1\right)}{2} + \frac{\omega\left(\frac{\delta g_2(t)}{2}+1\right)}{2} + \frac{J_1(t)}{4}\right) - \frac{\rho_{22}^{I} J_1(t)}{2} + \frac{\left(\rho_{01}^{I}\cos\left(\phi(t)\right) + \rho_{01}^{R}\sin\left(\phi(t)\right)\right)\Omega(t)}{2}$$
$$- \frac{\left(-\rho_{02}^{I}\cos\left(\phi(t)\right) - \rho_{02}^{R}\sin\left(\phi(t)\right)\right)\Omega(t)}{2} + \frac{\left(-\rho_{13}^{I}\cos\left(\phi(t)\right) - \rho_{13}^{R}\sin\left(\phi(t)\right)\right)\Omega(t)}{2}$$
$$- \frac{\left(\rho_{23}^{I}\cos\left(\phi(t)\right) + \rho_{23}^{R}\sin\left(\phi(t)\right)\right)\Omega(t)}{2} - \frac{2\rho_{12}^{R}}{T_2} - \frac{\rho_{12}^{R}a_1}{2T_1} - \frac{\rho_{12}^{R}a_2}{2T_1} - \frac{\rho_{12}^{R}p_1}{2T_1} - \frac{\rho_{12}^{R}p_2}{2T_1}$$

$$\frac{d\rho_{21}^I}{dt} = -\frac{\rho_{11}^R J_1(t)}{2} - \rho_{12}^R \left(-\frac{\omega\left(\frac{\delta g_1(t)}{2}+1\right)}{2} + \frac{\omega\left(\frac{\delta g_2(t)}{2}+1\right)}{2} - \frac{J_1(t)}{4} \right)$$
$$- \rho_{12}^R \left(-\frac{\omega\left(\frac{\delta g_1(t)}{2}+1\right)}{2} + \frac{\omega\left(\frac{\delta g_2(t)}{2}+1\right)}{2} + \frac{J_1(t)}{4} \right) + \frac{\rho_{22}^R J_1(t)}{2} - \frac{\left(-\rho_{01}^I \sin\left(\phi(t)\right) + \rho_{01}^R \cos\left(\phi(t)\right)\right)\Omega(t)}{2}$$
$$+ \frac{\left(-\rho_{02}^I \sin\left(\phi(t)\right) + \rho_{02}^R \cos\left(\phi(t)\right)\right)\Omega(t)}{2} - \frac{\left(-\rho_{13}^I \sin\left(\phi(t)\right) + \rho_{13}^R \cos\left(\phi(t)\right)\right)\Omega(t)}{2}$$
$$+ \frac{\left(-\rho_{23}^I \sin\left(\phi(t)\right) + \rho_{23}^R \cos\left(\phi(t)\right)\right)\Omega(t)}{2} + \frac{2\rho_{12}^I}{T_2} + \frac{\rho_{12}^I a_1}{2T_1} + \frac{\rho_{12}^I a_2}{2T_1} + \frac{\rho_{12}^I p_1}{2T_1} + \frac{\rho_{12}^I p_2}{2T_1}$$

$$\frac{d\rho_{22}^R}{dt} = \rho_{12}^I J_1(t) - \frac{\left(-\rho_{02}^I \cos\left(\phi(t)\right) - \rho_{02}^R \sin\left(\phi(t)\right)\right)\Omega(t)}{2} + \frac{\left(\rho_{02}^I \cos\left(\phi(t)\right) + \rho_{02}^R \sin\left(\phi(t)\right)\right)\Omega(t)}{2}$$
$$+ \frac{\left(-\rho_{23}^I \cos\left(\phi(t)\right) - \rho_{23}^R \sin\left(\phi(t)\right)\right)\Omega(t)}{2} - \frac{\left(\rho_{23}^I \cos\left(\phi(t)\right) + \rho_{23}^R \sin\left(\phi(t)\right)\right)\Omega(t)}{2}$$
$$+ \frac{\rho_{00}^R a_1}{T_1} - \frac{\rho_{22}^R a_2}{T_1} - \frac{\rho_{22}^R p_1}{T_1} + \frac{\rho_{33}^R p_2}{T_1}$$

$$\frac{d\rho_{22}^I}{dt} = \frac{\rho_{00}^I a_1}{T_1} - \frac{\rho_{22}^I a_2}{T_1} - \frac{\rho_{22}^I p_1}{T_1} + \frac{\rho_{33}^I p_2}{T_1}$$

$$\frac{d\rho_{30}^{R}}{dt} = -\rho_{03}^{I}\left(-\frac{\omega\left(\frac{\delta g_1(t)}{2}+1\right)}{2}-\frac{\omega\left(\frac{\delta g_2(t)}{2}+1\right)}{2}+\omega_{RF}-\frac{J_1(t)}{4}\right)$$
$$-\rho_{03}^{I}\left(-\frac{\omega\left(\frac{\delta g_1(t)}{2}+1\right)}{2}-\frac{\omega\left(\frac{\delta g_2(t)}{2}+1\right)}{2}+\omega_{RF}+\frac{J_1(t)}{4}\right)+\frac{\left(-\rho_{01}^{I}\cos\left(\phi(t)\right)+\rho_{01}^{R}\sin\left(\phi(t)\right)\right)\Omega(t)}{2}$$
$$+\frac{\left(-\rho_{02}^{I}\cos\left(\phi(t)\right)+\rho_{02}^{R}\sin\left(\phi(t)\right)\right)\Omega(t)}{2}-\frac{\left(-\rho_{13}^{I}\cos\left(\phi(t)\right)+\rho_{13}^{R}\sin\left(\phi(t)\right)\right)\Omega(t)}{2}$$
$$-\frac{\left(-\rho_{23}^{I}\cos\left(\phi(t)\right)+\rho_{23}^{R}\sin\left(\phi(t)\right)\right)\Omega(t)}{2}-\frac{2\rho_{03}^{R}}{T_2}-\frac{\rho_{03}^{R}a_1}{2T_1}-\frac{\rho_{03}^{R}a_2}{2T_1}-\frac{\rho_{03}^{R}p_1}{2T_1}-\frac{\rho_{03}^{R}p_2}{2T_1}$$

$$\frac{d\rho_{30}^{I}}{dt} = -\rho_{03}^{R}\left(-\frac{\omega\left(\frac{\delta g_1(t)}{2}+1\right)}{2}-\frac{\omega\left(\frac{\delta g_2(t)}{2}+1\right)}{2}+\omega_{RF}-\frac{J_1(t)}{4}\right)$$
$$-\rho_{03}^{R}\left(-\frac{\omega\left(\frac{\delta g_1(t)}{2}+1\right)}{2}-\frac{\omega\left(\frac{\delta g_2(t)}{2}+1\right)}{2}+\omega_{RF}+\frac{J_1(t)}{4}\right)-\frac{\left(\rho_{01}^{I}\sin\left(\phi(t)\right)+\rho_{01}^{R}\cos\left(\phi(t)\right)\right)\Omega(t)}{2}$$
$$-\frac{\left(\rho_{02}^{I}\sin\left(\phi(t)\right)+\rho_{02}^{R}\cos\left(\phi(t)\right)\right)\Omega(t)}{2}+\frac{\left(\rho_{13}^{I}\sin\left(\phi(t)\right)+\rho_{13}^{R}\cos\left(\phi(t)\right)\right)\Omega(t)}{2}$$
$$+\frac{\left(\rho_{23}^{I}\sin\left(\phi(t)\right)+\rho_{23}^{R}\cos\left(\phi(t)\right)\right)\Omega(t)}{2}+\frac{2\rho_{03}^{I}}{T_2}+\frac{\rho_{03}^{I}a_1}{2T_1}+\frac{\rho_{03}^{I}a_2}{2T_1}+\frac{\rho_{03}^{I}p_1}{2T_1}+\frac{\rho_{03}^{I}p_2}{2T_1}$$

$$\frac{d\rho_{31}^R}{dt} = -\rho_{13}^I \left(-\frac{\omega\left(\frac{\delta g_1(t)}{2}+1\right)}{2} + \frac{\omega\left(\frac{\delta g_2(t)}{2}+1\right)}{2} + \frac{J_1(t)}{4} \right)$$
$$- \rho_{13}^I \left(-\frac{\omega\left(\frac{\delta g_1(t)}{2}+1\right)}{2} - \frac{\omega\left(\frac{\delta g_2(t)}{2}+1\right)}{2} + \omega_{RF} + \frac{J_1(t)}{4} \right) + \frac{\rho_{23}^I J_1(t)}{2}$$
$$- \frac{\left(-\rho_{03}^I \cos\left(\phi(t)\right) - \rho_{03}^R \sin\left(\phi(t)\right)\right)\Omega(t)}{2} + \frac{\left(\rho_{11}^I \cos\left(\phi(t)\right) + \rho_{11}^R \sin\left(\phi(t)\right)\right)\Omega(t)}{2}$$
$$+ \frac{\left(-\rho_{12}^I \cos\left(\phi(t)\right) + \rho_{12}^R \sin\left(\phi(t)\right)\right)\Omega(t)}{2} - \frac{\left(\rho_{33}^I \cos\left(\phi(t)\right) + \rho_{33}^R \sin\left(\phi(t)\right)\right)\Omega(t)}{2}$$
$$- \frac{\rho_{13}^R}{T_2} + \frac{\rho_{02}^R a_2}{T_1} - \frac{\rho_{13}^R a_1}{2T_1} - \frac{\rho_{13}^R p_1}{2T_1} - \frac{\rho_{13}^R p_2}{T_1}$$

$$\frac{d\rho_{31}^I}{dt} = -\rho_{13}^R \left(-\frac{\omega\left(\frac{\delta g_1(t)}{2}+1\right)}{2} + \frac{\omega\left(\frac{\delta g_2(t)}{2}+1\right)}{2} + \frac{J_1(t)}{4} \right)$$
$$- \rho_{13}^R \left(-\frac{\omega\left(\frac{\delta g_1(t)}{2}+1\right)}{2} - \frac{\omega\left(\frac{\delta g_2(t)}{2}+1\right)}{2} + \omega_{RF} + \frac{J_1(t)}{4} \right) + \frac{\rho_{23}^R J_1(t)}{2}$$
$$+ \frac{\left(-\rho_{03}^I \sin\left(\phi(t)\right) + \rho_{03}^R \cos\left(\phi(t)\right)\right)\Omega(t)}{2} - \frac{\left(-\rho_{11}^I \sin\left(\phi(t)\right) + \rho_{11}^R \cos\left(\phi(t)\right)\right)\Omega(t)}{2}$$
$$- \frac{\left(\rho_{12}^I \sin\left(\phi(t)\right) + \rho_{12}^R \cos\left(\phi(t)\right)\right)\Omega(t)}{2} + \frac{\left(-\rho_{33}^I \sin\left(\phi(t)\right) + \rho_{33}^R \cos\left(\phi(t)\right)\right)\Omega(t)}{2}$$
$$+ \frac{\rho_{13}^I}{T_2} - \frac{\rho_{02}^I a_2}{T_1} + \frac{\rho_{13}^I a_1}{2T_1} + \frac{\rho_{13}^I p_1}{2T_1} + \frac{\rho_{13}^I p_2}{T_1}$$

$$\frac{d\rho_{32}^R}{dt} = \frac{\rho_{13}^I J_1(t)}{2} - \rho_{23}^I \left(\frac{\omega\left(\frac{\delta g_1(t)}{2}+1\right)}{2} - \frac{\omega\left(\frac{\delta g_2(t)}{2}+1\right)}{2} + \frac{J_1(t)}{4} \right)$$
$$- \rho_{23}^I \left(-\frac{\omega\left(\frac{\delta g_1(t)}{2}+1\right)}{2} - \frac{\omega\left(\frac{\delta g_2(t)}{2}+1\right)}{2} + \omega_{RF} + \frac{J_1(t)}{4} \right) - \frac{\left(-\rho_{03}^I \cos\left(\phi(t)\right) - \rho_{03}^R \sin\left(\phi(t)\right)\right)\Omega(t)}{2}$$
$$+ \frac{\left(\rho_{12}^I \cos\left(\phi(t)\right) + \rho_{12}^R \sin\left(\phi(t)\right)\right)\Omega(t)}{2} + \frac{\left(\rho_{22}^I \cos\left(\phi(t)\right) + \rho_{22}^R \sin\left(\phi(t)\right)\right)\Omega(t)}{2}$$
$$- \frac{\left(\rho_{33}^I \cos\left(\phi(t)\right) + \rho_{33}^R \sin\left(\phi(t)\right)\right)\Omega(t)}{2} - \frac{\rho_{23}^R}{T_2} + \frac{\rho_{01}^R a_1}{T_1} - \frac{\rho_{23}^R a_2}{2T_1} - \frac{\rho_{23}^R p_1}{T_1} - \frac{\rho_{23}^R p_2}{2T_1}$$

$$\frac{d\rho_{32}^I}{dt} = \frac{\rho_{13}^R J_1(t)}{2} - \rho_{23}^R \left(\frac{\omega\left(\frac{\delta g_1(t)}{2}+1\right)}{2} - \frac{\omega\left(\frac{\delta g_2(t)}{2}+1\right)}{2} + \frac{J_1(t)}{4} \right)$$
$$- \rho_{23}^R \left(-\frac{\omega\left(\frac{\delta g_1(t)}{2}+1\right)}{2} - \frac{\omega\left(\frac{\delta g_2(t)}{2}+1\right)}{2} + \omega_{RF} + \frac{J_1(t)}{4} \right) + \frac{\left(-\rho_{03}^I \sin\left(\phi(t)\right) + \rho_{03}^R \cos\left(\phi(t)\right)\right)\Omega(t)}{2}$$
$$- \frac{\left(-\rho_{12}^I \sin\left(\phi(t)\right) + \rho_{12}^R \cos\left(\phi(t)\right)\right)\Omega(t)}{2} - \frac{\left(-\rho_{22}^I \sin\left(\phi(t)\right) + \rho_{22}^R \cos\left(\phi(t)\right)\right)\Omega(t)}{2}$$
$$+ \frac{\left(-\rho_{33}^I \sin\left(\phi(t)\right) + \rho_{33}^R \cos\left(\phi(t)\right)\right)\Omega(t)}{2} + \frac{\rho_{23}^I}{T_2} - \frac{\rho_{01}^I a_1}{T_1} + \frac{\rho_{23}^I a_2}{2T_1} + \frac{\rho_{23}^I p_1}{T_1} + \frac{\rho_{23}^I p_2}{2T_1}$$

$$\frac{d\rho_{33}^R}{dt} = -\frac{\left(-\rho_{13}^I \cos\left(\phi(t)\right) - \rho_{13}^R \sin\left(\phi(t)\right)\right)\Omega(t)}{2} + \frac{\left(\rho_{13}^I \cos\left(\phi(t)\right) + \rho_{13}^R \sin\left(\phi(t)\right)\right)\Omega(t)}{2}$$
$$- \frac{\left(-\rho_{23}^I \cos\left(\phi(t)\right) - \rho_{23}^R \sin\left(\phi(t)\right)\right)\Omega(t)}{2} + \frac{\left(\rho_{23}^I \cos\left(\phi(t)\right) + \rho_{23}^R \sin\left(\phi(t)\right)\right)\Omega(t)}{2}$$
$$+ \frac{\rho_{11}^R a_1}{T_1} + \frac{\rho_{22}^R a_2}{T_1} - \frac{\rho_{33}^R p_1}{T_1} - \frac{\rho_{33}^R p_2}{T_1}$$

$$\frac{d\rho_{33}^I}{dt} = \frac{\rho_{11}^I a_1}{T_1} + \frac{\rho_{22}^I a_2}{T_1} - \frac{\rho_{33}^I p_1}{T_1} - \frac{\rho_{33}^I p_2}{T_1}$$

Appendix B

Photodetector Supplementary Information

B.1 Nanocrystal (NC) Characterization

Figures B.1 and B.2 provide information on the size and shape distributions of the WO_{3-x} and Cs_yWO_{3-x} NCs, as determined from TEM images. Figure B.3 shows energy dispersive X-ray spectroscopy results that were used to determine the composition of the Cs_yWO_{3-x} NCs. Figures B.4 and B.5 show the crystalline and optical characterization for WO_{3-x} and Cs_yWO_{3-x} NCs, respectively. Tables B.1 and B.2 present a summary of these results.

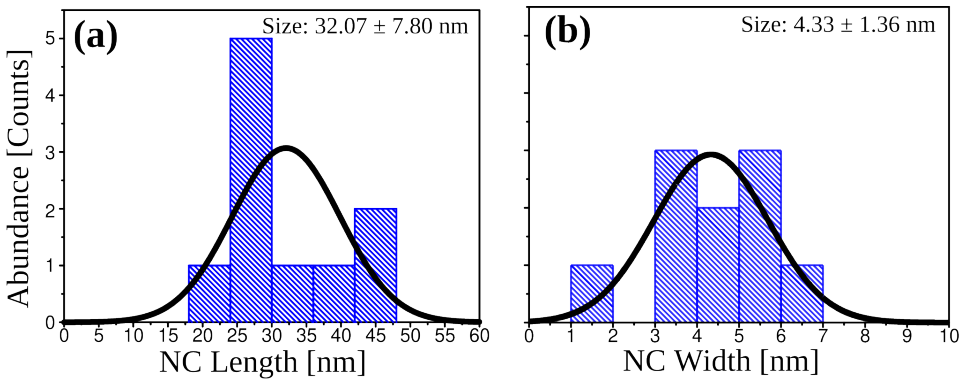


Figure B.1: Length and width distributions of WO_{3-x} NCs determined from post-processed TEM images using ImageJ software.

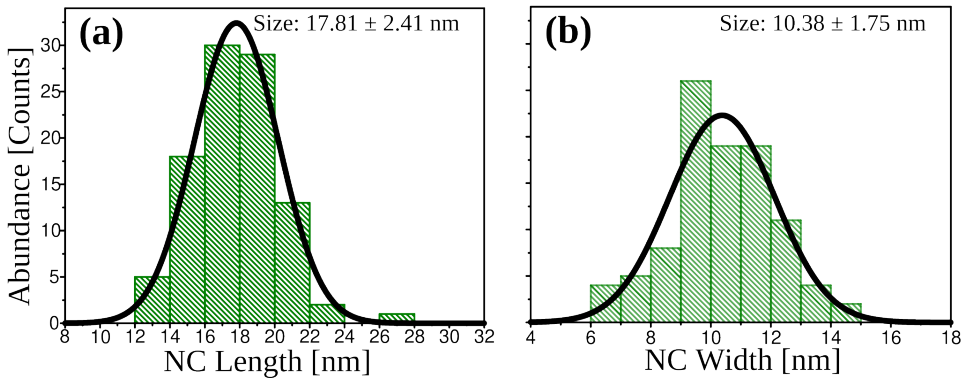


Figure B.2: Length and width of distributions Cs_yWO_{3-x} NCs determined from post-processed TEM images using ImageJ software.

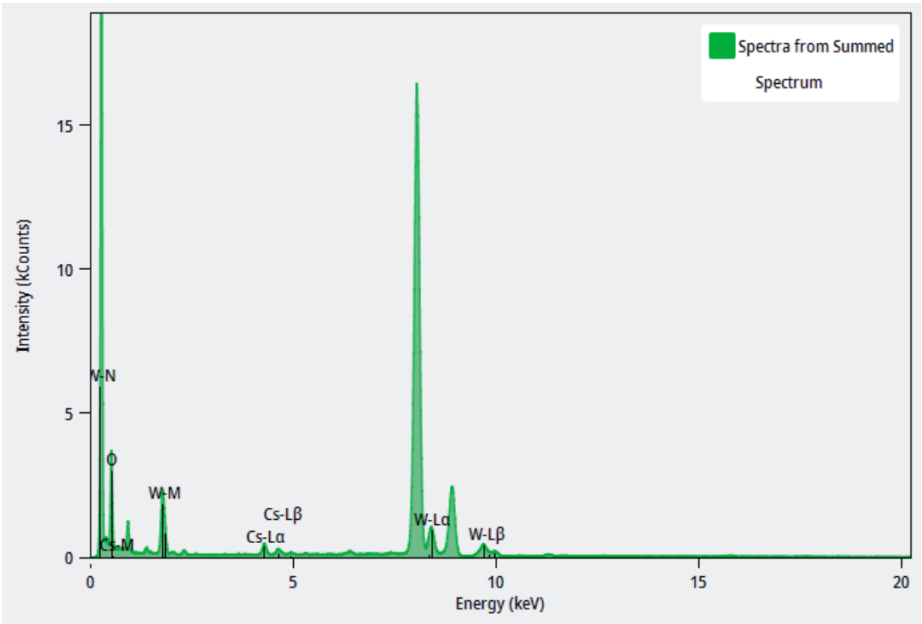


Figure B.3: Energy dispersive X-ray spectroscopy (EDS) measurement on Cs_yWO_{3-x} NCs that determined the atomic fraction of Cs and W to be 4.78% and 17.67%, respectively. From this, the ratio of Cs/W in Cs_yWO_{3-x} NCs was determined to be $y = 0.27$.

Table B.1: Summary of crystallographic and optical characterization of WO_{3-x} NC samples from independent syntheses. The maximum plasmonic resonant wavelengths from extinction measurements (UV-NIR) and peak XRD angles for a given crystal orientation with Full-Width Half-Maximum ((crystal orientation)-FWHM) are tabulated. This demonstrates a high degree of reproducibility in the synthesis of WO_{3-x} NCs.

Sample	**UV-NIR** Max [nm]	**XRD** (010)	**XRD** (020)
WO3-x	1126	23.4-0.5	48.3-0.8
WO-S1	1098	23.8-0.5	48.3-0.6
WO-S2	1153	23.7-0.7	48.3-1.3

Table B.2: Summary of crystallographic and optical characterization of Cs_yWO_{3-x} NC samples from independent syntheses. The aspect ratios (AR), maximum plasmonic resonant wavelengths from extinction measurements (UV-NIR), and peak XRD angles for a given crystal orientation with Full-Width Half-Maximum ((crystal orientation)-FWHM) are tabulated. This demonstrates a high degree of reproducibility in the synthesis of Cs_yWO_{3-x} NCs.

Sample	**AR**	**UV-NIR** Max [nm]	**XRD** (002)	**XRD** (200)	**XRD** (112)	**XRD** (202)
CsyWO3-x	1.6	1442	23.4-0.8	27.7-1.3	33.8-0.8	36.7-0.9
CsWO-S1	1.5	1363	23.6-0.8	28.0-1.4	34.2-0.9	37.0-0.8
CsWO-S2	1.6	1449	23.8-0.8	28.1-1.3	33.9-1.0	36.9-0.9

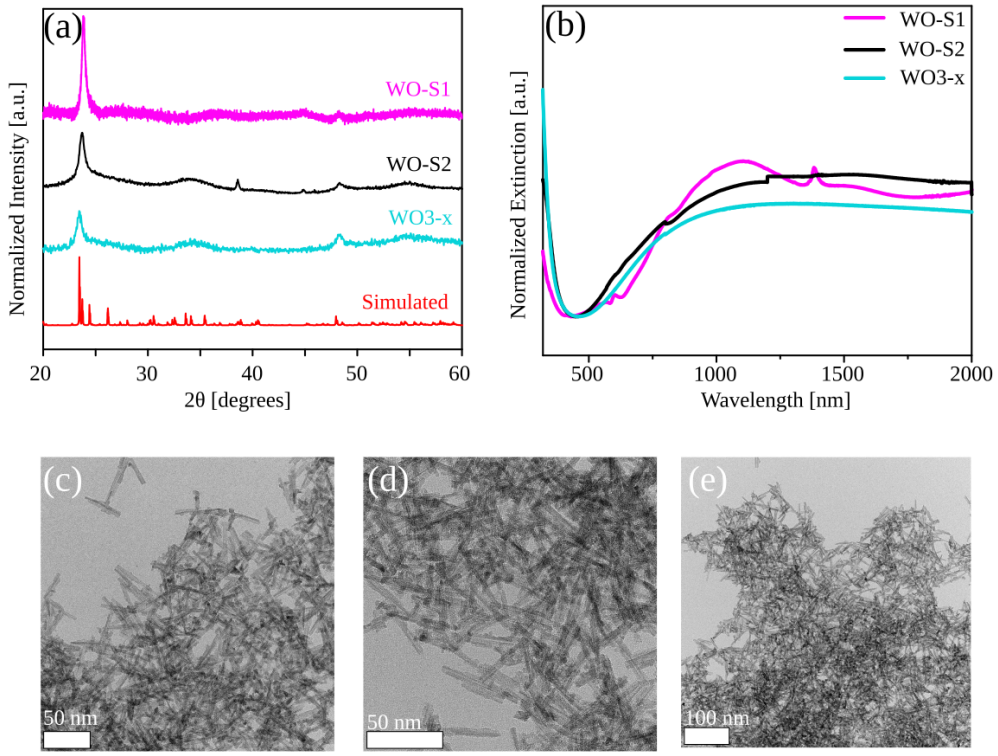


Figure B.4: Characterization of two additional substoichiometric monoclinic WO_{3-x} NC samples demonstrating the synthetic reproducibility of the NCs via XRD patterns (a), UV-Vis-NIR spectra (b), and (c-e) TEM micrographs. (Blue traces in (a) and (b) correspond to the WO_{3-x} in the main text. The red trace in (a) is a simulated pattern of bulk monoclinic WO_3 (ICSD no. 24731).

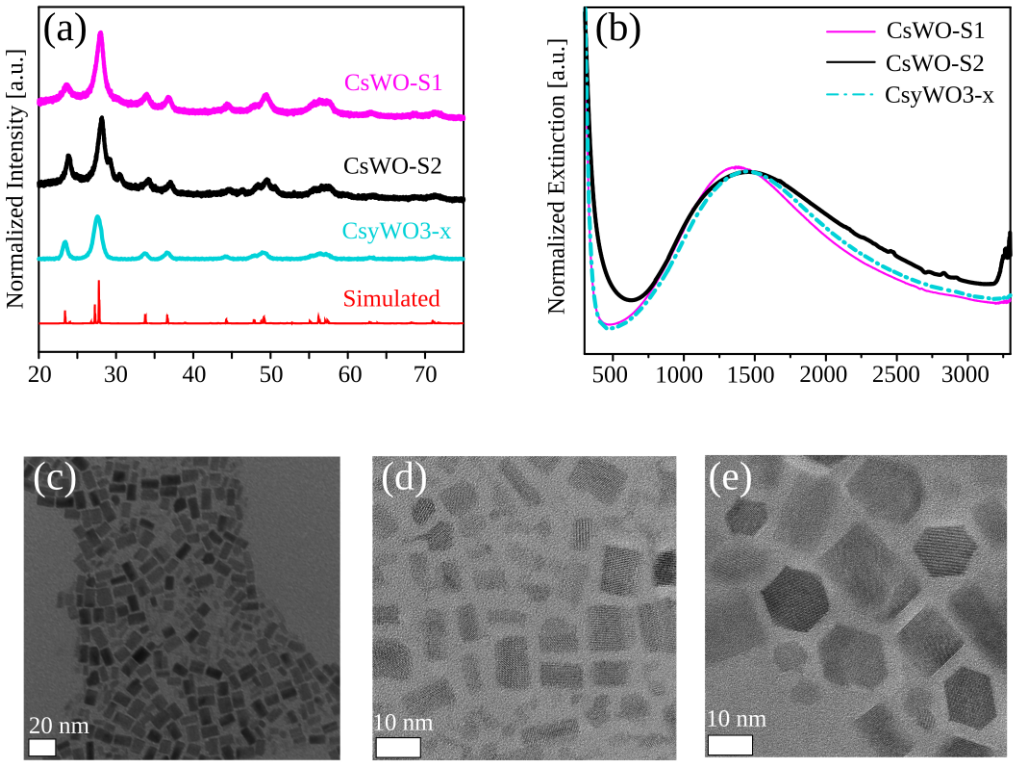


Figure B.5: Characterization of two additional Cs_yWO_{3-x} bronze NCs demonstrating the synthetic reproducibility of the samples. (a) XRD patterns, (b) UV-Vis-NIR spectra, and (c-e) TEM micrographs of the Cs_yWO_{3-x} NCs. (Blue traces in (a) and (b) are the data shown in the main text. The red trace in (a) is the simulated pattern of bulk $Cs_{0.29}WO_3$ (ICSD no. 56223)).

B.2 Light Source Characterization

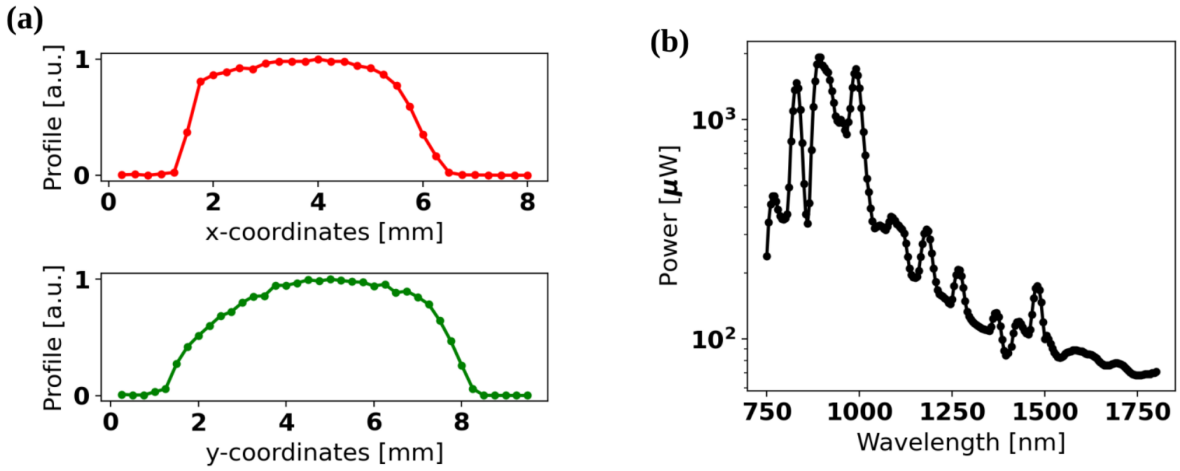


Figure B.6: Xenon-Halogen light source (a) beam profile upon exiting the monochromator and (b) power spectrum over a wavelength range 750-1800 nm, where a 750 nm or 1400 nm filter was used to block higher-order modes of diffracted light from the monochromator gratings.

Cross-sections of the beam profile are shown attached to a head-on image of the beam at 550 nm wavelength. The image of the beam is not to scale with the cross-sectional beam profiles. The beam profiles were measured using a standard knife-edge measurement.

B.3 Spectral Responsivity Normalization and Incident Power

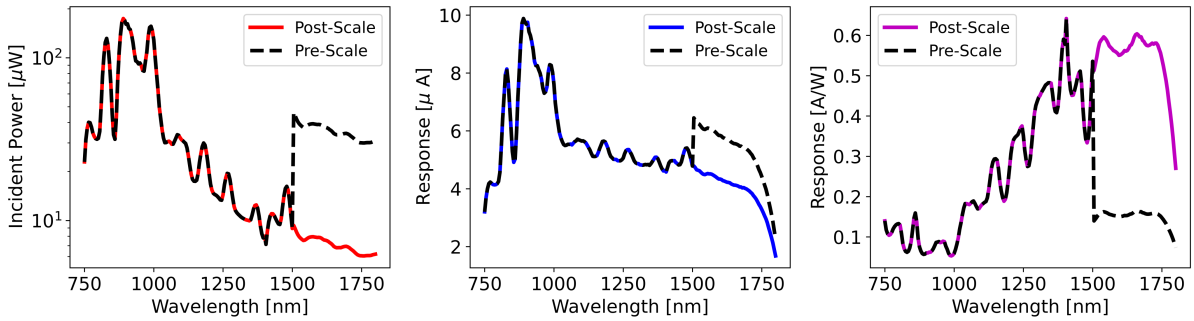


Figure B.7: Example showing how the power spectrum and photocurrent data are processed to account for changes in power transmission through different diffraction gratings used in the monochromator. Two gratings are used over the range of wavelength values selected; the grating change occurs at 1500 nm.

The total integrated power, $P_{total}(\lambda)$, incident on a power sensor photodiode area is recorded over a band of wavelengths. From the beam profile measurements above, the photodetector was positioned in a region of the beam profile with maximal power density, $\Delta P/\Delta r$. For the typical photodetector active area, the power density is nearly constant across the device. Calculating the total power incident on the photodetector, $P_{device}(\lambda)$, is performed by numerical integration of $\Delta P/\Delta r$ along $\Delta r \in \{\Delta x, \Delta y\}$ cross sections over the dimensions of the device active area position relative to the beam profile. The $P_{device}(\lambda = 550\text{nm})$ was calculated from a beam profile measurement taken at a wavelength of 550 nm. Assuming the beam profile does not vary with wavelength, $P_{device}(\lambda)$ was calculated as the normalized total integrated power:

$$P_{device}(\lambda) \coloneqq \frac{P_{device}(\lambda = 550\text{nm})}{P_{total}(\lambda = 550\text{nm})} \times P_{total}(\lambda) \tag{B.1}$$

This method is a reasonable lower-bound approximation for the incident power seen by the photodetectors. Since refractive optics were used for beam collimation and focusing, the beam spot size will slightly increase for $\lambda > 550\text{nm}$ due to chromatic aberrations, decreasing the power density.

Measuring the photodetector current or the light source power spectrum yields discontinuities in the measured spectra due to the change of the diffraction grating at a wavelength

of 1500 nm. The power density at the focal plane of the photodetectors changes due to power transmission variation between the two diffraction gratings used to perform each wavelength sweep measurement. The discontinuity is removed by properly normalizing the current and power spectra for the wavelength range associated with one of the diffraction gratings. The wavelength range, which is normalized, is 1500-1800 nm, and the spectra are normalized by α or β, defined as:

$$\alpha, \beta \coloneqq \frac{f_{G1}^{(I,P)}(\lambda = 1500\text{nm})}{f_{G2}^{(I,P)}(\lambda = 1500\text{nm})} \tag{B.2}$$

where G1/G2 refer to diffraction blaze gratings (G1 $\coloneqq$ grating 1, G2 $\coloneqq$ grating 2) utilized for $f_{G1}^{(I,P)}(\lambda = 1500\text{nm})$ and $f_{G2}^{(I,P)}(\lambda = 1500\text{nm})$ which represent the measured quantities: (current $I \coloneqq f^{(I)}$) or (power $P \coloneqq f^{(P)}$). The normalized response is then calculated using the scale factors α and β:

$$R(\lambda) = \frac{I_{\lambda_1} \cup (\alpha \times I_{\lambda_2})}{P_{\lambda_1} \cup (\beta \times P_{\lambda_2})} \tag{B.3}$$

where $\lambda_1 \in [750\text{ nm}, 1500\text{ nm}]$, $\lambda_2 \in (1500\text{ nm}, 1800\text{ nm}]$, and $\cup$ represents the union of two data sets collected from measurements.

The power and photocurrent measurements are scaled independently such that the last/first values in the wavelength ranges 750-1500 nm and 1505-1800 nm are equivalent for both power and photocurrent spectra. The pre- and post-scaled spectra are plotted in Figure B.7, where the dashed lines are the pre-scaled portions of the respective spectra.

B.4 $In_{0.52}Al_{0.48}As/In_{0.53}Ga_{0.47}As$ Wafer Morphology

As stated in the main text, we observed larger than expected dark currents in the MSM photodetectors, despite having an $In_{0.52}Al_{0.48}As$ barrier layer present. From Nomarski microscope images (see figure S6) of the InAlAs surface, pitting defects can be observed with a density of $\sim 10^6 cm^{-2}$. Such defects can provide low-resistance pathways between the metal electrodes and the InGaAs active layer. Based on previous MBE growths in the same system, we suspect that these defects originate from defects native to the InP growth wafer.

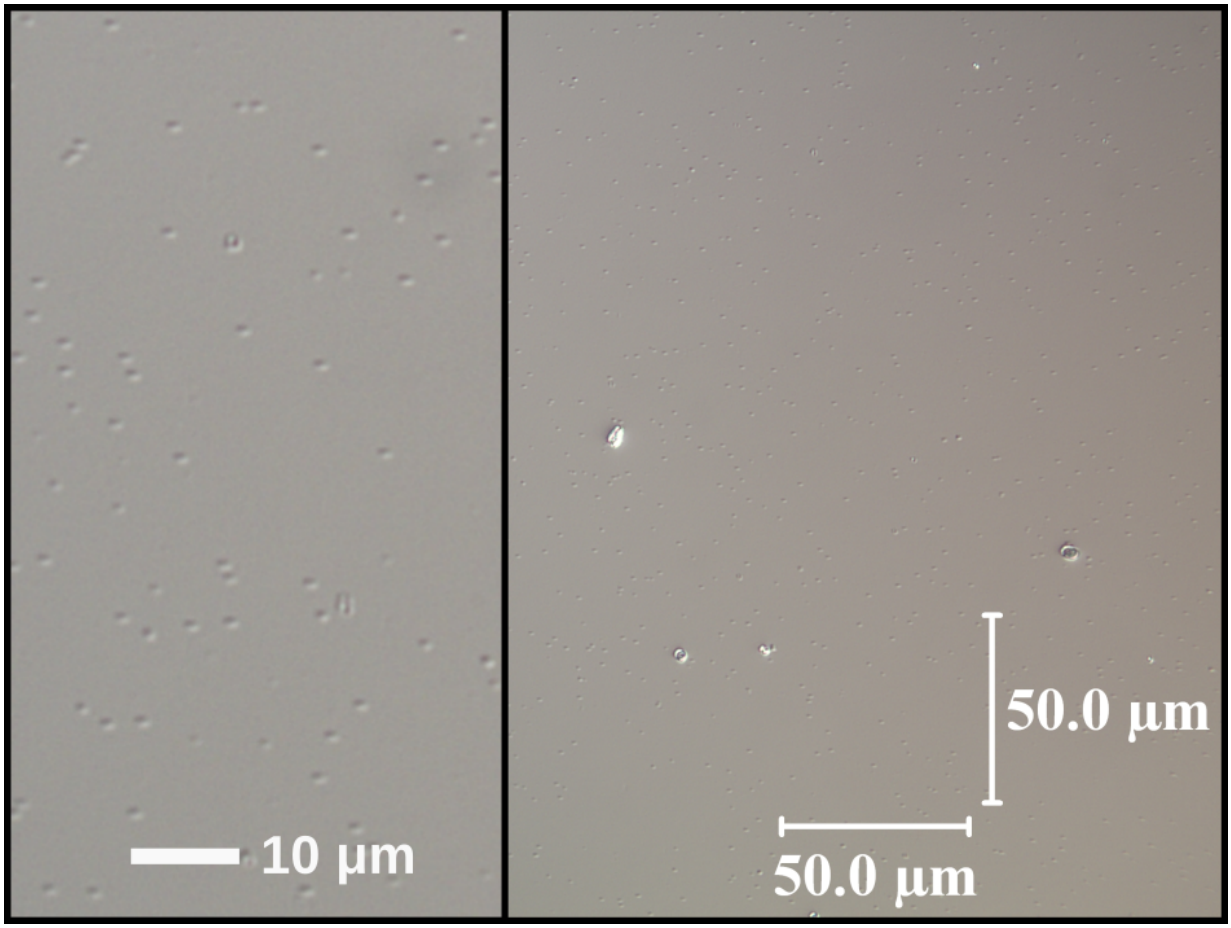


Figure B.8: Characterization of surface defects using a Nomarski microscopy scan of MBE-grown $In_{0.52}Al_{0.48}As/In_{0.53}Ga_{0.47}As$ on InP, taken at the center of the wafer. (left inset) Magnified view of pitting surface defects suspected to result from defects in the InP growth substrate.

B.5 Schottky Contact Model

Using a thermionic emission model for a double Schottky diode from [210], the dark current through the device is given by:

$$J(V) = \frac{2J_S(\Phi_1)J_S(\Phi_2)\sinh\left(\frac{\beta V}{2n}\right)}{J_S(\Phi_1)\exp\left(\frac{\beta V}{2n}\right) + J_S(\Phi_2)\exp\left(\frac{-\beta V}{2n}\right)},$$

where

$$J_S(\Phi_{1/2}) = A_{1/2} A^* T^2 \exp\left(-\beta \Phi_{1/2}\right),$$

and where $\beta = 1/k_B T$, $\Phi_{1/2}$ is the Schottky barrier for either contact, n is the ideality factor assumed to be the same for both contacts, $A_1 = A_2 = 3.342 \times 10^{-7} m^{-2}$ is the area of the contact, $A^* = 1.01 \times 10^5$ A m^{-2} K^{-2} is the Richardson constant for InAlAs, and $J_S(\Phi_{1/2})$ are the thermionic saturation current densities for either contact. From fitting our dark current data to this model, the Schottky barriers and ideality factor are estimated to be: (device A) $\Phi_1 = 0.51$ eV, $\Phi_2 = 0.54$ eV, and $n = 11.92$ (device B) $\Phi_1 = 0.50$ eV, $\Phi_2 = 0.49$ eV, and $n = 18.84$. The theoretically expected Schottky barrier for Ti/InAlAs is 0.7 eV [210]. Figure B.9 shows each model fit and the experimental dark current data with the Normalized Root Mean Square Error (NRMSE) calculated using the equation NRMSE = RMSE/$[max(I_{dark}) - min(I_{dark})]$). NRMSE$_A = 7.6 \times 10^{-4}$ and NRMSE$_B = 9.4 \times 10^{-4}$ for devices A and B, respectively.

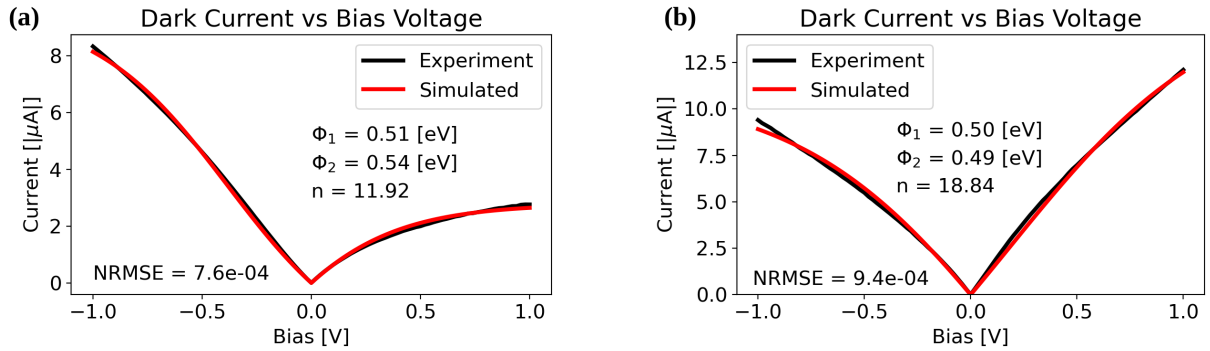


Figure B.9: Dark current versus bias voltage for the as-fabricated InGaAs photodetectors A (a) and B (b) used in this study (black lines). Plotted in red are simulated I-V curves from the double Schottky barrier model described above. Schottky barriers (Φ), ideality factors (n), and Normalized Root Mean Square Errors (NRMSE) determine by the fitting are listed.

B.6 Spectral Specific Detectivity $D^*(\lambda)$

Figure B.10 plots the Specific Detectivity as a function of wavelength for both photodetectors used in this study, before and after NCs were deposited in the active areas.

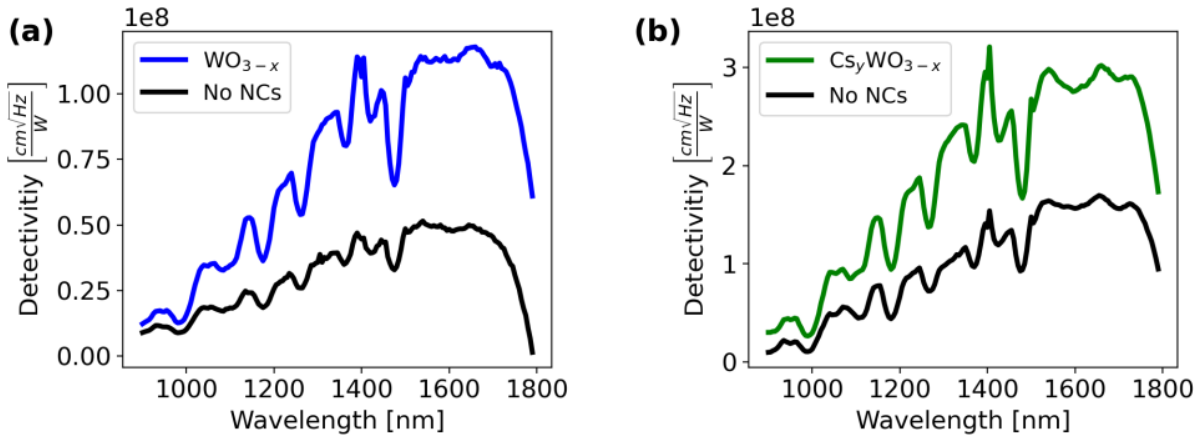


Figure B.10: Specific Detectivity (in Jones, i.e. $\frac{cm\sqrt{Hz}}{W}$) is plotted as a function of incident wavelength for devices A and B, with and without the addition of NCs. Maxmum detectivity prior to adding NCs is $\sim 10^9$ Jones for device A and $\sim 10^{10}$ Jones for device B.

B.7 Photodetector Drop-Casts

A range of photodetector parameters were tested in various combinations creating 4 sets of photodetectors with the same geometries, L $\in \{400\ \mu m,\ 500\ \mu m\}$, S $\in \{3\ \mu m,\ 10\ \mu m\}$, and A $\in \{400\ \mu m \times 440\ \mu m,\ 500\ \mu m \times 540\ \mu m,\ 980\ \mu m \times 540\ \mu m\}$. Selected photodetectors were used for characterizing the quality and variability of drop-cast NCs as seen in figures: B.11, B.12, B.13, B.14, and B.15.

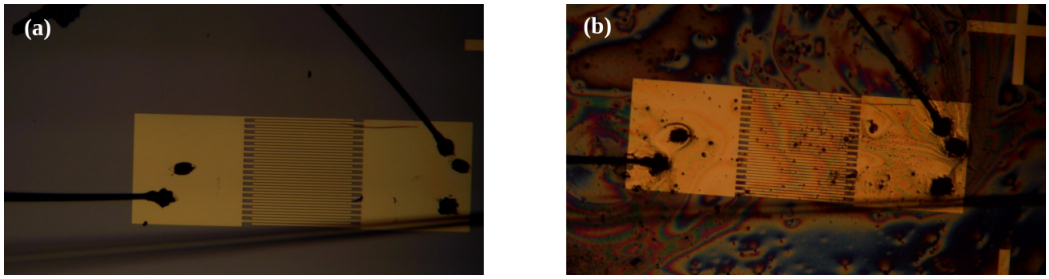


Figure B.11: Optical image of a photodetector taken at 5X magnification (a) before and (b) after drop-casting of WO_{3-x} NCs. The NC concentration and quality of the drop-cast yielded an increased photoresponse compared to the bare photodetector.

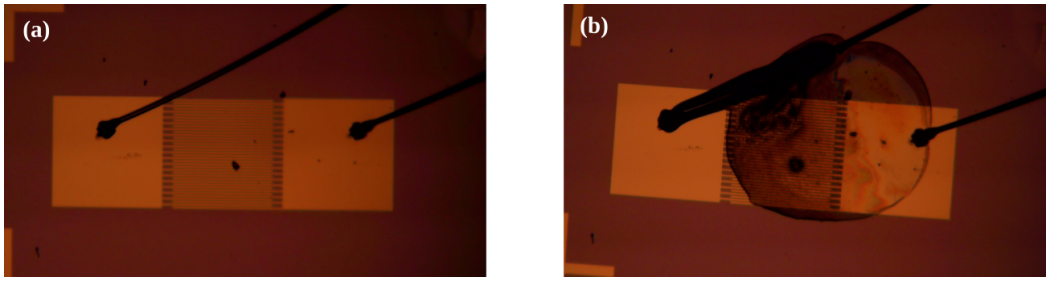


Figure B.12: Optical image of a photodetector taken at 5X magnification (a) before and (b) after drop-casting Cs_yWO_{3-x} NCs. The NC concentration and poor quality of the drop-cast yielded a decreased photoresponse compared to the bare photodetector.

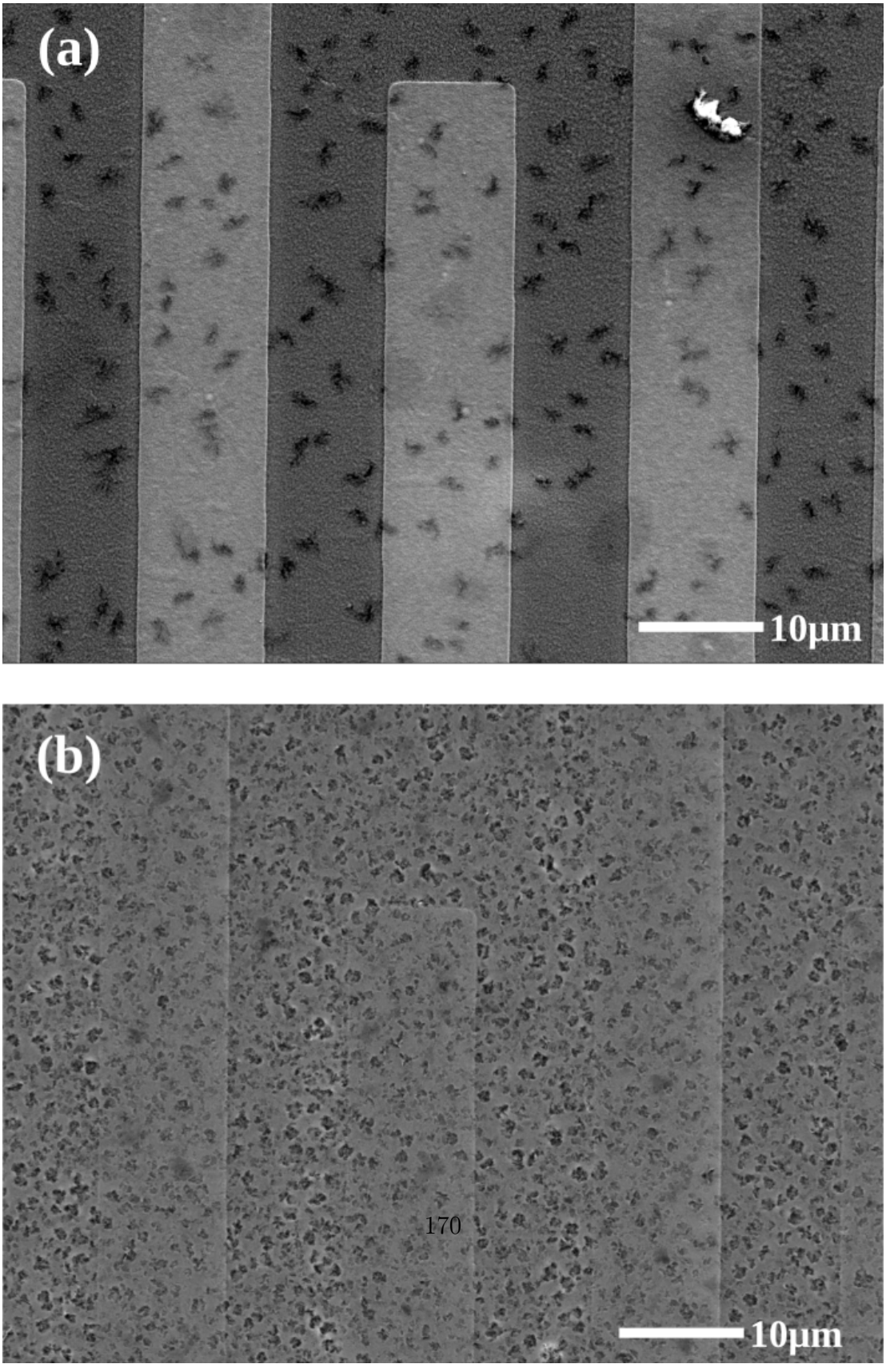


Figure B.13: Scanning electron microscope (SEM) images of drop-cast NC films on the active areas of MSM photodetectors. Images show the distribution of (a) Cs_xWO_{3-y} NCs

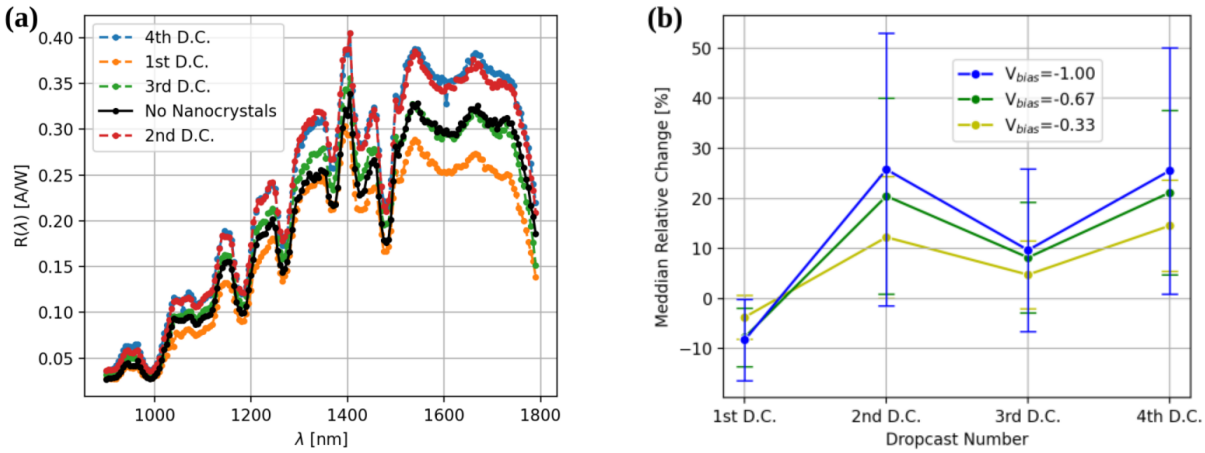


Figure B.14: The effect of successive drop-casts of Cs_yWO_{3-x} NCs using a concentration of 135g/L. (a) Responsivity as a function of wavelength for successive drop-casts. (b) Relative percent difference in responsivity for successive drop-casts, measured at several bias voltages. The median (data points) and standard deviation (bars) of the relative percent difference are calculated over the full wavelength range shown in (a).

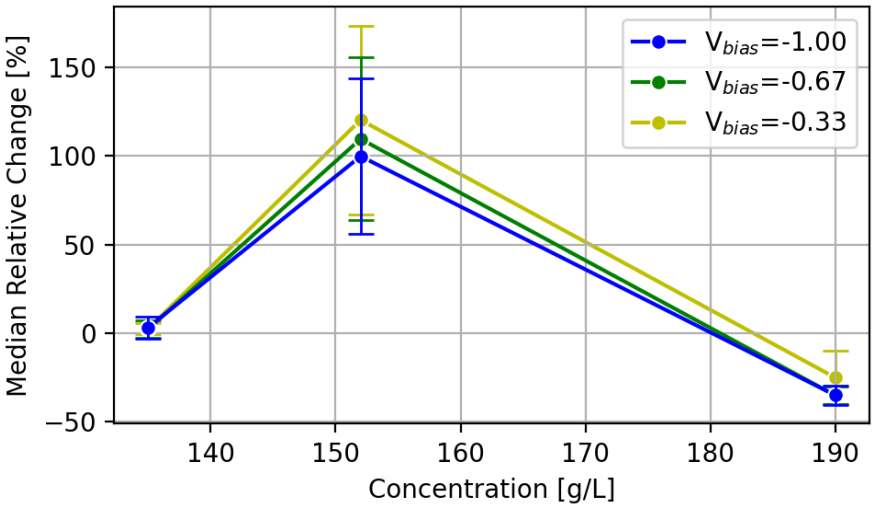


Figure B.15: The effect of drop-cast concentration on the change in responsivity (RPD) for Cs_yWO_{3-x} NCs. Samples were diluted in hexane. The RPD is measured over the full spectrum (900-1800 nm), and the median value is plotted (bars indicate the standard deviation).